

(NASA-CR-151562) STUDY TO INVESTIGATE AND
EVALUATE MEANS OF OPTIMIZING THE Ku-BAND
COMBINED RADAR/COMMUNICATION FUNCTIONS FOR
THE SPACE SHUTTLE Final Report (Axiomatix,
Marina del Rey, Calif.) 355 p HC A16/MF A01 G3/32

N78-13281

Unclas
53658

NASA CR
151562



Axiomatix



Marina del Rey • California

STUDY TO INVESTIGATE AND EVALUATE MEANS OF OPTIMIZING
THE KU-BAND COMBINED RADAR/COMMUNICATION
FUNCTIONS FOR THE SPACE SHUTTLE

FINAL REPORT

Contract No. NAS 9-14614
Exhibit D

Prepared for
NASA Lyndon B. Johnson Space Center
Houston, Texas 77058

Prepared by
Charles L. Weber
Waddah K. Alem
Marvin K. Simon
Axiomatix
13900 Panay Way, Suite 110M
Marina del Rey, California 90291

Axiomatix Report No. R7710-5
October 28, 1977

TABLE OF CONTENTS

	Page
LIST OF TABLES	vi
LIST OF FIGURES.	vii
1.0 INTRODUCTION AND OVERVIEW	1
2.0 DESCRIPTION OF RADAR MODES.	5
3.0 RADAR SYSTEM DESCRIPTION.	9
4.0 POWER BUDGET FOR RADAR PASSIVE TARGET DETECTION	14
5.0 RADAR SEARCH AND TRACK MODES.	19
6.0 TIME MULTIPLEXED SINGLE-CHANNEL ANGLE TRACKING AND ANGLE RATE ESTIMATION OF PASSIVE TARGETS.	27
7.0 RANGE TRACKING OF PASSIVE TARGETS	32
8.0 RANGE RATE TRACKING OF PASSIVE TARGETS.	37
9.0 REDUCTION IN SIGNAL-TO-NOISE RATIO DUE TO QUANTIZATION AND SATURATION NOISE IN A/D CONVERSION.	40
10.0 MAXIMUM LIKELIHOOD ESTIMATOR DESCRIPTION.	43
11.0 POWER ALLOCATION PROPERTIES OF THE THREE-CHANNEL MODULATOR.	45
12.0 CONCLUSIONS AND RECOMMENDATIONS	49
12.1 Power Budgets	49
12.2 Angle Track and Angle Rate Estimation	49
12.3 Range Tracking	50
12.4 Doppler Tracking.	51
APPENDIX	
A. POWER BUDGETS FOR THE KU-BAND RADAR FOR THE SPACE SHUTTLE ORBITER VEHICLE	A-1
1.0 Introduction.	-1
2.0 The Radar Equation.	-1
3.0 Search Radar System Parameters.	-2
4.0 Power Budgets for Passive Search.	-15

		Page
B.	RADAR PASSIVE SEARCH AND TRACK MODES DESCRIPTION	B-1
1.0	Introduction	-1
2.0	Radar Block Diagram.	-2
3.0	Antenna Assembly	-4
4.0	IF Mixing and I-Q Stages	-6
5.0	Signal Parameters.	-6
6.0	The Search Mode.	-8
7.0	The Track Mode	-12
C.	TIME MULTIPLEXED SINGLE CHANNEL ANGLE TRACKING OF PASSIVE TARGETS.	C-1
1.0	Introduction	-1
2.0	Single Channel Amplitude Monopulse	-2
3.0	Description of Single Channel Monopulse.	-5
4.0	Performance of the Amplitude Monopulse Angle Tracking Loop.	-26
5.0	Performance Computations	-29
6.0	Comments Concerning the Filter Response of the Discrete Fourier Transform	-34
D.	THE ESTIMATION OF ANGLE RATE	D-1
E.	TIME-MULTIPLEXED SINGLE CHANNEL RANGE TRACKING OF PASSIVE TARGETS.	E-1
1.0	Introduction	-1
2.0	Description of Single-Channel Monopulse Tracking Block Diagram.	-1
3.0	Pre-Sum (Range Gates).	-7
4.0	Doppler Filters (Range Rate Tracking).	-8
5.0	Statistical Parameters of Doppler Filters Outputs	-9
6.0	Range Tracking Discriminant Generator.	-13
7.0	Performance of Range Tracking Loop	-20
8.0	Performance Computations	-23
9.0	Signal-to-Noise Ratio Coupling Loss.	-25

		Page
F.	CONTINUOUS TIME α - β TRACKER MODEL FOR RANGE TRACKING. . . .	F-1
1.0	Introduction.	-1
2.0	Equivalent Continuous - Tracker Transfer Function.	-1
3.0	Range Tracking Loop Noise Bandwidth	-5
G.	TIME MULTIPLEXED SINGLE CHANNEL RANGE RATE TRACKING OF PASSIVE TARGETS	G-1
1.0	Introduction.	-1
2.0	Description of Single Channel Monopulse Tracking System.	-2
3.0	Pre-Sum (Range Gates)	-6
4.0	Doppler Filtering	-7
5.0	Statistical Parameters in Doppler Filter Outputs.	-10
6.0	Range Rate Tracking Discriminant Generator.	-14
7.0	Performance of Range Rate Tracking Loop	-20
8.0	Performance Calculations.	-24
9.0	Doppler Ambiguity Resolution.	-26
H.	REDUCTION IN SIGNAL-TO-NOISE RATIO DUE TO QUANTIZATION AND SATURATION NOISE IN A/D CONVERSION.	H-1
1.0	Introduction.	-1
2.0	Quantization and Saturation Noise	-2
3.0	Performance	-7
I.	SHORT RANGE POWER BUDGET FOR THE KU-BAND RADAR PASSIVE SEARCH.	I-1
1.0	Introduction.	-1
2.0	Detection Procedure at Short Ranges	-1
3.0	Radar Equation.	-4
4.0	Search Radar System Parameters.	-5
5.0	Power Budget for Short Range Passive Search	-12

J.	MAXIMUM LIKELIHOOD ESTIMATION OF THE RATIO OF POWERS IN TWO NARROWBAND PROCESSES	J-1
1.0	Introduction.	-1
2.0	The Maximum Likelihood Estimate of Power Ratio. .	-1
3.0	Statistical Characteristics of the Observations .	-2
4.0	Performance of M.L. Estimate of Power Ratio . . .	-4
K.	POWER ALLOCATION PROPERTIES AND COSTAS LOOP SUBCARRIER TRACKING PERFORMANCE ASSOCIATED WITH A DIGITAL SHIFT IMPL- EMENTATION OF THE THREE-CHANNEL ORBITER KU-BAND MODULATOR. .	K-1

LIST OF TABLES

		Page
(1)	Signal Parameters During Search	7
(2)	Signal Parameters During Track	7
(3)	Number of Independent Samples Used for a Single Measurement	8
(4)	Radar Transmit Frequencies Synthesis	11
(5)	Power Budget for Short Ranges	18
(6)	Ku-Band Radar RF Frequencies and Their Corresponding PRF Frequencies	22
(7)	Signal and Noise Powers Available for Data Detection	54
(8)	Squaring Loss and RMS Tracking Jitter	55

LIST OF FIGURES

	Page
1. Radar Modes	6
2. Functional Block Diagram for the Integrated Ku-Band Radar/Communication Equipment	10
3. Straddling Loss vs. Range R	15
4. Design Margin vs. Range for the Fast Fading Case. . .	16
5. Radar Block Diagram	20
6. Long Range Search Signals	23
7. Search Mode Signal Processing	24
8. Track Mode Signal Format	26
9. Block Diagram of Single Channel Monopulse Angle Tracking Loop	28
10. RMS Angle Tracking Error of Passive Radar vs. Range (n.mi.)	29
11. Performance of Angle Rate Estimation vs. Range in Nautical Miles	31
12. Block Diagram of Single Channel Monopulse Range Tracking Loop	33
13. Standard Deviation of the Output of the Logarithmic Discriminant Generator vs. Signal-to-Noise Ratio at the Output of the Doppler Filters for Certain Values of N.	34
14. Range RMS Error vs. Range with α as a Parameter . . .	35
15. Block Diagram of Single Channel Monopulse Range Rate Tracking Loop	38
16. Standard Deviation of the Output of the Logarithmic Discriminant Generator vs. Signal-to-Noise Ratio for N = 20, 40	39
17. RMS Range Rate Tracking Error of Passive Targets vs. Range	41
18. Doppler Frequency Location	42
19. Mean of Range Rate Logarithmic Discriminant Output. .	44
20. Range Rate Discriminant Error with a Straight Line Mapping whose Slope is Equal to the Slope of E(z) at No Doppler and SNR $\rightarrow \infty$	45
21. Expected Value of Logarithmic Discriminant Output vs. SNR for Various Values of $\xi = \Delta f_d/B_F$	46

		Page
22.	Normalized Quantization and Saturation Loss vs. Input Signal-to-Noise Ratio for M=3 to M=6 Bits of Quantization	48
23.	Output Signal-to-Noise Ratio vs. Input Signal- to-Noise Ratio for M=3 to M=10 Bits of Quantization	49
24.	Standard Deviation of the Random Variable z as a Function of Correlation	51

1.0 INTRODUCTION AND OVERVIEW

This is the final report for the "Study to Investigate and Evaluate Means of Optimizing the Ku-Band Combined Radar/Communication Functions for Space Shuttle" (Contract NAS 9-14614, Exhibit D). The study consists of analytical tasks directed towards optimizing the design of a baseline configuration for the Ku-Band Integrated Radar and Communication Equipment. The Ku-Band equipment described and analyzed in this report is being developed by Hughes Aircraft Company for the Rockwell International/Space Division, Downey, California. The equipment contractor is presently proceeding with implementation of its proposed and continuously updated baseline design. There are a number of areas still outstanding which require analytical support in order to make the performance compatible with the requirements. Most of these topics are addressed in this final report.

Although, as the description implies, the Integrated Equipment performs both the radar and the communication functions, the tasks described in this report pertain primarily to the radar mode of operation. The only aspect of the communication mode analyzed in this report is the power allocation properties and the Costas loop subcarrier tracking performance associated with the Hughes baseline digital phase shift implementation of the three-channel orbiter Ku-band modulator. Analysis of other facets of the optimized communication mode operation has been described in one of the recent Axiomatix reports [2].

Briefly, the Ku-Band Integrated Radar and Communication Equipment time shares the two respective functions during the various phases of the Space Shuttle orbital flights. The radar is used for rendezvous with orbiting passive targets, as well as with cooperative (transponder-equipped) targets. Rendezvous requirements include initial detection of passive targets at the maximum range of 12 nmi. The active targets are to be detected at a 300 nmi maximum range.

Subsequent to detection, the radar is expected to track its targets to a range as short as 100 feet in some cases, where the station-keeping and rendezvous take place. Target parameters measured by the radar during the tracking phase include: (1) range, (2) range rate, (3) angle (azimuth and elevation), and (4) angle rate (azimuth and elevation). The radar is a coherent pulse doppler type with a peak

transmitter power of 60 watts nominal. A 36-inch diameter center-fed parabolic dish is used as the primary antenna, whose terminals also provide the two-axis monopulse difference signals used for angle tracking. Both the transmitter, which is a TWT amplifier, and the antenna with its associated monopulse electronics are shared with the communication mode.

In the communication mode, the Integrated Equipment is used as a spaceborne terminal to provide a Ku-band two-way link between the Shuttle Orbiter and the ground. This Ku-band link is via the TDRS. The forward link to the Shuttle consists of a 216 kbps data stream spread by a 3.03 Mcps PN code to reduce the power density incident upon the earth.

The return link consists of three independent data streams phase-multiplexed for transmission on a single carrier. The data rates of the three channels range from about 200 kbps for the lowest rate channel to as high as 50 Mbps for the wideband channel.

The forward link communication signal is received at the Shuttle on the nominal frequency of 13.775 GHz. The return link communication transmission to the TDRS is on a 15,003 MHz carrier. The radar operates in the approximate vicinity of the communication receive frequency. This permits time sharing of the receiver and the monopulse electronics between the two functions. The radar operating frequency is hopped over approximately 200 MHz to reduce target scintillation.

The baseline design proposed for the Ku-Band Integrated Radar and Communication Equipment by Hughes [3] is based upon a subdivision of the equipment into five subunits which are:

- (1) Deployed Mechanism Assembly (DMA)
- (2) Deployed Electronics Assembly (DEA)
- (3) Electronics Assembly 1 (EA-1)
- (4) Electronics Assembly 2 (EA-2)
- (5) Signal Processor Assembly (SPA).

The deployed mechanism assembly (DMA) includes the antenna reflector, feed, antenna gimbals, drive motors, gyros, digital shaft encoders, rotary joints and connecting waveguides, and associated wires and cables.

The deployed electronics assembly (DEA) consists of a common receiver and transmitter, used for both radar and communication, and a common crystal-controlled exciter/LO generator, also shared by the two functions. The interconnection between the DEA and the DMA is via two rotary joints and cable wraps.

Both the DMA and the DEA are located within the Shuttle payload bay and thus have to be deployed for their operation upon the opening of the payload bay doors.

The communications electronics assembly 1 (EA-1) includes the PN despreaders, the Costas loop phase-lock demodulator, the antenna servo control electronics and motor drive amplifiers, the data multiplexer/demultiplexer, and input/output buffers. As a subunit of the communication receiving equipment, the EA-1 also contributes to the TDRS signal acquisition and forward link data detection.

The electronics assembly 2 (EA-2) consists of the radar second mixer, second IF amplifier, I/Q detectors, digital Fourier transform (DFT) doppler processor, radar angle tracking circuits, radar range tracking circuits, radar range rate tracking circuits, radar timing and control, and the radar AGC detector.

The signal processing assembly (SPA) includes management logic, forward data processing, and return link data multiplexing.

Both of the electronics assemblies, as well as the signal processor assembly, are located in the avionics bay of the Shuttle. The interconnection with the two deployed assemblies is via wires and coaxial cables.

Of the five assemblies listed above, the functions performed by the EA-2 are given main consideration in this report. The functions of other assemblies are described only where necessary to explain equipment operation in the radar mode.

Section 2.0 discusses the various radar modes of operation, while Section 3.0 presents the description of the radar system as configured by the appropriate assemblies. The summary of the power budgets for passive radar detection is given in Section 4.0, with the supporting analysis contained in Appendices A and I for long range and short range detection, respectively.

Section 5.0 summarizes radar search and track operations, with detailed description given in Appendix B.

Time-multiplexed single-channel angle tracking and angle rate estimation of passive targets are described briefly in Section 6.0 and in detail in Appendices C and D, respectively. A summary of range tracking performance is presented in Section 7.0 and analyzed in Appendices E and F. The problems associated with range rate tracking are outlined in Section 8.0 with the detailed analysis presented in Appendix G.

The reduction of signal-to-noise ratio due to quantization and saturation noise in A/D conversion is analyzed in Appendix H. A summary of the results is presented in Section 9.0. Section 10.0 describes the maximum likelihood estimator used for the range, range rate and angle tracking. Supporting analysis is given in Appendix J.

In Section 11.0, a summary of the results for the power allocation properties and the subcarrier tracking performance for the three-channel orbiter modulator in the communication mode is presented. The detailed analysis is given in Appendix K.

Conclusions and recommendations are presented in Section 12.0.

2.0 DESCRIPTION OF RADAR MODES

In this section, the various modes of operation that are required of the Ku-Band Radar are outlined.

There are essentially two basic radar modes, the passive mode and the active mode, depending on whether the target is passive (no transponder) or active (with transponder). These two modes have four sub-modes of operation:

- (1) GPC ACQ: General Processing Computer Acquisition Mode.
- (2) GPS DES: General Processing Computer Designation Mode.
- (3) Manual Mode.
- (4) Autotrack Mode.

In addition to these is a radar self-test mode. Figure (1) illustrates the relation between these modes [1].

In the GPC-ACQ mode, the antenna is inertially stabilized and, upon target detection, automatically tracks the target providing estimates of target angle, range, and range rate.

In the GPC-DES mode, the antenna stabilization is externally selectable and can be referenced to either inertial space or the spacecraft axes. In this mode, angle track is inhibited. Upon target detection, the target is tracked and estimates of range and range rate are provided.

In the manual mode, the antenna position is determined by external slew commands. Angle track is also inhibited in this mode. Upon detection, the target is tracked and estimates of range and range rate are provided.

In the autotrack mode, the antenna is inertially stabilized and, upon target detection, automatically tracks the target providing estimates of target angle, range, and range rate.

The basic difference between the passive mode and the active mode stems from the fact that a cooperative target is assumed in the active mode. The signal format for the various modes depends on whether the radar is searching or tracking and also on the range to the target. Table (1) summarizes the various signal parameters during search, while Table (2) lists the parameters during tracking.

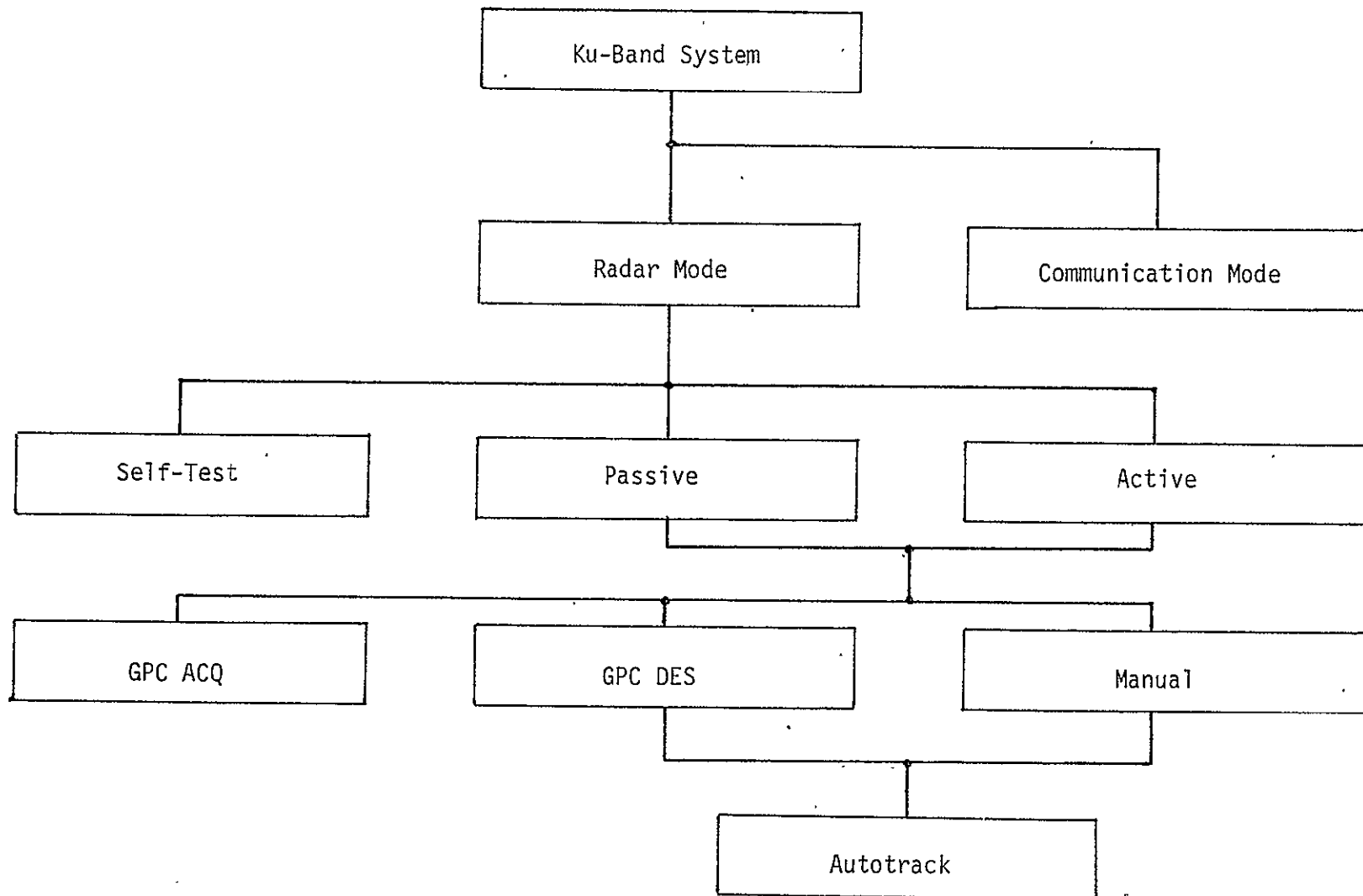


Figure 1. Radar Modes.

Table (1)
Signal Parameters During Search

Mode	Sub-Mode	Range (nmi)	PRF (hz)	N _{RB}	N _{PDI}	Pulse Width μsec
Passive	GPC ACQ/ DES	>7.2	2987	2	5	66.4
		3.8 - 7.2	6970	2	5	33.2
		1.9 - 3.8	6970	2	5	16.6
		0.95 - 1.9	6970	2	5	8.3
		0.42 - 0.95	6970	2	5	4.15
		<0.42	6970	50	1	0.122
	Manual	>0.42	2987	4	5	66.4
		<0.42	6970	50	1	0.122
Active		>10	268	1800	1	4.15
		<10	268	50	1	0.122

Table (2)
Signal Parameters During Track

Mode	Sub-Mode	Range (nmi)	PRF (Hz)	Pulse Width (μ sec)	Duty Factor
Passive	All Submodes	>9.5	2987	33.2	0.0992
		3.8 - 9.5	6970	16.6	0.1157
		1.9 - 9.8	6970	8.3	0.0578
		0.95 - 1.9	6970	4.15	0.0289
		0.42 - 0.95	6970	2.07	0.0144
		<0.42	6970	0.122	8.5×10^{-4}
Active		10 - 300	268	4.15	1.2×10^{-3}
		<10	6790	0.122	8.5×10^{-4}

Table (1) shows the PRF and the pulse lengths selected for the GPC modes where the range to the target is designated to the radar with an accuracy of 10 percent. In each case, two overlapping range gates with width equal to $3/2$ of the pulse width are selected so as to cover the range uncertainty completely. In the manual mode, no range designation is provided. In that mode, four range windows are provided with each repetition rate which cover the entire range interval. As for the active mode, a PRF of 268 Hz is selected so as to assure an unambiguous range of about 300 n.mi.

Since there are 5 RF frequencies that are transmitted, the PRF's in the track mode are adjusted so as to insure a constant product of wavelength and operating PRF. This keeps the doppler frequency shift constant over the 5 RF frequencies and thereby simplifies greatly the computations. The variations of PRF with the RF frequency are shown in Appendix B.

Tracking errors of the four target parameters, range, range rate, azimuth angle and elevation angle, are obtained via the difference of two logarithmic measurements of the target parameter. The number of independent samples per measurement is explained in detail in Appendix B. Table (3) summarizes the results.

Table (3)
Number of Independent Samples used for a Single Measurement

Parameter Being Tracked	Number of Independent Samples	Description
Angle	10	2 (range gates) x 5 (RF Frequencies)
Range	20	4 (Time Slots) x 5 (RF Frequencies)
Range Rate	40	4 (Time Slots) x 2 (Range Gates) x x 5(RF Frequencies)

Reference is made throughout to the various radar modes of operation. Particular emphasis is placed on the GPC DES mode for a passive target, since that is expected to be the most commonly used.

3.0 RADAR SYSTEM DESCRIPTION

The functional block diagram for the Integrated Ku-Band Radar/Communication Equipment operating in the "Radar" mode is shown in Figure (2). The diagram is presented in a manner which reveals the signal flow interaction between the assemblies utilized for the radar operation. Sub-units utilized for the communication function are shown in this diagram only if they are time-shared with the radar function.

The four subassemblies of the Ku-Band Integrated Equipment shown in Figure (2) are: Deployed Electronics Assembly (DEA), (2) Deployed Mechanism Assembly (DMA), (3) Electronics Assembly 2 (EA-2), and (4) Electronics Assembly 1 (EA-1). The function of each assembly, as well as that of the overall system, can be understood best by following the signal flow.

The coherent frequency synthesizer located within the DEA provides all the RF, LO, and IF signals required to generate, transmit, receive and demodulate the radar signals. The radar signal originates in the Radar Modulator located within the DEA. The modulator accepts a 651 MHz CW signal from the synthesizer and keys it in accordance with a selected transmit/receive T/R pulse modulation format. The latter is developed by the timing and control unit within the EA-2. The passive mode of the radar employs frequency diversity at all times. As a result, the pulse modulated 651 MHz signal is up-converted to the 13.8 GHz (approximate) radar operating band by mixing with the five hopped frequencies of the translation oscillator (TO) signal. This upper side-band translation is shown in Table 4.*

As shown in Table 4, the radar frequencies are spaced 52 MHz apart, resulting in a total diversity bandwidth ΔF of 208 MHz.

The output of the up-converter is applied to a preamplifier, which consists of a high frequency FET device. The preamplifier, in addition to supplying the gain, provides limiting prior to the TWT. This limiting minimizes the AM-to-PM conversion of the transmitted signal passing through the TWT. The power output P_1 of the FET limiting preamplifier unit is about +7 dBm.

*In the communication mode, only the 13,128 MHz TO signal is mixed with the 1,875 MHz communication modulator carrier, resulting in a single transmit center frequency of 15,003 MHz (15.003 GHz).

Table 4. Radar Transmit Frequencies Synthesis

T.O. Frequencies (MHz)	Radar Modulator Center Frequency (MHz)	Up-Converter Output (T _x Frequencies) (MHz)	
13,128	Add 651	13,779	Radar Freq. (Upper Side- band)
13,180		13,831	
13,232		13,883	
13,284		13,935	
13,336		13,987	

In the search mode and the "long range" (over 3000 feet) track mode, the radar signal is amplified by the TWT. This amplification brings the drive power P_1 to the nominal 60 watts peak output power P_2 . The tube gain assumed for this case is 44 dB. The function of the variable attenuator is to reduce the TWT output power for the short-range operation.

The output of the TWT is also gated in accordance with the T/R signal. Such gating prevents the tube noise from interfering with the low level signals received during the search and the long range tracking operations. Note that the TWT output is delivered to the High Power Pulser by means of Diplexer 1. This diplexer restricts the gating function only to radar region of the TWT output signal. Diplexer 2 re-inserts the gated radar signal into the main transmitter output RF line. The latter connects the transmitted signals (both radar and comm), via a circulator and a rotary joint, to the main antenna. Switch 3 is used only in the communications mode. For the initial acquisition of the TDRS, the TWT output is radiated via the auxiliary horn to facilitate spatial search for the TDRS signal by the TDRS.

In the short range radar mode, the TWT amplifier is bypassed and the preamplifier output is applied directly to Diplexer 2. Switch 1 is used to gate the low level signal and Switch 2 is in the SR position. The gated low level signal, like the TWT output, is applied to

the main antenna via the circulator and the rotary joints. The position of Switch 2 therefore determines whether the TWT or the preamplifier output is applied directly to the main antenna.

The main antenna, which is a 36-inch diameter, prime-fed parabola, is a part of the deployed mechanism assembly (DMA). The antenna uses a five-element monopulse feed. Four elements are used to generate the Δ AZ and Δ EL errors in the monopulse bridge. The fifth element is used for transmission and reception of either the radar or the communication signals. During the reception, the fifth antenna element provides the sum (Σ) channel signal. The polarization of the main antenna is selectable. For the communication mode, it is circular (RHC) for both transmit and receive. During the radar mode, the polarization is linear and transmission is only via the main antenna.

The reception of the signal returned by either a passive or an active target is performed by both the main parabolic and auxiliary horn antennas. The purpose of the horn reception is to guard against the sidelobe lock-ons. The main antenna provides the sum (Σ) signal to the receiver. The monopulse bridge provides the two difference (Δ) signals, i.e., Δ AZ and Δ EL. The sum channel output $R_x(s)$ passes through rotary joint 1, the circulator, the transmit/receive (T/R) switch, and terminates at the input of the Σ -channel first mixer, $M(\Sigma)$.

The two Δ AZ and Δ EL signals are time-multiplexed into a common channel, henceforth referred to simply as the Δ -channel. During the spatial search for the radar target, the receiver channel, which is used exclusively for Δ -signal amplification during the track mode, amplifies the output of the auxiliary horn. This is accomplished with Switch 4 in the "Guard" position. The guard signal passes through rotary joint 2, Switch 5, the T/R switch, and terminates at the input of the Δ -channel receiver first mixer $M(\Delta)$.

The first mixers translate their respective Ku-band input signals to the first IF frequency. In the radar mode, the first LO signal applied to these mixers is the same frequency-hopped signal which is used for the up-conversion in the radar transmitter. The incoming frequency-hopped signal is therefore de-hopped in a similar manner to that shown in Table 4.

For monopulse tracking in both the radar and communication modes, a portion of the Σ -channel signal is applied to the Δ -channel, thus forming $\Sigma \pm \Delta AZ$ and $\Sigma \pm \Delta EL$ signals. As shown in Figure 2, this summation is performed at the first IF. Because the guard channel is not required in the tracking mode, Switch 6 remains in the $\Sigma \pm \Delta$ position during tracking.

During the search phase, the guard channel has to be sampled periodically to prevent the lock-up onto the sidelobes. The sampled guard channel output is then compared to the main lobe, i.e., the sum channel signal. Alternating the position of Switch 6 between the $\Sigma \pm \Delta$ and the GD (Guard) terminals permits time-sharing of the single second IF channel of the radar receiver. It must also be noted that, during search, the Δ -signals are not used and, consequently, the signal which is $\Sigma \pm \Delta$ during tracking is actually only Σ during acquisition. Furthermore, as explained in Sections 5.0 to 7.0, the tracking of salient radar measurement parameters such as range, velocity (range rate), and angle are performed on the $\Sigma \pm \Delta AZ \pm \Delta EL$ signal, which is the only signal supplied to the third IF of electronics assembly 2 (EA-2).*

The second IF radar signal is amplified and applied to a coherent processor which consists of in-phase (I) and quadrature (Q) detectors. The analog outputs of these detectors are low-pass filtered and then converted to digital data which contains both the amplitude and phase information of the received signal.

The subsequent processing of the radar signal is all digital. The processing consists of presum, digital Fourier transform (DFT), post-detection integration (PDI), and logarithmic discriminant generator. During the search mode, the output of the PDI is applied to the threshold detector which stops the antenna search pattern when the target is detected. Subsequently, the angle and range tracking units take over and the system is switched from the "track" mode to the "search" mode. Descriptions of the search and track modes are presented in Section 5.0 and Appendix B of this report.

*For the communication mode only, the Σ -channel is translated to the third IF located in EA-1. The recovery of the angle tracking information is performed by envelope detection of the $\Sigma \pm \Delta AZ \pm \Delta EL$ signal at the first IF and by subsequent demultiplexing.

4.0 POWER BUDGET FOR RADAR PASSIVE TARGET DETECTION

The initial detection of the passive 1 m^2 target at the 12 nmi range is the driving requirement for the radar system's power budget. The search power budget for the long ranges is explained in Appendix A, while the power budget for short ranges is obtained in Appendix I. There are two basic modes of operation in search, one with range designation from the GPC and the other without any designation. In the first mode, two overlapping range gates with width equal to $3/2$ the transmitted pulse width are used to collect the return pulse energy while in the second mode, four range gates are used to cover the unambiguous range. The basic difference between the two modes lies in the amount of range gate straddling loss as explained in Appendix A. Figure (3) summarizes the straddling loss for the two modes. It is noted that while the loss varies from zero to six (dB) in the undesignated mode, it is always equal to a maximum of 1.76 dB in the designated mode.

Assuming a fast fading target (SWERLING II) model for long ranges, the design margin for the two modes are shown in Figure (4). It is noted that there is a negative design margin down to $R=8.4$ nmi for the designated mode. The margin at 12 (nmi) is equal to -6.3 dB for the designated range and -6.8 dB for the nondesignated range as compared to -1.0 dB and +0.1 dB, respectively obtained by HAC calculations as presented in their Monthly Review [11].

There are two major reasons for the difference.

- 1) Doppler filter loss of 3.9 dB is calculated in this report assuming DFT operation while a loss of 1.1 dB only is quoted by HAC. The 3.9 dB loss stems from the fact that the DFT results in a filter with frequency response $\left| \frac{\sin Nx}{N \sin x} \right|^2$ rather than $\left| \frac{\sin Nx}{Nx} \right|^2$.
- 2) The beam shape loss used in this report and calculated in [4] is equal to 3.2 dB as opposed to 2 dB used by HAC.

As for short ranges, $R < 0.42$ (nmi) Swerling IV model is assumed for the target in Appendix I, which gives a pessimistic assumption. The basic difference between target detection for long and short ranges lies in the fact that while 16 pulses are coherently added (presumming) and

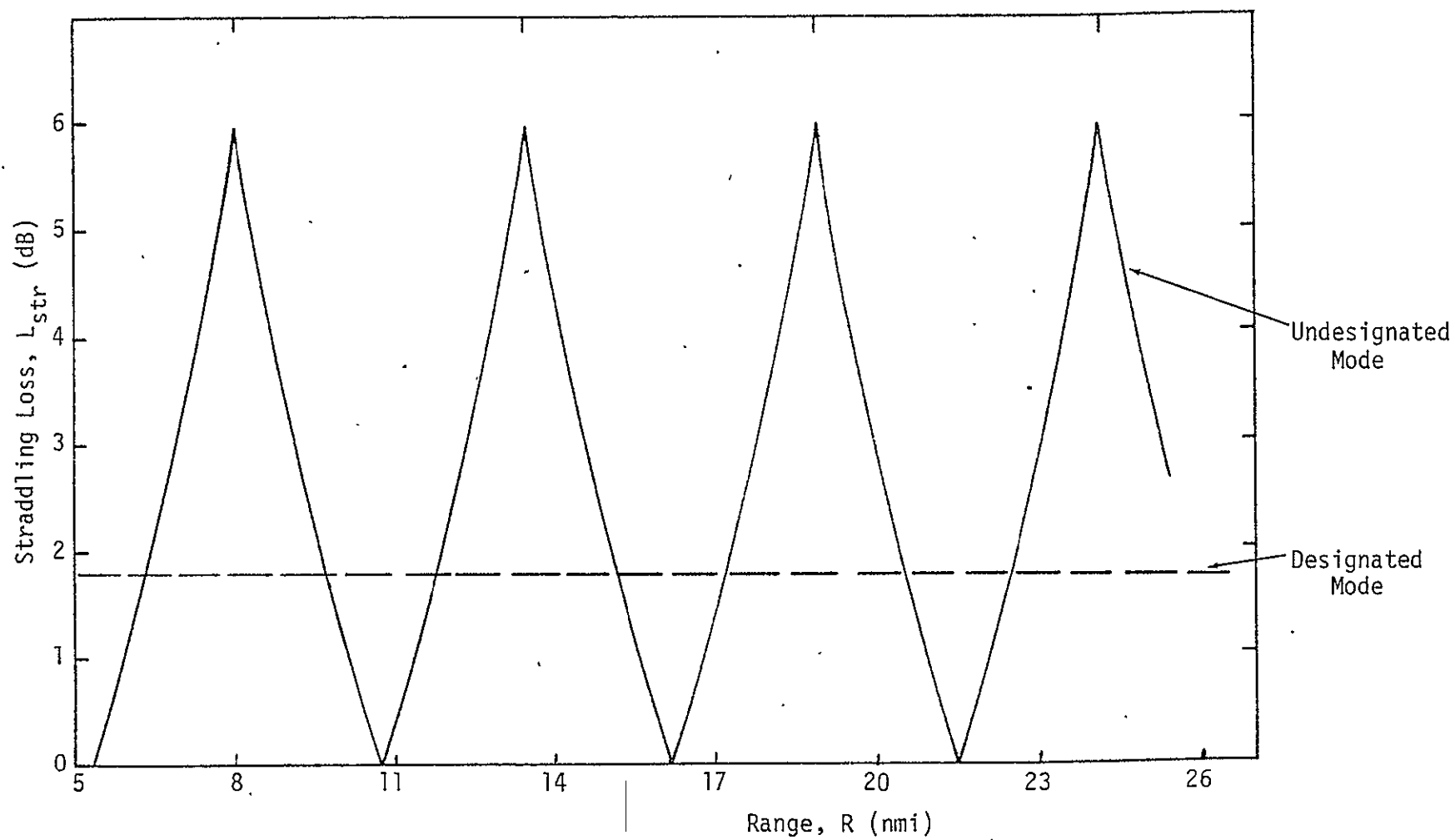


Figure 3. Straddling Loss vs. Range R

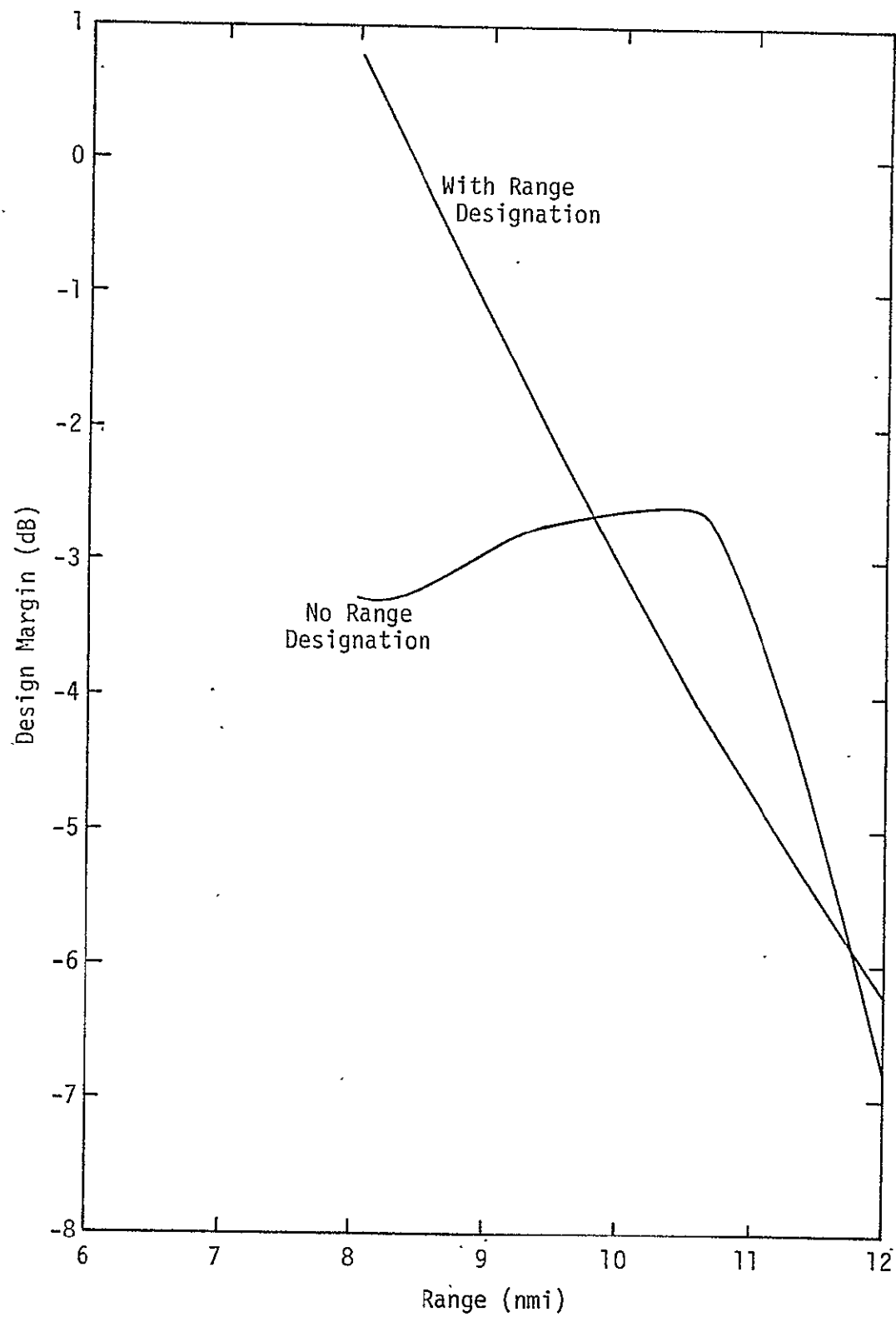


Figure 4. Design Margin vs. Range for the Fast Fading Case

passed through a bank of doppler filters in the first case, a single pulse detection without filtering is implemented in the second case. Table (5) summarizes the power budget calculations at the indicated ranges.

TABLE 5. Power Budget for Short Ranges

Term	Value	Budget, dB
\bar{R}_p	Required Peak SNR	17.6
G^2	$G = 38.5$ dB	-77.0
λ^2	$\lambda = 0.0216$ m	33.31
σ	1 m^2	0.0
$(4\pi)^3$	-	32.98
R^4	$R = 2550, 800, 250$ ft.	115.65, 45.49, 75.28
k	3.8×10^{-23} Joules/ $^{\circ}\text{K}$	-228.6
T_s	1500 $^{\circ}\text{K}$	31.76
τ	Pulsewidth: 0.122 μsec	69.14
	Factor of 2	-3.0
<u>Losses</u>		
Transmit	REP	3.7
Beam Shape	Scan Alignment	2.0
Threshold	Constant FAP	1.0
Straddling	Spreading of Pulse	6.5
P_p	Required Peak Powers	4.94 -15.22 -35.44 dBw (34.94) (19.78) (-5.44)dBm

Comparing the required peak powers to the existing available power of 47 dBm, 23 dBm, and 7 dBm, it is found that

- (1) Design margin at 2550 feet compared to the available 47 dBm
= 12.06 dB.
- (2) Design margin at 800 feet compared to the available 23 dBm
= 8.22 dB.
- (3) Design margin at 250 feet compared to the available 7 dBm
= 12.44 dB.

5.0 RADAR SEARCH AND TRACK MODES

The objective of the Ku-band radar system on the Shuttle Orbiter is to detect the presence of a target and then obtain continuous accurate estimates of the various target parameters, namely, its range, range rate (velocity), azimuth angle, elevation angle, and angle rates. The target is first detected when the radar is in the search mode; then the accurate estimates are obtained in the track mode.

The radar employs coherent processing over each RF frequency transmitted and noncoherent postdetection integration (PDI). Following the intermediate amplifiers, in-phase and quadrature phase signals are sampled and digitized (A/D converted), providing target amplitude and phase information. For longer range search and acquisition ($R > 3000$ ft), 16 doppler filters are formed, covering the doppler interval defined by the repetition rate. This is an ambiguous doppler interval; this ambiguity is removed via differentiation of the range estimates.

Following the filters, the target magnitude is determined, summed over the number of RF frequencies (noncoherent postdetection integration) and compared to a threshold. The threshold is set from noise measurements, so as to maintain a constant false alarm probability (CFAP). This can be implemented by any of several methods.

In the search mode, only the sum channel data is processed. When the threshold is exceeded and target detection is declared, the auxiliary antenna signal is processed and its magnitude is compared with that of the main antenna to eliminate sidelobe detected targets. The auxiliary antenna has a peak gain which is approximately 20 dB less than that of the main antenna. Also, the sidelobes of the main antenna are approximately 20 dB down from the main lobe. This provides roughly a 20 dB main lobe/guard antenna ratio to detect and eliminate sidelobe targets.

In the modes for which angle tracking is required, namely, GPC acquisition and autotrack, the sum-plus-angle error channels are processed. The azimuth and elevation error signals are time-multiplexed, thereby eliminating the need for a second and third matched processing channel.

The Shuttle Ku-band radar signal flow block diagram is shown in Figure 5. The antenna assembly consists of a main antenna and an auxiliary antenna, which are subunits of the deployed mechanism assembly (DMA). Further processing of antenna signals takes place in the deployed

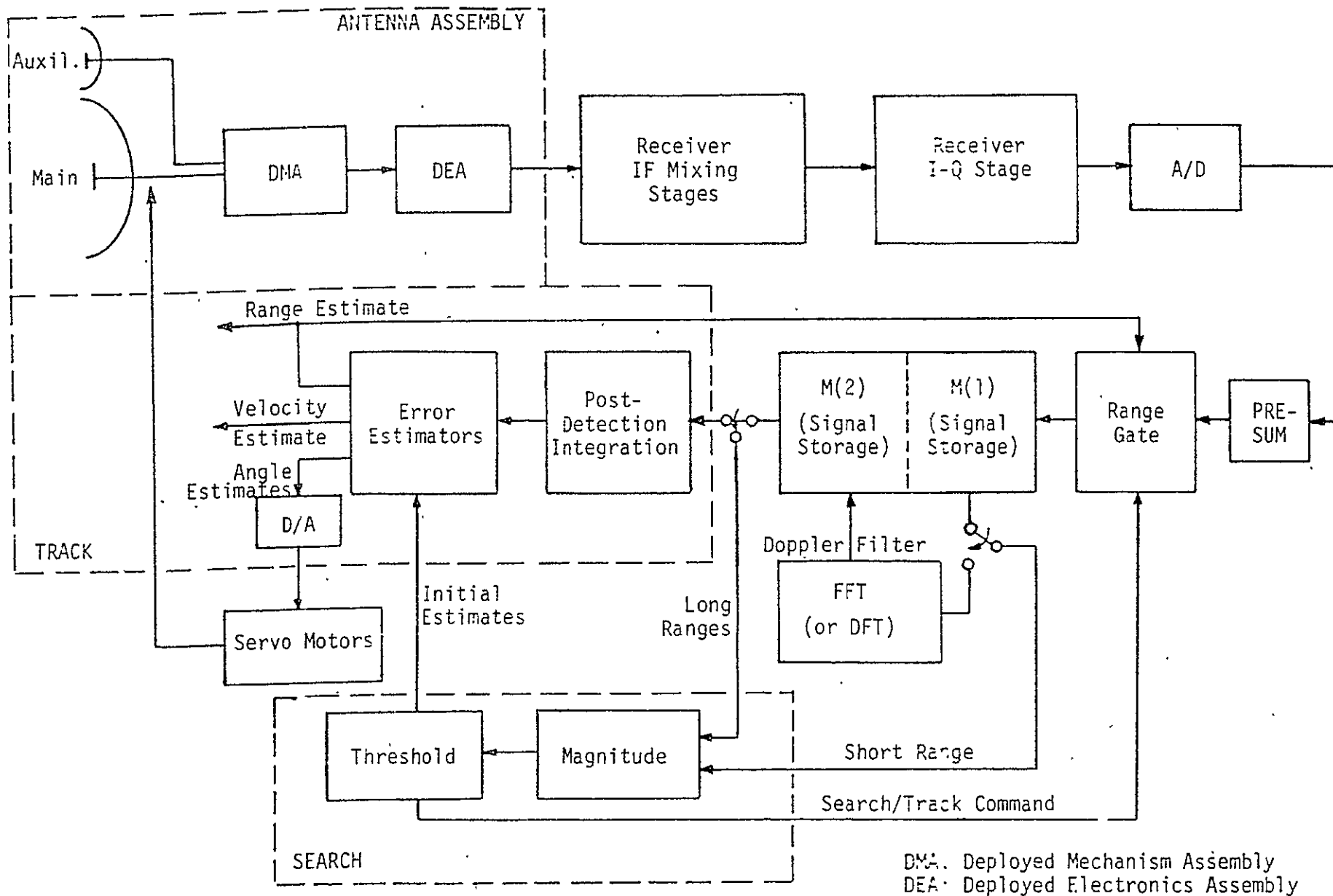


Figure 5. Radar Block Diagram

electronics assembly (DEA), where various switching and filtering operations take place. The antenna assembly is followed by several IF mixing stages to bring the carrier frequency down to a stable IF of $f_0 = 78.143$ MHz. The output of the I-Q stage that follows is a pair of baseband signals which are in phase and in quadrature with the input signal.

The available information is converted by an A/D converter to digital data which samples both channels at a rate of $f_s = 480$ kHz, which is slightly larger than the Nyquist rate of the baseband signals at the output of the I-Q stage. (The LPF bandwidth in both the I and Q channels is equal to 237 kHz.) The output of the A/D converter is a set of complex numbers which undergo various stages of digital processing before estimates of the target parameters (range, velocity, azimuth angle, elevation angle) are obtained. The first processing stage is a presuming stage, followed by a set of range gates and doppler filters consecutively. The arrangement of the gates is varied for the two modes of operation. In the search mode, where range designation is not present, there are four range gates per pulse, while in the track mode, there are only two non-overlapping gates: an early gate and a late gate.

For long ranges, the magnitudes of the outputs of the doppler filters are summed over the RF frequencies and compared to a threshold to detect the existence of a target. For short ranges ($R < 0.42$ nmi), the detection takes place without using any doppler filtering.

Once a target is detected, the radar is switched to a track mode and the digital signals undergo postdetection integration, followed by an error estimation unit which is initiated by a crude estimate obtained by the search mode operation. The final estimates of the various parameters are:

- (1) Fed as inputs to the servo motors for angle track.
- (2) Used to adjust the position of the early and late gates for range track.
- (3) Displayed for the astronauts for visual reading (all variables being tracked).
- (4) Utilized to update the state of the error estimates to obtain new estimates.

Frequency diversity, using five RF frequencies, is employed in both the search and track modes. Table 6 lists these frequencies.

TABLE 6. Ku-Band Radar RF Frequencies
and Their Corresponding PRF Frequencies

RF Frequency		F_1	F_2	F_3	F_4	F_5
		13.779	13.831	13.883	13.935	13.987
PRF	$R > 9.5$ nmi	3009	2998	2987	2976	2965
	$R < 9.5$ nmi	7017	6994	6970	6946	6923

The radar modulation parameters for the search and track modes are summarized in Tables 1 and 2.

In explaining the search mode operation, the low range signal format is chosen for demonstration. All other ranges follow identical processing except for the short range (< 0.42 nmi) which does not utilize the doppler filters.

Sixteen pulses are transmitted at each RF frequency. The duration of each pulse is $66.4 \mu\text{sec}$, while the time between consecutive pulses is $335 \mu\text{sec}$, as shown in Figure 6. Four range gates (R_1 through R_4) are used to cover the designated range. It is important to note that no doppler correction is used at the presummer in the search mode. For each RF frequency, 64 complex numbers are stored in a memory designated at $M(1)$, as shown in Figure 7. The output of each range gate at every RF frequency is passed through a bank of 16 doppler filters, implemented as discrete Fourier transforms (DFT) or fast Fourier transforms (FFT), and the magnitudes of the outputs of these filters are calculated and compared to precalculated thresholds. The target is detected when the magnitude of one or two outputs of adjacent doppler filters pertaining to one or two range gates is exceeded. Initial estimates of the range and the range rate of the target are calculated from the knowledge of the doppler filters and the range gates whose outputs have exceeded the threshold. These initial estimates are fed into the error estimators as initial conditions to start the successive estimation process in the track mode. Thresholds are calculated to produce error alarm rate of one false alarm per hour.

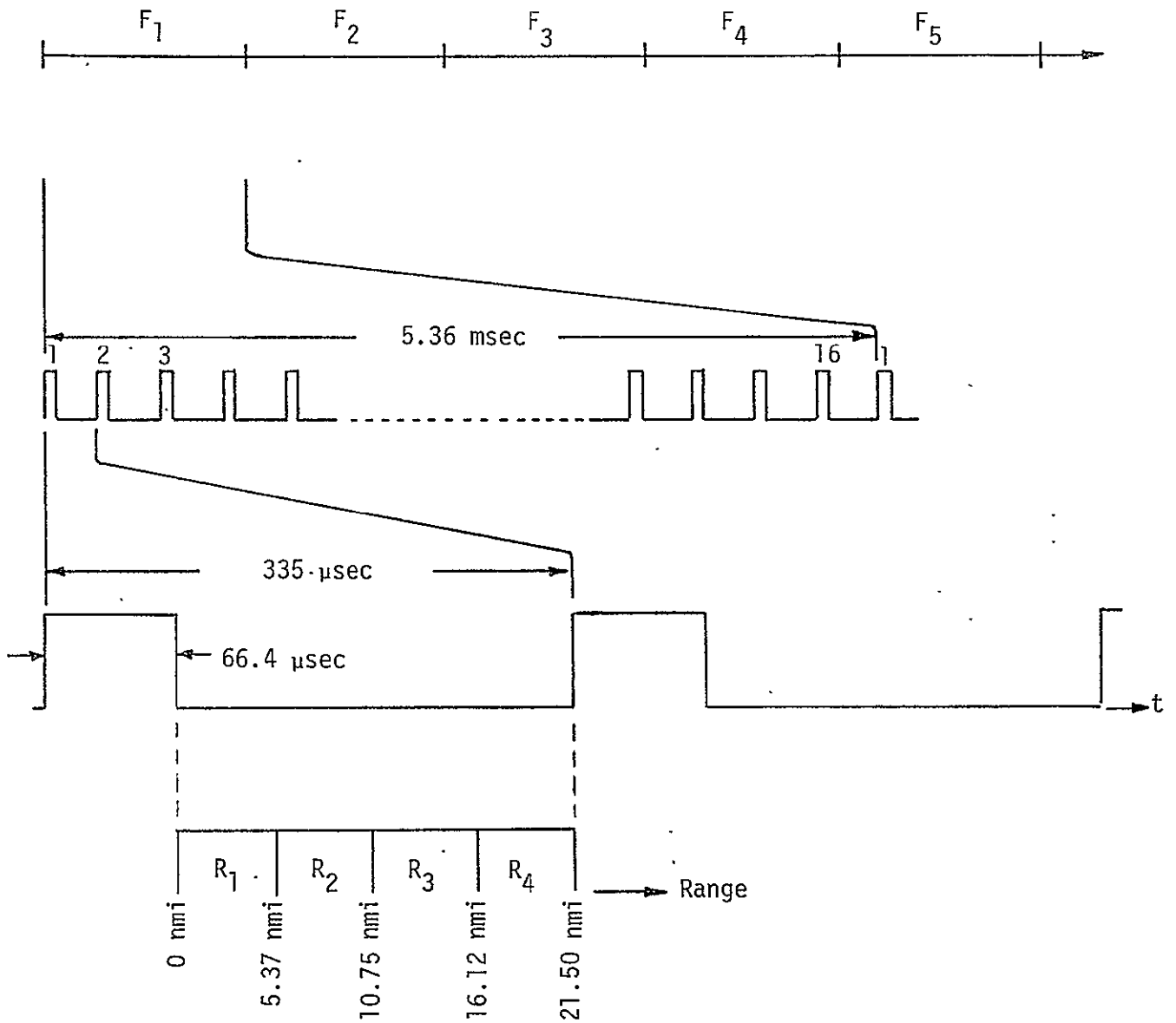


Figure 6. Long Range Search Signals

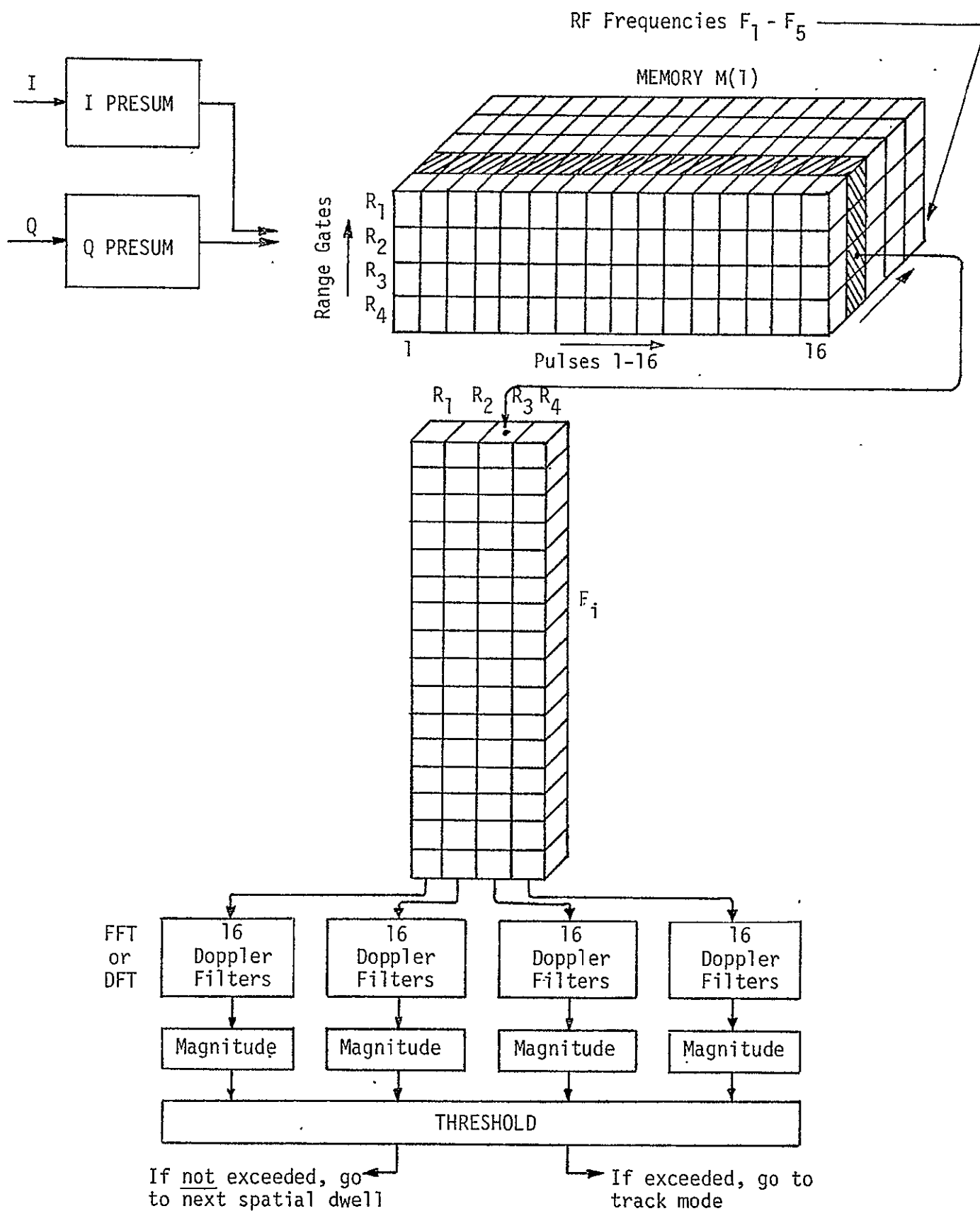


Figure 7. Search Mode Signal Processing

Figure 8 illustrates the signal format in the track mode. As shown in the Figure, the signal in the track mode consists of 64 pulses for each RF frequency, instead of the 16 pulses of the search mode. For long range tracking, the frequency dwell time is equal to 21.44 msec. Each frequency dwell time is divided into four time slots by the switching combination of SW1 and the phase encoder switch in the antenna assembly. The signals in the succeeding time slots are $\Sigma + \Delta AZ$, $\Sigma - \Delta AZ$, $\Sigma + \Delta EL$, and $\Sigma - \Delta EL$, respectively. The time slots are arranged so that the first two are used to measure the azimuth angle, while the last two are used for the elevation angle. Each one of the previous time slots consists of 16 pulses. The pulses are passed through an early gate and a late gate, which are located around a predicted estimate of the range, $R_p(n)$, from the processor timing unit. The width of each gate is equal to the pulse width. The output of each range gate is a complex number $z(I, J, L, K)$, which is a function of four parameters (I, J, L, K):

I denotes the RF frequency being transmitted; $I = 1, 2, \dots, 5$.

J denotes the time slot in each frequency such that

$J = 1$ corresponds to $\Sigma + \Delta AZ$

$J = 2$ corresponds to $\Sigma - \Delta AZ$

$J = 3$ corresponds to $\Sigma + \Delta EL$

$J = 4$ corresponds to $\Sigma - \Delta EL$.

K denotes a particular pulse in each time slot; $K = 1, \dots, 16$.

L denotes the range gate under consideration:

$L = -1$ corresponds to Early Gate.

$L = +1$ corresponds to Late Gate.

The detailed description of signal processing involved in the search and track modes is presented in Appendix B.

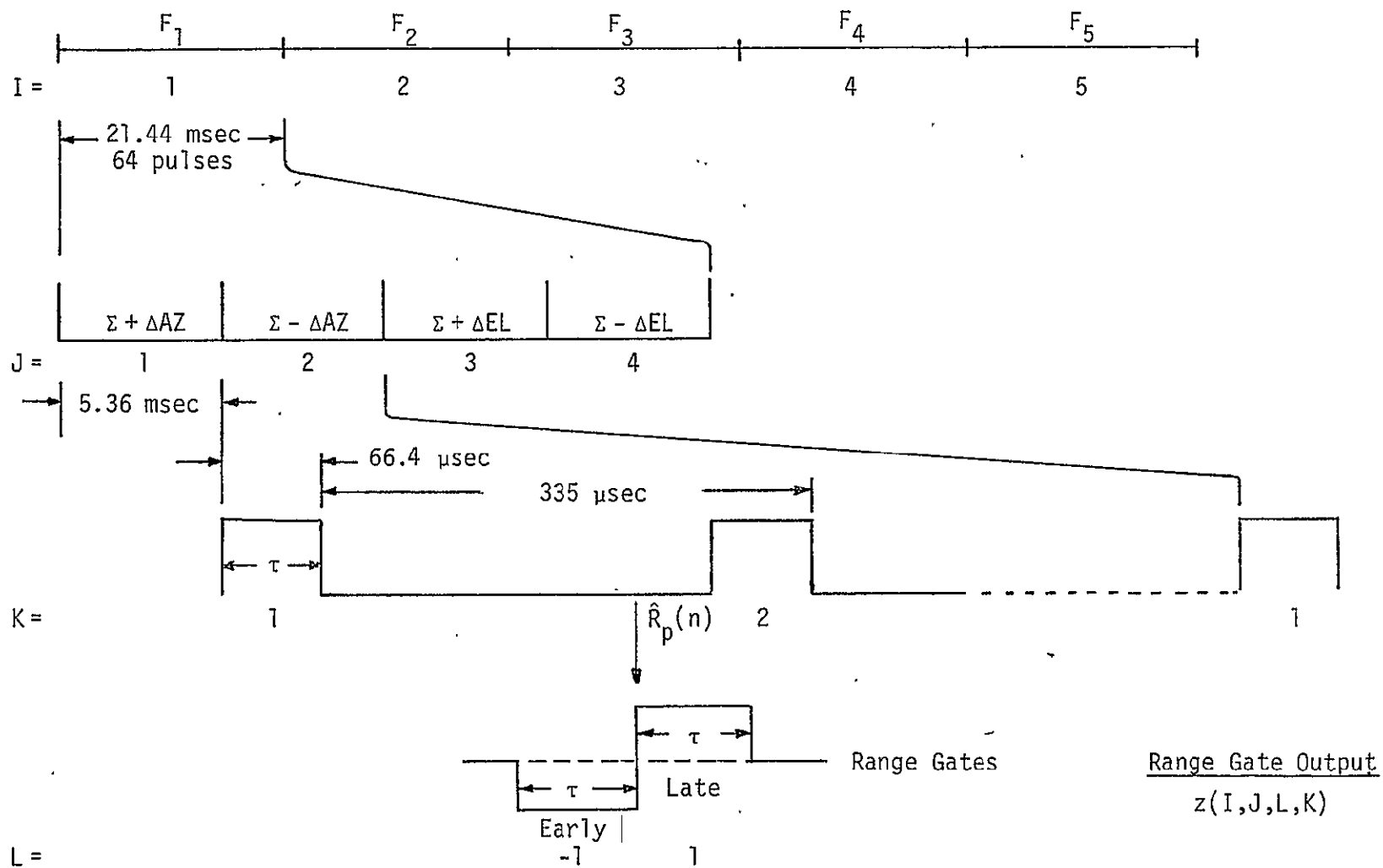


Figure 8. Track Mode Signal Format

6.0 TIME MULTIPLEXED SINGLE-CHANNEL ANGLE TRACKING AND ANGLE RATE ESTIMATION OF PASSIVE TARGETS

In the Ku-band integrated radar and communications for the Orbiter, the angle tracking subsystem, when operating in the communications mode, has received extensive attention [7]. In Appendices C and D of this report, the radar angle tracking and angle rate estimation of passive targets are studied. Both thermal noise and target scintillation are taken into account. It is shown that the performance requirements for the angle tracking of passive targets meets the specification requirements with a design margin of approximately 9.5 dB at 10 nmi and closer. The angle rate estimation study in Appendix D shows that the spec. is met when $R < 10$ n.miles when target scintillation and thermal noise are taken into account.

A block diagram of the single channel* monopulse angle tracking loop is shown in Figure 9. All of the operations pertinent to the angle tracking functions are as shown in this figure. In particular, the pre-sum operation assumes that the range gate tracking loop is also tracking satisfactorily. Degradations in signal-to-noise ratio due to errors in the range gate tracking loop would not seriously affect the operation of the angle tracking loop unless these degradations were very significant. This is because of the ample design margin of the angle tracking loops.

The same comments can also be made about the doppler tracking loop, which sets the centers of the doppler filters.

The performance of the angle tracking loop is shown in Figure 10, where the RMS tracking error due to thermal noise and target scintillation is plotted against range in nautical miles. For all ranges less than 18 nmi, the RMS error is below the specification value of 0.153 deg, and naturally improves as the range decreases.

In summary, there appears to be no difficulty in angle tracking capability of the radar for passive targets from the standpoint of the thermal noise. The passive mode was chosen for this detailed study since it imposes the most severe requirements on signal-to-noise ratio.

*Single channel implies multiplexing of three information channels (Σ , ΔAZ and ΔEL) into a single channel.

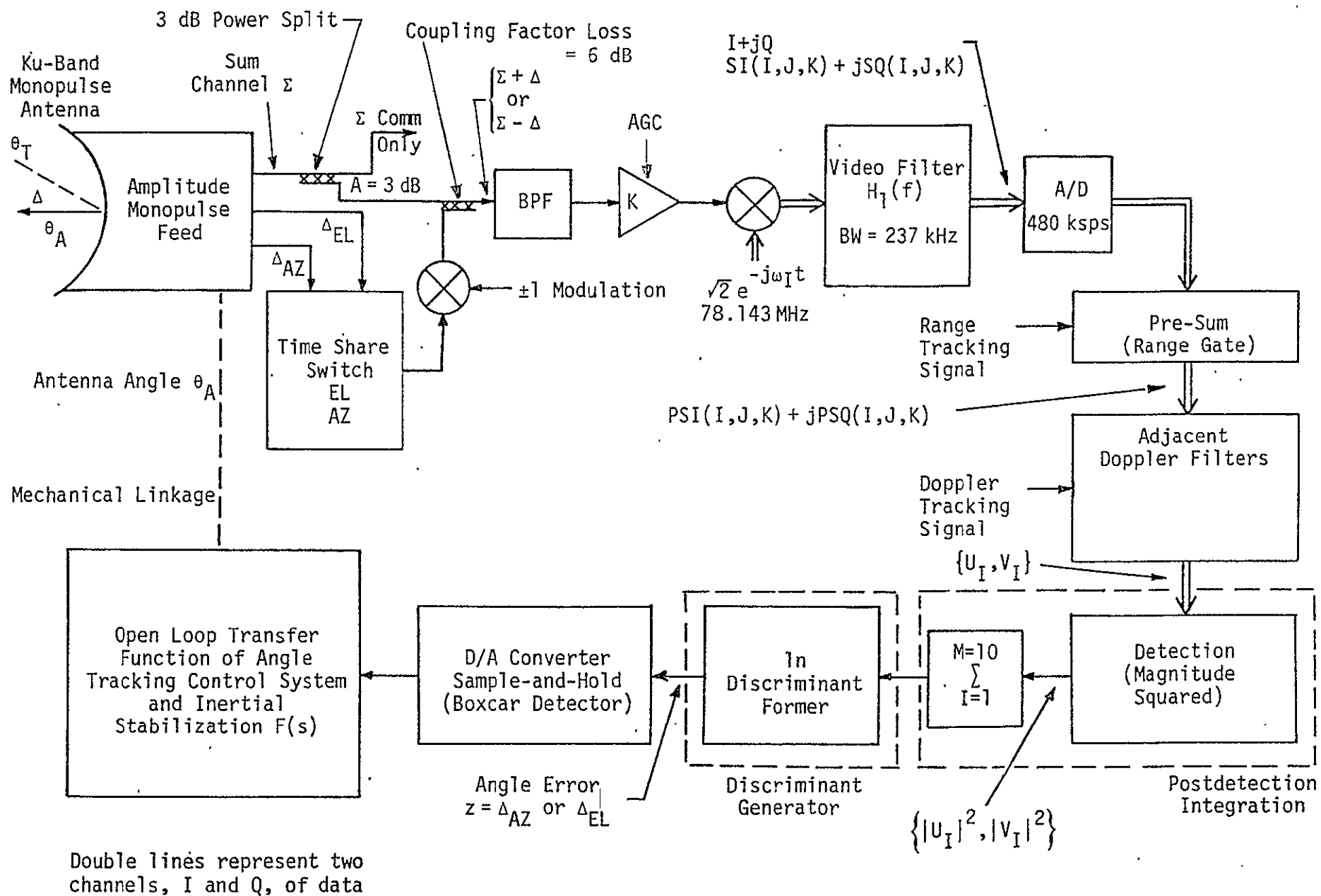


Figure 9. Block Diagram of Single Channel Monopulse Angle Tracking Loop

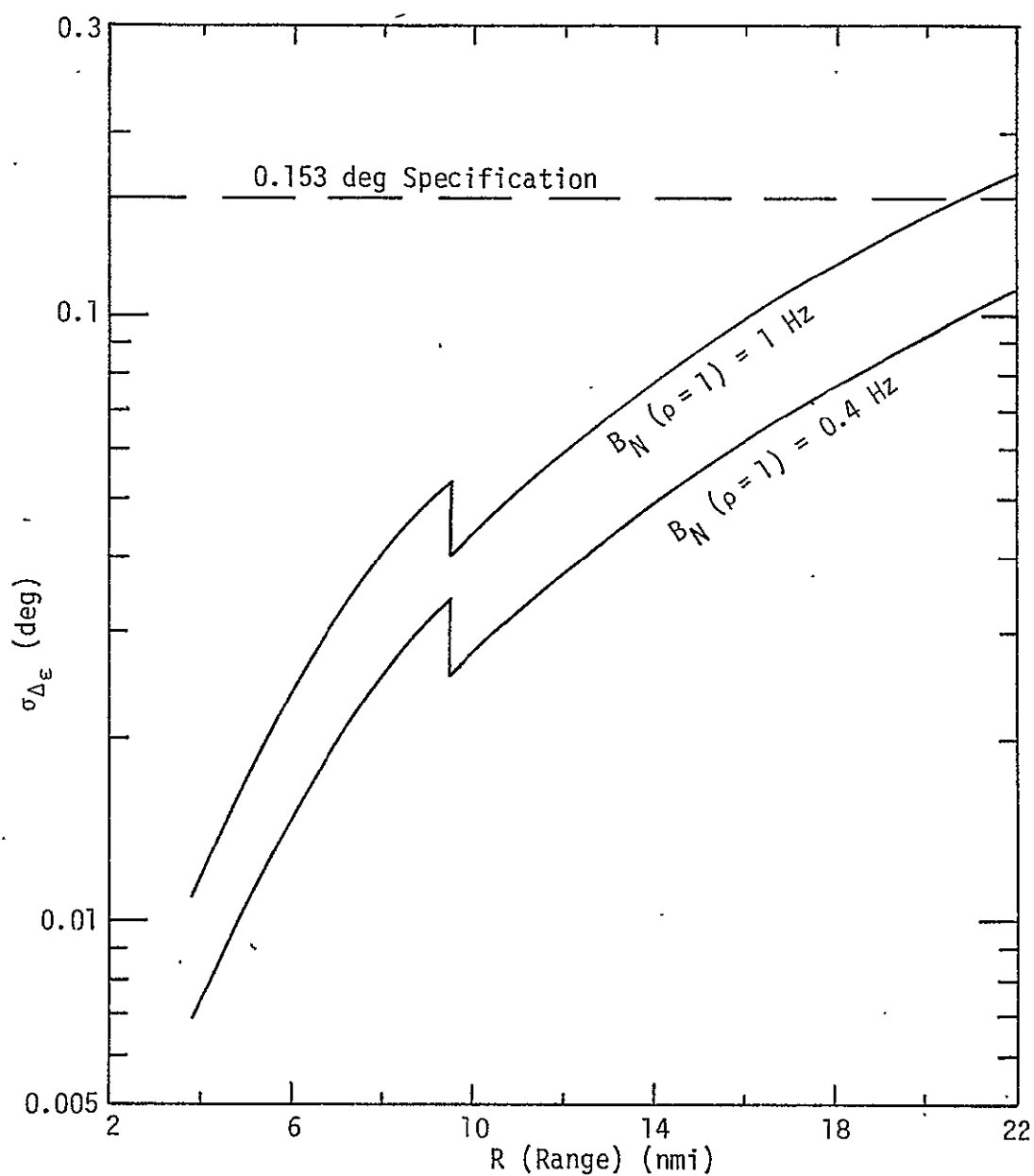


Figure 10. RMS Angle Tracking Error of Passive Radar vs. Range (nmi)

The performance of angle rate estimation is shown in Figure 11. This is taken from the development in Appendix D, wherein it is shown that when target scintillation and receiver front end thermal noise are taken into account, that the spec. is met for ranges less than 10 n.mi. It should be emphasized that only point targets were considered so that the degradation in angle tracking and angle rate estimation due to glint has not been taken into account.

In Figures 10 and 11, the pertinent values used in the radar equation to relate SNR to range are detailed in Appendices A and C.

Appendices C and D evaluate the effects of target scintillation and thermal noise on angle track performance and angle rate estimation. These appendices do not determine the effects of target angular acceleration on angle track performance. These effects will be reported in a forthcoming report. Preliminary computations show that there is a significant settling time after a target angular acceleration.

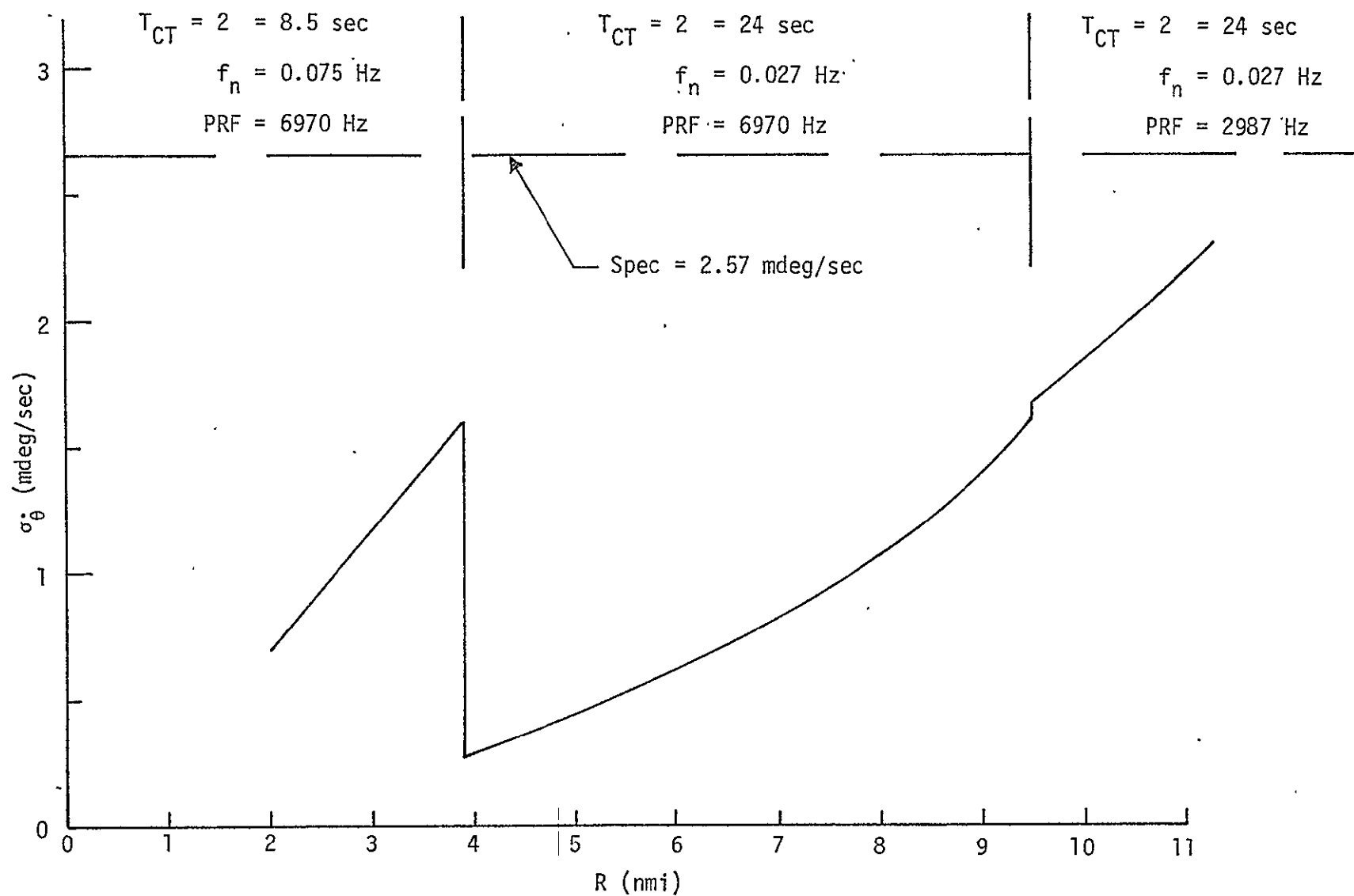


Figure 11. Performance of Angle Rate Estimation vs. Range in Nautical Miles - Pertinent System Parameters as Indicated

7.0 RANGE TRACKING OF PASSIVE TARGETS

The range tracking accuracy is analyzed in Appendix E and the operation of the α - β tracker in the range tracking loop is explained in Appendix F. Figure (12) illustrates the range tracking loop. The range error standard deviation is given by

$$\sigma_R = \frac{\tau c}{16} \left(1 + \frac{4}{\text{SNR}}\right)^{1/2} \left(\frac{8\alpha^2 + \beta}{4\alpha}\right)^{1/2} \sigma_x (N, \text{SNR}) \quad (1)$$

where

τ : pulse width in sec shown in Table (2) for various ranges.

c : velocity of light in free space.

$$c = 2.997925 \times 10^8 \text{ m/sec}$$

or

$$c = 9.835692 \times 10^8 \text{ ft/sec}$$

SNR: signal-to-noise ratio at the output of the doppler filters. It is equal to $P_{\text{avg } r} / N_0 B_F$, where $P_{\text{avg } r}$ is the average received power, B_F is the doppler filter single sided noise bandwidth and N_0 is the single sided noise power spectral density.

α, β : parameters of the α - β tracker.

σ_x : standard deviation of the maximum likelihood estimate of $\ln(P_u/P_v)$. As is explicitly shown in Appendix E, σ_x is a function of the number of independent samples per calculation ($N = 20$ for range) and signal-to-noise ratio (SNR). Figure (13) illustrates the variations of σ_x as a function of SNR for various N .

Using the latest HAC numbers of α and β , the range error standard deviation (RMS) as a function of range for the passive mode is shown in Figure (14). Since $\alpha \cong 0.05$ is used for $R > 9.5$ (n.mi) and $\alpha \cong 0.1$ is used for 3.8 (n.mi.) $< R < 9.5$ (n.mi.), it is noted that the radar range measurements are expected to meet the specifications of ($\sigma_R = 30.47$ m) up to 9.5 n.mi. It should be noted that the values of range error obtained in this report agree to a large extent with those presented by Hughes Aircraft Company in their Monthly Review [11], 13 October 1977.

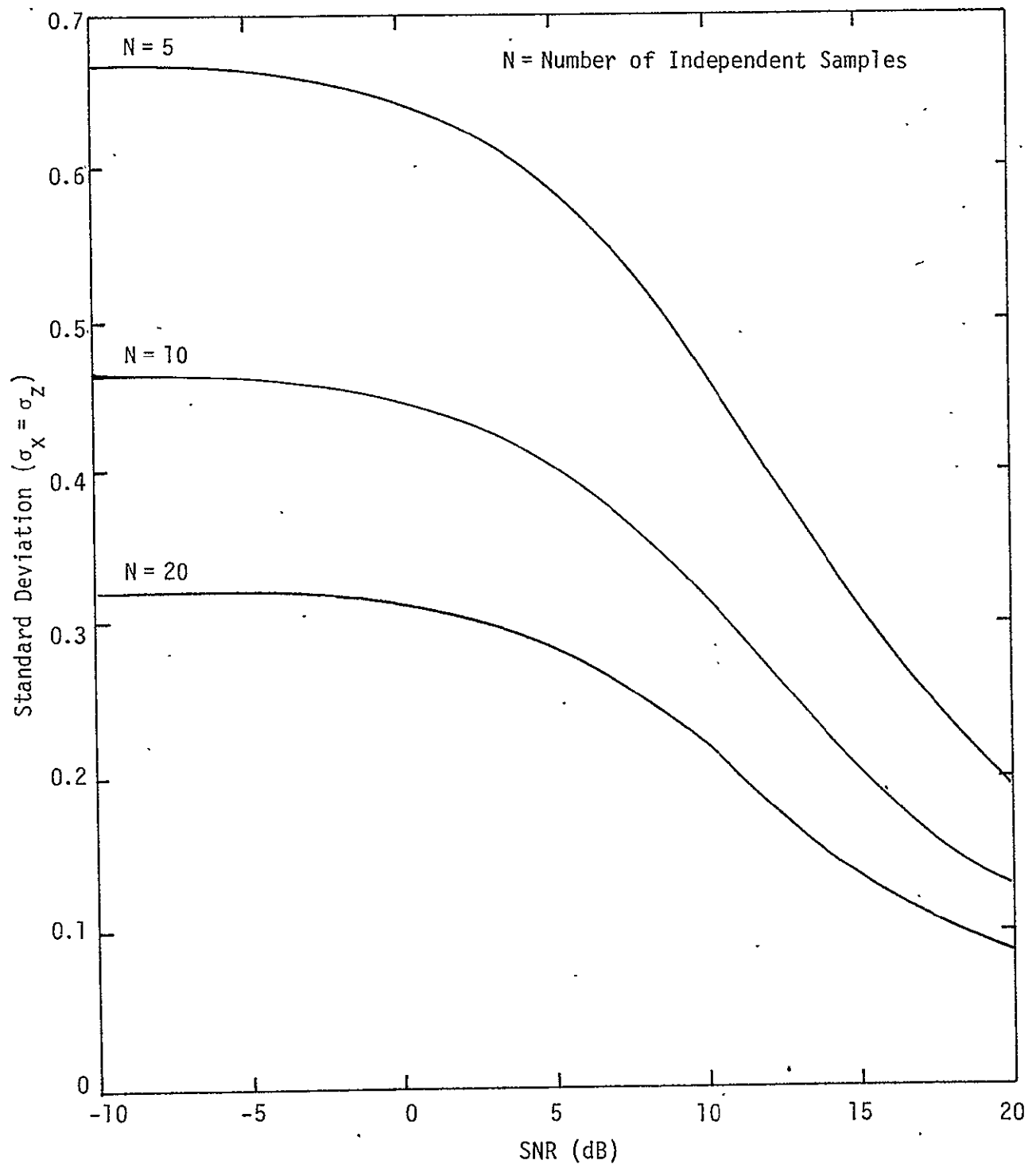


Figure 13. Standard Deviation of the Output of the Logarithmic Discriminant Generator vs. Signal-to-Noise Ratio at the Output of the Doppler Filters for Certain Values of N

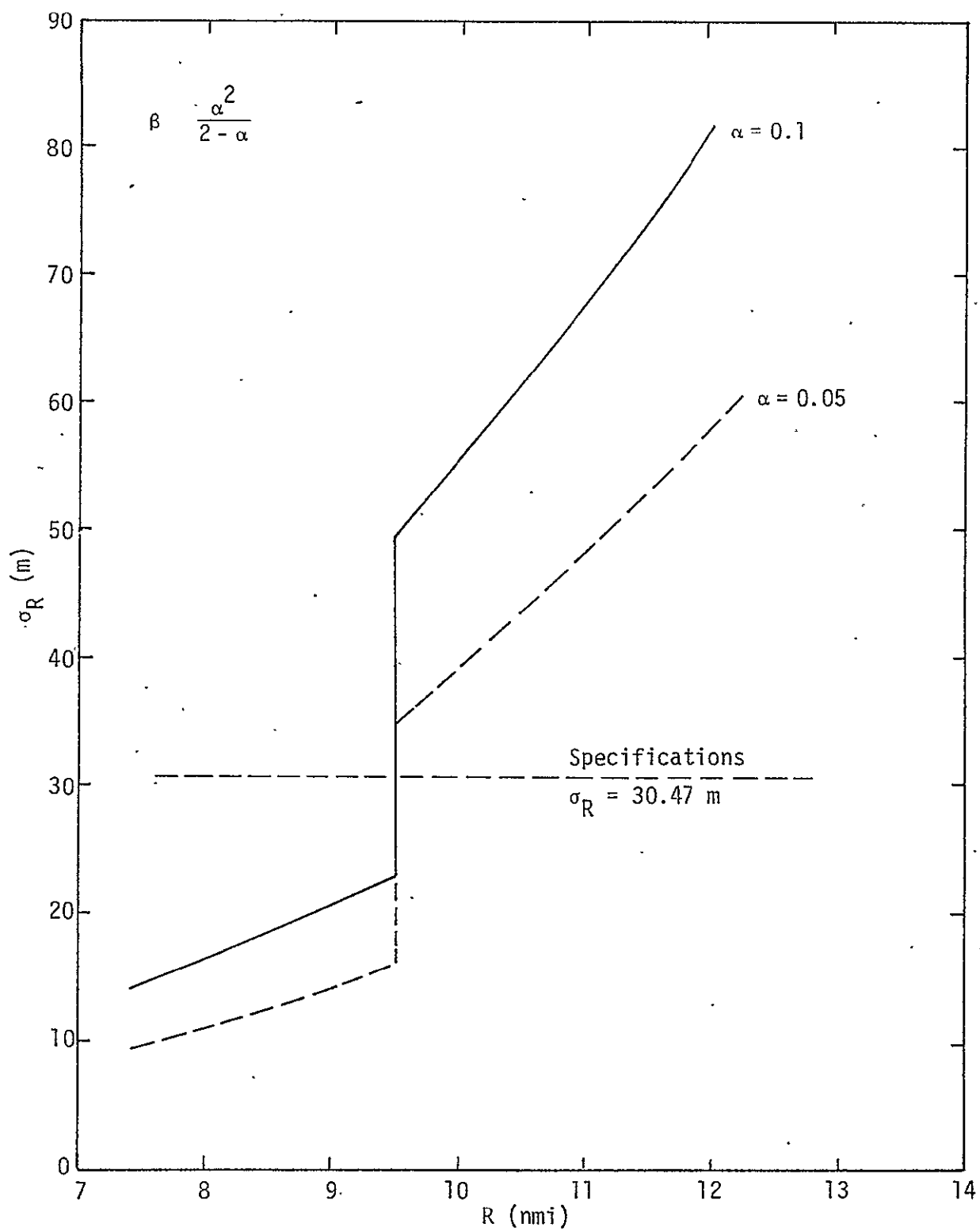


Figure 14. Range RMS Error vs. Range with α as a Parameter

In obtaining the above results, the following radar equation was used

$$\text{SNR} = \frac{[G^2 \sigma \lambda^2][d_t P_p \tau_E]}{(4\pi)^3 L [k T_{\text{sys}}] R^4} \quad (2)$$

where all the parameters in the equation remain unchanged from those in the tracking case except for the loss factor, L , which for range tracking is found in Appendix E to equal 9.49 dB for $R > 9.5$ n.mi. and 9.12 dB for $3.8 < R < 9.5$ n.mi.

8.0 RANGE RATE TRACKING OF PASSIVE TARGETS

The range rate tracking loop is shown in Figure (15). There are 32 doppler filters used for range rate tracking. The location of these filters is fixed as opposed to the adjustable range gates location in the range tracking loop. The operation of the range rate tracking loop is explained in detail in Appendix G.

Two types of range rate errors exist. The first is the error due to thermal noise and the second, which will be referred to as the logarithmic discriminant error, is due to the fact that the location of the doppler filters is fixed and the actual received signal-to-noise ratio is unknown due to target effects and range measurement accuracy. Each of these error contributions is addressed in the next two sections.

8.1 Range Rate Errors Due to Thermal Noise.

The value of the RMS range rate error due to thermal noise is found in Appendix G to be:

$$\sigma_R^* = \left(\frac{c}{f_c}\right) \frac{B_F}{16} \left(1 + \frac{\pi^2}{\text{SNR}}\right)^{1/2} \left(\frac{1}{m}\right)^{1/2} \sigma_x(N, \text{SNR}) \quad (3)$$

where:

- c: velocity of light in free space
- f_c : the RF frequency
- B_F : one-sided bandwidth of the doppler filter
- m: The number of samples averaged to obtain a single reading.

$$m = 2 \text{ for } R > 9.5 \text{ n.mi.}$$

$$m = 4 \text{ for } R < 9.5 \text{ n.mi.}$$

$\sigma_x(N, \text{SNR})$: standard deviation of the maximum likelihood estimate of $\ln(P_u/P_v)$ which is also the standard deviation per sample of the noise in the range rate tracking loop. Figure (16) illustrates the variations of σ_x with N and SNR for range rate tracking.

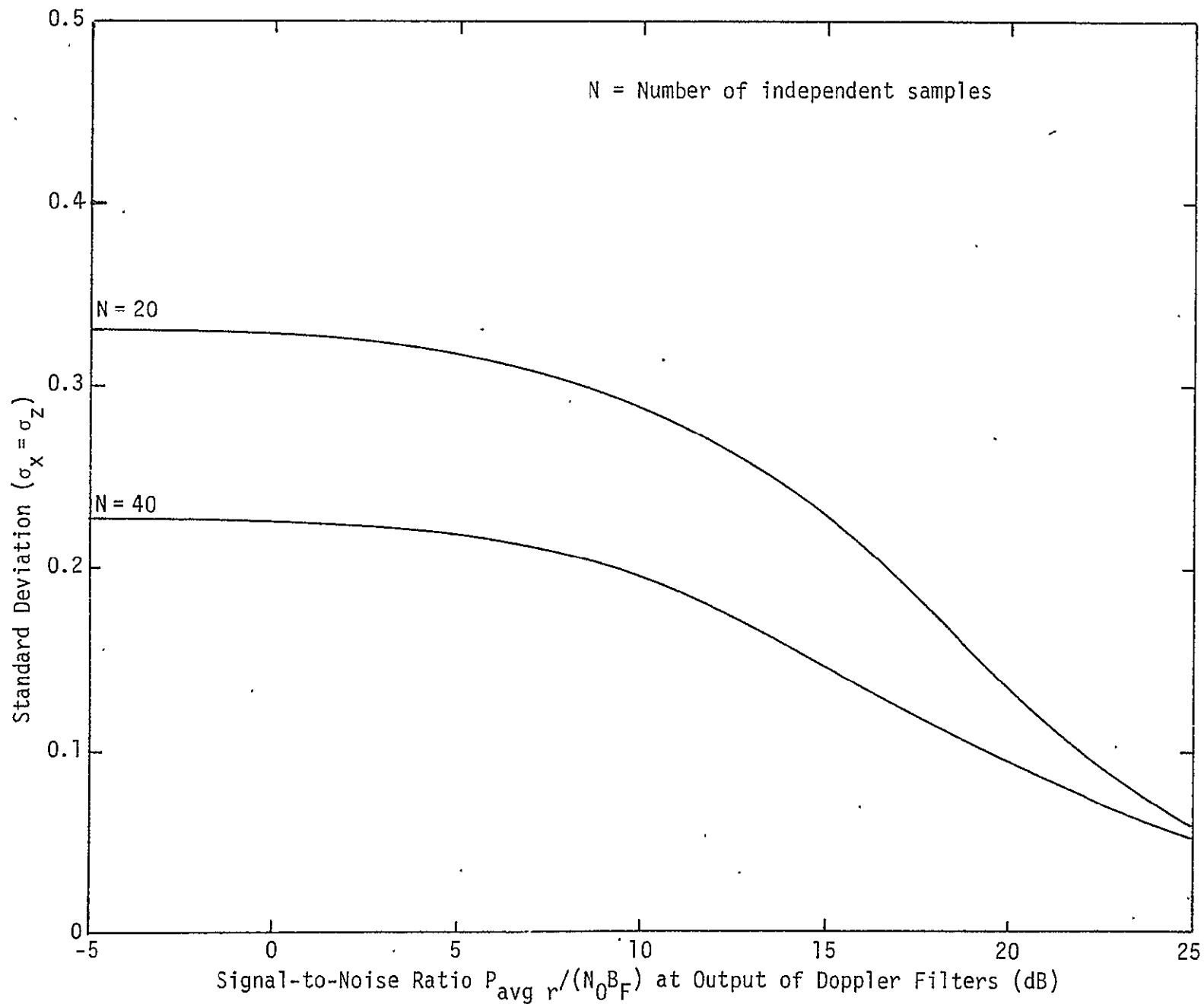


Figure 16. Standard Deviation of the Output of the Logarithmic Discriminant Generator Versus Signal-to-Noise Ratio for N = 20, 40

The radar equation which is used to obtain the RMS of range rate error as a function of range is similar to that in Equation (2). The losses (L) in this case, as found in Appendix G, are 8.39 dB for $R > 9.5$ n.mi. and 8.32 dB for $3.8 < R < 9.5$ (n.mi.).

The RMS range rate tracking error due to thermal noise is shown in Figure (17) for $m = 1, 2, 4$ samples. In the present state of the range rate loop design, the number of samples used is $m = 2$ for $R > 9.5$ n.mi. and $m = 4$ for $R < 9.5$ n.mi.[11]. This results in a design margin of 2.5 dB at 9.5 n.mi.

The obtained accuracies in the range rate tracking errors due to thermal noise agree reasonably well with those presented by Hughes Aircraft Company in their Monthly Review [11].

8.2 Range Rate Logarithmic Discriminant Error.

This error arises from the fact that the doppler filters positions are fixed and that the signal-to-noise ratio is unknown due to target effects and inaccuracy in range measurement. This is best explained by writing the expression for the mean of the output of the logarithmic discriminant, namely

$$E(z) = \ln \left[\frac{\frac{\cos^2(\pi\zeta)}{(256) \sin^2 \left[\frac{\pi}{32} (1 - 2\zeta) \right]} + \frac{4}{\text{SNR}}}{\frac{\cos^2(\pi\zeta)}{(256) \sin^2 \left[\frac{\pi}{32} (1 + 2\zeta) \right]} + \frac{4}{\text{SNR}}} \right] \quad (4)$$

where

$\zeta = \frac{\Delta f_d}{B_F}$ is the ratio between the doppler offset from the closest center of two doppler filters, as shown in Figure (18).

B_F = Doppler filter single sided bandwidth.

Since the signal to noise ratio is unknown, then the mapping between $E(z)$ and ζ is not one-to-one. That is, knowing $E(z)$ does not result in a single measurement of ζ and, hence, the range rate. In order to obtain the reading of ζ or range rate, an assumption has to be made concerning the signal-to-noise ratio; since this assumption is more often than not different from the actual signal-to-noise ratio, a logarithmic discriminant error results. Several assumptions can be made,

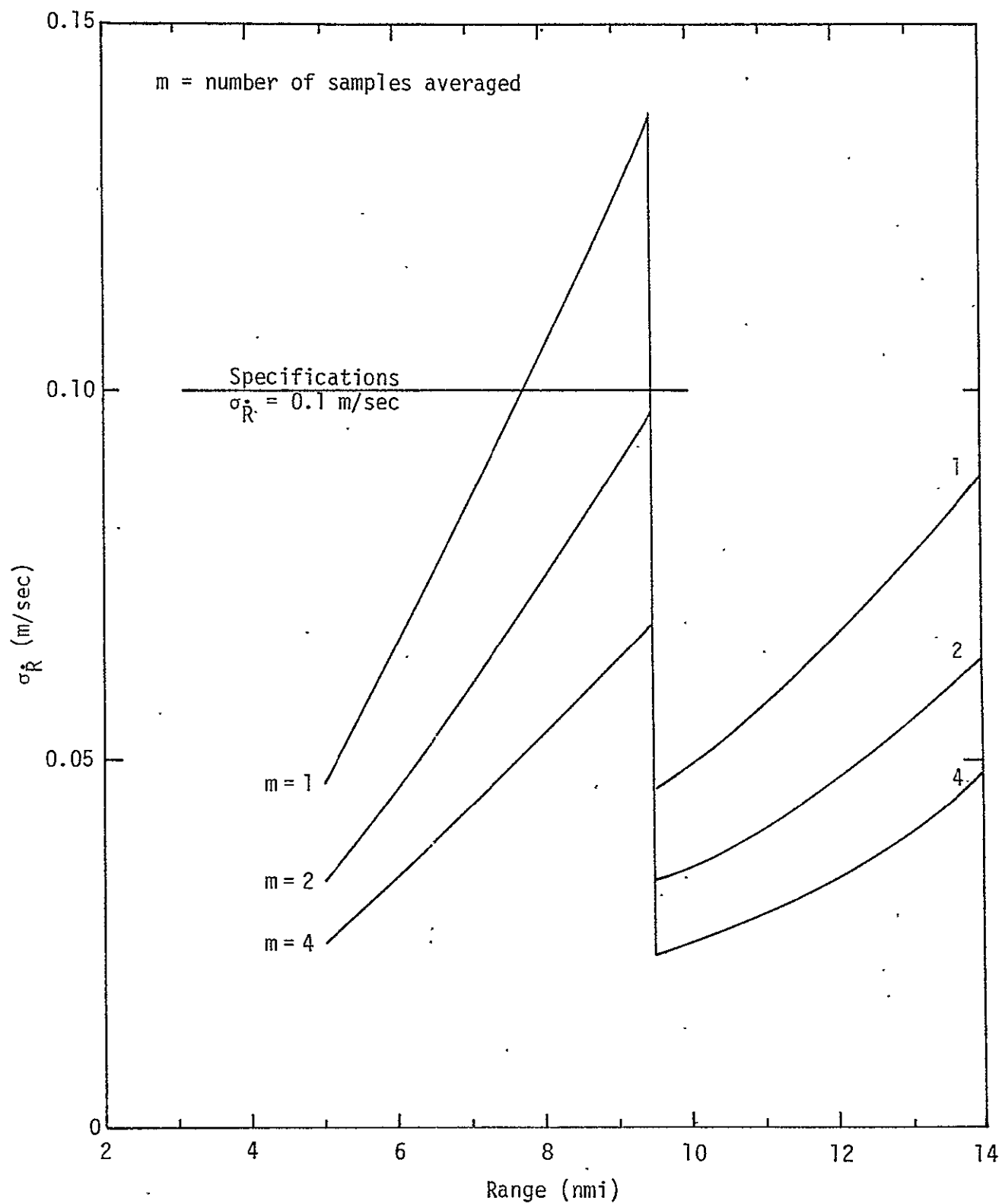


Figure 17. RMS Range Rate Tracking Error of Passive Targets Vs. Range

$$\Delta f_d = \frac{\Delta \omega_d}{2\pi}$$

$$\xi \triangleq \frac{\Delta f_d}{B_F}$$

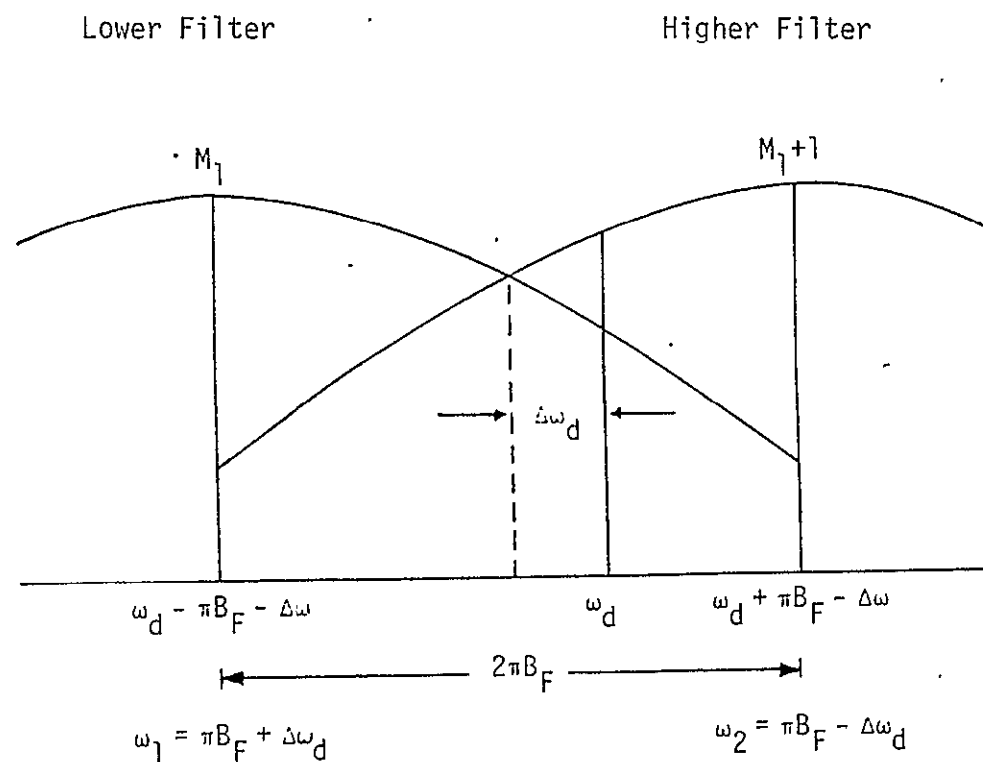


Figure 18. Doppler Frequency Location

ORIGINAL PAGE IS
OF POOR QUALITY

1. The assumed signal-to-noise ratio $\text{SNR}_1 = \infty$
The value of ζ obtained, which is denoted as ζ_1 , can be found by letting $\text{SNR} \rightarrow \infty$ in Equation (4). This results in

$$E(z) = 2 \ln \left[\frac{\sin \frac{\pi}{32} (1 + 2\zeta_1)}{\sin \left(\frac{\pi}{32} (1 - 2\zeta_1) \right)} \right] \quad (5)$$

or

$$\zeta_1 = \frac{1}{2} \left[\frac{2 e^{E(z)/2}}{1 + e^{E(z)/2}} - 1 \right] \quad (6)$$

2. A straight line that passes through the origin with a slope equal to the slope of the $E(z)$ when $\text{SNR} \rightarrow \infty$ at the origin is used to map $E(z)$ into ζ . The plot of $E(z)$ for various signal-to-noise ratios versus ζ along with the mentioned straight line is shown in Figure (19). The resulting error in this case as a function of SNR for PRF = 6970 hz is shown in Figure (20).
3. A straight line fitting can be achieved by setting

$$E(z) = 8 \left(1 + \frac{\pi^2}{\text{SNR}} \right)^{-1} \zeta \alpha \quad (7)$$

which results in

$$\zeta_1 = \left(1 + \frac{\pi^2}{\text{SNR}_1} \right) \frac{E(z)}{8\alpha}$$

where SNR_1 is the assumed SNR and ζ_1 is the resulting normalized doppler offset. Also, α is a number that can be obtained by proper numerical methods so as to minimize the mean square discriminant error for a given range of SNR. An interesting figure results from plotting $E(z)$ as a function of SNR for various ζ , as shown in Figure 21. It is noted that the maximum range rate discriminant error for $\text{SNR} > 30$ dB, assuming $\text{SNR}_1 = 30$ dB is less than 0.062 ft/sec, which suggests that this error should not constitute a major problem at close range.

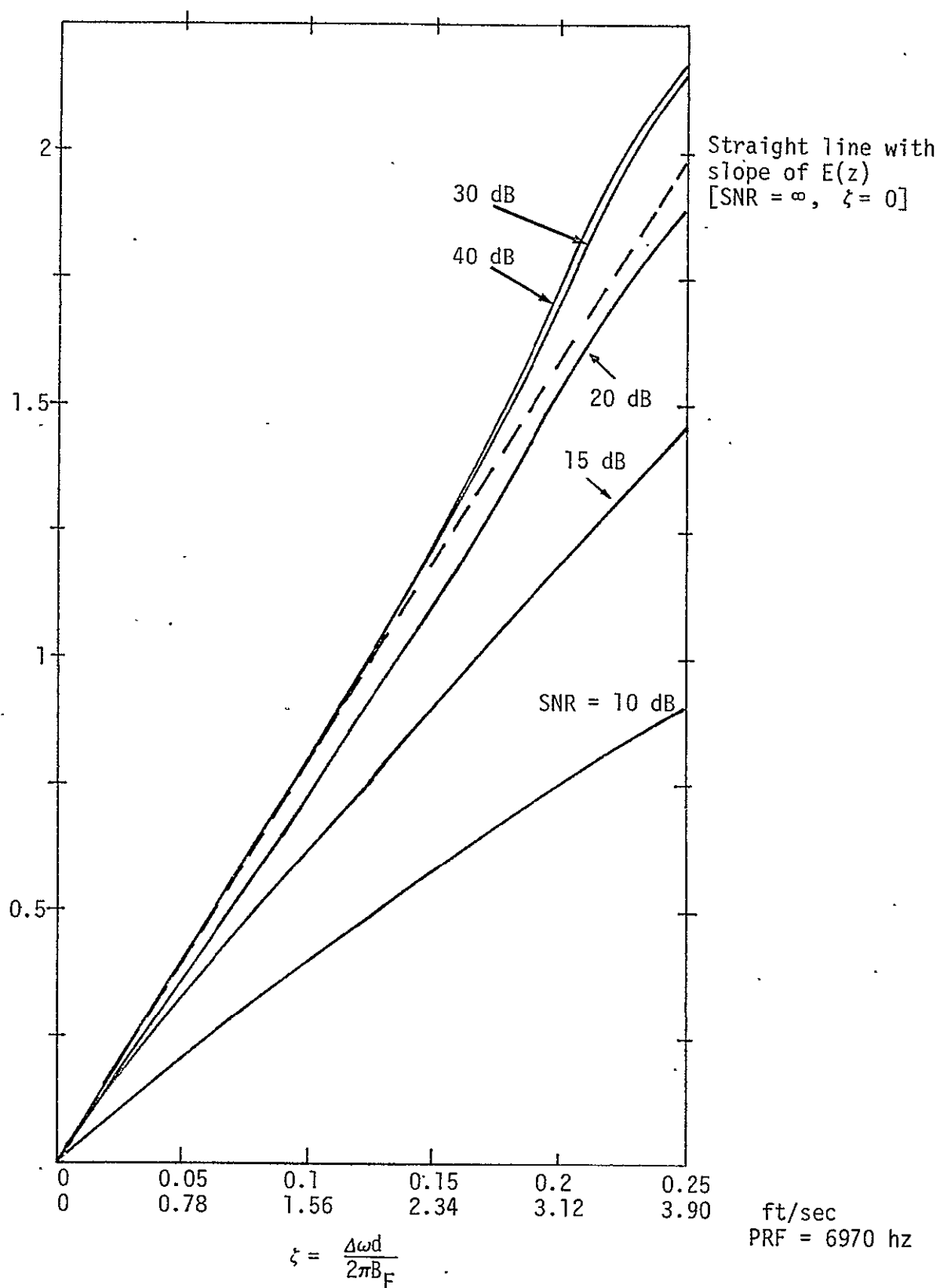


Figure 19. Mean of Range Rate Logarithmic Discriminant Output

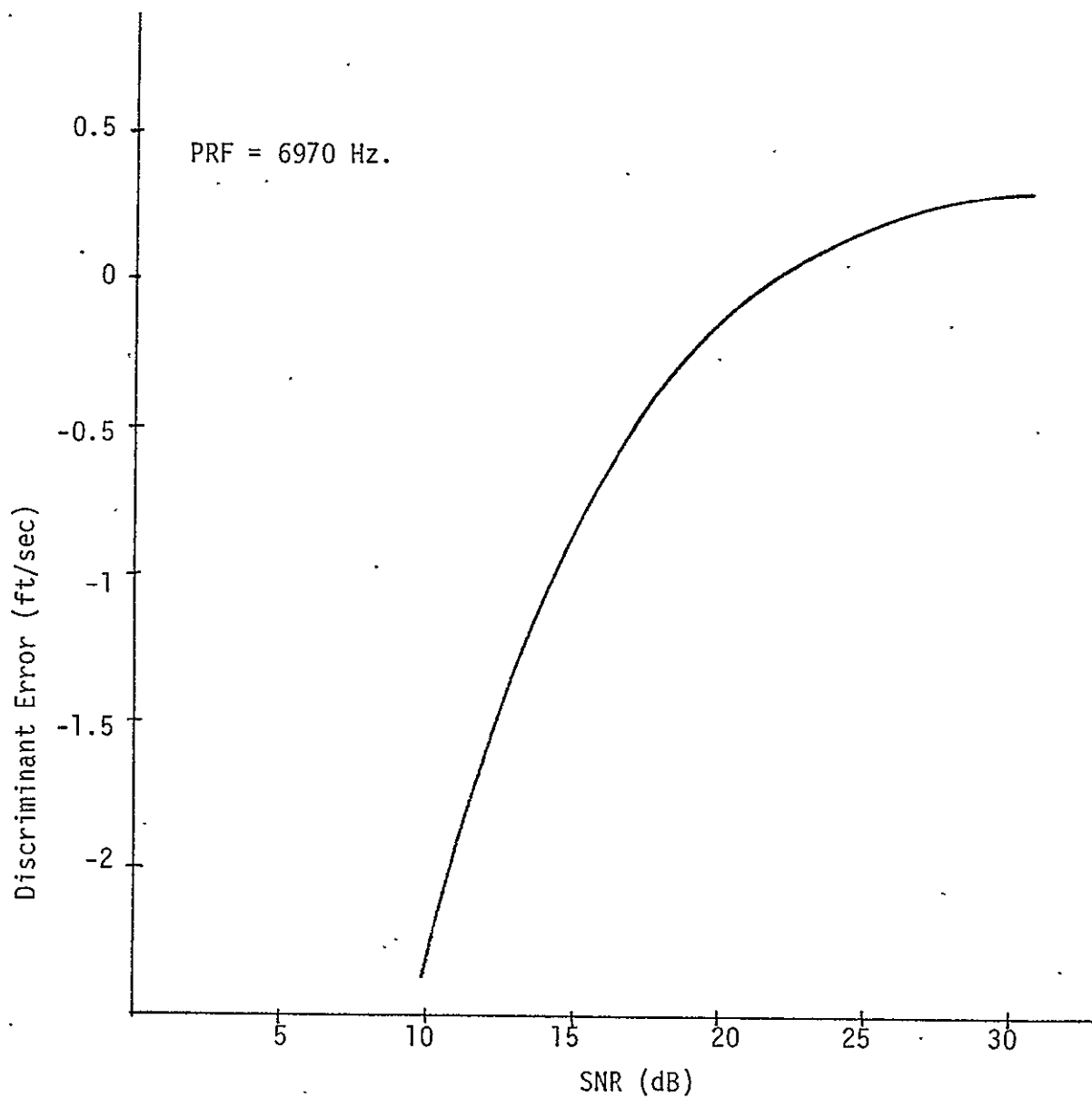


Figure 20. Range Rate Discriminant Error with a Straight Line Mapping Whose Slope is Equal to the Slope of $E(z)$ at no Doppler and $\text{SNR} \rightarrow \infty$.

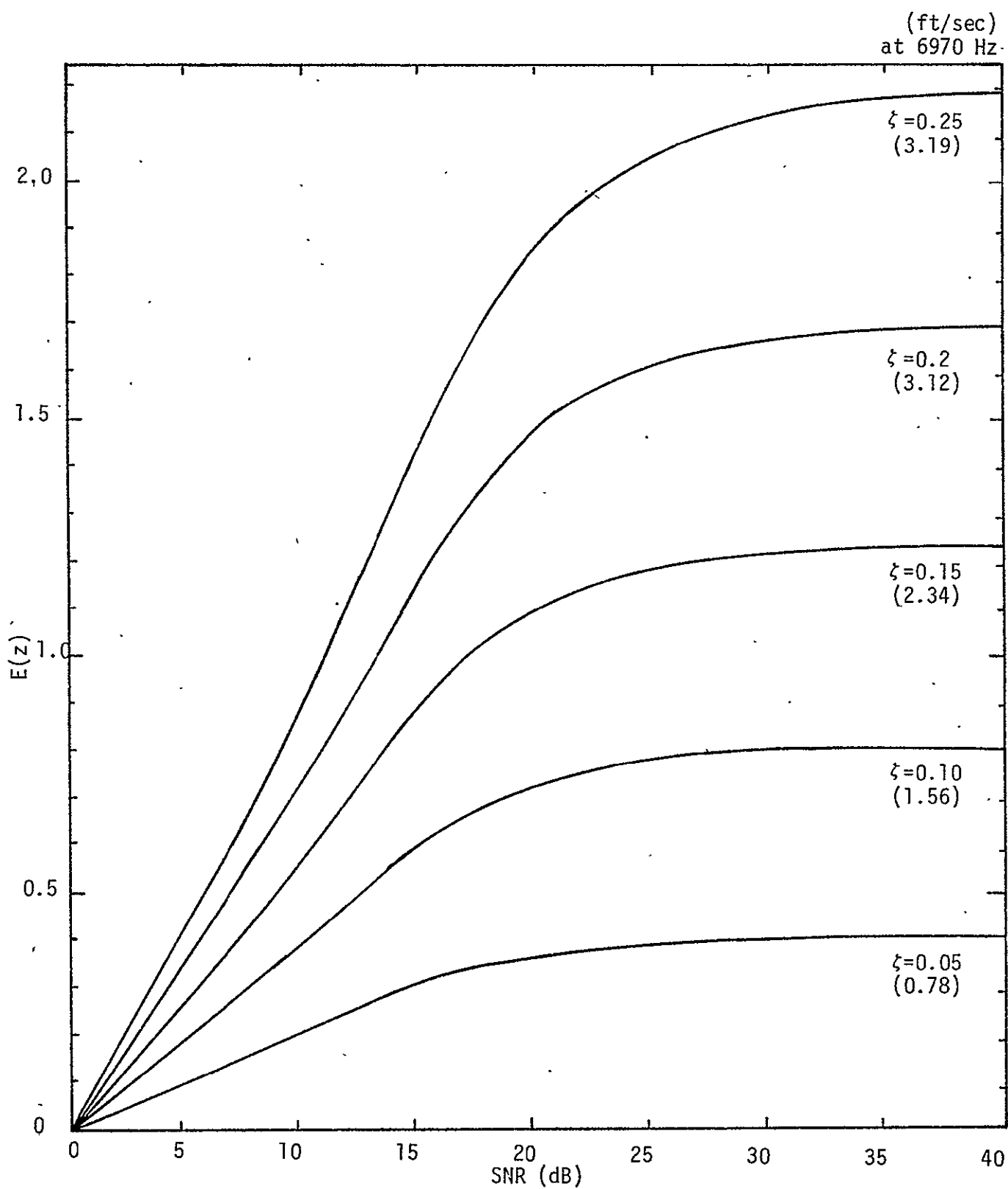


Figure 21. Expected Value of Logarithm Discriminant Output Versus SNR for Various Values of $\zeta = \Delta f_d / B_F$.

9.0 REDUCTION IN SIGNAL-TO-NOISE RATIO DUE TO QUANTIZATION AND SATURATION NOISE IN A/D CONVERSION

The signal-to-noise ratio (SNR) at the output of an analog-to-digital (A/D) converter is determined as a function of the input signal-to-noise ratio in Appendix H. Both quantization and saturation noise contributions are taken into account. Values of A/D converter parameters are determined to minimize the sum of quantization and saturation noise. In Figures 22 and 23, which are developed in Appendix H, it is seen that the A/D output SNR saturates as the input SNR increases. In the radar system being developed, an $M=4$ -bit A/D converter is used, in which case the output SNR saturates at 18.9 dB. At long ranges, where the input SNR to the A/D converter is very low (less than 6 dB), the reduction in SNR due to the A/D is negligible, as can be seen from Figure 22. At short ranges, however, the signal-to-noise ratio at the input to the A/D becomes quite large; at those ranges, the radar is essentially A/D converter limited. In a forthcoming report, the effect of A/D at short ranges is taken into account. At the longer ranges ($R > 3$ n.mi.), the effect of the A/D converter can be neglected.

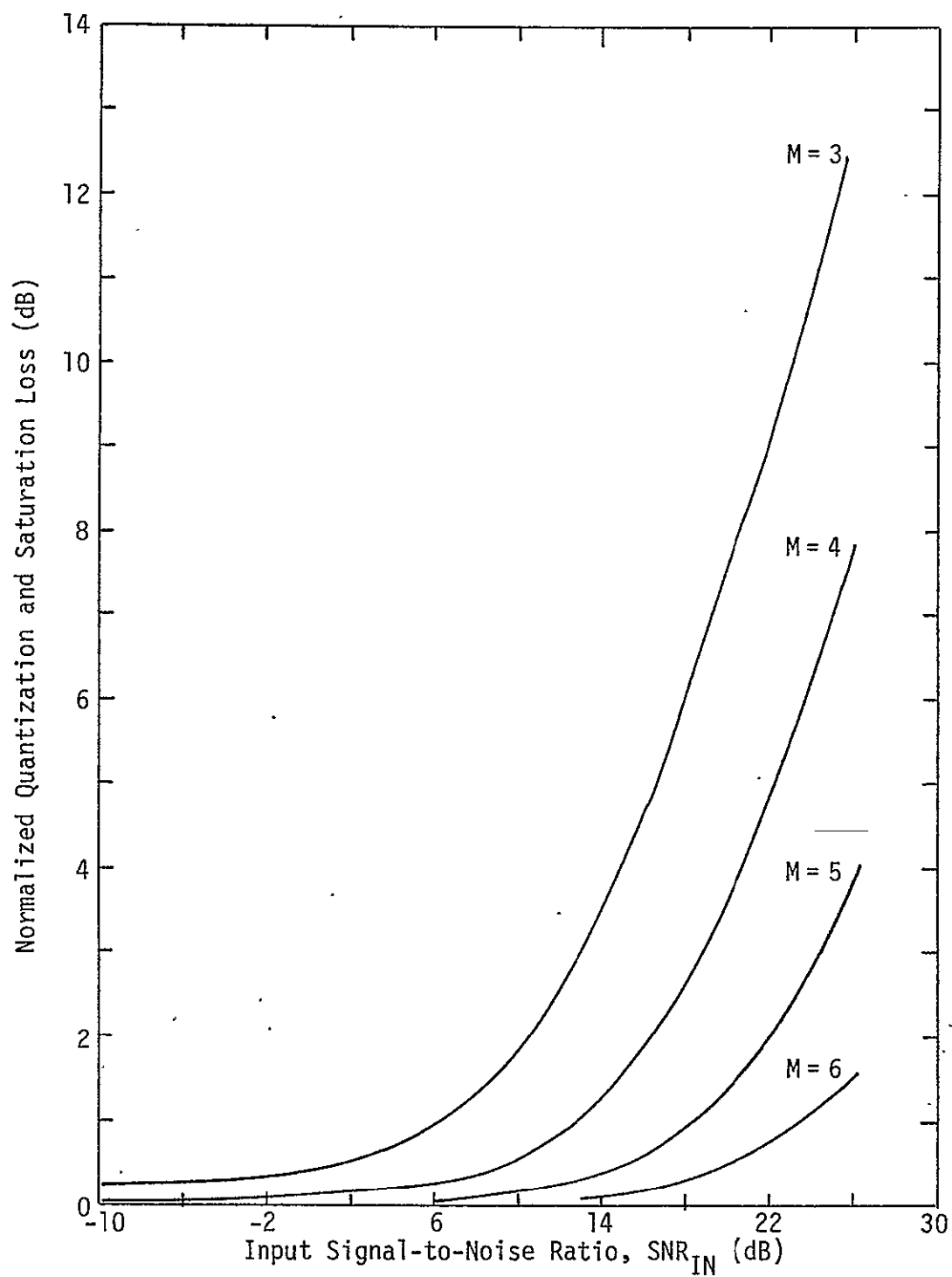


Figure 22. Normalized Quantization and Saturation Loss Versus Input Signal-to-Noise Ratio for $M=3$ to $M=6$ Bits of Quantization

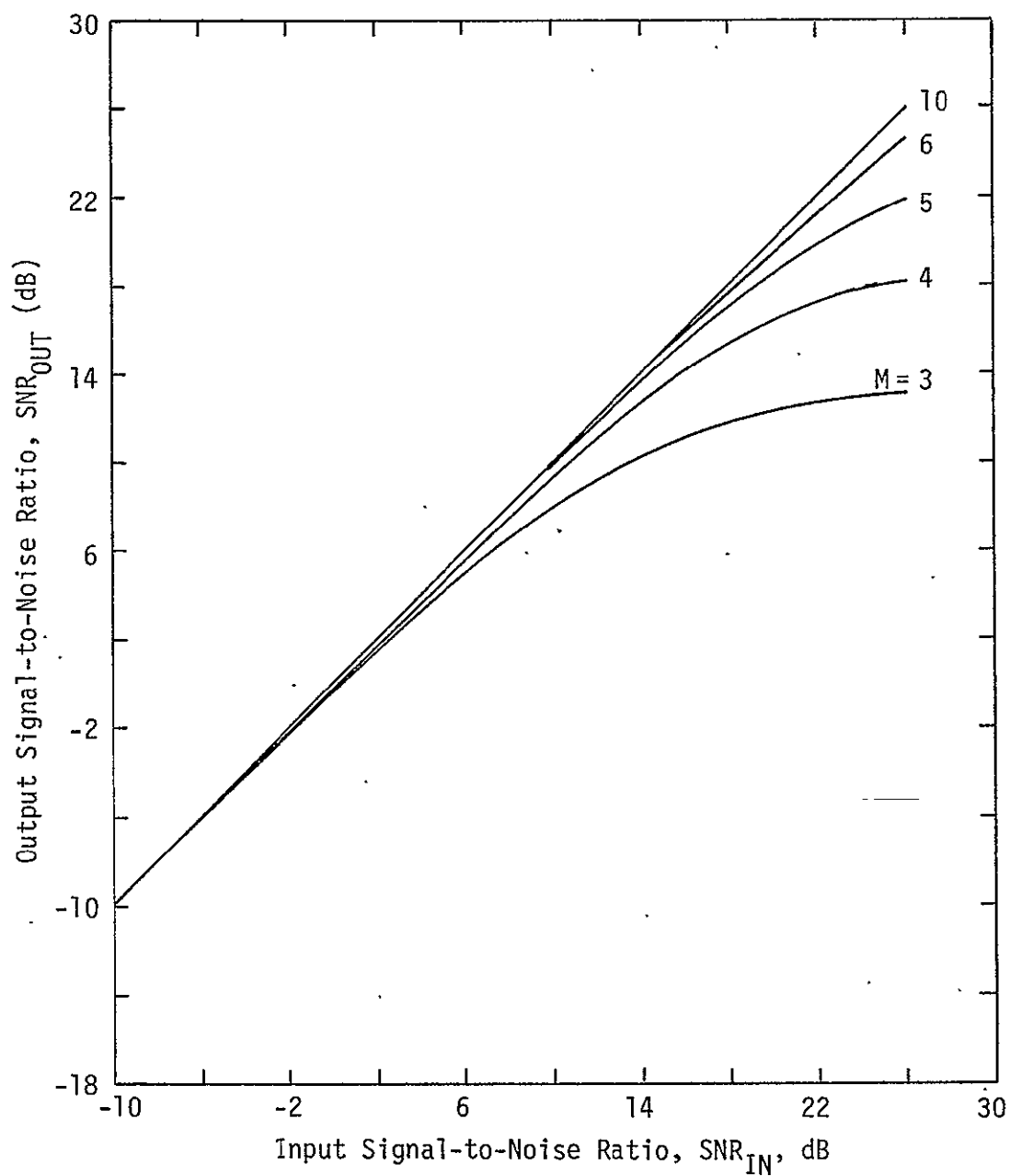


Figure 23. Output Signal-to-Noise Ratio Versus Input Signal-to-Noise Ratio for $M=3$ to $M=10$ Bits of Quantization

10.0 MAXIMUM LIKELIHOOD ESTIMATOR DESCRIPTION

In the radar tracking mode, a logarithmic error discriminant is used [10] to obtain error signals for the various parameters of interest, namely, range, range rate, azimuth angle, and elevation angle. All of these parameters are mathematical duals of each other and a single model can apply to all of them. In each case, the information is imbedded in a pair of voltages \underline{U} and \underline{V} , whose difference is approximately proportional to the target parameter under consideration.

Both \underline{U} and \underline{V} can be assumed to be narrowband processes and a maximum likelihood estimate of any desired parameter can be deduced by taking the logarithm of the powers of the two vectors; thus,

$$z = \log (\underline{U}^T \underline{U} / \underline{V}^T \underline{V}) .$$

In Appendix J, the maximum likelihood (M.L.) estimate of the ratio of the power in two narrowband processes is considered. These processes are assumed to be Gaussian and, in general, will be correlated. The in-phase and quadrature phase components of each process are sampled N times, where the time between samples is assumed to be large enough so that the samples are statistically independent. Numerical computation of the standard deviation formula (31) in Appendix J is shown in Figure 24 for $N = 2, 5, 10$. In the figure, ρ is the normalized correlation coefficient between the two processes. The results agree closely with those derived from an empirical formula in [10].

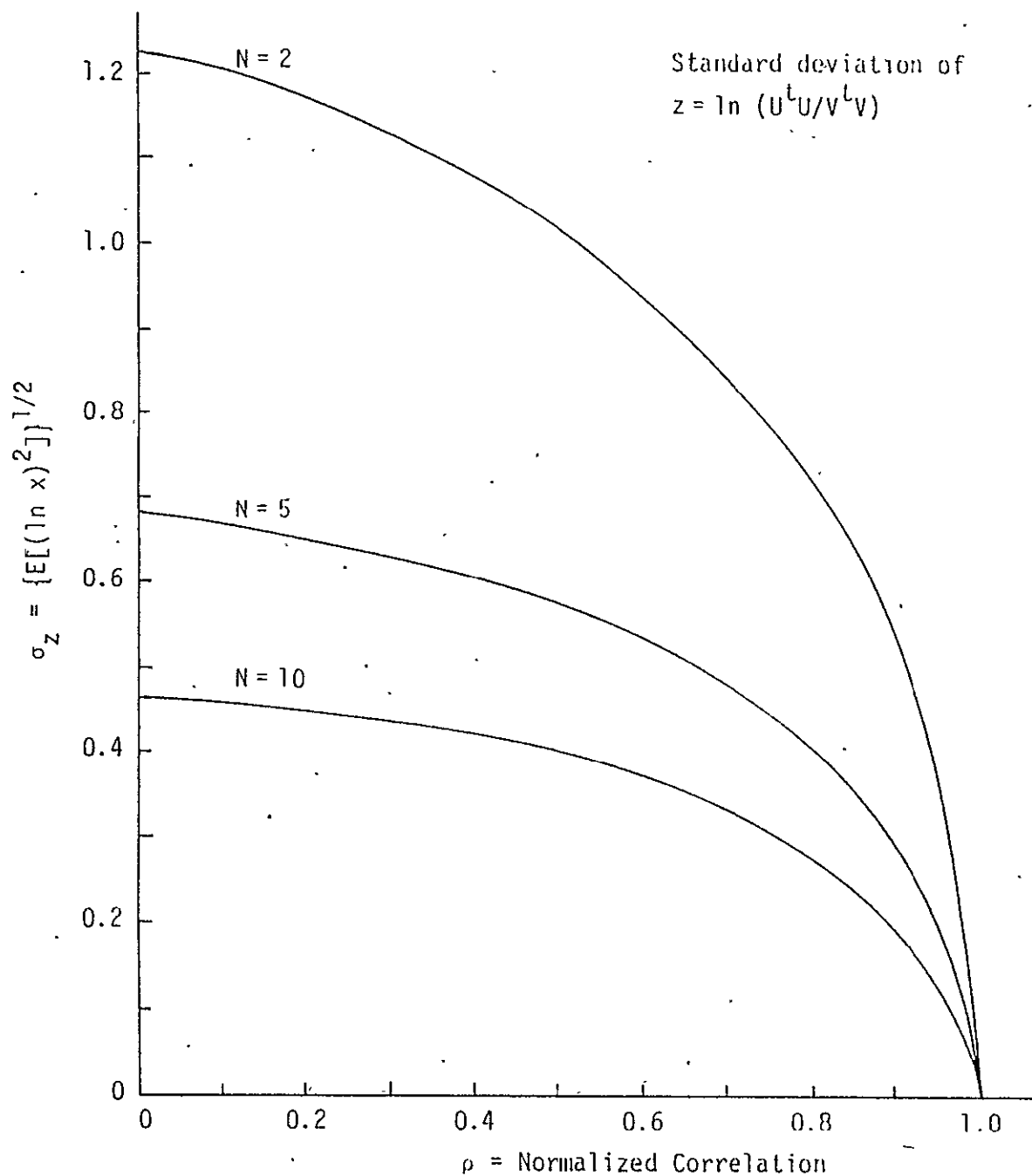


Figure 24. Standard Deviation of the Random Variable z as a Function of Correlation

11.0 POWER ALLOCATION PROPERTIES OF THE THREE-CHANNEL MODULATOR

In this respect, Appendix K examines and compares the performance of several implementations of the three-channel Ku-band modulator on-board the SS0. In particular, the appendix studies the power allocation properties both at the transmitter and the receiver (after demodulation) of these configurations and their ability, in terms of squaring loss and subcarrier phase jitter, to be tracked by an in-phase-quadrature type subcarrier reconstruction loop, e.g., a Costas loop.

It is found from the power allocation study that much care must be exercised in choosing a modulation angle for the unbalanced QPSK subcarrier since, depending on the modulator implementation, the transmitted and demodulated power ratio can be considerably different. For example, for the NASA version and the HAC version with a bandpass filter following the subcarrier modulator, the transmitted and demodulated power ratios are identical, whereas for the unfiltered HAC version, the demodulated power ratio is the square of the transmitted ratio.

In all cases, a Costas-type tracking loop with switching type in-phase and quadrature phase detectors, single pole (RC) Butterworth arm filters, and an analog type error signal multiplier has been assumed. This is not to say that the analyses cannot be carried out for the case where the error signal multiplier is of the switching type. However, due to the increased complexity of calculating the equivalent noise spectral density, it was decided to first present the tradeoff study for the simpler-to-analyze case of the analog error signal multiplier. It is also pointed out that one should not attempt to draw conclusions, either quantitative or qualitative, about the performance of the loop with a switching error signal multiplier from the results given in this report for the analog error signal multiplier case. Indeed, the S-curves are quite different for the two cases and, moreover, the tracking performance as measured by mean-squared jitter would be similarly different.

To conclude, the tables below summarize the principal results obtained. Table 7 gives the signal and noise powers available in each channel for data detection and the detection signal-to-noise ratio obtained by taking the ratio of these two powers. The assumption made is that the outputs of the input in-phase and quadrature phase detectors

in the Costas loop demodulator are filtered with integrate-and-dump circuits respectively matched to the data rates R_2 and R_3 . The outputs of these filters in the absence of crosstalk, namely,

$$z_s^* = \frac{1}{T_2} \int_0^{T_2} \epsilon_s(t) \bigg|_{\varphi=0} dt$$

$$z_c^* = \frac{1}{T_3} \int_0^{T_3} \epsilon_c(t) \bigg|_{\varphi=0} dt,$$

have signal and noise components whose powers are, respectively, the channel 2 and channel 3 entries in Table 7. In all cases, the ratio of detected signal power in channel 2 to detected signal power in channel 3 is chosen equal to 4.

In Table 8, the squaring loss and rms tracking jitter are given for several values of arm filter bandwidth (two-sided) to high-data rate.

Table 7.

	Modulation Angle θ_0	Detected Signal Power Channel 2	Detected Signal Power Channel 3	Detected Noise Power Channel 2	Detected Noise Power Channel 3	$\frac{(\text{SNR})_2}{P_s T_2 / N_0}$	$\frac{(\text{SNR})_3}{P_s T_3 / N_0}$
HAC Version	30°	$(1 - \frac{2}{\pi} \theta_0)^2 P_s$ $= 4/9 P_s$	$(\frac{2}{\pi} \theta_0)^2 P_s$ $= 1/9 P_s$	$(\frac{8}{\pi^2}) \frac{N_0}{T_2}$	$(\frac{8}{\pi^2}) \frac{N_0}{T_3}$	0.548	0.137
Filter HAC Version	26.57°	$(\frac{8}{\pi^2})^2 \cos^2 \theta_0 P_s$ $= 0.8 (\frac{8}{\pi^2})^2 P_s$	$(\frac{8}{\pi^2})^2 \sin^2 \theta_0 P_s$ $= 0.2 (\frac{8}{\pi^2})^2 P_s$	$(\frac{8}{\pi^2}) \frac{N_0}{T_2}$	$(\frac{8}{\pi^2}) \frac{N_0}{T_3}$	0.648	0.162
NASA Version with Squarewave Subcarriers	26.57°	$\cos^2 \theta_0 P_s$ $= 0.8 P_s$	$\sin^2 \theta_0 P_s$ $= 0.2 P_s$	$(\frac{8}{\pi^2})^2 \frac{N_0}{T_2}$	$(\frac{8}{\pi^2})^2 \frac{N_0}{T_3}$	0.987	0.247
HAC Version with Demodulation by Equivalent In-Phase and Quadrature Subcarriers	30°	$(1 - \frac{2}{\pi} \theta_0)^2 P_s$ $= 4/9 P_s$	$(\frac{2}{\pi} \theta_0)^2 P_s$ $= 1/9 P_s$	$(\frac{8}{\pi^2} \cos^2 \theta_0) \frac{N_0}{T_2}$	$(\frac{8}{\pi^2} \sin^2 \theta_0) \frac{N_0}{T_3}$	0.731	0.548

Table 8.

$m_2(t)$ is NRZ data at $R_2 = 2$ Mbps;

$m_3(t)$ is Manchester coded data at $R_3 = 192$ kbps

$\frac{P_{s2}}{N_0} = 10$ dB	$B_i/R_2 = 5$		$B_i/R_2 = 10$		$B_i/R_2 = 20$	
	S_L , dB	$\sigma_{2\varphi}$ (%) radians)	S_L , dB	$\sigma_{2\varphi}$ (%) radians)	S_L , dB	$\sigma_{2\varphi}$ (%) radians)
HAC Version	-16.42	9.36	-15.93	12.5	-16.04	17.92
Filtered HAC Version	-11.73	5.46	-11.44	7.47	-11.56	10.71
NASA Version with Squarewave Subcarriers	-15.12	8.07	-14.72	10.89	-14.66	15.29
HAC Version with Demodulation by Equivalent In-Phase and Quadrature Subcarriers	-21.28	16.38	-20.56	21.33	-20.31	29.3

$\frac{P_{s2}}{N_0} = 15$ dB	$B_i/R_2 = 5$		$B_i/R_2 = 10$		$B_i/R_2 = 20$	
	S_L , dB	$\sigma_{2\varphi}$ (%) radians)	S_L , dB	$\sigma_{2\varphi}$ (%) radians)	S_L , dB	$\sigma_{2\varphi}$ (%) radians)
HAC Version	-20.16	8.1	-19.41	10.51	-19.1	14.36
Filtered HAC Version	-15.66	4.82	-15.16	6.44	-14.95	8.9
NASA Version with Squarewave Subcarriers	-19.4	7.42	-18.9	9.89	-18.64	13.61
HAC Version with Demodulation by Equivalent In-Phase and Quadrature Subcarriers	-25.8	15.49	-25.0	20.0	-24.63	27.1

12.0 CONCLUSIONS AND RECOMMENDATIONS

12.1 Power Budgets

It has been shown that, with the present set of system parameters (as of October 1977 [11]), when the radar is searching for a 1 m^2 passive target in the "Autotrack mode at 12 nmi, the design margin is -13.1 dB for the slow fading case and -6.8 dB for the fast fading case. This illustrates the effect of frequency diversity in the second case. A peak power of 50 watts was used in these calculations. A peak power of 60 watts is presently quoted, which provides an 0.8 dB improvement on each of the above design margins. See Appendix A for details.

Given the present system configuration, there are various ways to improve the design margin deficit, among which are the following:

- i) Allow more than 60 seconds to illuminate the search volume.
- ii) Allow the range at which the detection probability is to be 99 percent to decrease to something less than 12 nmi.
- iii) Allow the system to operate as is. The detection probability at 12 nmi will then be less than 99 percent.

In a forthcoming report, quantitative values will be determined for the range at which performance will be 99 percent. Also, the additional time required beyond the present 60 seconds to meet a detection probability of 99 percent at 12 nmi will be determined.

In the absence of these values, the recommendation is to allow more than 60 seconds to illuminate the search volume.

12.2 Angle Track and Angle Rate Estimation

A thorough analysis of the Ku-band radar, which is angle tracking a passive target is presented in Appendix C. The analysis is applicable to all modes of operation which require angle tracking, namely, GPC-ACQ, GPC-DES, and Autotrack. At all ranges of interest ($R < 10$ nmi) for passive targets, the angle tracking system has a design margin of approximately 9.5 dB. The crosscoupling errors into the angle tracking loops

from the range and doppler tracking loops are described but not evaluated. With the present design margin and the fact that the range and doppler crosstalk errors are not very significant, it is expected that the design margin for the angle tracking loop will remain adequate.

The analysis takes into account the effects of receiver front end thermal noise and scintillation from a point target. The effects of glint from a large target and target angular acceleration are not taken into account. These effects will be taken into account in a forthcoming report. The effects of angular acceleration and target glint are expected to be significant, particularly at short ranges.

The performance of angle rate estimation is described in Appendix D. It is shown therein that the RMS error of angle rate estimation is below the spec. value for all values of range less than 11 nmi. It should be emphasized, however, that as in the angle tracking analysis, only target scintillation and receiver front end noise are taken into account. It is expected that angular acceleration and target glint will deteriorate angle rate performance faster than angle tracking performance. It is expected that the convergence time, the angle tracking natural frequency and the angle tracking damping factor cannot be chosen so that all specs are met under all conditions. The followup report will provide more precise values for the design parameters listed above than is suggested in Appendix D.

12.3 Range Tracking

Range tracking is carried out by sequential processing of monopulse signals as in the case for angle tracking. The performance of the range tracking loop employing standard nonoverlapping early and late gates is developed in Appendix E. The present set of radar parameters (as of October 1977 [11]) is used in the performance computations. It is concluded that the range tracking loop meets specs for a point target when the noise bandwidth of the loop is less than 3 Hertz and the range is less than 9.5 nmi. For values of range greater than 9.5 nmi, a noise bandwidth of 0.4 Hz or less is required, and with that, the spec is met only for ranges up to 11 nmi.

This analysis does not take into account target acceleration in the LOS direction. This will be addressed in the forthcoming report.

It is recommended that the range tracking loop be accepted as is. If the noise bandwidth of the range tracking loop is decreased much more, then the settling time after a target acceleration along the LOS may become excessive.

12.4 Doppler Tracking

Range rate tracking is also carried out in a manner similar to the other tracking loops, with the exception that the bank of doppler filters is moved discretely. This is described in detail in Appendices B and G. Also, the range rate estimates are averaged to improve performance. In particular, for $R > 9.5$ nmi, two consecutive estimates are averaged, and for $R < 9.5$ nmi, four consecutive estimates are averaged. The performance analysis developed in Appendix G shows that this averaging is necessary to meet the spec value for $R < 9.5$ nmi. The averaging is not necessary for $R > 9.5$ nmi, although by doing so, the design margin is increased. At 9.5 nmi with the averaging described above, the design margin for the range rate tracking loop is approximately 2.5 dB.

REFERENCES

1. "Procurement Specification MC409-0025, Ku-Band Integrated Radar and Communications Equipment," Vol. II, Space Division/Rockwell International, March 15, 1976.
2. M. K. Simon, S. Udalov, and G. K. Huth, "Study to Investigate and Evaluate Means of Optimizing the Ku-Band Communication Function for the Space Shuttle," Axiomatix Report No. R7703-2 (under NASA Contract NAS 9-14614), March 31, 1977.
3. "Proposal for Ku-Band Integrated Radar and Communication Equipment for the Space Shuttle Orbiter Vehicle," Vol. II, Hughes Aircraft Company, Ref. No. D7768/SCG 60176P, May 1976.
4. C. L. Weber, "Optimization of Proposed Radar for the Integrated Ku-Band Radar Communication System," Axiomatix Report No. R7408-5, August 1974.
5. "Ku-Band Integrated Radar and Communication Equipment for the Space Shuttle Orbiter Vehicle," Hughes Aircraft Company, Ref. No. D7738-SCG 76075V, HS 237-202, Conceptual Design Review, January 31, 1977.
6. S. Udalov, "Power Budgets for Passive Target Detection - Pulse Doppler Radar," Appendix N in "Study to Investigate and Evaluate Means of Optimizing the Radar Function for the Space Shuttle," Axiomatix Report No. R7607-4, July 1976.
7. "Study to Investigate and Evaluate Means of Optimizing the Radar Function for the Space Shuttle," Axiomatix Report No. R7607-4 (under NASA Contract NAS 9-1461-), July 31, 1976.
8. R. Becker, "Rendezvous Profile Summary," Ku-Band Monthly Report, April 15, 1977.
9. "Ku-Band Integrated Radar and Communication Equipment for the Space Shuttle Orbiter Vehicle," Hughes Aircraft Company Monthly Program Status Report, May 24, 1976.
10. "Space Shuttle Ku-Band Integrated Rendezvous Radar/Communications System Study," Hughes Aircraft Company, Report No. D4148 SCG 60041R, for NASA-JSC under Contract NAS 9-14595, March 1976.
11. Hughes Aircraft Company, "Ku-Band Integrated Radar and Communication System for the Space Shuttle Orbiter," Program Status Report, 13 October 1977.

APPENDIX A

POWER BUDGETS FOR THE KU-BAND RADAR FOR THE SPACE SHUTTLE ORBITER VEHICLE

APPENDIX A

POWER BUDGETS FOR THE KU-BAND RADAR FOR THE SPACE SHUTTLE ORBITER VEHICLE

by

Charles L. Weber
Waddah K. Alem

1.0 INTRODUCTION

Sample power budgets are presented for the Orbiter Ku-band radar described in [1]. Most of the hardware losses predicted in [1] are used in the budget computations in this report. The passive automatic search-and-detect mode only is considered. This mode is the most critical from the required transmitted power point of view. Each of the parameters is considered individually before the composite power budgets are assembled.

2.0 THE RADAR EQUATION

The radar equation that is appropriate for passive mode detection of a pulse doppler radar which is essentially using an optimal receiver [2-4] is given by

$$\bar{R}_p = \frac{2E_p}{N_0} = \frac{[G^2 \bar{\sigma} \lambda^2][2P_p \tau_f]}{[(4\pi)^3 R^4][k T_{sys}][L]} \quad (1)$$

where \bar{R}_p = ensemble averaged peak SNR required per pulse for a given probability of detection, P_d , and false alarm probability, P_{fa} . In the case of an optimal radar which employs frequency diversity, the time of the pulse corresponds to the total time during which coherent addition takes place during one frequency dwell time.

E_p = peak signal energy received during the time in which coherent addition takes place

N_0 = equivalent one-sided noise power spectral density of the entire receiver system = kT_s

$\bar{\sigma}$ = average target cross section

λ = radar RF wavelength

G = peak antenna power gain

P_p = peak transmit power = P_{avg}/d_t

d_t = transmitter duty factor

P_{avg} = average transmit power

τ_f = total time of coherent addition at one RF = τN

- τ = transmitted pulse width
- N = number of transmitted pulses per RF frequency
- R = range
- k = Boltzmann constant = 1.38×10^{-23} Joules/°K
- T_{sys} = system noise temperature, °K
- L = total system losses.

3.0 SEARCH RADAR SYSTEM PARAMETERS

Each of the above parameters is now considered in regard to the Ku-band radar for the Space Shuttle Orbiter Vehicle described in [1]. The reasoning and/or source of the choice of each parameter value is indicated.

3.1 Required Peak Signal-to-Noise Ratio Per Pulse

$$\bar{R}_p = \frac{2E_p}{N_0}$$

This value is dependent on the assumptions made about the mode of detection. The assumptions to be used in these power budgets are among the following cases. The overall probability of detection is 0.99 and the false alarm probability is 10^{-6} . The 0.99 value is a specification requirement, and the $\alpha = 10^{-6}$ value is approximately equivalent to one false alarm per hour, which is the specified value. The value of R_p is relatively insensitive to the choice of α . Hence, the choice is not critical. The cases shown in Table 1 all assume two scans, so that the probability of detection per scan is 0.9. The following definitions are used in Table 1:

- I = number of pulses, noncoherently added
- P_d = probability of detection per scan
- n' = false alarm number
- $\alpha = 0.693/n'$.

The table takes into account target fluctuation loss in both the slow and fast fading cases. The values in Table 1 were derived from Figure 1 which illustrates the maximum signal-to-noise ratio ($R_p = 2E_p/N_0$) as a function of I , the number of pulses incoherently integrated, for Swerling I and Swerling II.

Table 1. Required Value of Signal-to-Noise Ratio to Meet the Indicated Performance Levels Under the Indicated Assumptions

Case	Requirements				SNR Needed	
	Description	I	P_d^{**}	n'	R_p (dB)	E_p/N_0 (dB)
1	Swerling I (Slow Fading)*	5 ***	0.9	10^6	18.7	15.7
2	Swerling II (Fast Fading)*	5	0.9	10^6	12.4	9.4

*The phraseology being adopted (somewhat incorrectly) is that the Swerling I model corresponds to slow fading and Swerling II to fast fading. The interpretation is based on the following assumptions, namely, that frequency diversity is being employed and that the target is initially modeled by Swerling I fluctuations. If the frequency diversity is not effective so that the Swerling I model still applies, then the term "slow fading" is used. If the frequency diversity is completely effective, and independent samples are being received upon changes in RF, then Swerling II applies, and it is called "fast fading."

**The cumulative probability of detection is specified at 0.99. With two scans of the column in 60 seconds, each scan then has a probability of detection of $P_d = 0.9$. For scan angles of 40° ($\pm 20^\circ$) or less, there are always at least two scans on the target in the specified maximum search time of 60 seconds [1].

*** If the number of RF frequencies is set to be $N = 6$, the needed E_p/N_0 decreases to 15.2 dB and 8.7 dB for Swerling I and II, respectively.

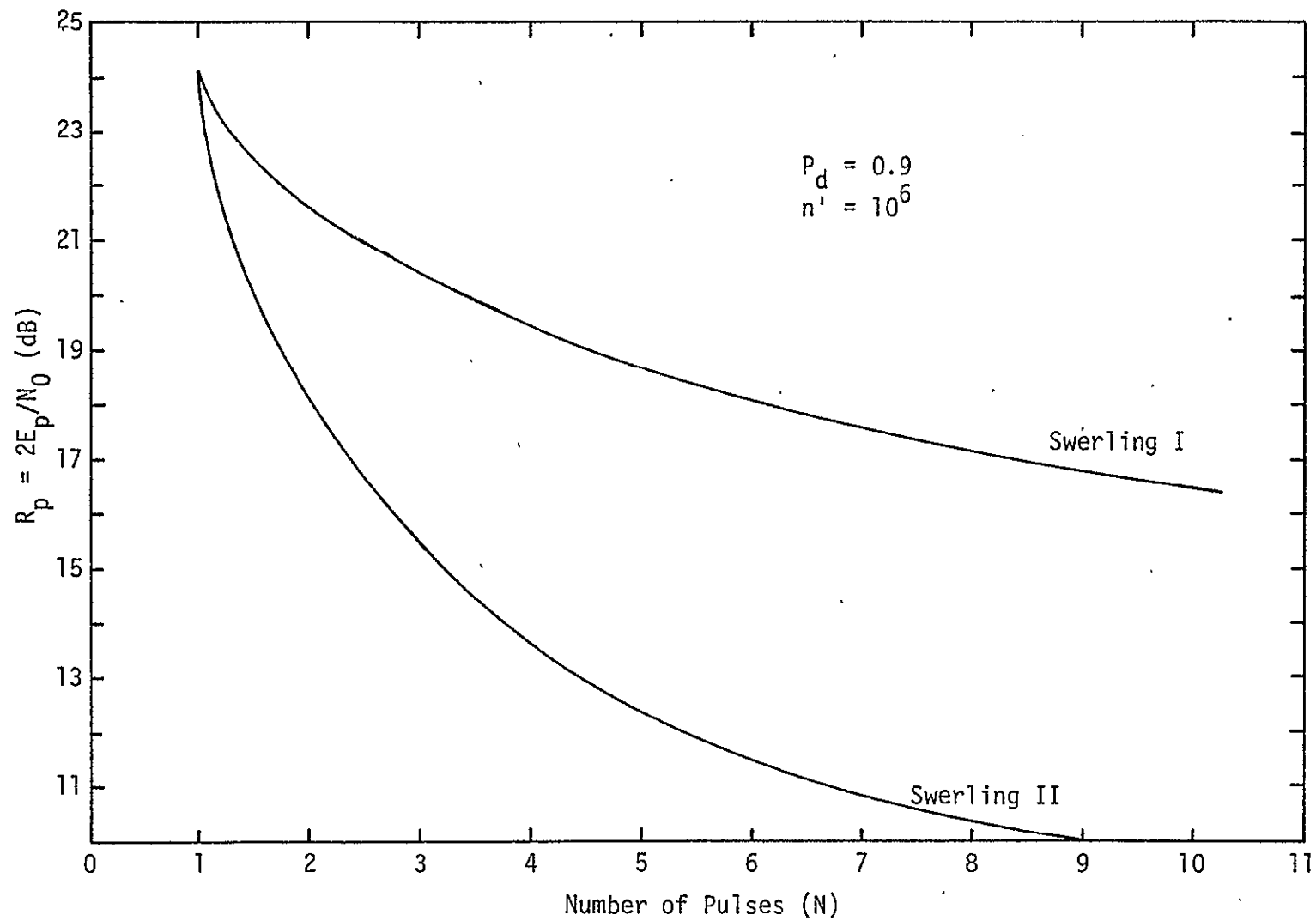


Figure 1. Peak Signal-to-Noise Ratio vs. Number of Pulses Incoherently Integrated

3.2 Average Target Cross-Section

$$\begin{aligned}\bar{\sigma} &= 1 \text{ m}^2, \text{ as per specification} \\ &= 0 \text{ dB.}\end{aligned}$$

3.3 Radar RF Wavelength

There are five RF frequencies being used for the Ku-band radar; they are:

13.779 GHz
13.831 GHz
13.883 GHz
13.937 GHz
13.987 GHz

The center RF for the radar is 13.883 GHz. This corresponds to

$$\begin{aligned}\lambda &= 0.0216 \text{ meters} \\ \lambda^2 &= -33.31 \text{ dB.}\end{aligned}$$

3.4 Peak Antenna Power Gain

The antenna diameter has been specified as $d = 36'' = 0.914 \text{ m}$. Based on the rule of thumb:

$$\theta_B \text{ (deg)} \approx (180/\pi)(d/\lambda),$$

the 3 dB beamwidth is $\theta_B \approx 1.32 \text{ deg}$. The 3 dB beamwidth quoted in [1] is 1.6 deg. Based on the rule of thumb [8],

$$G \approx \frac{32,000}{(\theta_B)^2} \quad (\theta_B \text{ in deg}),$$

the peak power gain of the antenna is

$$G \approx 41 \text{ dB.}$$

The peak power gain in [1] is 38.9 dB, so that

$$G^2 = 77.8 \text{ dB.}$$

More recently, however, the peak power gain is given as 38.5 dB [9], so that

$$G^2 = 77.0 \text{ dB.}$$

The latter value is used in the power budgets in this report.

3.5 Transmitted Signal Characteristics

$$P_p = \text{peak transmitter power}$$

Given all other parameters and assumptions in the radar equation, the required peak transmitter power will then be obtained.

For the automatic search mode of a passive target, the PRF is presently set at 2987 [10], so that the pulse repetition interval (PRI) is

$$\text{PRI} \triangleq T_p = 335 \text{ } \mu\text{sec}.$$

Also, the pulse width is

$$\tau = 66.4 \text{ } \mu\text{sec},$$

so that the transmitter duty factor is

$$d_t = 0.20$$

and the maximum unambiguous range is 27.11 nmi. The spatial dwell time, T_d , based on the algorithm described in [1] is

$$T_d = 28.6 \text{ msec}.$$

This also agrees with that developed by Udalov [5] for the Ku-band radar search mode of a passive target.

The timing of the RF signal during one spatial dwell time is as shown in Table 2, where the frequency dwell time is seen to be 5.36 msec over each of the five RFs. Five RF frequencies are assumed to be processed during each spatial dwell time. This is a conservative assumption, since T_d is larger than $5 t_f$.

Table 2. One Spatial Dwell Time

RF	F_1	F_2	F_3	F_4	F_5	Total
Number of RF Pulses	16	16	16	16	16	80
t_f (msec)	5.36	5.36	5.36	5.36	5.36	26.80

There are 16 RF pulses during each RF frequency dwell time. These are coherently added in the digital implementation, since the bandwidth of each of the doppler filters is matched to that associated with 16 pulses at one RF.

This is not a centerline radar, since there is no centerline filter and since wideband sampling is performed at IF. This allows the coherent addition of all coherent lines in the receiver RF spectrum over the entire IF bandwidth.

The total time of coherent addition at one RF is

$$\tau_f = \tau N,$$

where $\tau = 66.4 \mu\text{sec}$

$N = 16$ pulses.

Therefore,

$$\begin{aligned}\tau_f &= \text{total time of coherent addition} \\ &= 1.062 \text{ msec} \\ &= -29.74 \text{ dB.}\end{aligned}$$

3.6 Range

The specification calls for meeting the above requirements for a $\sigma = m^2$ passive target at 12 nmi = 22.236 km. However, the range will be kept as a parameter in the power budget calculations.

3.7 Receiver Noise Parameters

The equivalent one-sided power spectral density of the receiver noise is

$$N_0 = kT_{\text{sys}} \text{ watts/Hz},$$

where $k = \text{Boltzmann's constant} = 1.38 \times 10^{-23} \text{ Joules/}^\circ\text{K}$
 $= -228.6 \text{ dB}$

$T_{\text{sys}} = \text{overall system noise temperature.}$

The components in the overall system noise temperature can be computed from the diagram shown in Figure 2. The receiver is assumed to have a noise figure of 5 dB. All component losses [1] between the antenna and the receiver add to 2.8 dB.

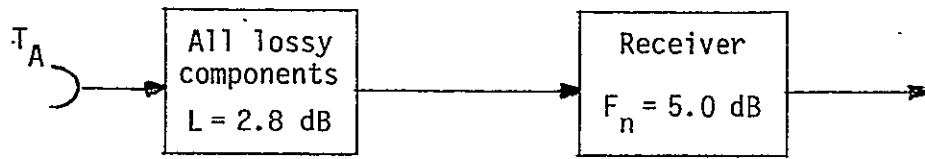


Figure.2. Simplified Diagram of Losses for Ku-Band Radar Receiver

When the first stage of a receiver is an attenuator, as is the case here, it can be shown [6] that the system noise temperature, computed at the antenna, is

$$T_{\text{sys}} = T_A + T_c + (L-1)T_0 + LT_e,$$

where T_A = antenna temperature

T_c = additional antenna temperature due to clutter

L = total attenuation from all lossy components between the antenna and receiver input

T_e = receiver noise temperature = $(F_n - 1)T_0$

F_n = receiver noise figure

T_0 = standard room temperature = 290°K.

The design in [1] assumes the receiver noise figure is $F_n = 5.0$ dB or, equivalently, $T_e = 627^\circ\text{K}$, and the attenuation from all lossy components between the antenna and receiver front end is $L = 2.8$ dB. The antenna temperature is assumed to be $T_A = 5.5^\circ\text{K}$ and the additional antenna temperature due to earth clutter when looking horizontally is $T_c = 36.5^\circ\text{K}$. Then,

$$\begin{aligned} T_{\text{sys}} &= T_A + T_c + (L-1)T_0 + LT_e \\ &= 5.5 + 36.5 + 263 + 1195 \\ &= 1500^\circ\text{K} \\ &= 31.76 \text{ dB.} \end{aligned}$$

This is increased somewhat as the look angle increases. When looking directly towards the earth, the clutter temperature increases to 263.5°K and T_{sys} increases to

$$T_{\text{sys}} = 1727^\circ\text{K} = 32.37 \text{ dB.}$$

3.8 Losses

In this section, the pertinent losses are listed, along with the references where values were derived or where the losses were specified.

3.8.1 Transmit Losses

The RFP and the response [1] have specified the transmit losses at 3.5 dB. A new value of 3.7 dB has been used recently. This value will be used in the power budget calculations without any attempt to dispute it.

3.8.2 Scan Alignment Loss and Lateral Scan Loss

The specification calls for a total beam shape loss of 2 dB. In [3], it is shown that the scan alignment loss is 1.03 dB each way and the lateral scan loss is 0.58 dB each way when the antenna movement from one circle to the next in the spiral scan is $0.6 \theta_B$. The spiral scan described in [1,5] calls for an antenna movement of $0.7 \theta_B$. The difference in scan alignment loss and lateral scan loss between adjacent antenna paths of $0.6 \theta_B$ and $0.7 \theta_B$ is negligible. Thus, the two-way loss due to beam shape which includes scan alignment loss and lateral scan loss is set at $2(1.03 + 0.58) = 3.2$ dB.

3.8.3 Threshold Loss (Constant FAP)

The specification calls for a threshold loss of 1 dB due to maintaining a constant false alarm probability by monitoring the system noise level. A value of 1.7 dB has been recently used; this value is used in the computation, realizing that it should be possible to reduce this value to a few tenths of a dB.

3.8.4 Processor Loss

It is estimated that the algorithms in the radar digital signal processor will result in approximately 1.7 dB loss [1]. This value is also used in the power budget, while anticipating that it may be possible to reduce it.

3.8.5 Range Gate Straddling

There are two modes to be considered when discussing the range gate straddling loss. The first is when no range designation is available from the GPC. In this mode, four nonoverlapping range gates are

used as shown in Figure 3. Each range gate is of the same width as the transmitted pulse. The corresponding value of the range is shown at the beginning of each range gate which corresponds to zero straddling loss. As the range (R) of the target varies from 5.37 nmi to 21.50 nmi, the straddling loss fluctuates from 0 dB at the ranges $R = 5.37n$ ($n = 1, 2, 3, 4$) to a maximum of 6 dB when the pulse lies halfway between two range gates, that is, at $R = 5.37(n + 1/2)$.

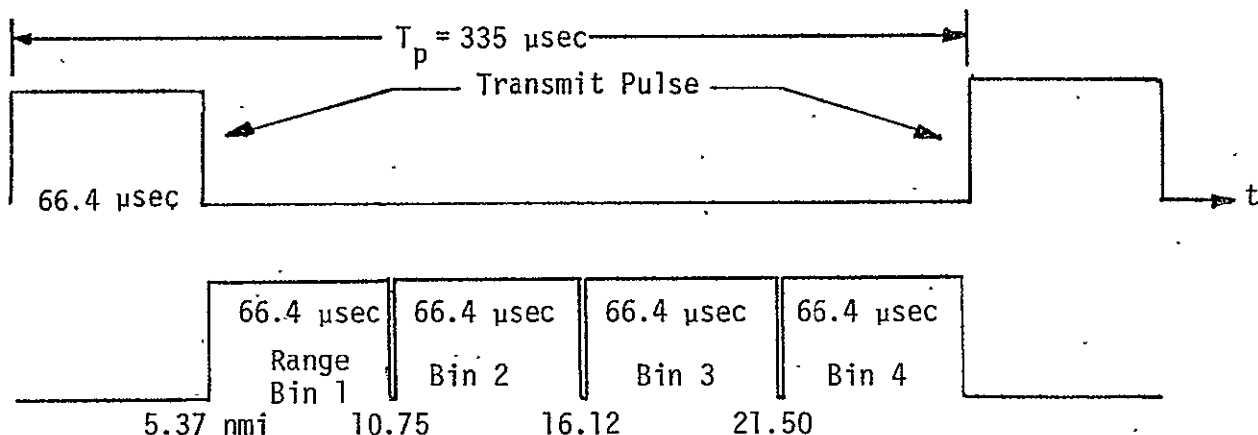


Figure 3. Range Gate Diagram

In general, the straddling loss can be given by

$$L_{\text{str}} = \min \left[\left| 10 \log \left(\frac{H-R}{5.37} \right)^2 \right|, \left| 10 \log \left(\frac{R-L}{5.37} \right)^2 \right| \right], \quad (2)$$

where "min" denotes the minimum of the two numbers, $H = 5.37(n+1)$, and $L = 5.37n$, such that

$$L < R < H.$$

The squares in (2) are due to the fact that magnitude detection is implemented at the output of the doppler filters bank before threshold comparison (see Appendix B). A plot of the straddling loss without range designation, as a function of range, is shown in Figure 4.

In the second mode, when range designation is provided by the GPC, two overlapping range gates, which are centered around the designated range R_d , are used (see Appendix B) as shown in Figure 5 [10].

For $R_d > 7.2$ nmi, the pulse width in nmi is equal to 5.37 nmi.

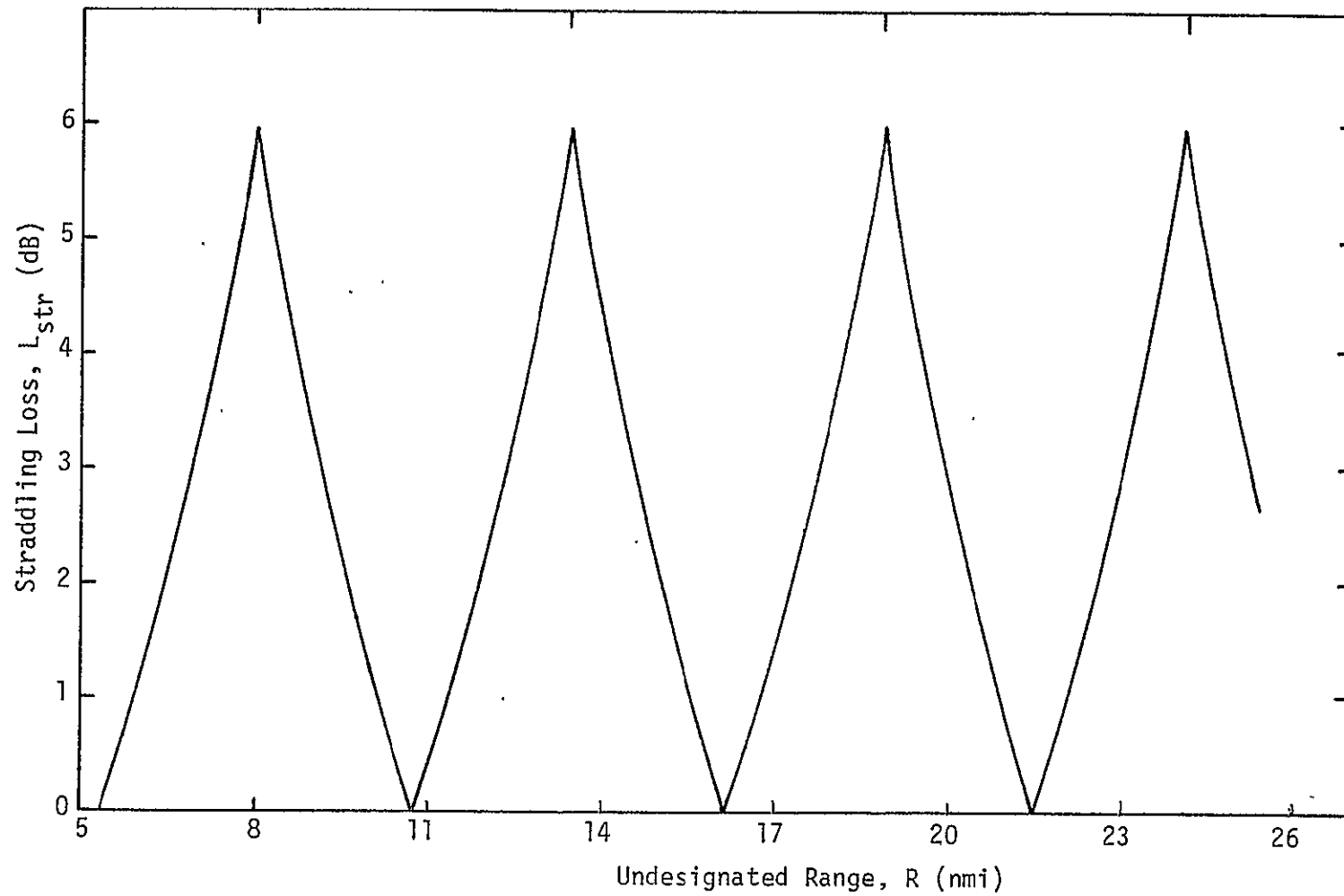


Figure 4. Straddling Loss vs. Undesignated Range R

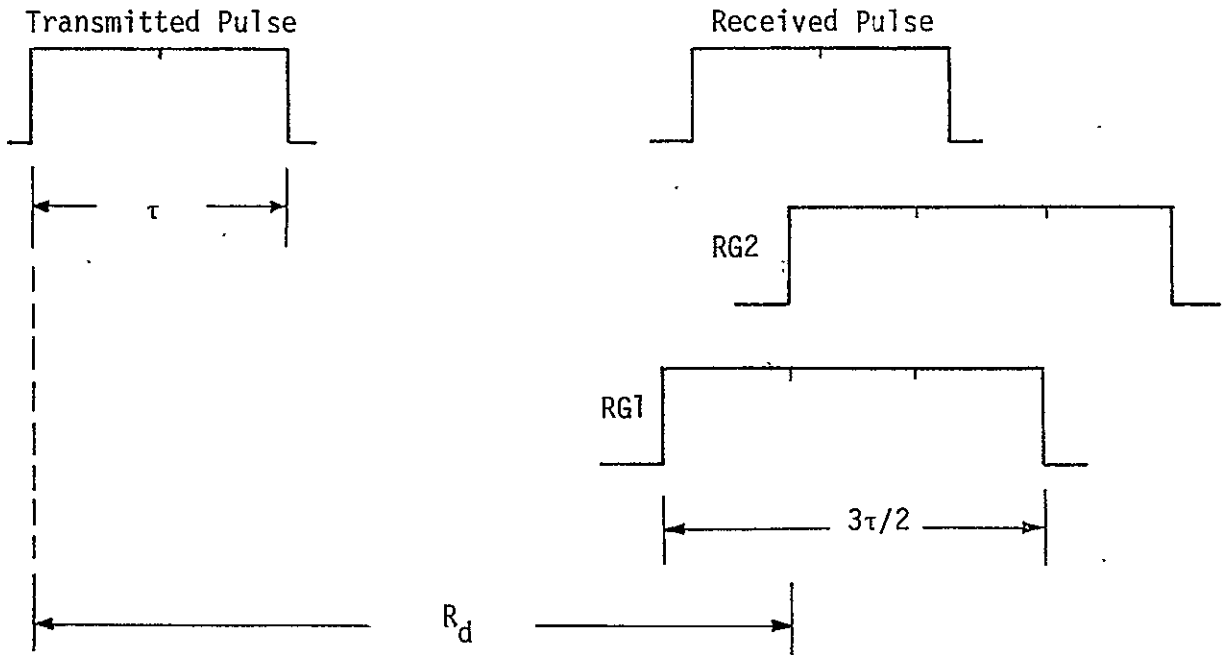


Figure 5. Range Gates with GPC Designation

If the range designation is accurate to within 20% of the actual range, then the maximum range error at 12 nmi would be 2.4 nmi, which is still less than half a pulse width (5.37 nmi). Hence, all the signal energy can be detected in one of the gates. This gate, in turn, is used in the threshold detection (see Appendix B). Since the pre-summing is carried out over $3\tau/2$, which is the gate width, it effectively increases the variance of the output noise by 3/2 (1.76 dB), which is the straddling loss in this mode.

3.8.6 Doppler Filter Loss

Following each of the four range bins is a bank of 16 doppler filters, as shown in the block diagram of Figure 6. These filters are uniformly spaced over the frequency range $[f_c, f_c + f_{PRF}]$. For passive search and detection above 7.2 nmi, the PRF is 2987 Hz, so that the frequency difference between the center of adjacent filters is 186 Hz, as shown in Figure 6. If the 3 dB (one-sided) is set at $f_{PRF}/16$, then at the points where the adjacent filter gains cross (at ± 93 Hz about the center of the filter), the gain is down approximately 0.7 dB for a $[(\sin x)/x]^2$ filter. This loss is classified as mismatch due to doppler.

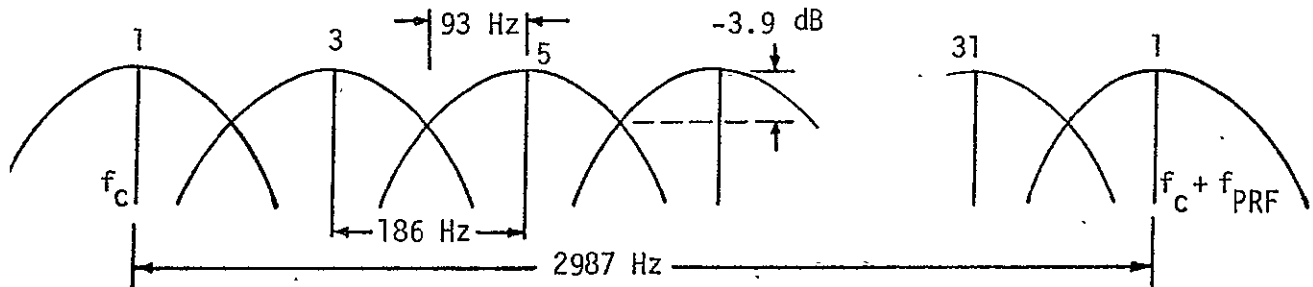


Figure 6. Description of Bank of Doppler Filters

Since discrete Fourier transforms (DFT) are used as a means of doppler filtering, the square of the doppler filter transfer function is given of the form

$$\left(\frac{\sin(\Delta\omega N T_p / 2)}{N \sin(\Delta\omega T_p / 2)} \right)^2$$

where $T_p = 335 \mu\text{sec}$ and $N = 16$. At the center frequency between two filters, $\Delta\omega = 2\pi/(2NT_p)$, which results in 3.9 dB loss due to doppler filtering.

There may be additional loss due to the lack of a proper match between the pulse bandwidth, the PRF, and the bandwidth of the FFT.

3.8.7 Pre-Sum Mismatch

There is an additional loss due to doppler in the pre-sum. The pre-sum adds all samples over the width of one range bin from a transmitted pulse. There is no doppler compensation in the pre-sum. If there is no doppler, then this coherent addition is ideal and there is no loss. As the doppler frequency increases, the pre-sum loss increases. This loss is in both the I and Q channels and can be described in terms of the following integral and is shown in Figure 7.

$$L_{\text{PRE-SUM}} = \left| \frac{1}{\tau_p} \int_0^{\tau_p} e^{j2\pi f_D t} dt \right|^2$$

where τ_p is the transmitted pulse width and f_D is the doppler frequency. This is a very close approximation to the actual pre-sum loss, since

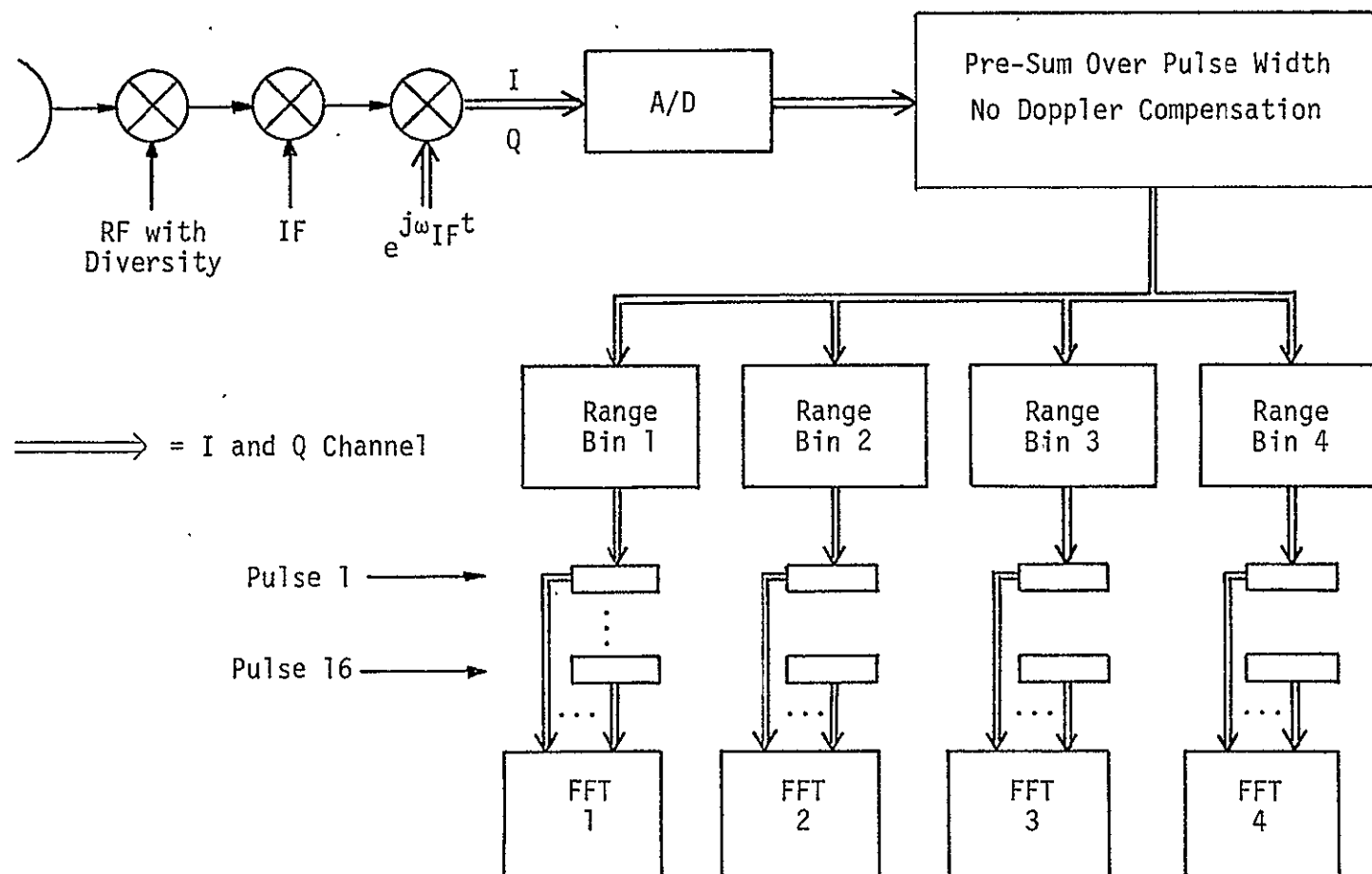


Figure 7. Block Diagram of Digital Pulse Doppler Detection

the sampling rate is high. The pre-sum loss becomes

$$L_{\text{PRE-SUM}} = \left| \frac{\sin(\pi f_D \tau_p)}{\pi f_D \tau_p} \right|^2,$$

which is plotted in Figure 8. For the radar in [1], $\tau_p = 66.4 \mu\text{sec}$. The range rate varies over -75 fps to $+148 \text{ fps}$. At $f_c = 13.775 \text{ GHz}$, each fps is equal to approximately 28 Hz , so that the doppler frequency is within the range

$$f_D \in [-2100, +4144 \text{ Hz}].$$

Ambiguity clearly exists, since the $\text{PRF} = 2987 \text{ Hz}$. This ambiguity is being resolved by filtering and differentiating the range measurements. The maximum pre-sum loss therefore occurs at $f_D = 2987 \text{ Hz}$. Then,

$$\tau f_D = (66.4 \mu\text{sec})(2987 \text{ Hz}) = 0.2.$$

This is shown as the dot in Figure 8, and the resulting maximum pre-sum loss is 0.57 dB .

4.0 POWER BUDGETS FOR PASSIVE SEARCH

In Table 3, the results of the previous sections (except for range dependent parameters) are summarized for the slow and fast fading cases, while Table 4 lists all the losses involved. The assumption that the target detection must be accomplished at $R = 12 \text{ nmi}$ is still maintained.

Budget I, the slow fading case, assumes frequency diversity is present but totally ineffective and that independent samples are not obtained when the RF frequency is switched. As a result, we have a Swerling I target. The post-detection integration is still noncoherent from frequency to frequency.

With all the parameters listed in Table 3, the required peak power for the nondesignated range case is given by

$$(P_p)_{\text{dB}} = -145.07 + 40 \log (R)_m + L_{\text{str}} \quad (4)$$

for the slow fading case and

$$(P_p)_{\text{dB}} = -152.37 + 40 \log (R)_m + L_{\text{str}} \quad (5)$$

for the fast fading case.

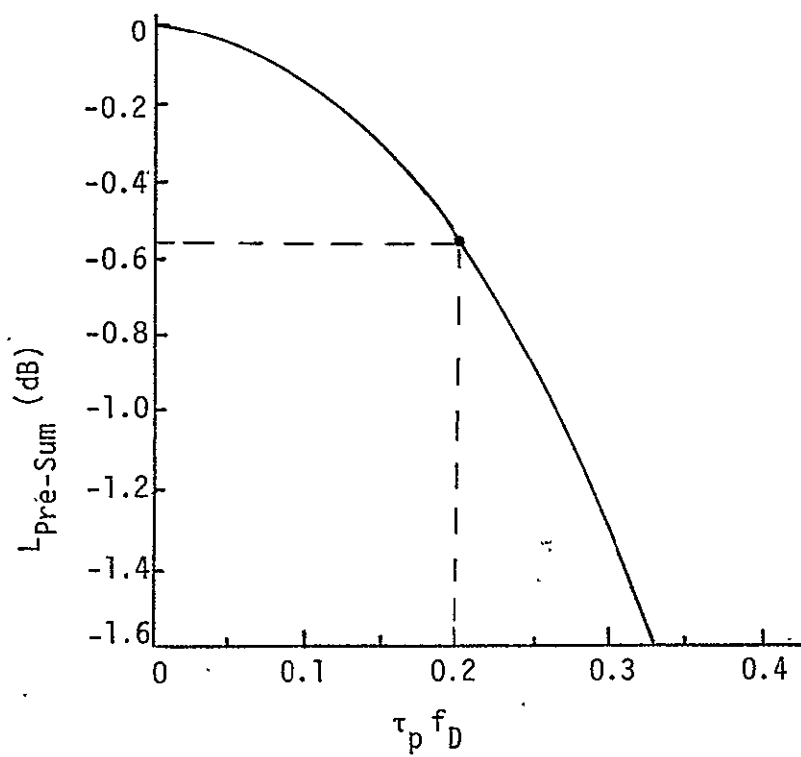


Figure 8. Pre-Sum Loss as a Function of the Pulse Width-Doppler Frequency Product

Table 3. Power Budget Parameters for Passive Search
Without Range Designation Based on Two Hits

Item	Term	Section	Value	Budget (Case I) Slow Fading (dB)	Budget (Case II) Fast Fading (dB)
1	R_p	3.1	Required Peak SNR	18.7	12.4
2	G^2	3.4	$G = 38.5$ dB	-77.0	-77.0
3	λ^2	3.3	$\lambda = 0.0216$ m	33.31	33.31
4	$\bar{\sigma}$	3.2	1 m^2	0	0
5	$(4\pi)^2$			33	33
6	R^4	3.6	Range (m)	$40 \log R$	$40 \log R$
7	k	3.7	$1.38 \times 10^{-23} \text{ J/}^\circ\text{K}$	-228.6	-228.6
8	T_{sys}	3.7	1500°K	31.76	31.76
9	τ_f	3.5	1.062 msec	29.74	29.74
10	Factor	2.0	2	-3.0	-3.0
11	Total Losses		No Range Designation*	$16.02 + L_{\text{str}}$	$16.02 + L_{\text{str}}$

* With range designation, the straddling loss (L_{str}) is equal to 1.76 dB.

Table 4. Detection Losses for Passive Search Without Range Designation

Item	Term	Section	Description	Value (dB)
1	Transmit Losses	3.8.1	REP	3.7
2	Beam Shape	3.8.2	Scan Alignment	3.2
3	Threshold	3.8.3	Constant FAP	1.7
4	Processor Loss	3.8.4		1.7
5	Range Gate Straddling Loss	3.8.5	Function of R	L_{str}
6	Doppler Losses	3.8.6	Mismatch	3.9
7	PDI		Post-Detection Integration [1]	1.25
8	Pre-Sum Mismatch	3.8.7	Due to Doppler	0.57
Σ				$16.02 + L_{\text{str}}$

The available peak power is 50 w* (17 dBw) and the average power is 10 w (10 dBw). Comparing the average powers that result from (4) and (5) with a duty factor $d_t = 0.2$ to the available average power results in Figures 9 and 10 for the slow fading and fast fading cases, respectively.

The design margin at 12 nmi is -13.10 dB for the slow fading case and -6.80 dB for the fast fading case, which illustrates the effect of frequency diversity in the second case.

Figures 9 and 10 also illustrate the design margin for the designated range case where the straddling loss is kept constant (1.76 dB). The design margin in this case is better except for $9.8 < R < 11.8$ nmi, when the nondesignated case provides less straddling loss than the designated case.

It is noted that all the previous calculations are based on two scans with a cumulative probability of detection of 0.99. This is only possible if the search angle is limited to $\pm 20^\circ$. For larger angles, only one scan is feasible, which results in worse design margins.

It is believed that, in order to improve the design margins, the various system losses should be improved and/or the integration time should be increased in order to increase the signal energy.

* A peak power of 60 w has been quoted recently. The old, conservative value of 50 w will still be used in the calculations.

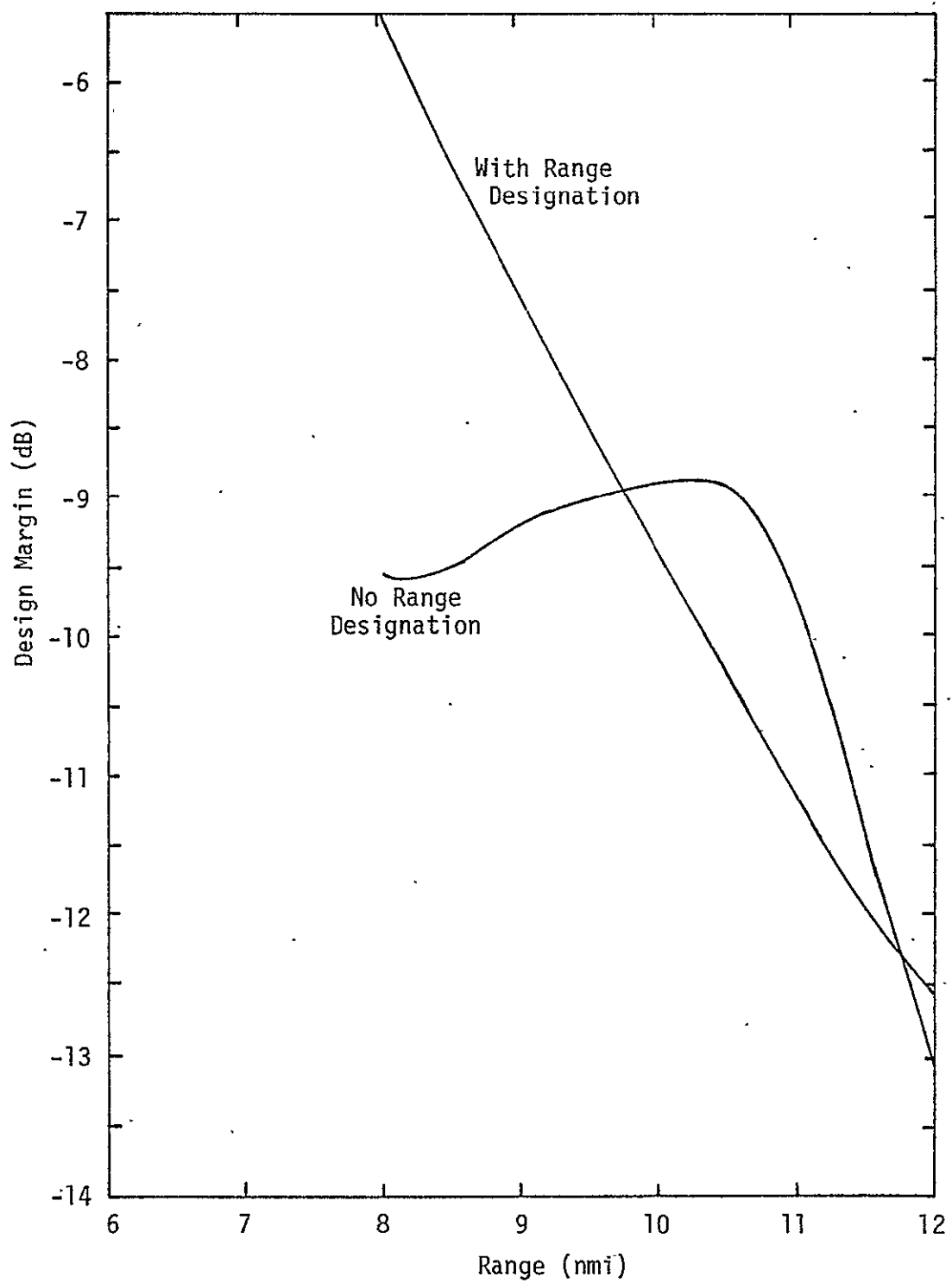


Figure 9. Design Margin vs. Range for the Slow Fading Case

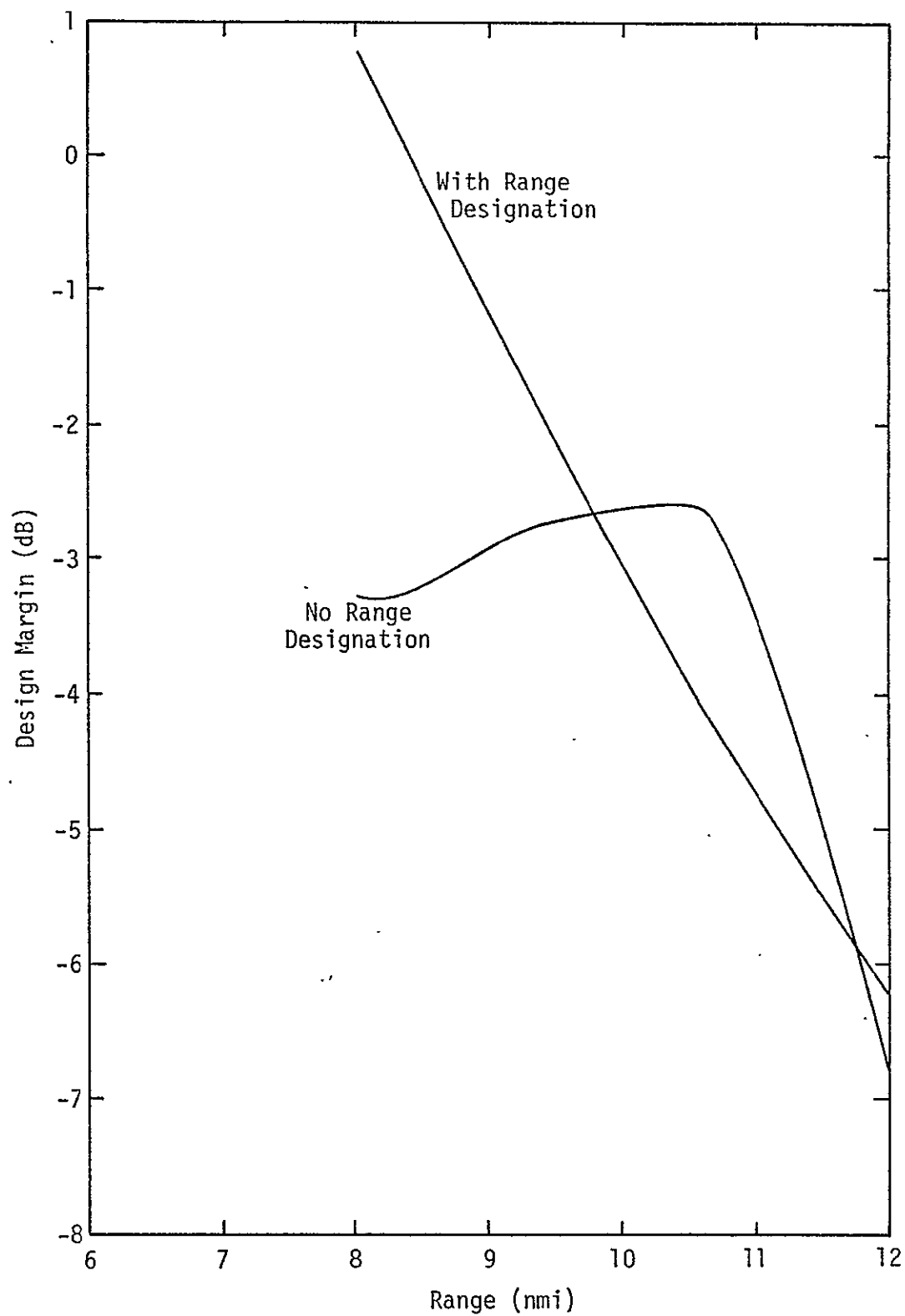


Figure 10. Design Margin vs. Range for the Fast Fading Case

REFERENCES

1. Hughes Aircraft Co. "Ku-Band Integrated Radar and Communication Equipment for the Space Shuttle Orbiter Vehicle," Ref. No. D7738-SCG76075V, HS237-202, Conceptual Design Review, January 31, 1977.
2. S. Udalov. "Power Budgets for Passive Target Detection - Pulse Doppler Radar," Appendix N in "Study to Investigate and Evaluate Means of Optimizing the Radar Function for the Space Shuttle," Axiomatix Report No. R7607-4, July 1976.
3. C. L. Weber. "Optimization of Proposed Radar for the Integrated Ku-Band Radar Communication System," Axiomatix Report No. R7408-5, August 1974.
4. J. V. DiFranco and W. L. Rubin. Radar Detection. Prentice-Hall, 1968.
5. S. Udalov. "Spiral Scan Analysis," Appendix M in "Study to Investigate and Evaluate Means of Optimizing the Radar Function for the Space Shuttle," Axiomatix Report No. R7607-4, July 1976.
6. A. B. Carlson. Communication Systems, An Introduction to Signals and Noise in Electrical Communication. McGraw-Hill, 1968.
7. C. L. Weber. "Analysis of a Center Line Pulsed Doppler Radar Operating in the Search Mode," Axiomatix Report No. R7407-1, July 1974.
8. M. Skolnik. Radar Handbook. McGraw-Hill, 1970.
9. Hughes Aircraft Co. "Ku-Band Integrated Radar and Communication System for the Space Shuttle Orbiter Vehicle," Monthly Review, April 20, 1977.
10. Hughes Aircraft Co. "Ku-Band Integrated Radar and Communication Equipment for the Space Shuttle Orbiter Vehicle," Schematic Review, Vol. I, June 20, 1977.

1

•

APPENDIX B

RADAR PASSIVE SEARCH AND TRACK MODES DESCRIPTION

by

Charles L. Weber
Waddah K. Alem

1.0 INTRODUCTION

The objective of the Ku-band radar system on the Shuttle Orbiter is to detect the presence of a target and then obtain continuous accurate estimates of the various target parameters, namely, its range, range rate (velocity), azimuth, elevation angle, and angle rates. The target is usually detected when the radar is in the search mode, while the accurate estimates are obtained in the track mode. It is the objective of this appendix to clarify the overall radar block diagram and to explain its operation in both the search and track modes.

The radar employs coherent processing over each RF frequency transmitted, and noncoherent postdetection integration (PDI). Following the intermediate amplifiers, in-phase and quadrature phase signals are sampled and digitized (A/D converted), providing target amplitude and phase information. For longer range search and acquisition ($R > 0.42$ nmi), 16 doppler filters are formed, covering the doppler interval defined by the repetition rate. This is an ambiguous doppler interval; this ambiguity is removed via differentiation of the range estimates.

Following the filters, the target magnitude is determined, summed over the number of RF frequencies (noncoherent postdetection integration) and compared to a threshold. The threshold is set from noise measurements, so as to maintain a constant false alarm probability (CFAP). This can be implemented by any of several methods.

In the search mode, only the sum channel is processed. When the threshold is exceeded and target detection is declared, the auxiliary antenna signal is processed and its magnitude is compared with that of the main antenna to eliminate sidelobe detected targets. The auxiliary antenna has a peak gain which is approximately 20 dB less than that of the main antenna. Also, the sidelobes of the main antenna are approximately 20 dB down from the main lobe. This provides roughly a 20 dB main lobe/guard antenna ratio to detect and eliminate sidelobe targets.

In the modes for which angle tracking is required, namely, GPC acquisition and autotrack, the sum plus angle error channels are processed. The azimuth and elevation error signals are time-multiplexed, thereby eliminating the need for a second and third matched processing channel.

In Section 2.0, a general block diagram is drawn and explained in more detail; the functions of the individual blocks are described in the subsequent sections.

2.0 RADAR BLOCK DIAGRAM

The Shuttle Ku-band radar block diagram is shown in Figure 1. The antenna assembly consists of a main antenna and an auxiliary antenna, followed by the deployed mechanism assembly (DMA) and the deployed electrical assembly (DEA), where various switching and filtering operations take place, as explained in Section 3.0. The antenna assembly is followed by several IF mixing stages to bring the carrier frequency down to a stable IF of $f_0 = 78.143$ MHz. The output of the I-Q stage that follows is a pair of baseband signals which are in phase and in quadrature with the input signal. The operation of the previous two stages is discussed in Section 4.0. The available information is converted by an A/D converter to digital data which samples both channels at a rate of $f_s = 480$ kHz, which is slightly larger than the Nyquist rate of the baseband signals at the output of the I-Q stage. (The LPF bandwidth in both the I and Q channels is equal to 237 kHz.) The output of the A/D converter is a set of complex numbers which undergo various stages of digital processing before estimates of the target parameters (range, velocity, azimuth angle, elevation angle) are obtained. The first processing stage is a presumming stage, followed by a set of range gates and doppler filters consecutively. The arrangement of the gates is varied for the two modes of operation. Two cases are distinguished in the search mode. When a range designation is not available, four range gates per pulse are used, whereas two overlapping range gates are used when range designation is provided [9]. The width of each of the two range gates is $(3\tau/2)$, where τ is the pulse width. In the track mode, there are only two nonoverlapping gates—an early gate and a late gate.

For long ranges, the magnitudes of the outputs of the doppler filters are summed over the RF frequencies and compared to a threshold to detect the existence of a target. For short ranges ($R < 0.42$ nmi), the detection takes place without using any doppler filtering.

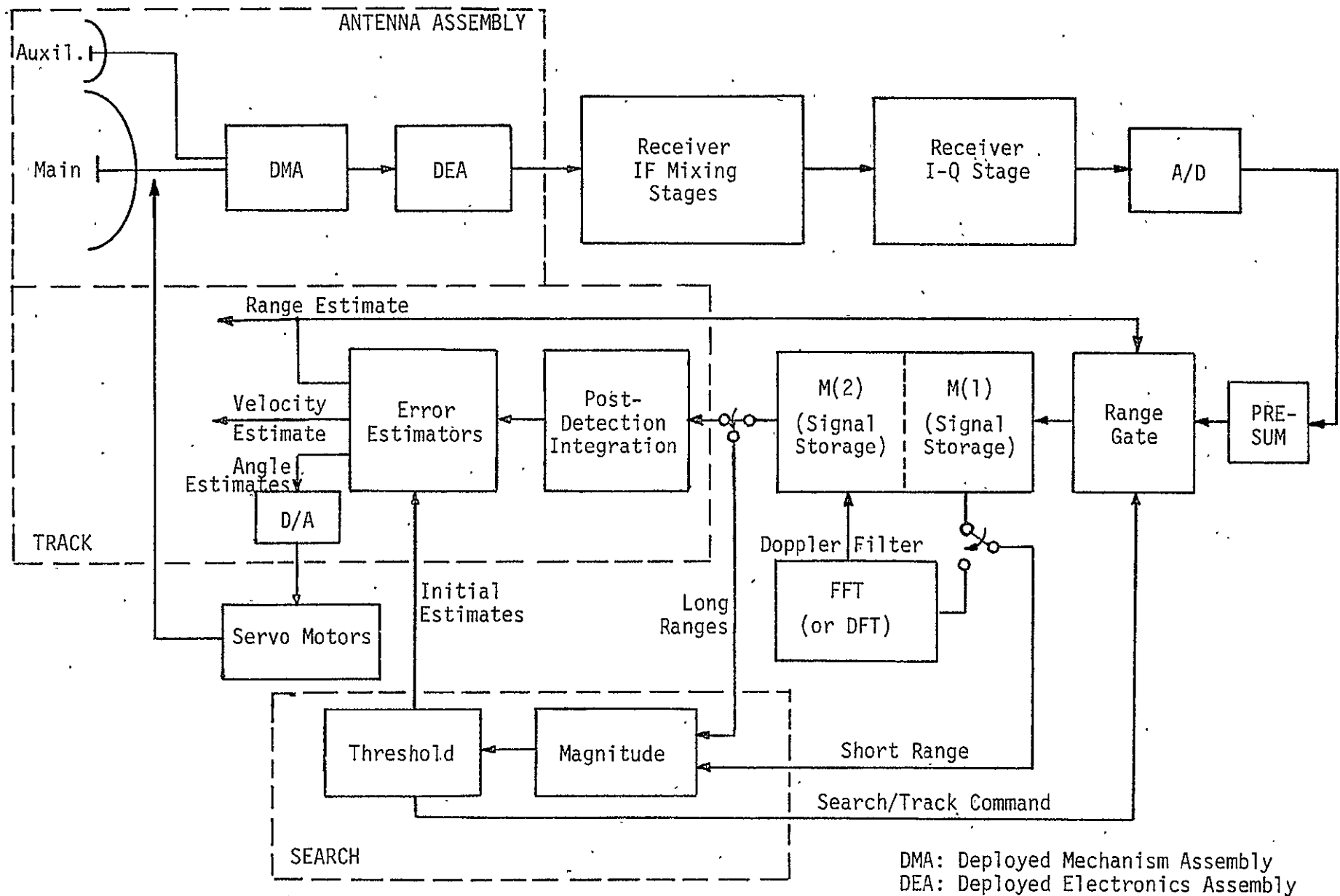


Figure 1. Radar Block Diagram

Once a target is detected, the radar is switched to a track mode and the digital signals undergo post-detection integration, followed by an error estimation unit which is initiated by a crude estimate obtained by the search mode operation. The final estimates of the various parameters are:

- (1) Fed as inputs to the servo motors for angle track.
- (2) Used to adjust the position of the early and late gates for range track and to select the proper doppler filter for range rate tracking.
- (3) Displayed for the astronauts for visual reading (all variables being tracked).
- (4) Utilized to update the state of the error estimators to obtain new estimates.

In the following sections, a detailed discussion of the various stages in the block diagram is presented, along with an analysis of the signal timing in both the search mode and the track mode.

3.0 ANTENNA ASSEMBLY

The antenna assembly is illustrated in Figure 2. The main antenna has a gain $G = 38.5$ dB. There is also an auxiliary antenna whose gain is $G = 20$ dB, which is used to guard against target effect on the sidelobes of the main antenna. Three signals emerge from the antenna, namely, the sum signal (Σ) which carries the received signal, and two angle signals (ΔAZ and ΔEL) which supply the azimuth and elevation angle information. The Σ signal is passed through a bandpass filter (BPF), whose center frequency can be adjusted, by a centralized frequency synthesizer, to be one of the five frequencies (13.779, 13.831, 13.883, 13.935, 13.987 GHz). The angle signals ΔAZ and ΔEL are passed through a selecting switch which selects one of the signals at a time at a rate of 93 Hz. The output of the switch is then passed through a phase encoder whose rate is twice that of the selecting switch. A typical sequence of signals out of the encoder is shown in Figure 3. The encoded angle signal is then passed through a matching BPF to that of the Σ signal. The two signals are then passed through the T/R switch to the receiver IF mixing stage.

When angle track is operating, there are four antenna error dwell periods at each RF, during which the azimuth and elevation error signals are processed. During each error dwell period, 32 doppler filter outputs (via DFT or FFT) are computed.

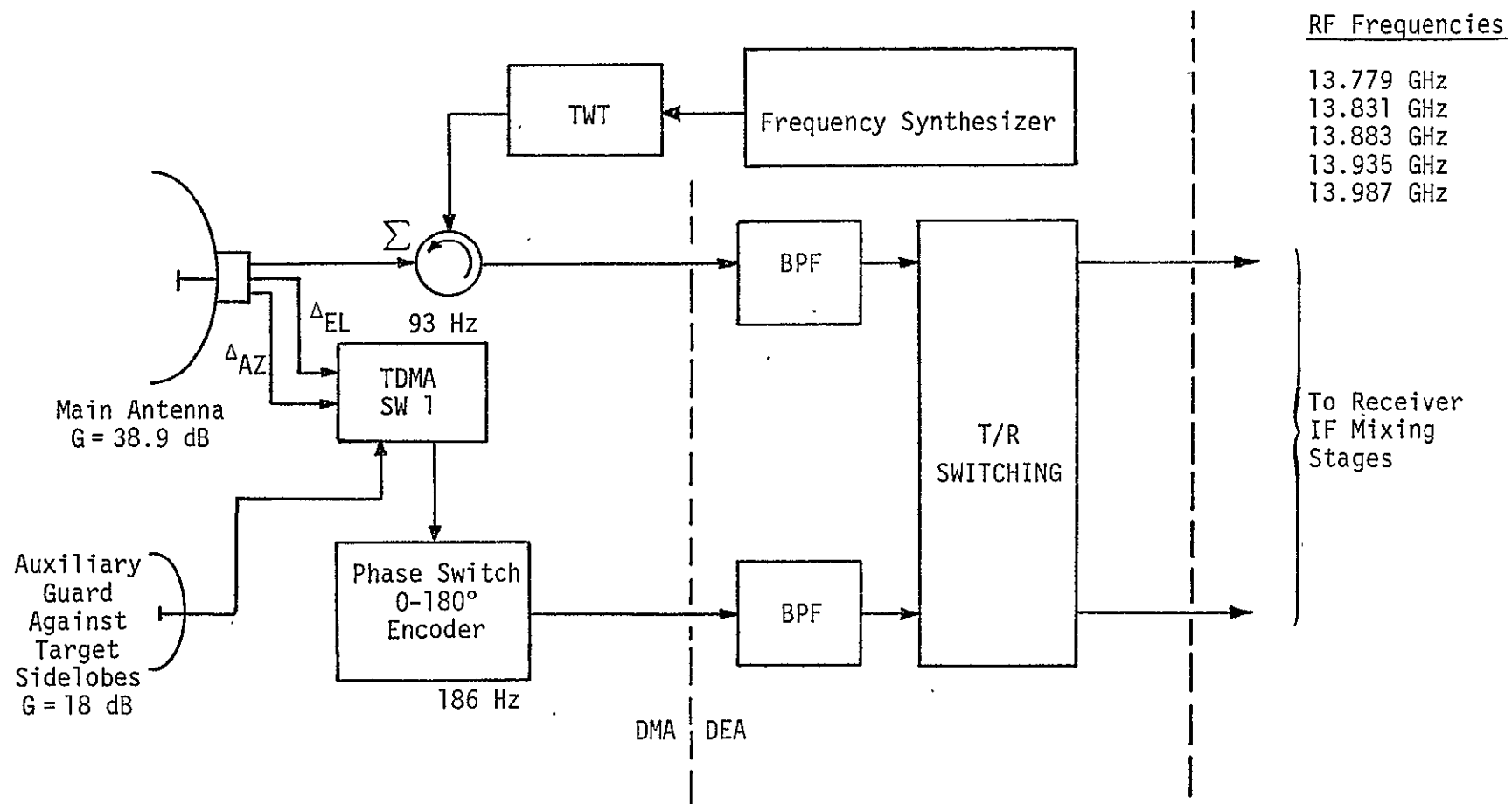


Figure 2. Antenna Assembly

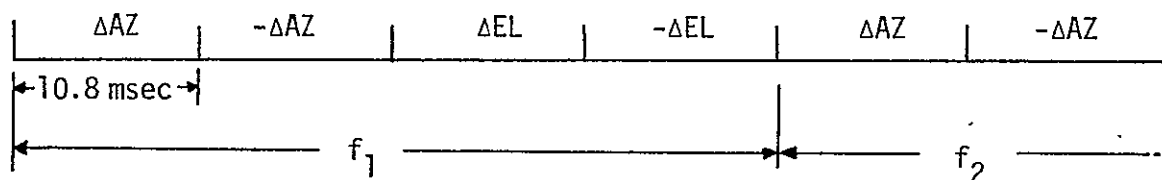


Figure 3. TDMA and Phase Encoder Output of Angle Error Information, During Angle Track

4.0 IF MIXING AND I-Q STAGES

The antenna assembly is followed by two stages of intermediate amplifiers and IF filters, where the frequency of the signal is beaten down to a stable 78.143 MHz, as shown in Figure 4. In this stage, the power in the Σ -channel is divided in two equal parts to be used for communication and the radar. This results in a loss of 3 dB in signal-to-noise ratio due to this power split. The radar Σ -channel is then combined with the Δ -channel to form the multiplexed signal ($\Sigma \pm \Delta$). Only 1/4 of the power available in the Δ -channel is used when forming $\Sigma \pm \Delta$, as seen in Figure 4. The multiplexed signal is then passed through an in-phase detector and a quadrature detector (I-Q), where it is converted to two baseband signals. The two signals are converted to digital data using an A/D converter whose sampling frequency is slightly higher than twice the bandwidth of the signal to reduce the aliasing error to less than 0.5 dB. All computations after the A/D converter are carried out digitally. The sampling frequency is equal to 480 Hz. For long-range search, when the pulse width is 66.4 μ sec, this corresponds to 32 samples/pulse from each channel of the I-Q detector for each range gate period. These samples are summed at the PRESUM stage to give a complex number that represents every received pulse.

5.0 SIGNAL PARAMETERS

Before explaining the different modes of operation, it is important to discuss the signals that are being used. The signals are RF pulses with a duration (τ) and a pulse repetition frequency (PRF) that

C-2

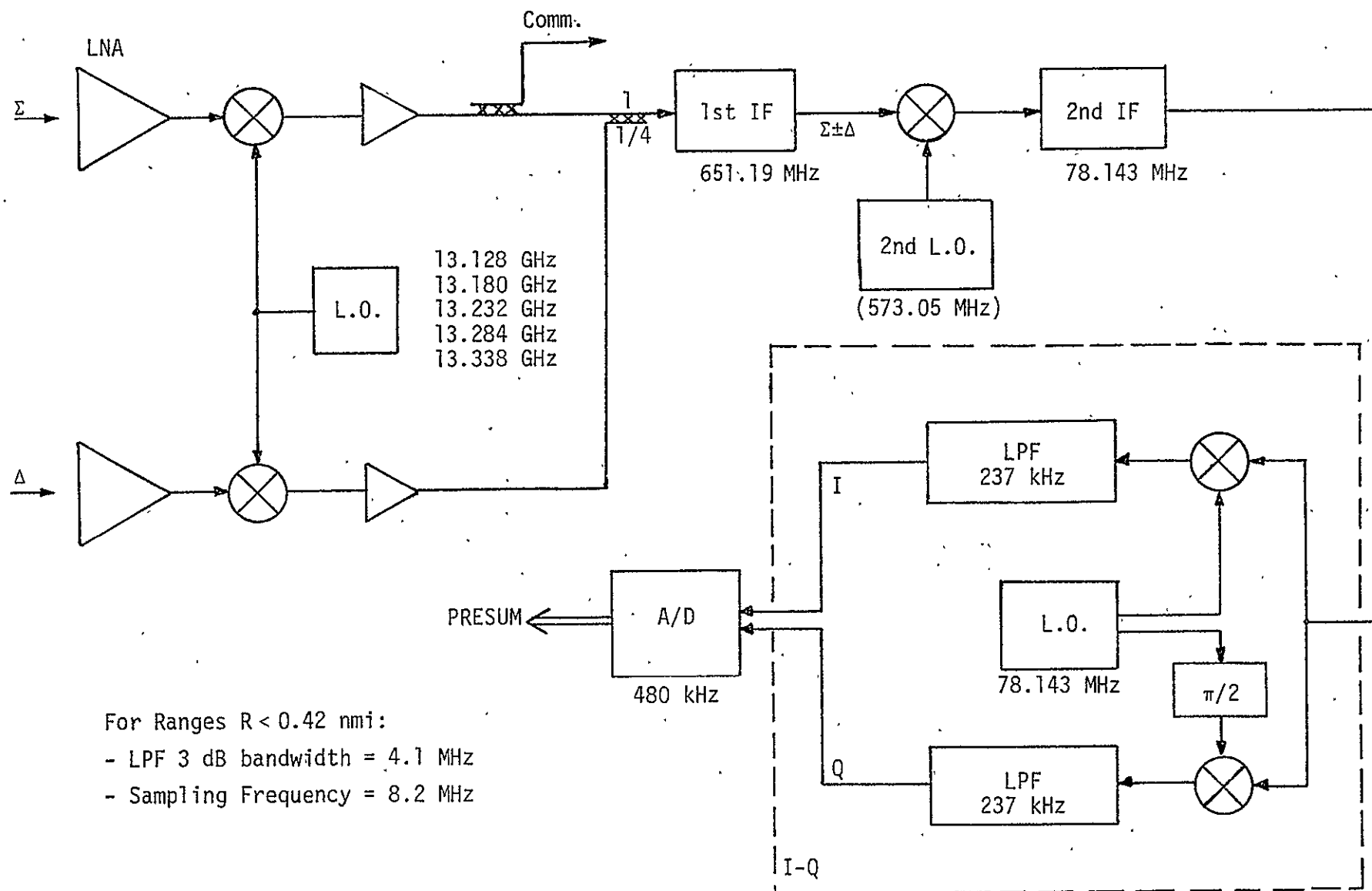


Figure 4. IF Mixing and I-Q Stages

are functions of the designated range. Frequency diversity, using five RF frequencies, is used in both the search and track modes. Table 1 lists these frequencies [9] which are cycled in a given pattern which is convenient for the manual operation mode [1]. The table also shows the associated PRFs for different ranges [8]. The various signal timings are summarized in Table 2 for the search mode and in Table 3 for the track mode [8]. The PRF values used in the tables are those corresponding to the middle IF frequency. It is noted that the integration time corresponds to slightly more than five frequency dwell times in order to allow for computation time at the end of every spatial dwell in the search mode and every accuracy estimate calculation in the track mode.

6.0 THE SEARCH MODE

In explaining the search mode operation, long-range signal format is chosen for demonstration. All other ranges follow identical processing except for the short range (<0.42 nmi), which does not utilize the doppler filters.

Sixteen pulses are transmitted at each RF frequency. The duration of each pulse is $66.4 \mu\text{sec}$, while the time between consecutive pulses is $335 \mu\text{sec}$, as shown in Figure 5. Four range gates (R_1, R_2, R_3, R_4) are used to cover the target range when no range designation is available. When range designation is available, two overlapping range gates are used around the designated range. The width of each gate in this case is three-halves the pulse width [8].

For each RF frequency, 64 complex numbers are stored in a memory designated as $M(1)$, as shown in Figure 6. The output of each range gate at every RF frequency is passed through a bank of 16 doppler filters, uniformly spread over $f_c, f_c + \text{PRF}$ (implemented as discrete Fourier transforms, DFT, or fast Fourier transforms, FFT) and the magnitudes of the outputs of these filters are calculated and compared to precalculated thresholds. The target is detected when the magnitude of one or two outputs of adjacent doppler filters pertaining to one or two range gates is exceeded. An initial estimate of the range and the range rate of the target are calculated from the knowledge of the doppler filters and range gates whose outputs have exceeded the threshold. These initial estimates are fed into the error estimators as initial conditions to start the successive estimation process in the track mode. The

Table 1. Frequency Synthesizer Frequencies for
the First IF Mixing L.O. (in GHz)

Frequency		F ₁	F ₂	F ₃	F ₄	F ₅
		13.779	13.831	13.883	13.935	13.987
PRF (Hz)	Long Ranges R > 9.5 nmi	3009	2998	2987	2976	2965
	Short Ranges R < 9.5 nmi	7017	6994	6970	6946	6923

Table 2. Signal Parameters for Various Designated Ranges in Search Mode

Designated Range (nmi)	τ (μ sec)	PRF (Hz)	Frequency Dwell Time (msec)	Integration Period (msec)
7.2 -	66.4	2987	5.36	28.6
3.8 - 7.2	33.2	6970	2.29	12.2
1.9 - 3.8	16.6	6970	2.29	12.2
0.95 - 1.9	8.3	6970	2.29	12.2
0.42 - 0.95	4.15	6970	2.29	12.2
- 0.42	0.122	6970	2.29	12.2

Table 3. Signal Parameters for Various Designated Ranges in Track Mode

Designated Range (nmi)	τ (μ sec)	PRF (Hz)	Frequency Dwell Time (msec)	Integration Period (msec)
9.5 -	33.2	2987	21.44	116
3.8 - 9.5	16.6	6970	9.18	51.2
1.9 - 3.8	8.3	6970	9.18	51.2
0.95 - 1.9	4.15	6970	9.18	51.2
0.42 - 0.95	2.07	6970	9.18	51.2
- 0.42	0.122	6970	9.18	51.2

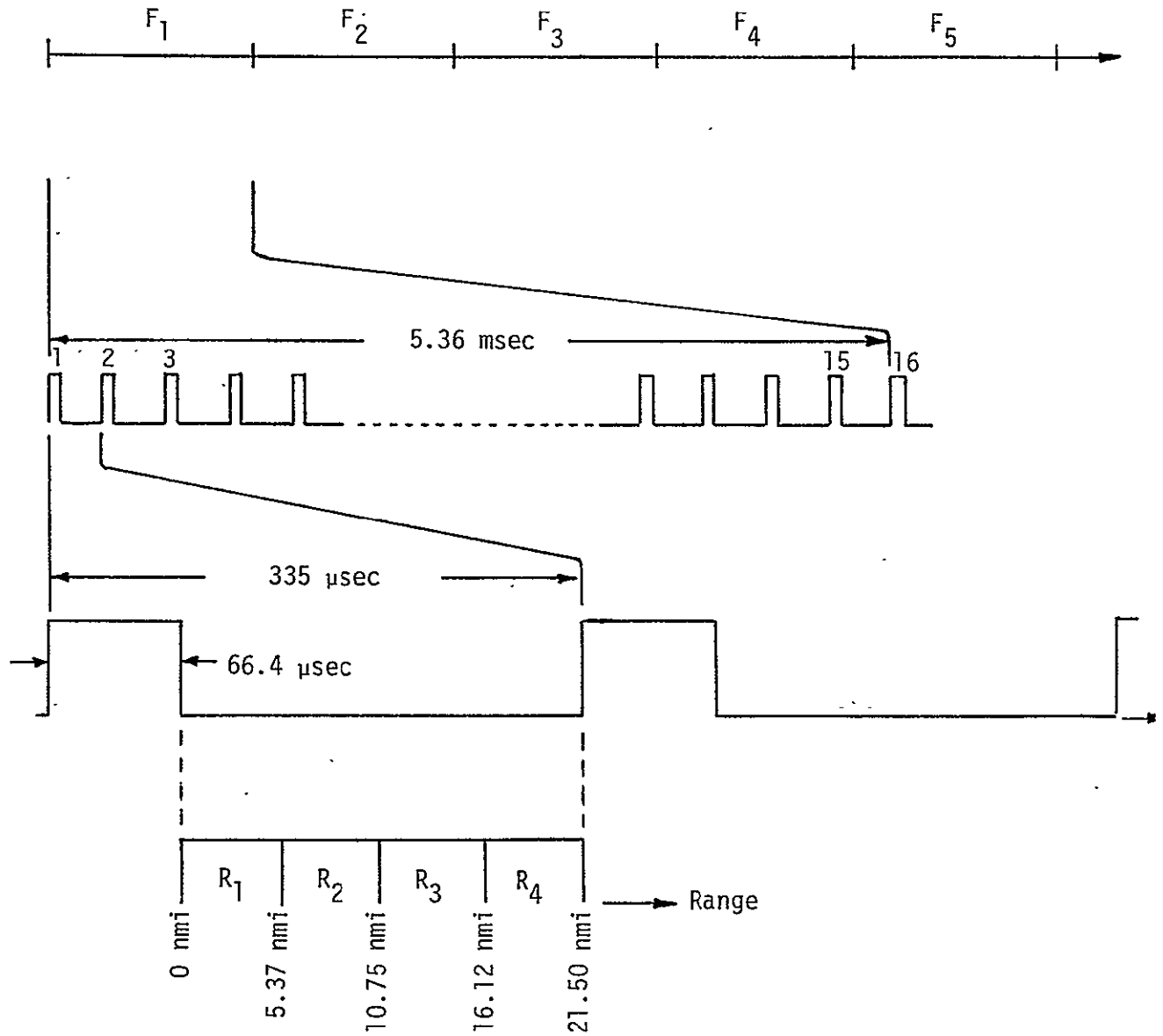


Figure 5. Long Range Search Signals

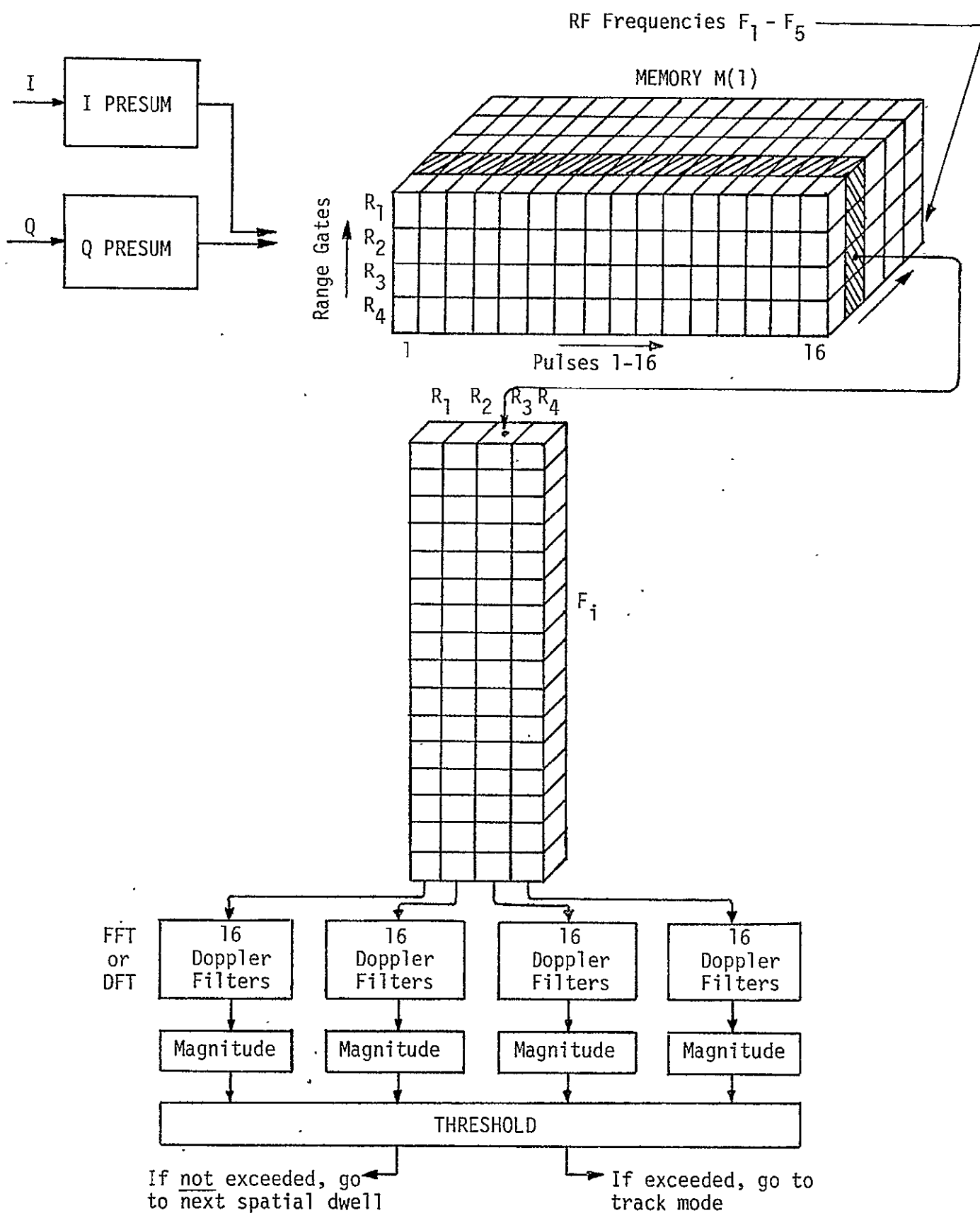


Figure 6. Search Mode Signal Processing

thresholds are calculated to produce an error alarm rate of one false alarm per hour.

For short ranges ($R < 0.42$ nmi), a single short pulse is transmitted at a PRF of 6970 Hz [8]. The width of the pulse is equal to $0.122 \mu\text{sec}$. The detection is carried out by finding the magnitude of the return signal over the time period corresponding to 0.42 nmi and comparing it continuously to a threshold. If the threshold is not exceeded, the receiver waits for the second transmitted pulse and the process is repeated. The number of pulses transmitted at every RF frequency is 16. The RF frequencies used in the short-range detection are the same as those used in long-range detection.

Once the threshold is exceeded, a hit is declared. Five hits are required before declaring detection. Tracking is started once the target is detected. The initial range estimate is obtained by finding the time that elapses between the transmission of the pulse and the exceeding of the threshold. This is done by implementing a range bin clock and a counter, as seen in Figure 7.

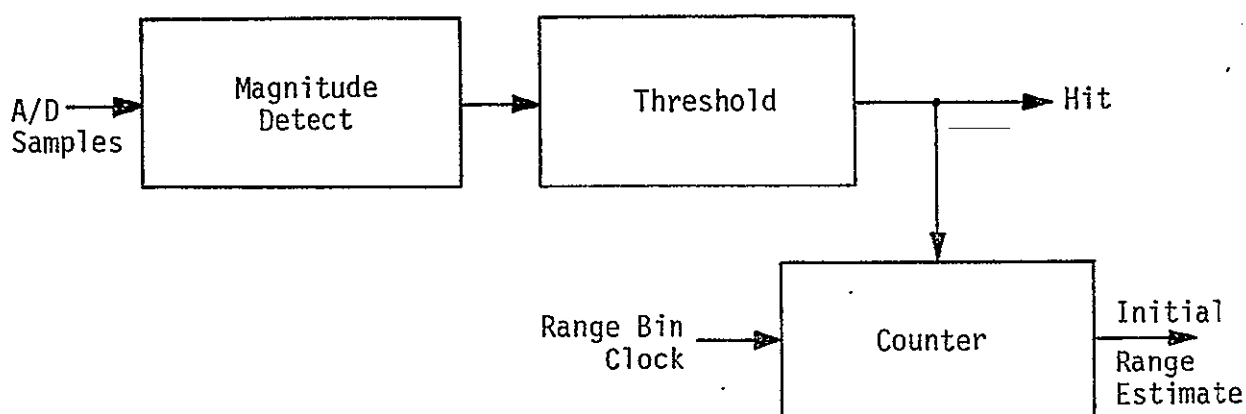


Figure 7. Short-Range Detection

7.0 THE TRACK MODE

7.1 Signal Format and Block Diagram

The block diagram for track mode processing is shown in Figure 8. All the computations involved in obtaining the tracking accuracies are digital. The separate blocks in the figure are explained in detail in subsequent sections.

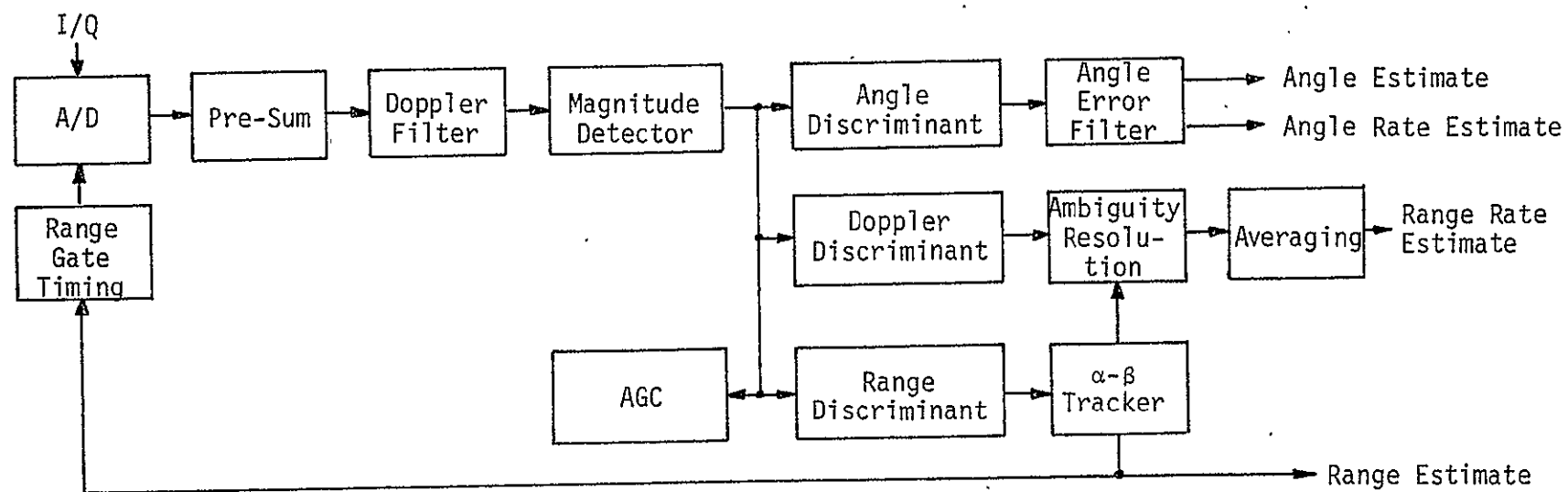


Figure 8. Track Processing Block Diagram

The signal in the track mode consists of 64 pulses for each RF frequency, instead of the 16 pulses in the search mode, as shown in Figure 9 [1,2]. For long-range tracking, the frequency dwell time is equal to 21.44 msec. Each frequency dwell time is divided into four time slots by the switching combination of SW1 and the phase encoder switch in the antenna assembly. The signals in the succeeding time slots are $\Sigma + \Delta Z$, $\Sigma - \Delta Z$, $\Sigma + \Delta EL$, and $\Sigma - \Delta EL$, respectively. The time slots are arranged so that the first two are used to measure the azimuth angle, while the last two are used for the elevation angle. Each one of the previous time slots consists of 16 pulses. The pulses are passed through two nonoverlapping gates, an early gate and a late gate, which are located around a predicted estimate of the range $[R_p(n)]$ from the processor timing unit. The width of each gate is equal to the pulse width. The output of each range gate is a complex number $z(I,J,L,K)$, which is a function of four parameters (I,J,L,K):

I denotes the RF frequency being transmitted; $I = 1, 2, \dots, 5$

J denotes the time slot in each frequency such that

$J = 1$ corresponds to $\Sigma + \Delta Z$

$J = 2$ corresponds to $\Sigma - \Delta Z$

$J = 3$ corresponds to $\Sigma + \Delta EL$

$J = 4$ corresponds to $\Sigma - \Delta EL$

K denotes a particular pulse in each time slot; $K = 1, \dots, 16$

L denotes the range gate under consideration;

$L = -1$ corresponds to early gate

$L = +1$ corresponds to late gate.

Figure 9 illustrates the signal format in the track mode. The computation time is not included in the figure.

7.2 Doppler Filtering

The outputs of the range gates are stored in a memory bank designated for illustration as $M(1)$. For all combinations of I, J, and L, the series of 16 pulses ($K = 1, \dots, 16$) are passed through a bank of 32 doppler filters, as shown in Figure 10 [9]. The doppler filters are uniformly spread over $f_c, f_c + f_{PRF}$. The overlapping of adjacent filters results in doppler filter loss, which has to be taken into consideration. The outputs of the doppler filters are designated as $\omega(I,J,L,M)$, where M denotes

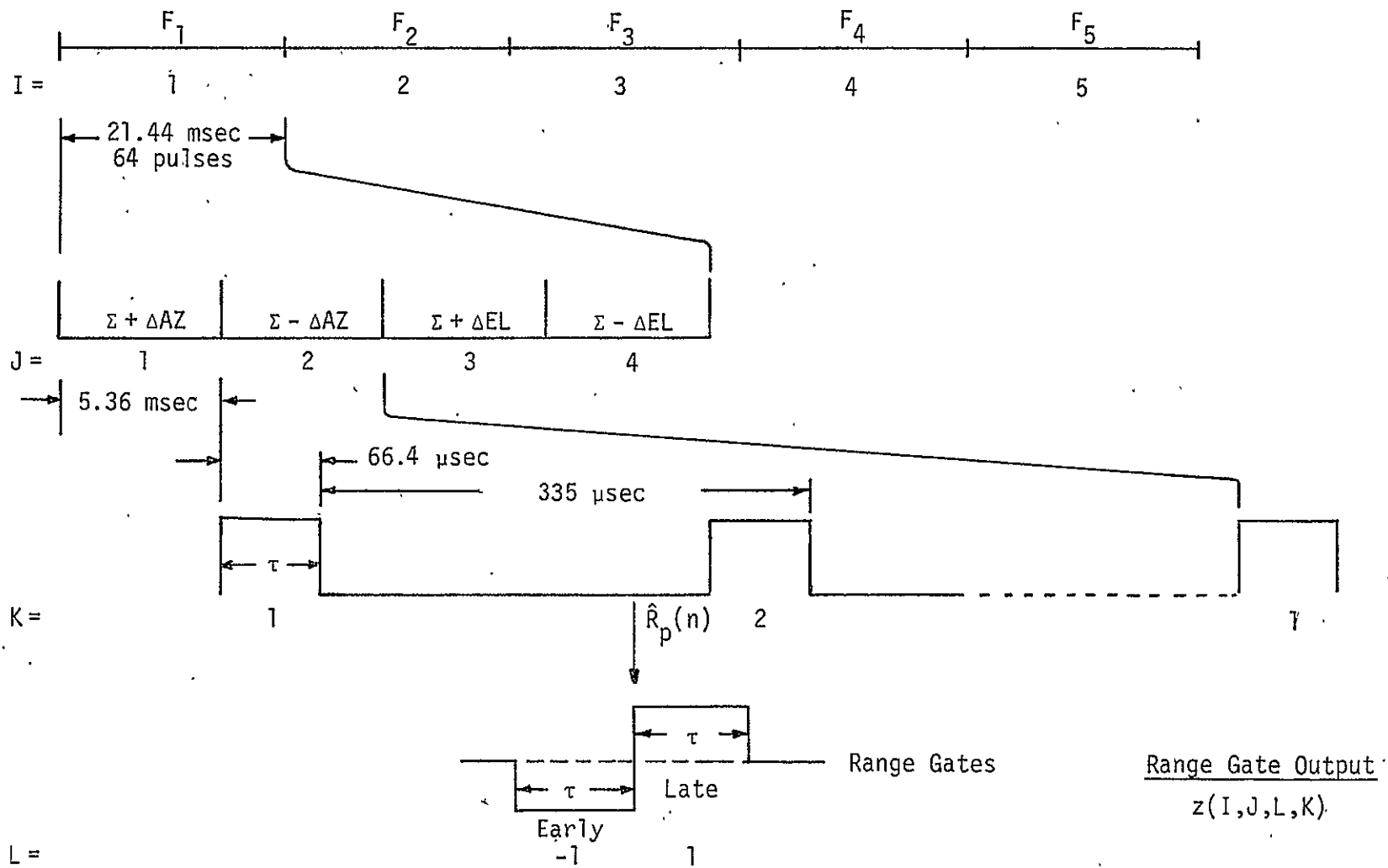


Figure 9. Track Mode Signal Format

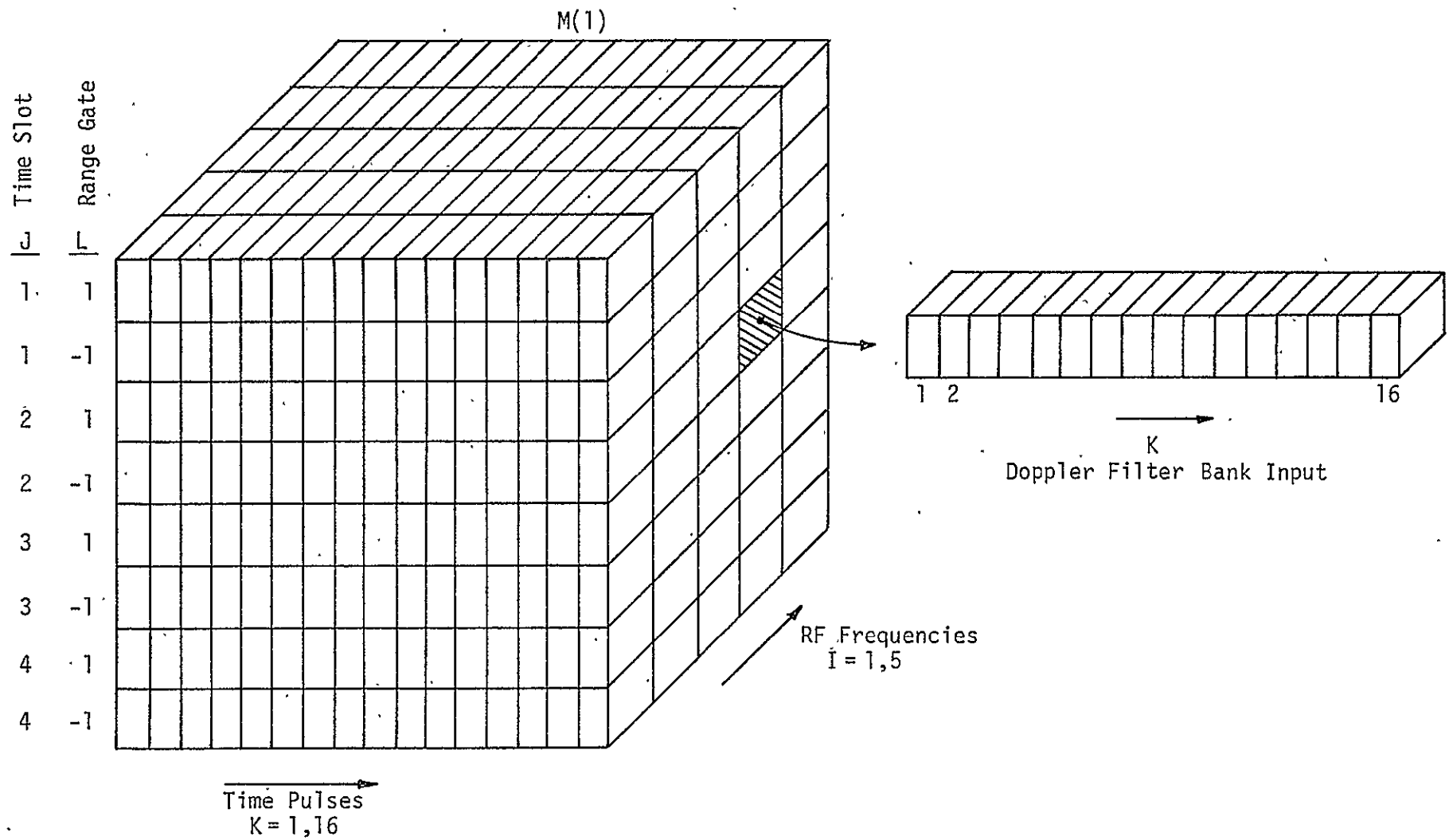


Figure 10. Pictorial Illustration of Memory Bank $M(1)$

a particular filter ($M=0,\dots,31$). I , J , and L represent the RF frequency, the time slot, and the range gate, respectively. Since doppler filtering is accomplished by digital Fourier transforms (DFT), $\omega(I,J,L,M)$ is given by

$$\omega(I,J,L,M) = \sum_{K=1}^{16} z(I,J,L,K) e^{-j2\pi KM/16} \quad (1)$$

Implementing doppler filters using FFT might result in losses due to the lack of proper match between the pulse bandwidth, the PRF, and the bandwidth of the FFT.

The outputs of the doppler filters are stored in a memory bank designated as $M(2)$, as shown in Figure 11. Only the outputs of three adjacent filters are processed further, namely, the output of the filter whose center frequency is closest to the actual doppler and the outputs of the filters adjacent to it. If the middle filter is designated as M_1 , then the outputs of filters M_1-1 , M_1 , and M_1+1 are processed further through the post-integration stage. The output of M_1 is used in computing the range, as well as the angle discriminants, while the outputs of M_1-1 and M_1+1 are used in computing the range rate (doppler) discriminant.

7.3 Post-Integration

The outputs of each of the doppler filters M_1-1 , M_1 , and M_1+1 consist of 40 memory cells from the memory $M(2)$, as shown in Figure 11. The 40 cells correspond to five RF frequencies ($I=1,\dots,5$), two range gates ($L=\pm 1$), and four time slots ($J=1,\dots,4$). Each one of these cells carries a complex number $\omega(I,J,L,M)$, whose magnitude is found by multiplying it with its conjugate. The squares of these magnitudes are added in different manners to form the post-detection integration (PDI) outputs. To be able to demonstrate the logical procedure for adding these magnitudes, the memory cells under consideration are redrawn for a given RF frequency F_1 , as shown in Figure 12.

Eight sums are formed at the output of the post-detection integrator—two corresponding to each of the four parameters of interest, namely, range, range gate, azimuth angle, and elevation angle. As mentioned previously, for range and angle accuracy computations, the output of the doppler filter M_1 is used, whereas the outputs of the two

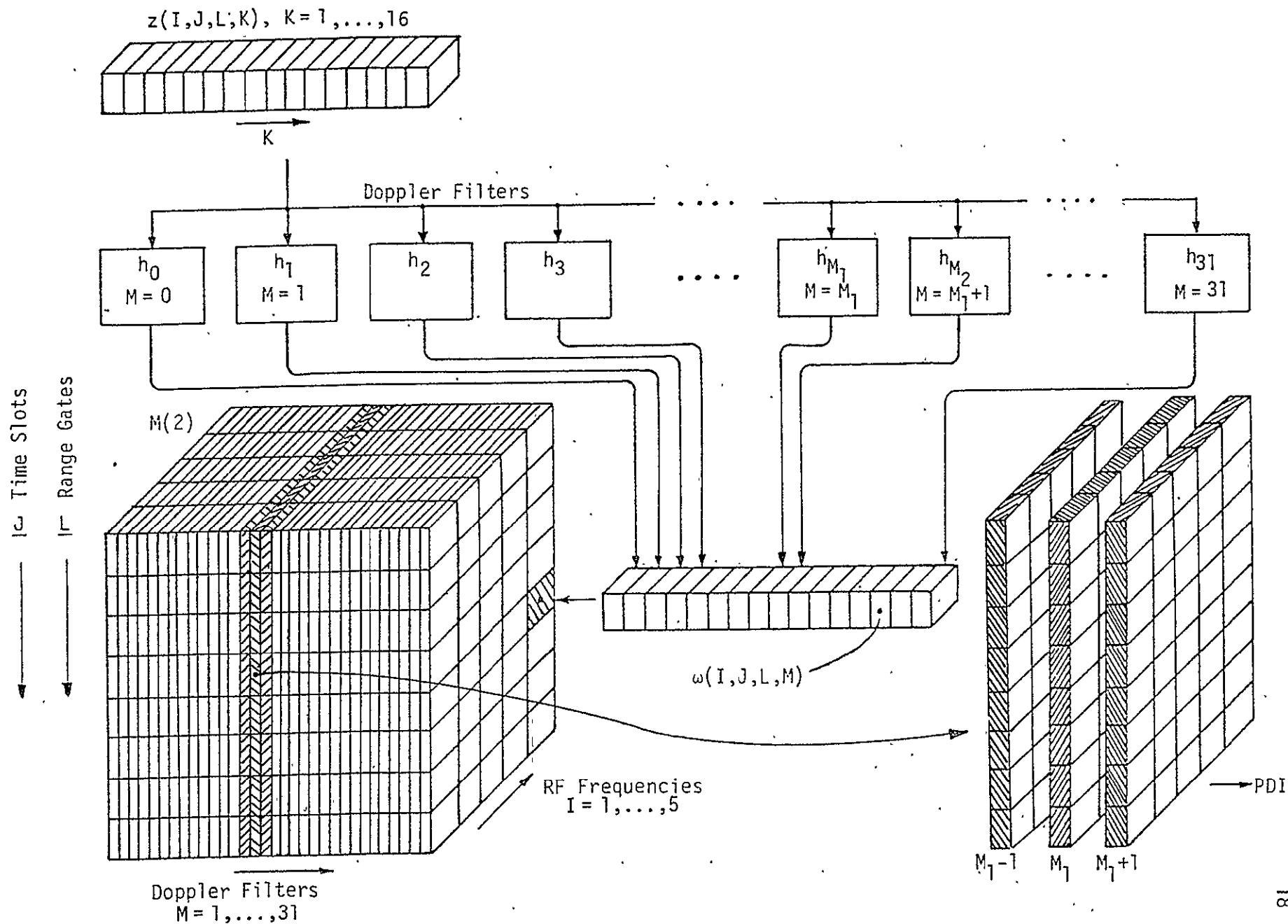


Figure 11. Pictorial Illustration of Memory Bank $M(2)$

adjacent filters M_1-1 and M_1+1 are used for range rate computation.

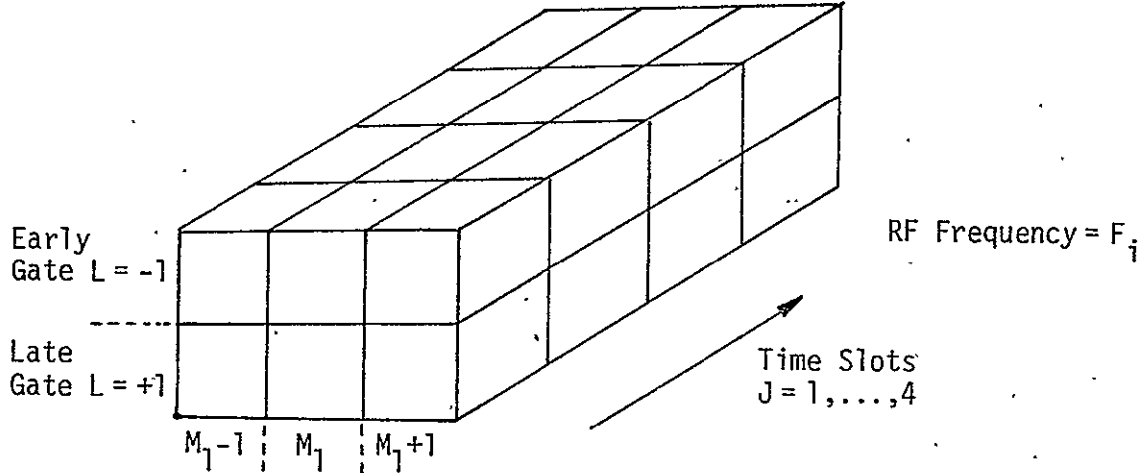


Figure 12. Memory Cells Storing $\omega(i,j,L,M)$ for a Given RF

7.3.1 Range PDI Outputs

The two range outputs are formed by the post-detection integration, one corresponding to the early gate and the other corresponding to the late gate. They are denoted by $S_R(L=-1)$ and $S_R(L=+1)$. The R denotes the range and the L denotes the early or late gate. They are formed by using the output of the middle doppler filter (M_1). Thus, to obtain $S_R(L=-1)$, the square of all the complex numbers pertaining to the early gate and the filter M_1 are added over all the RF frequencies. $S_R(L=+1)$ is obtained in a similar fashion, using the late gate; hence,

$$S_R(L=-1) = \sum_{i=1}^5 \sum_{j=1}^4 |\omega(i,j,-1,M_1)|^2 \quad (2)$$

$$S_R(L=+1) = \sum_{i=1}^5 \sum_{j=1}^4 |\omega(i,j,1,M_1)|^2. \quad (3)$$

7.3.2 Range Rate (Doppler) PDI Outputs

The doppler PDI outputs $S_D(M=M_1-1)$ and $S_D(M=M_1+1)$ are obtained by summing the square of the magnitudes of the numbers out of the doppler filters M_1-1 and M_1+1 , respectively; each sum is taken over the two gates, the four time slots and all the RF frequencies. Therefore,

$$S_D(M=M_1-1) = \sum_{i=1}^5 \sum_{j=1}^4 |\omega(i,j,-1,M_1-1)|^2 + |\omega(i,j,1,M_1-1)|^2 \quad (4)$$

$$S_D(M=M_1+1) = \sum_{i=1}^5 \sum_{j=1}^4 |\omega(i,j,-1,M_1+1)|^2 + |\omega(i,j,1,M_1+1)|^2 \quad (5)$$

7.3.3 Angle PDI Outputs

To obtain the two PDI outputs for the azimuth (elevation) angle information, the output of the doppler filter M_1 is used to obtain the squares of the magnitudes of the first (last) two time slots corresponding to $\Sigma + \Delta AZ$ and $\Sigma - \Delta AZ$ ($\Sigma + \Delta EL$ and $\Sigma - \Delta EL$) which are added over all Rf frequencies to give $S_{AZ}(J=1)$ and $S_{AZ}(J=2)$ [$S_{EL}(J=3)$ and $S_{EL}(J=4)$], respectively. As in the range rate case, the outputs of both the early and late gates are used. The various angle PDI outputs are shown in equations (6) through (9).

$$S_{AZ}(J=1) = \sum_{i=1}^5 |\omega(i,1,-1,M_1)|^2 + |\omega(i,1,+1,M_1)|^2 \quad (6)$$

$$S_{AZ}(J=2) = \sum_{i=1}^5 |\omega(i,2,-1,M_1)|^2 + |\omega(i,2,+1,M_1)|^2 \quad (7)$$

$$S_{EL}(J=3) = \sum_{i=1}^5 |\omega(i,3,-1,M_1)|^2 + |\omega(i,3,+1,M_1)|^2 \quad (8)$$

$$S_{EL}(J=4) = \sum_{i=1}^5 |\omega(i,4,-1,M_1)|^2 + |\omega(i,4,+1,M_1)|^2 \quad (9)$$

7.4 Logarithm Discriminant Formation

The purpose of the logarithm discriminant is to obtain an estimate of the error (error signal), including sign, of the various parameters under consideration. The idea is best explained by using the well known

Taylor series expansion of $\ln [(1+x)/(1-x)]$.

$$\ln \frac{1+x}{1-x} = 2x + \frac{x^3}{3} + \frac{x^5}{5} + \dots; \quad |x| < 1. \quad (10)$$

For small x , the following approximation is valid:

$$\ln \frac{1+x}{1-x} \approx 2x; \quad x \ll 1. \quad (11)$$

Thus, if x represents the errors in the parameters under consideration, then by forming the logarithm of $(1+x)/(1-x)$, this error can be computed. The mathematical derivation of the variance of the logarithmic estimator is formed in [3], where the maximum likelihood estimator of the form

$$\hat{x} = \log \frac{\sum_i |U_i|^2}{\sum_i |V_i|^2} \quad (12)$$

is analyzed. U_i and V_i represent a pair of voltages whose difference is proportional to the target parameter being measured. Since the target range, range rate, and orientation angles are mathematical duals of each other, it is the objective of the following discussion to relate $|U_i|^2$ and $|V_i|^2$, shown in (12), to the various outputs of the PDI.

7.4.1 Range Discriminant

In the formation of the range discriminant, a sum signal (S) and a difference signal (D) are formed such that

$$S = S_R(L=-1) + S_R(L=+1) \quad (13)$$

$$D = S_R(L=-1) - S_R(L=+1), \quad (14)$$

where $S_R(\)$ is defined in equations (2) and (3).

Since the output of the early gate is a measure of $R - \Delta R$, where ΔR is an absolute error in the range, and the output of the late gate is a measure of $R + \Delta R$, then S is a measure of the range R and D is a measure of the absolute range error. Then, replacing S by R and D by ΔR , it can be stated that

$$S_R(L = -1) \propto R - \Delta R \quad (15)$$

$$S_R(L = +1) \propto R + \Delta R. \quad (16)$$

(A proportionality constant might be added; however, this coefficient will drop when taking the logarithms.)

Letting

$$S_R(L = -1) \equiv \sum_{i=1}^{20} |u_i|^2 \quad (17)$$

$$S_R(L = +1) \equiv \sum_{i=1}^{20} |v_i|^2, \quad (18)$$

the range of i , which is the number of samples used in calculating a single range error estimate, is equal to 20 in equations (17) and (18). It corresponds to four time-slots over five RF frequencies. It is easy to see that, using (15) through (18),

$$\ln \frac{\sum_{i=1}^{20} |u_i|^2}{\sum_{i=1}^{20} |v_i|^2} = \frac{2\Delta R}{R} \triangleq 2R_\epsilon, \quad (19)$$

where R_ϵ is the required range error signal. The procedure is illustrated in Figure 13.

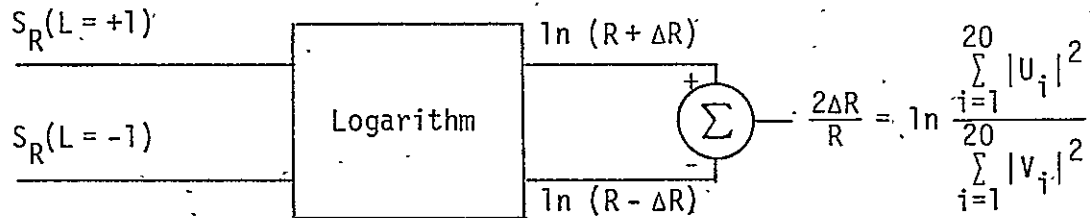


Figure 13. Range Discriminant

7.4.2 Doppler (Range Rate) Discriminant

A similar argument can be stated for the doppler discriminant. In this case, however, the number of samples used to calculate a doppler error estimate is equal to 40. This is because both the outputs of the early gate and late gate are used in the computation which is also carried over four time slots and five RF frequencies. Thus, from (4) and (5),

$$\sum_{i=1}^{40} |U_i|^2 = S_D(M=M_1-1)$$

$$\sum_{i=1}^{40} |V_i|^2 = S_D(M=M_1+1),$$

from which

$$\ln \frac{\sum_{i=1}^{40} |U_i|^2}{\sum_{i=1}^{40} |V_i|^2} \approx 2 \frac{S_D(M=M_1-1) + S_D(M=M_1+1)}{S_D(M=M_1-1) - S_D(M=M_1+1)} \approx 2 \dot{R}_e. \quad (20)$$

7.4.3 Angle Discriminants

As has already been noted, the magnitudes of the samples from the DFT corresponding to both the early and late range gates are summed to form an on-target gate, and then integrated over the transmitter frequency cycle. This means that the number of samples used per calculation of an angle error estimate is equal to 10 for two range gates and five RF frequencies. The sum and difference samples of an angle error are then log-converted and subtracted to form the normalized angle errors for the elevation and azimuth channels. The error signals are then D/A converted and sent to the servo filters, and finally to the servo motors.

In particular, for the azimuth angle, the estimation vectors U_i and V_i satisfy [from (6) and (7)]:

$$\sum_{i=1}^{10} |U_i|^2 = S_{AZ}(J=1)$$

$$\sum_{i=1}^{10} |V_i|^2 = S_{AZ}(J=2).$$

Similarly, for the elevation angle [from (8) and (9)]:

$$\sum_{i=1}^{10} |u_i|^2 = S_{EL} (J=3)$$

$$\sum_{i=1}^{10} |v_i|^2 = S_{EL} (J=4),$$

from which the error signals become

$$2 \Delta_{\epsilon} AZ \triangleq \ln \frac{S_{AZ}(J=1)}{S_{AZ}(J=2)} = \frac{2 \Delta AZ}{\Sigma} \quad (21)$$

$$2 \Delta_{\epsilon} EL \triangleq \ln \frac{S_{EL}(J=3)}{S_{EL}(J=4)} = \frac{2 \Delta EL}{\Sigma} \quad (22)$$

The error signals in (19) through (22) are used to obtain the various required estimates pertaining to the parameters under consideration.

Since the error signals are obtained successively as new readings are processed, they will be denoted by $R_{\epsilon}(n)$, $\dot{R}_{\epsilon}(n)$, $\Delta_{\epsilon} AZ(n)$, and $\Delta_{\epsilon} EL(n)$, where (n) denotes the n th error signal being processed.

The angle error signals $\Delta_{\epsilon} AZ$ and $\Delta_{\epsilon} EL$ are fed into loop filters as shown in Figure 14 to obtain two sets of estimates:

(1) Angle estimates $\hat{\Delta} AZ$ and $\hat{\Delta} EL$, which are fed back to the servo motors.

(2) Angle rate estimates $\hat{\Delta} \dot{A} Z$ and $\hat{\Delta} \dot{E} L$, which are displayed for the astronauts for visual reading.

The range and range rate error signals, however, are fed into the processor timing unit to obtain various required estimates, as discussed in the following section.

7.5 Processor Timing, Range and Range Rate Prediction

The processor timing stage consists of two substages. The first is called the α - β tracker [4] and the second is designated as the ambiguous doppler resolver and corrector, as shown in Figure 15. The α - β tracker is employed to give a smoothed estimate of the current range $\hat{R}_S(n)$, a predicted estimate of the next range reading $\hat{R}_P(n+1)$, and a smoothed estimate of the range rate $\hat{\dot{R}}_S(n)$. This latter value is

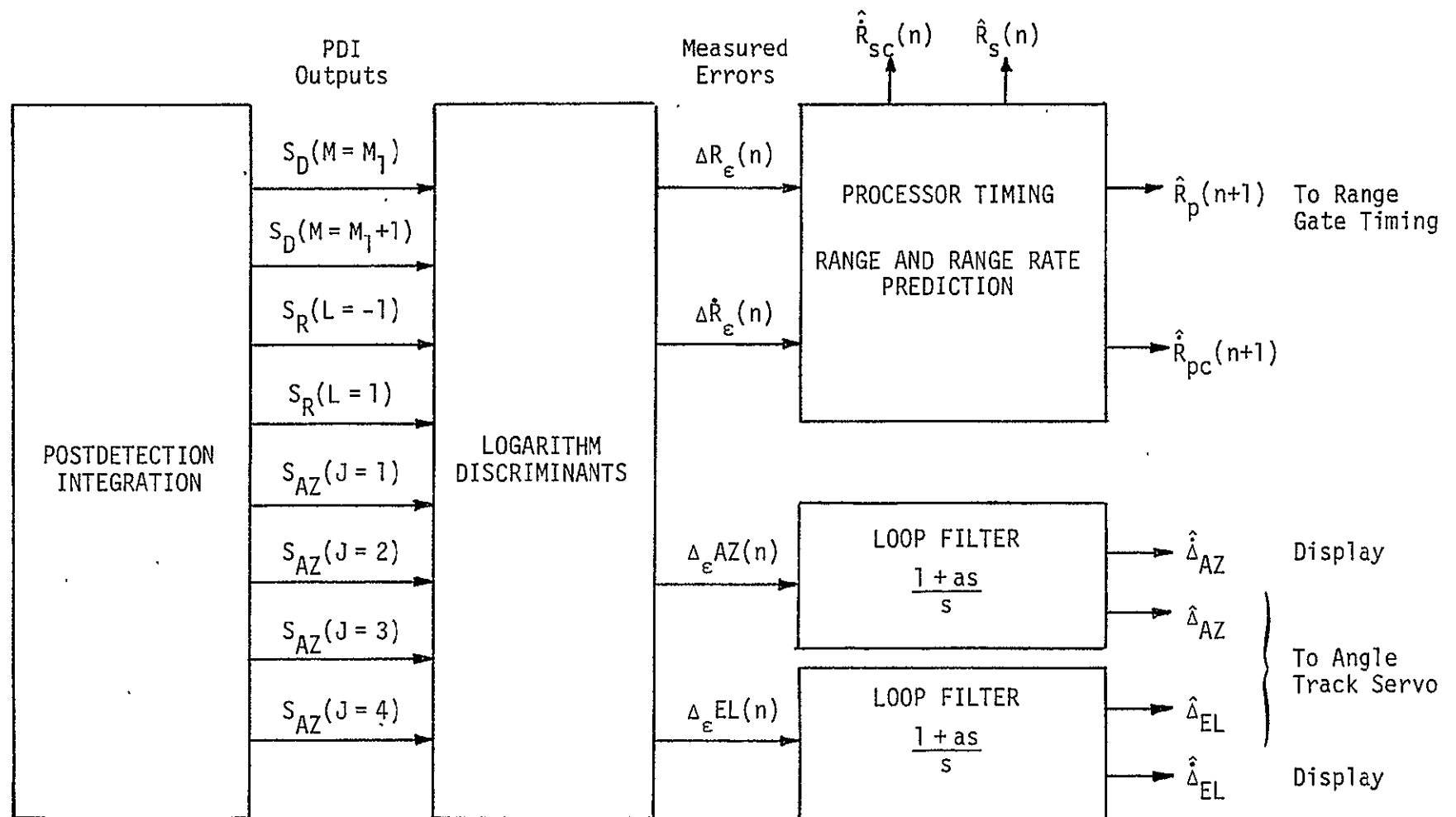


Figure 14. PDI and Parameter Estimators

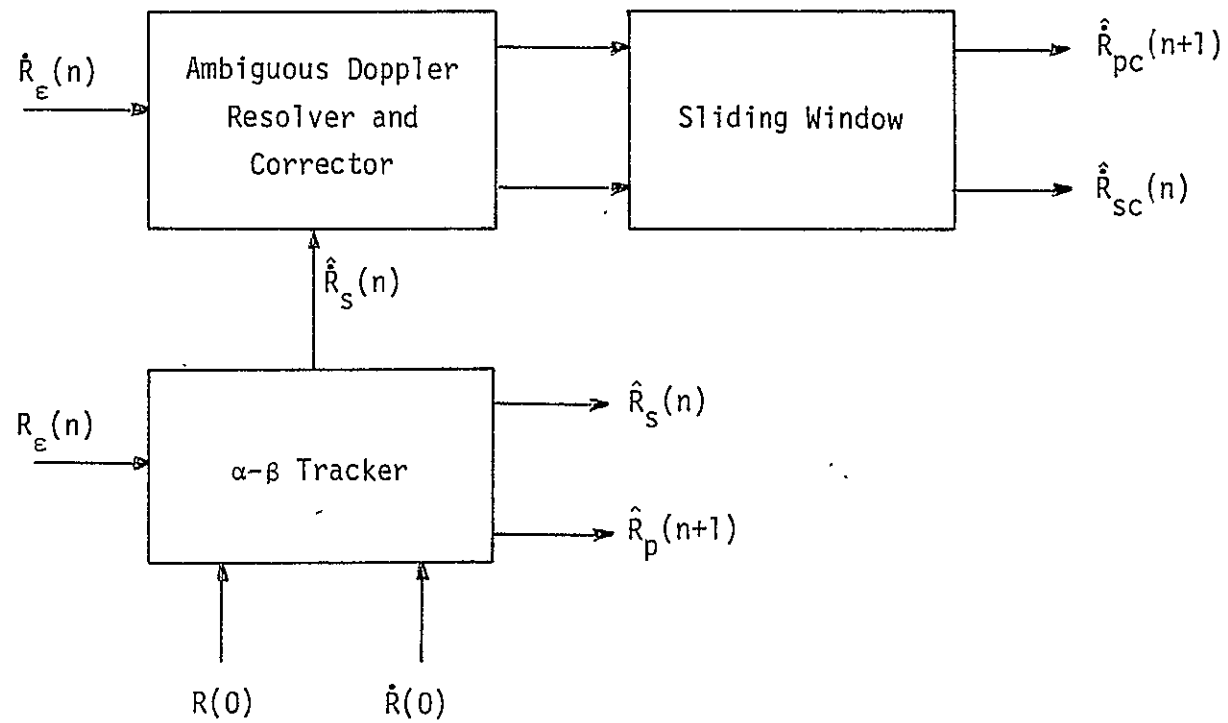


Figure 15. Processor Timing Stage

used along with the range rate error signal $\dot{\hat{R}}_e(n)$ as inputs to the ambiguous doppler resolver and corrector whose output is fed through a sliding window to produce a smoothed corrected doppler estimate $\hat{\hat{R}}_{sc}(n)$ and a predicted corrected doppler estimate $\hat{\hat{R}}_{pc}(n+1)$. The doppler estimates $\hat{\hat{R}}_{sc}(n)$ and $\hat{\hat{R}}_{pc}(n+1)$ are obtained by averaging (smoothing) m previous estimated values that are stored in a special memory (sliding window averaging). The number of estimates (m) being used is dependent on the designated range [8]. For long ranges ($R > 9.5$ nmi), m is equal to 2 while, for shorter ranges, it is equal to 4.

The previous estimates are used for various purposes as summarized in Table 4.

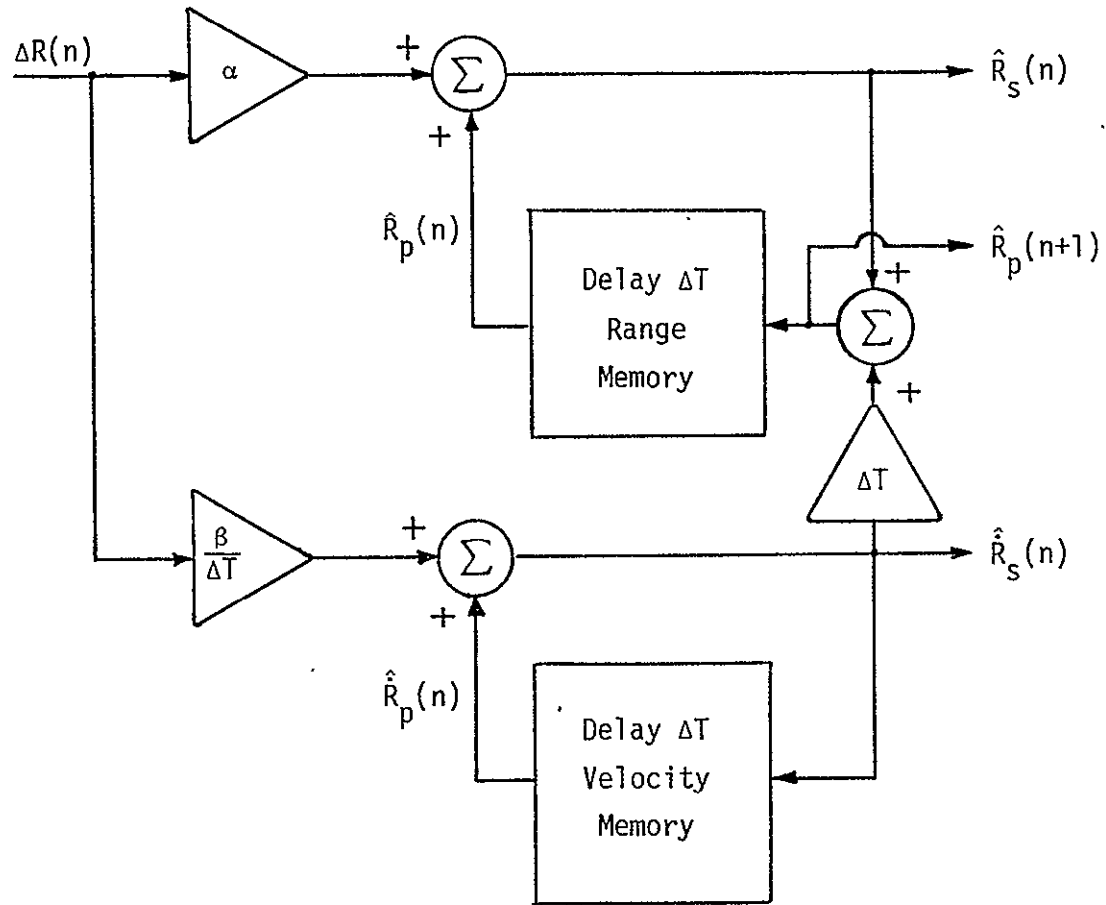
Table 4. Processor Timing Stage Outputs

Estimate	$\hat{\hat{R}}_p(n+1)$	$\hat{\hat{R}}_s(n)$	$\hat{\hat{R}}_{sc}(n)$	$\hat{\hat{R}}_{pc}(n+1)$
Use	Adjust early and late gates location	Display	Display	Select doppler filters

Whereas the location of the range gates is adjusted as a result of every new range estimate, the location of the doppler filters remains unchanged. The range rate estimates are used to select the filter M_1 whose center frequency is closest to the estimated doppler. This filter remains unchanged until the doppler error changes appreciably to make the estimated doppler closer to a different filter center frequency.

The one-step prediction and smoothing equations of the α - β tracker, as well as a block diagram of a possible implementation of the tracker are shown in Figure 16. The equations were derived in [3,4], along with the variances of these estimates. The initial conditions $R(0)$ and $\dot{R}(0)$, which are necessary to start the α - β tracker operation, are supplied by the search mode operation after the target is detected.

The operation of the ambiguous doppler resolver and corrector is explained in Section 7.6.



Prediction Formula

$$\hat{R}_p(n+1) = \hat{R}_s(n) + \Delta T \hat{R}_s(n)$$

$$\hat{R}_p(n+1) = \hat{R}_s(n)$$

Smoothing Formula

$$\hat{R}_s(n) = \hat{R}_p(n) + \alpha \Delta R(n)$$

$$\hat{R}_s(n) = \hat{R}_p(n) + \frac{\beta}{\Delta T} \Delta R(n)$$

$$R_e(n) \equiv R(n) - \hat{R}_p(n)$$

$\Delta T \equiv$ time between two computation steps

Figure 16. α - β Tracker for Range Tracking and Coarse Range Rate Estimation

7.6 Doppler Ambiguity Resolution

The doppler discriminant and resulting estimation will give a value between $[0, \text{PRF}]$. The maximum closing velocity is +148 fps, and the maximum opening velocity is -75 fps. At 13.9 GHz, this corresponds to approximately 28 Hz/fps doppler. The maximum opening doppler is therefore -2100 Hz and maximum closing doppler is +4144 Hz, as shown in Figure 17.

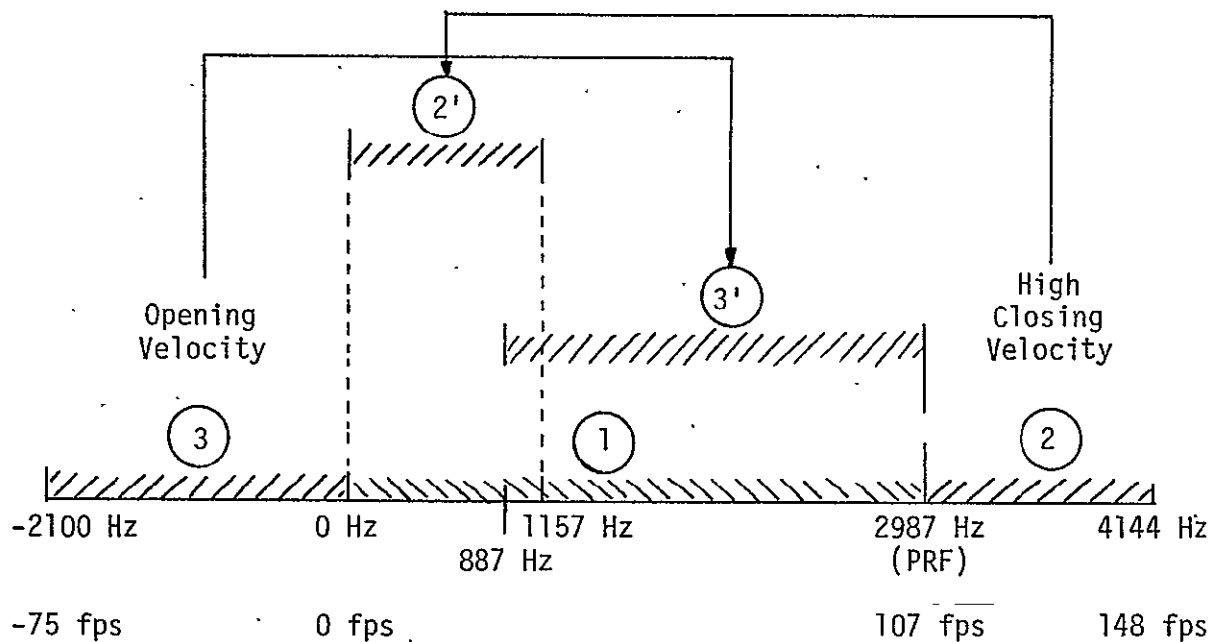


Figure 17. Resolution of Doppler Ambiguity

When the high PRF of 6970 is used, there is no doppler ambiguity from the doppler estimation from the α - β tracker. For the low PRF at longer ranges, namely, 2987, there is a doppler ambiguity as indicated in Figure 17. The resolution is easily resolved from the coarser estimation of range rate from the α - β tracker by noting the following:

(a) If the coarse $\hat{R}_S(n) > 0$ (opening), then the fine estimation $\hat{R}_{SC}(n)$ will be in Region 3', whereas the actual estimate should be in Region 3. In this case, $\hat{R}_{SC}(n)$ is adjusted by subtracting the PRF equal to 2987 Hz.

(b) If the coarse $\hat{R}_S(n)$ is longer than 2987 Hz (high closing velocity), the estimate $\hat{R}_{SC}(n)$ will be in Region 2'. In this case, $\hat{R}_{SC}(n)$ is adjusted by adding the PRF.

(c) If the coarse estimate is between 0 and 2987 Hz, the fine estimate is not altered.

It is assumed that the resolution of the ambiguity is carried out ideally, so that it does not contribute to the RMS tracking error.

REFERENCES

1. Hughes Aircraft Co.. "Ku-Band Integrated Radar and Communication Equipment for the Space Shuttle Orbiter Vehicle," Ref. D7738-SCG 76075V, HS237-202, Conceptual Design Review, January 31, 1977.
2. Hughes Aircraft Co. "Ku-Band Integrated Radar and Communication System for the Space Shuttle Orbiter Vehicle," Monthly Review, April 20, 1977.
3. C. L. Weber. "Maximum Likelihood Estimation of the Ratio of Powers in Two Narrowband Processes," Axiomatix Report No. R7701-3, January 31, 1977.
4. C. L. Weber. "Study to Investigate and Evaluate Means of Optimizing the Radar Function," Axiomatix Report No. R7511-3, Appendix D, November 24, 1975.
5. Hughes Aircraft Co. "Proposal for Ku-Band Integrated Radar and Communication Equipment for the Space Shuttle Orbiter Vehicle," Vol. II, Technical Proposal, Ref. D7768.60176P, May 1976.
6. D. Barton and H. Ward. Handbook of Radar Measurement. Prentice-Hall, Inc., 1969.
7. M. Skolnik. Radar Handbook. McGraw-Hill, 1970.
8. Hughes Aircraft Co. "Ku-Band Integrated Radar and Communication Equipment for the Space Shuttle Orbiter Vehicle," Schematic Review, Vol. I, July 19, 1977.
9. Hughes Aircraft Co. "Ku-Band Integrated Radar and Communication Equipment for the Space Shuttle Orbiter Vehicle," Schematic Review, Vol. II, July 20, 1977.

APPENDIX C

TIME MULTIPLEXED SINGLE CHANNEL ANGLE TRACKING OF PASSIVE TARGETS

APPENDIX C

TIME MULTIPLEXED SINGLE CHANNEL ANGLE TRACKING OF PASSIVE TARGETS

by

Charles L. Weber
Waddah K. Alem

1.0 INTRODUCTION

Angle tracking is carried out by sequential processing of monopulse signals. The angle error signals are derived by sequentially processing the monopulse error signals. Angle tracking is potentially more critical than range or range rate tracking since angle monopulse signals are subject to angular (glint) and amplitude (scintillation) variations due to the target motions. The easiest method to reduce these effects is by postdetection integration over the RF frequencies before the tracking error signals are generated.

In the angle tracking loop analyzed in this appendix (and described in [1]), single channel processing is used for generation of the angle error signals. The single channel is time-division-multiplexed between the $\Sigma + \Delta_{AZ}$, $\Sigma - \Delta_{AZ}$, $\Sigma + \Delta_{EL}$, and $\Sigma - \Delta_{EL}$ error signals. The alternative is a two- or three-channel monopulse system. The primary advantage of the three-channel monopulse is that it allows angle error measurements to be derived from a single pulse. To reduce the effects of angular glint, however, several pulses are averaged to obtain smoothed data. The primary disadvantage of the three-channel monopulse system is the requirement that the two additional channels be phase and gain balanced to the first channel. Alternatively, the advantage of the single channel monopulse system is the simplicity in implementation and the noncriticality of phase and gain, at the expense of a 3 dB to 6 dB reduction in performance. A disadvantage is that it may be more suspect to target scintillation. As mentioned previously, this can be circumvented by frequency diversity.

In the next section, the single channel monopulse system under consideration is described, followed in subsequent sections by a performance analysis.

2.0 SINGLE CHANNEL AMPLITUDE MONOPULSE

A single channel monopulse system is described, where the channel is time-shared by the various error signals. The description of the various radar tracking functions has already been presented in Appendix B of [12]. From that description, a block diagram of the single monopulse is shown in Figure 1. Familiarity with [12], Appendix B, is assumed. Only those components of the radar that are pertinent to the angle tracking function are shown in Figure 1.

2.1 Ku-Band Amplitude Monopulse Antenna

Referring to Figure 1, the Ku-band monopulse antenna outputs a sum channel and two angle error signals, which are designated Δ_{AZ} and Δ_{EL} for the azimuth and elevation signals, respectively. With respect to the amplitude monopulse feed, sum and difference patterns of a monopulse antenna network are usually determined experimentally in order to account for the effects of coupling between horns and of introduction of high-order transmission modes at the mouth of the horn assembly.

Studies of the actual parabolic antenna patterns [2-4] have shown that the normalized sum (voltage) pattern can be represented very closely by

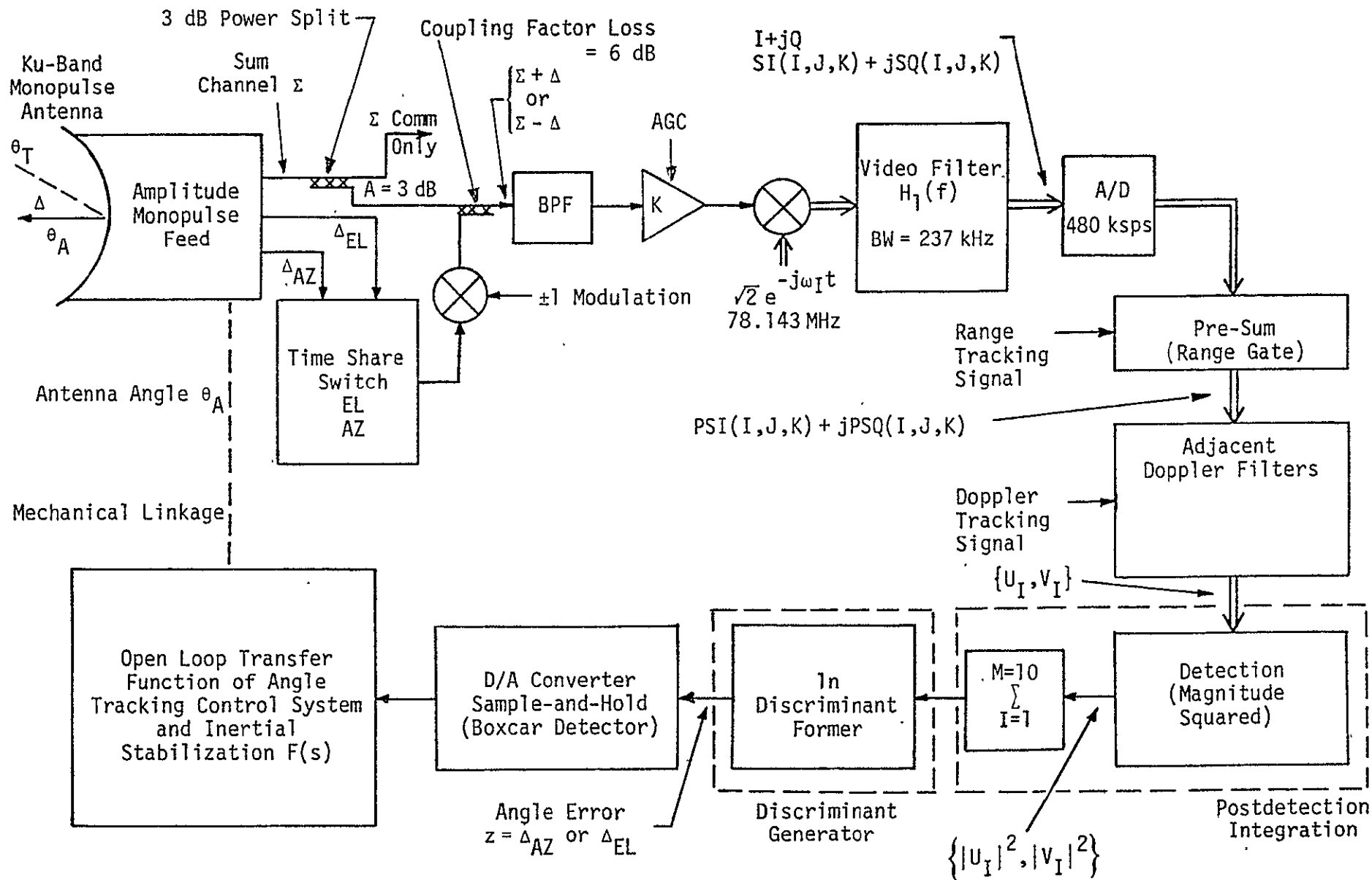
$$E_s = \cos^2 (1.18 \Delta_\epsilon / \theta_B), \quad (1a)$$

where Δ_ϵ is the angle off the boresight axis, azimuth or elevation, and θ_B is the 3 dB beamwidth. It is assumed that Δ_ϵ and θ_B are given in the same units. This representation of the normalized sum pattern is excellent to well below 3 dB from the boresight axis of the main lobe and is therefore a convenient representation when evaluating antenna tracking performance. At the lower gain portions of the main lobe and over the sidelobe, the above representation is not useful.

The measured difference (voltage) pattern for the same type parabolic antenna is well represented by

$$E_\Delta = 0.707 \sin (2.36 \Delta_\epsilon / \theta_B), \quad (1b)$$

where the same comments given above apply. Significant differences between these approximations and actual patterns appear only at the edges of the main beam, well beyond the 3 dB beamwidth.



Double lines represent two channels, I and Q, of data

Figure 1. Block Diagram of Single Channel Monopulse Angle Tracking Loop

In the angle tracking monopulse system under consideration, as well as in most cases, only the variation within the 3 dB beamwidth is of interest, in which case, the above approximations are very satisfactory. The actual error pattern is approximately linear to at least one-third of the beamwidth off the boresight. The normalized error pattern E_{Δ}/E_S which approximately results from the AGC and logarithmic discriminant operation in the receiver system (Figure 1) is linear over more than 0.6 of the beamwidth. The slope increases as the direction of the received signal approaches the half-power point of the sum channel beam. The antenna error slope is designated as k_m and is approximately 1.67 for the representations given above. This can be seen by observing that

$$\frac{E_{\Delta}}{E_S} = \sqrt{2} \tan \left(1.18 \frac{\Delta_{\epsilon}}{\theta_B} \right) \approx 1.67 \frac{\Delta_{\epsilon}}{\theta_B}$$

for small Δ_{ϵ} . Within the linear region, the error voltage is

$$\text{Error voltage} = \frac{E_{\Delta}}{E_S} = k_m (\Delta_{\epsilon} / \theta_B) \quad (2a)$$

or, equivalently,

$$\Delta_{\epsilon} | \text{deg} = \theta_B | \text{deg} k_m^{-1} \frac{E_{\Delta}}{E_S}. \quad (2b)$$

The actual value of the antenna error slope, k_m , varies over different monopulse antenna designs. A conservative interval is

$$1.0 \leq k_m \leq 1.9, \quad (3)$$

with typical values being 1.2 to 1.7.

The connection between $\Sigma \pm \Delta$ and (E_S, E_{Δ}) is that $\Sigma + \Delta$ is proportional to $E_S + E_{\Delta}$ and $\Sigma - \Delta$ is proportional to $E_S - E_{\Delta}$, where the proportionality constant is the same in both cases.

Since the antenna gain patterns discussed above have been normalized to 1, there is no loss in generality in equating

$$\Sigma + \Delta = E_S + E_{\Delta} \quad (4a)$$

where

$$\Sigma - \Delta = E_S - E_{\Delta}. \quad (4b)$$

Hence,

$$\frac{\Sigma + \Delta}{\Sigma - \Delta} = \frac{E_S + E_{\Delta}}{E_S - E_{\Delta}} \quad (5)$$

This will be used in the discriminant function to relate $\frac{\Sigma + \Delta}{\Sigma - \Delta}$ to E_{Δ}/E_S .

3.0 DESCRIPTION OF SINGLE CHANNEL MONOPULSE

The amplitude monopulse feed of the Ku-band antenna system outputs three channels of data—the sum channel Σ , the azimuth error channel Δ_{AZ} , and the elevation error channel Δ_{EL} , as shown in Figure 1. As described in more detail in Appendix B of [12], the elevation and azimuth error channels time-share the single signal processing channel. The modulation by ± 1 either passes the error signal unchanged or inverts the RF phase. After recombining the error channel with the sum channel, the time-sharing is as shown in Figure 2.

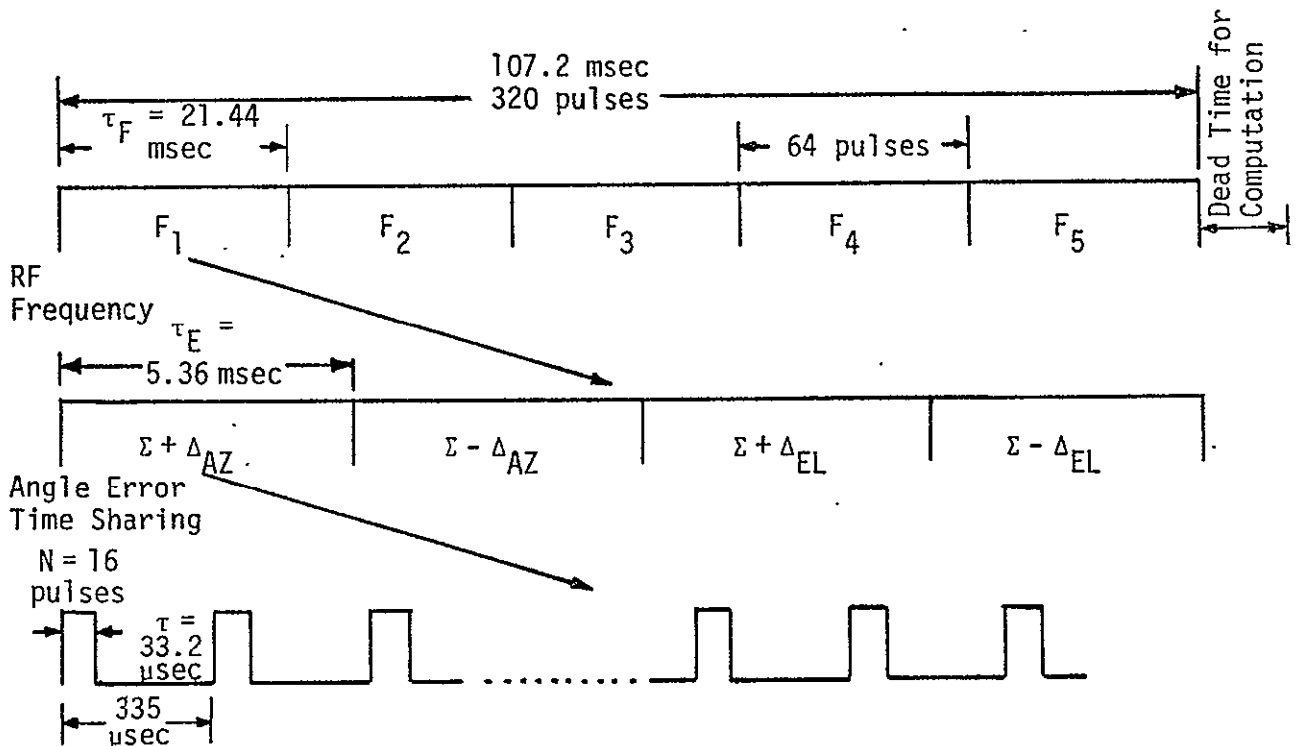


Figure 2. Timing for Single-Channel Time-Shared Monopulse Tracking, PRF = 2987

During the track mode of operation, the frequency diversity consists of 5 RFs, each of which operates for $\tau_F = 21.44$ msec. During each RF frequency, the single channel processing is equally time-shared among the four signals— $\Sigma + \Delta_{AZ}$, $\Sigma - \Delta_{AZ}$, $\Sigma + \Delta_{EL}$, $\Sigma - \Delta_{EL}$ —in the four time slots. Each of these is processed for $\tau_E = 5.36$ msec (designated the slot time), during which time 16 pulses are transmitted and received. Throughout this description, the system parameters corresponding to the largest range interval of interest are being employed. In particular [7],

$$\text{PRI} = T_p = \text{pulse repetition interval} = 335 \mu\text{sec}$$

$$\text{PRF} = 2987$$

$$\text{Pulse Width} = \tau = 33.2 \mu\text{sec}$$

$$\text{Frequency Dwell Time} = \tau_F = 21.44 \text{ msec/RF}.$$

τ_E is the dwell time of $\Sigma + \Delta_{AZ}$, which is one of four time slots for each frequency dwell, and the range interval for this set of parameters is 9.5 to 18.9 nmi. The equivalent coherent integration time/frequency is defined as $\tau_c \triangleq 16\tau$.

Referring again to Figure 1, the various stages of IF and AGC are simplified and consolidated into one bandpass filter (BPF) and AGC. The AGC is shown but not taken into account in the angle track performance analysis, since for angle tracking purposes, the logarithmic discriminant is already self-normalizing. The primary purpose of the AGC is to maintain satisfactory signal level in the receiver and avoid receiver saturation. The AGC is herein assumed to be performing its operation, so that all normalization can be accounted for in the discriminant.

The final stage of IF converts the sum plus error narrowband signals to I and Q (complex) baseband waveforms. The video filter before the A/D is a 2-pole Butterworth with transfer function

$$|H_1(f)|^2 = \left[1 + \left(\frac{f}{f_c} \right)^4 \right]^{-1}, \quad (6)$$

where $f_c = 237$ kHz. At these longer ranges, $R > 9.5$ nmi, where the pulse width is 33.2 sec, the signal can be assumed to be undistorted by $H_1(f)$.

The sampling frequency of the A/D is 480 ksps, which corresponds to 16 samples over each pulse width τ . This is a sufficiently large

number so that the pre-sum can be accurately approximated by analog integration.

The notation developed in the previous report [12] is maintained. In particular,

$I = 1, \dots, 5$ corresponds to RF frequency

$J = 1, \dots, 4$ corresponds to time slot;

$J = 1$ implies $\Sigma + \Delta_{AZ}$, also designated as $+\alpha$ in [13]

$J = 2$ implies $\Sigma - \Delta_{AZ}$, also designated as $-\alpha$

$J = 3$ implies $\Sigma + \Delta_{EL}$, also designated as $+\beta$

$J = 4$ implies $\Sigma - \Delta_{EL}$, also designated as $-\beta$

$K = 1, \dots, 16$ corresponds to the pulse number for a given I and J .

There are actually additional pulses transmitted periodically to allow time for signal processing, register resets, etc. Without loss of generality, only those signals which contribute to the angle tracking operation and performance are taken into account.

Now consider the complex baseband waveforms before the pre-sum for a given time slot J and restrict attention to that particular slot, where J can be 1, 2, 3, or 4, as described above. The I and Q waveforms are

$$SI(I, J, K) = \{ \sqrt{2} (\Sigma + \Delta_J) A_I P(t - kT_p) \cos [(\omega_I + \omega_d)t + \theta_I] + n(t) \} \sqrt{2} \cos (\omega_I t) \quad (7a)$$

and

$$SQ(I, J, K) = \{ \sqrt{2} (\Sigma + \Delta_J) A_I P(t - kT_p) \cos [(\omega_I + \omega_d)t + \theta_I] + n(t) \} \sqrt{2} \sin (\omega_I t) \quad (7b)$$

for the I channel and Q channel, respectively. The peak received signal power is given by

$$P_{pr} = E[A_I^2],$$

where it is assumed that $\Sigma + \Delta_J$ (which are the factors representing antenna processing) are normalized to 1 for all J . The average received power is

$$P_{avg} = d_t P_{pr}$$

where d_t is the duty factor of the radar pulse train. The duty factor is constant for a given range but does vary as a function of range.

Table 1 lists the values of the duty factor for various range intervals in the passive tracking mode, as given in [9, p. 44].

Table 1. Duty Factor d_t for Various Designated Ranges

	Designated Range (nmi)					
	> 9.5	9.5 - 3.8	3.8 - 1.9	1.9 - 0.95	0.95 - 0.42	< 0.42
Pulsewidth (μ sec)	33.2	16.6	8.3	4.15	2.07	0.122
PRF (Hz)	2987	6970	6970	6970	6970	6970
d_t	0.099	0.116	0.058	0.029	0.0144	0.00085

Except for the very short ranges, angle tracking will be most noisy at the maximum ranges. In this development, therefore, we consider primarily ranges greater than 4 nmi, and set $d_t = 0.099$.

When $J=1$, the amplitude is proportional to $\Sigma + \Delta_{AZ}$, and when $J=2$, the amplitude is proportional to $\Sigma - \Delta_{AZ}$. The amplitudes A_I are assumed to be Rayleigh random variables, since the target is assumed to be Swerling I. The random phase θ_I is assumed to be uniformly distributed over $(0, 2\pi)$. The Rayleigh and uniform random variables A_I and θ_I , respectively, are independent. The pulse $P(t)$ has magnitude of unity over the transmitted pulse width $\tau = 33.2 \mu$ sec. The doppler frequency shift is represented by ω_d .

The receiver system noise $n(t)$ after the bandpass filter has the narrowband representation

$$n(t) = \sqrt{2}[N_c(t) \cos \omega_I t - N_s(t) \sin \omega_I t], \quad (8)$$

where N_c and N_s are independent zero mean baseband Gaussian processes with one-sided power spectral density of N_0 watts/Hz, and one-sided noise bandwidth approximately equal to f_c ($f_c = 237$ kHz), which is the

3 dB bandwidth of $H_1(f)$. The one-sided power spectral density of $n(t)$ is also N_0 watts/Hz, and the total noise power in $n(t)$ is $\sigma_n^2 = 2 N_0 f_c$. The total noise power in $N_c(t)$ and $N_s(t)$ is $\sigma_N^2 = N_0 f_c$ each.

Before the A/D, the complex waveform is given by

$$\begin{aligned} SI + jSQ &= \left[\sqrt{2} (\Sigma + \Delta_J) A_I P(t - kT_p) \cos [(\omega_I + \omega_d)t + \theta_I] + n(t) \right] \sqrt{2} e^{-j\omega_I t} \\ &= (\Sigma + \Delta_J) A_I P(t - kT_p) e^{j[\omega_d t + \theta_I]} + N_c(t) + jN_s(t) . \end{aligned} \quad (9)$$

3.1 Pre-Sum (Range Gate)

After the A/D, each received pulse is pre-summed over the pulse width. The timing of this pre-sum is dependent on the setting of the range gate in the range tracking loop. The range tracking loop is presently assumed to be tracking ideally. Variations in tracking errors will be taken into account subsequently when design margins are considered.

With ideal range tracking, the pre-sum output is

$$\begin{aligned} PSI(I,J,K) + jPSQ(I,J,K) &= a \int_{kT_p}^{kT_p + \tau} [SI(t) + jSQ(t)] dt \\ &= a(\Sigma + \Delta_J) A_I \tau \left[\frac{\sin(\omega_d \tau/2)}{(\omega_d \tau/2)} \right] \exp \{j[\theta_I + \omega_d(kT_p + \tau/2)]\} \\ &\quad + \int_{kT_p}^{kT_p + \tau} [N_c(t) + jN_s(t)] dt , \end{aligned} \quad (10)$$

where the sum of the samples over the pulse width is approximated by analog integration. This is described in more detail in Section 6.2.

The description given in (10) is the optimal signal processing from the aspect of angle and velocity tracking performance. Equivalently stated, the integration in (10) is over the period of time during which the pulse arrives at the receiver. We shall see that this requires more computation than the implementation in [7,13].

In range tracking (see Appendix E), an early gate and a late gate are formed which are adjacent and nonoverlapping. These range bins (gates) are usually designed equal to the transmitted pulse width.

When range tracking is being carried out without error, one-half of the power is received through the early gate and one-half through the late gate. Since the signal is coherent, this corresponds to a 6 dB range gate straddling loss with respect to having a third gate midway between the early and late gates. In the radar described in [1,7,13], there is no center range gate as given in (10).

For all tracking loops, the array of doppler filter outputs is as shown in Figure 3.

During search, 16 doppler filters are used. For convenience, these are numbered 1, 3, 5, ..., 31. During track, these same 16 doppler filters are used but, in addition, the even numbered filters are also formed, numbered 2, 4, 6, ..., 32. For doppler tracking, filters F_n and F_{n+2} are used, during which time the output of F_{n+1} is used for angle and range track, as shown in Figure 3. These filters are not adjusted, so that the center of filter F_{n+1} corresponds to the doppler frequency received. Alternatively, the center frequency of all of these filters remains fixed until the error gets sufficiently large to shift filters. At the maximum offset of the center doppler filter, the loss incurred for not shifting is 0.91 dB, as will be shown in Section 3.3. This is accounted for in the power budget for angle tracking in Section 5. This doppler processing tracking technique is discussed in more detail in Appendices B and G.

During each computation period, 320 pulses are received in 107.2 msec; when the PRF is 2987, as shown in Figure 2. For each of the positions shown in Figure 3, there is a doppler filter output for each of the RF frequencies. From inspection of Figure 3, there is an early range gate and a late range gate only. For doppler tracking, the discriminant is formed from doppler filters F_n and F_{n+2} , as shown in Figure 3, when the actual doppler frequency is located in filter $n+1$. The output of the DFT for F_{n+1} is used for angle and range tracking.

For angle tracking of azimuth, therefore, there is an input to the discriminant from the time slot corresponding to $\Sigma + \Delta_{AZ}$ and the doppler filter output with center frequency F_{n+1} . There is such an input for each RF frequency from the early range gate and the late range gate.

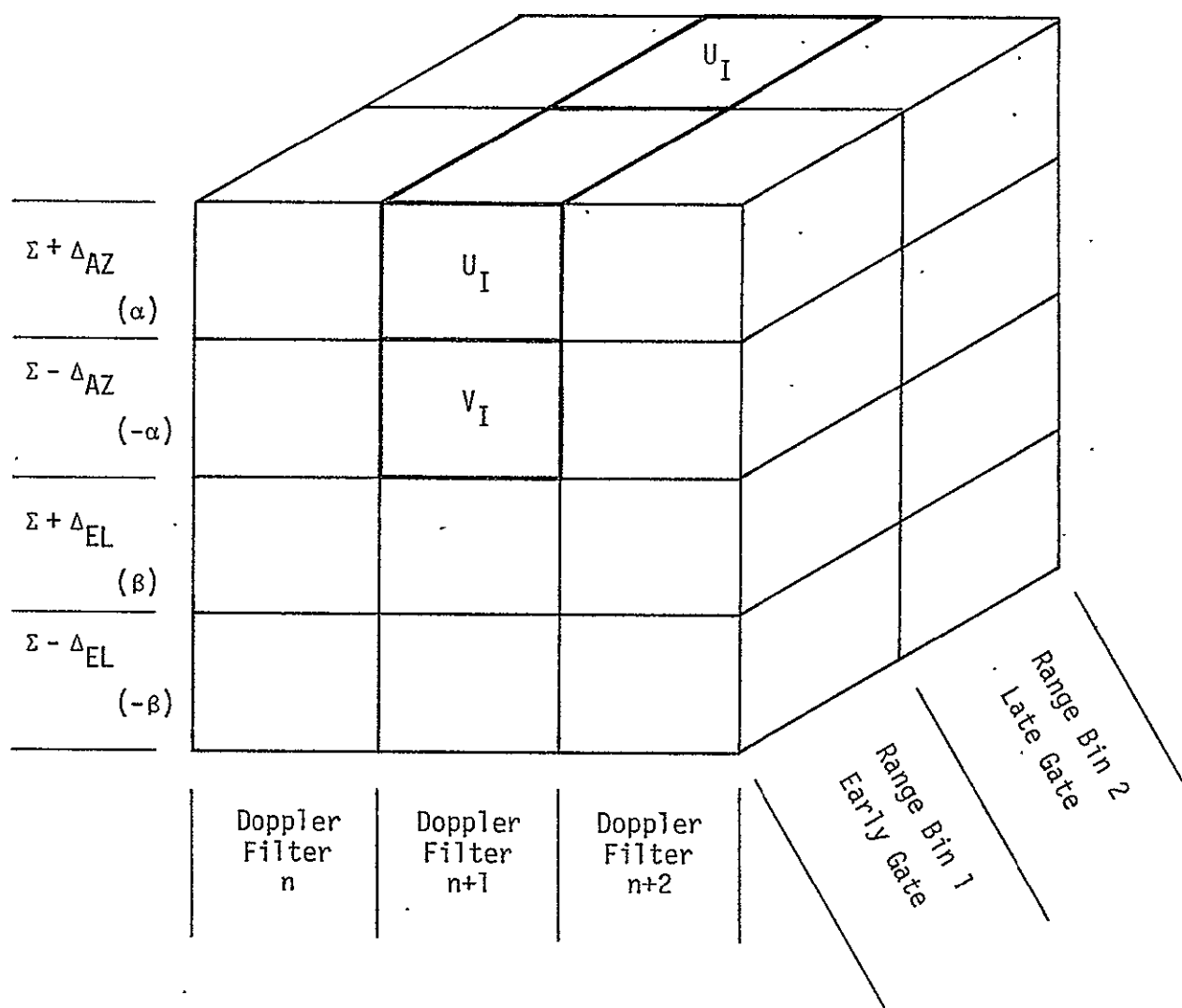


Figure 3. Storage Diagram of Doppler Filter Outputs During Radar Tracking Operations, Emphasizing Inputs Used for Azimuth Angle Tracking

In what follows, one set of equations is carried forward. This set applies for both the early and the late gate. The attenuation factor, a , in (10) accounts for the fact that the signal is only present one-half of the time in the early and late range gates. Hence, $a = 1/2$. Since there is coherent addition during the pre-sum operation, setting $a = 1/2$, which gives the idea that the signal amplitude is attenuated by a factor of 2, gives the same result as the actual situation. Namely, the actual situation is the fact that the signal is present at full strength during one-half of the range gate period and equal to zero during the other half.

Errors in range gate tracking are accounted for by errors in the limits of integration in (10), where again, the digital sum of the pre-sum is being approximated by analog integration.

3.2 Doppler Filters (Range Rate Tracking)

Doppler filters are being used for accurate range rate tracking, as described in the previous section and in [12], Appendix B. The frequency midway between the correct two tracking doppler filters F_n and F_{n+2} in the DFT is assumed to be at the frequency $\omega_d + \Delta\omega_d$, where $\Delta\omega_d$ represents the error in doppler tracking.

The DFT filtering operation in the center doppler filter, namely, F_{n+1} , is described by

$$\begin{aligned} \frac{1}{\tau_E} \sum_{k=0}^{N-1} \{ \text{PSI}(I, J, K) + j \text{PSQ}(I, J, K) \} \exp [-j(\omega_d + \Delta\omega_d)k T_p] \\ = a(\Sigma + \Delta_J) A_I d_t \left[\frac{\sin(\omega_d \tau/2)}{(\omega_d \tau/2)} \right] \left[\frac{\sin(\Delta\omega_d T_p N/2)}{N \sin(\Delta\omega_d T_p/2)} \right] \\ \cdot \exp \{ j[\theta_I + \omega_d \tau/2 - \Delta\omega_d T_p(N - 1/2)] \} + N_{CJ} + jN_{SJ}, \quad (11) \end{aligned}$$

where N_{CJ} and N_{SJ} are independent zero-mean Gaussian random variables, each with variance,

$$\sigma^2 \triangleq \frac{N_0 d_t B_F}{2}. \quad (12)$$

The computations are developed in more detail in Section 6, where a precise comparison is made between the optimal coherent radar receiver and the digital signal processor implementation developed here. The DFT one-sided filter bandwidth is $B_F \triangleq 1/\tau_E$. The dwell time at one RF for

$\Sigma + \Delta_J$ is τ_E . The bandwidth of each of the DFT filter is therefore matched to this dwell (or slot) time.

3.3 Statistical Parameters of Doppler Filter Outputs

As described in the previous section, the azimuth angle tracking corresponds to $J=1$ and $J=2$, while elevation angle tracking used $J=3$ and $J=4$. Azimuth is arbitrarily chosen. The output of the doppler filters that are used for azimuth angle tracking can then be represented by

$$\begin{bmatrix} U_I \\ V_I \end{bmatrix} = a \begin{bmatrix} \Sigma + \Delta_{AZ} \\ \Sigma - \Delta_{AZ} \end{bmatrix} A_I d_t \begin{bmatrix} \sin(\omega_d \tau/2) \\ (\omega_d \tau/2) \end{bmatrix} \begin{bmatrix} \sin(\Delta\omega_d T_p N/2) \\ N \sin(\Delta\omega_d T_p/2) \end{bmatrix} \cdot \exp \{j[\theta_I + \omega_d \tau/2 - \Delta\omega_d T_p (N - 1/2)]\} + \begin{bmatrix} N_{UI} \\ N_{VI} \end{bmatrix}, \quad (13)$$

where the first component represents the $\Sigma + \Delta_{AZ}$ measurement which results from setting $J=1$ in (1) and the second component represents $\Sigma - \Delta_{AZ}$ measurements which corresponds to $J=2$ in (10). The U_I term is the result of measurement and computation of the time period $(0, \tau_E)$ and V_I results from the time period $(\tau_E, 2\tau_E)$, as shown in Figure 2. There are, altogether, ten U_I inputs and $M=10$ V_I inputs used in the formation of the discriminant for azimuth angle tracking. For each of the two range gates, there are five RF frequencies, making a total of ten. All of the noise random variables in (12) are identically distributed and mutually independent.

At this point, the signal and noise have both been accounted for during both the $\Sigma + \Delta_{AZ}$ time slot for the I th RF, which is designated as U_I , and during the $\Sigma - \Delta_{AZ}$ time slot for the I th RF, which is designated as V_I . This is because the desired signal portions of U_I and V_I are correlated. The noise contributions remain uncorrelated.

From the signal standpoint, the effect of nonideal range rate tracking shows up in two factors:

(a) The attenuation

$$\left[\frac{\sin(\omega_d \tau/2)}{(\omega_d \tau/2)} \right]^2 \quad (14a)$$

in power is due to pre-sum loss when there is a doppler shift of ω_d rad/sec.

(b) The attenuation

$$\left[\frac{\sin(\Delta\omega_d N T_p / 2)}{N \sin(\Delta\omega_d T_p / 2)} \right]^2 \quad (14b)$$

represents the power loss due to doppler mismatch over the predetection summation of N pulses in the DFT. When $\Delta\omega_d \rightarrow 0$, the attenuation in (14b) goes to 0 dB, and when $\omega_d \neq 0$, the pre-sum loss in (14a) goes to 0 dB.

The 3σ specification on doppler tracking is 1 ft/sec, or 28 Hz at 13 GHz. If this is designated at the maximum doppler mismatch, then the loss in SNR in the angle tracking loop, as given in (14b), is -0.32 dB. The phase shift in (13) is inconsequential since θ_I is already uniform and independent of A_I .

From the angle tracking point of view, the maximum attenuation due to doppler mismatch is as shown in Figure 4. Adjacent doppler filters in the DFT are located $(NT_p)^{-1}$ Hz apart which, when the PRF = 2987 and $N = 16$, corresponds to 187 Hz. If only the doppler tracking filters were being used in angle track, the maximum attenuation would occur at the midpoint. Since the center frequencies of the doppler filters do not move, this corresponds to an attenuation of 3.9 dB, computed from (14b) when $\Delta\omega_d = (2\pi)(2NT_p)^{-1}$. This is point A in Figure 4. With the additional doppler filters inserted for angle and range tracking, namely, the dotted line filter in Figure 4, the maximum attenuation now corresponds to (14b) computed at $\Delta\omega_d = (2\pi)(4NT_p)^{-1}$. This results in a loss of 0.91 dB as shown, and is also shown in the power budget in Section 5.0.

For the present, the doppler tracking loop is assumed to be working ideally, so that $\Delta\omega_d = 0$, and the loss is accounted for in the power budget.

Another independent consideration is to determine whether the relative acceleration between the Shuttle and the target can be such that in one computation time the doppler would be outside the set of three doppler filters shown in Figure 4. The worst case corresponds to a shift from Point B to Point C in Figure 4. At Point C, the target would most likely still be observed by Filter $n+2$, but for this discussion, let us assume it does not. For the PRF = 2987 and $N = 16$, this corresponds to a doppler frequency shift of 93 Hz when the RF is 13.883 GHz. Therefore, the acceleration must be such that the doppler frequency shifts 93 Hz ($B_F/2$), in one computation time (107.2 msec). This corresponds to

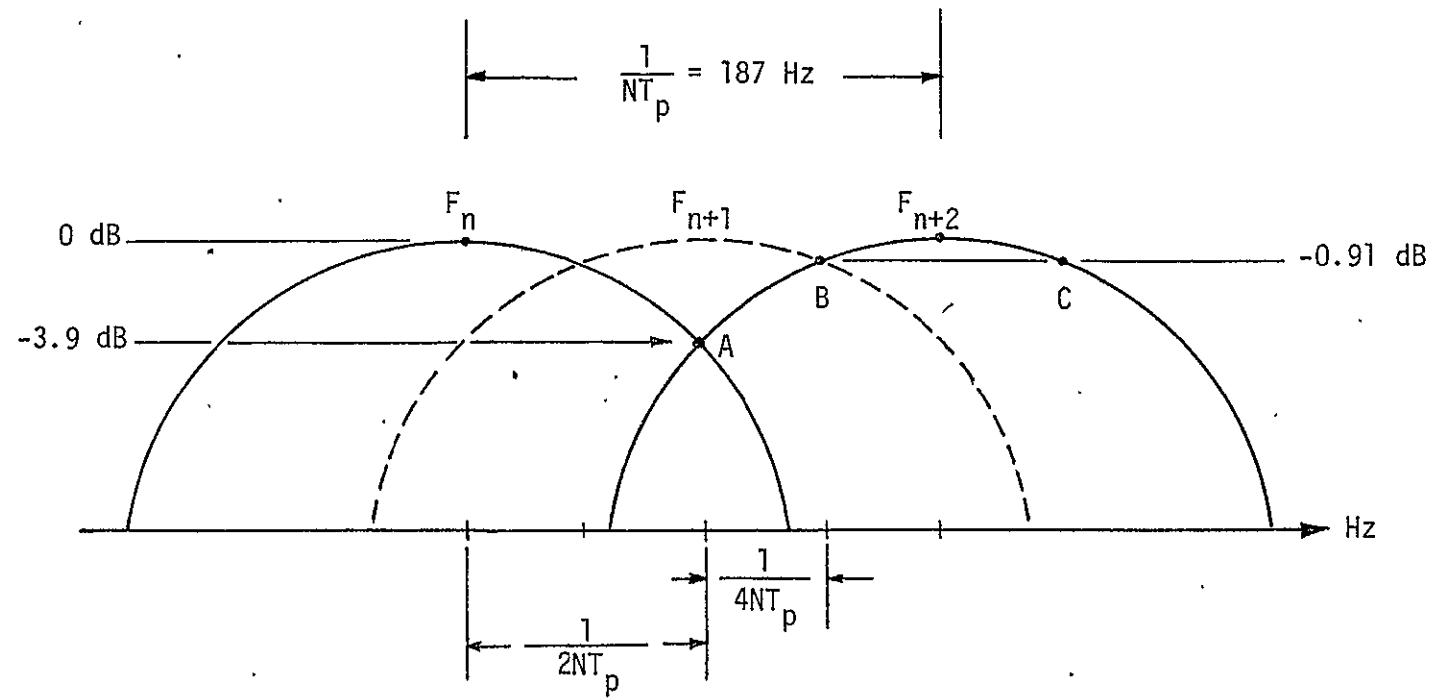


Figure 4. Signal Attenuations in Angle Tracking Loop Due to Doppler Mismatch

an acceleration of

$$\begin{aligned}
 a &= \frac{\dot{R}}{\text{one computation time}} = \left(\frac{\dot{R}}{T_s} \right) \left(\frac{c}{2F_{RF}} \right) \\
 &= \frac{(93 \text{ Hz})}{(107.2 \text{ msec})} \cdot \frac{3 \times 10^8 \text{ m/sec}}{2(13.883 \text{ GHz})} = 9.37 \text{ m/sec}^2.
 \end{aligned} \tag{15}$$

where $f_{\text{Doppler}} = 2\dot{R}F_{RF}/c$, and c is the speed of light.

This is an acceleration of almost 1 g, which is an order of magnitude greater than anything expected. There should therefore be no loss of doppler tracking due to acceleration.

Returning to the direct angle track analysis, in (13)

$$N_{UI} \triangleq N_{cI1} + jN_{sI1} \tag{16a}$$

and

$$N_{VI} \triangleq N_{cI2} + jN_{sI2}. \tag{16b}$$

The noise random variables N_{UI} and N_{VI} are complex and represent the contribution at the output of the DFT operation due to receiver front end noise. N_{UI} is the noise contribution when $\Sigma + \Delta_{AZ}$ ($J=1$) is measured, and N_{VI} is the noise contribution when $\Sigma - \Delta_{AZ}$ ($J=2$) is measured. All of these random variables are Gaussian with zero mean and variance.

$$\sigma^2 = E[N_{cI1}^2] = E[N_{sI1}^2] = E[N_{cI2}^2] = E[N_{sI2}^2] = N_0 B_F d_t / 2, \tag{17}$$

where B_F is the one-sided bandwidth of the DFT filters, namely, $B_F = \tau_E = 187 \text{ Hz}$. These random variables are all mutually independent.

With this information, the statistical parameters of the doppler filter outputs can be determined for a given RF. In particular, when $\Delta\omega_d = 0$, the power in U_I is

$$P_U \triangleq E[|U_I|^2] = a^2 d_t^2 (\Sigma + \Delta_{AZ})^2 E(A_I)^2 \left[\frac{\sin(\omega_d \tau / 2)}{(\omega_d \tau / 2)} \right]^2 + N_0 B_F d_t. \tag{18a}$$

The power in V_I is

$$P_V = E[|V_I|^2] = a^2 d_t^2 (\Sigma - \Delta_{AZ})^2 E(A_I)^2 \left[\frac{\sin(\omega_d \tau / 2)}{(\omega_d \tau / 2)} \right]^2 + N_0 B_F d_t, \tag{18b}$$

and the correlation (unnormalized) is

$$\begin{aligned}
P_{UV} &= E[U_I V_I^*] = P_{VU}^* \\
&= a^2 d_t^2 (\Sigma + \Delta_{AZ})(\Sigma - \Delta_{AZ}) E(A_I^2) \left[\frac{\sin(\omega_d \tau/2)}{(\omega_d \tau/2)} \right]^2,
\end{aligned} \tag{18c}$$

where (*) means complex conjugate and d_t is the duty factor of the signal; in the computations shown subsequently, we assume $\Delta\omega_d = 0$.

In general, P_{UV} would be complex. If there were an unaccounted-for RF phase shift in the antenna, DMA or DEA, then the angle error channels would not be exactly in phase with the sum channel when they are recombined into one channel (Figure 1). When this occurs, P_{UV} becomes a complex correlation. In this development, no RF phase difference between the sum and angle error channels is assumed. The effect of such errors on angle tracking performance is examined in [6].

If the doppler tracking loop is assumed to be working ideally, then $\Delta\omega_d = 0$. Recalling that the peak received signal power through either range gate is given by

$$P_{pr} = a^2 E(A_I^2) = \frac{1}{4} E(A_I^2) = \frac{1}{4} P_{pr \max}. \tag{19}$$

Then, when $\Delta\omega_d = 0$,

$$P_U = d_t^2 (\Sigma + \Delta_{AZ})^2 P_{pr} + N_0 B_F d_t \tag{20a}$$

$$P_V = d_t^2 (\Sigma - \Delta_{AZ})^2 P_{pr} + N_0 B_F d_t \tag{20b}$$

and

$$P_{UV} = d_t^2 (\Sigma + \Delta_{AZ})(\Sigma - \Delta_{AZ}) P_{pr}. \tag{20c}$$

The peak received signal power through either range gate is henceforth equated to $E(A_I^2)$ and the 6 dB range gate straddling loss is taken into account in the power budget in Section 5.0.

In (20), the pre-sum loss factor has been neglected, since it will be accounted for explicitly as a loss in the power budget computations in Section 5.0. Also note that the maximum signal-to-noise ratio that can be attained at the output of the DFT can now be defined. From (18), (19) and (20), define the maximum SNR as

$$\text{SNR} \Big|_{\max} = \frac{d_t^2 (\Sigma \pm \Delta_{AZ})^2 P_{pr}}{N_0 B_F d_t} = \frac{P_{pr} d_t \tau E}{N_0} = \frac{\mathcal{E}_r}{N_0}, \tag{21}$$

where \mathcal{E}_r is the total received signal energy in τ_E seconds, assuming one centered range gate. This is the maximum attainable SNR and shows that, except for pre-sum, signal processing and tracking losses, the digital signal process implementation described here is optimum. This optimality is described in detail in Section 6.0. In (21), as throughout, the antenna parameters, $\Sigma \pm \Delta_j$, are assumed to be normalized to unity.

Define the normalized correlation coefficient between U and V as

$$\rho^2 \triangleq \frac{|P_{UV}|^2}{P_U P_V} . \quad (22a)$$

When $\Delta\omega_d = 0$, ρ^2 is given by

$$\rho^2 = \left\{ \left[1 + \frac{N_0 B_F}{P_{avg} r (\Sigma + \Delta_{AZ})^2} \right] \left[1 + \frac{N_0 B_F}{P_{avg} r (\Sigma - \Delta_{AZ})^2} \right] \right\}^2 . \quad (22b)$$

From an average power point of view, $(\Sigma \pm \Delta)^2$ is normalized to unity, particularly for small angle errors, so that

$$\rho = \frac{1}{1 + \frac{N_0 B_F}{P_{avg} r}} = \frac{1}{1 + \frac{N_0}{P_{avg} r \tau_E}} = \frac{1}{1 + \frac{N_0}{\mathcal{E}_r}} . \quad (23)$$

The signal-to-noise ratio, $SNR = \mathcal{E}_r/N_0$, is the signal-energy-to-noise-spectral-density over the time slot τ_E , which is the dwell time of $\Sigma + \Delta_{AZ}$. Equivalently, this is the SNR in the doppler signal bandwidth.

The significant observation is that the normalized correlation coefficient is dependent on SNR, as given by (23). Note that, as $SNR \rightarrow \infty$, then $\rho \rightarrow 1$, and as $SNR \rightarrow 0$, then $\rho \rightarrow 0$. This will subsequently be related to the performance of the monopulse angle tracking loop.

With these statistical parameters of U_I and V_I now determined, the remainder of the angle tracking loop can be described and the performance analyzed.

3.4 Angle Tracking Discriminant Generator

Referring to Figure 1, the detector forms the magnitudes $|U_I|$ ($I=1, \dots, M$) and $|V_I|$ ($I=1, \dots, M$), where I represents the I th RF. The only correlation that exists is between U_I and V_I for each I.

As noted in the previous section, the statistical parameters of the complex Gaussian random variable $\{U_I, V_I\}$ are independent of I .

The magnitude detector forms the absolute value as opposed to the magnitude squared. The performance analysis in [5] uses magnitude squared for the variables U_I, V_I . There is a slight difference in tracking performance when magnitude squared is used as opposed to magnitude-to-the-one power. This difference is sufficiently small, however, that it is neglected. The magnitude squared is used here primarily since it is much more amenable to analysis than absolute values. It is expected that, from a performance viewpoint, the magnitude squared is the better of the two, particularly at small values of signal-to-noise ratio. This is the case in a detection environment, and can be expected to also carry over into the tracking environment.

The absolute value is implemented in the radar in [1, 7, 13] because of less complexity. The difference in tracking performance is sufficiently small that the complexity criterion is the preferred one to use in choosing between the two.

In this development, it is therefore assumed that the postdetection integration forms

$$\sum_{I=1}^M |U_I|^2, \quad \sum_{I=1}^M |V_I|^2$$

where, in this instance, $M=10$, as discussed previously.

Finally, the logarithmic discriminant generator forms

$$z = \hat{\Delta}_{AZ} = \ln \left[\frac{\sum_{I=1}^M |U_I|^2}{\sum_{I=1}^M |V_I|^2} \right] \quad (24)$$

as shown in Figure 1. The computation techniques for generating z are considered in [12], Appendix B.

The random variable z is the maximum likelihood (M.L.) estimate [5] of the logarithm of the ratio of the power in U_I to the power in V_I , i.e.,

$$z = \widehat{\ln [P_U/P_V]}, \quad (25)$$

where $(\hat{})$ means maximum likelihood estimate.

It has been shown in [5] that z is the M.L. estimate of $\ln (P_U/P_V)$ whether or not there exists correlation between U_I and V_I .

In order to see how z forms a measure of antenna angle error, note first that z is an unbiased estimate of $\ln(P_U/P_V)$ [8], namely,

$$z = \ln[P_U/P_V] + x, \quad (26)$$

where [5]:

$$E(x) = 0 \quad (27)$$

and $\sigma_x^2 = \sigma_z^2$ is the variance of the estimate of P_U/P_V . Equivalently stated,

$$E(z) = \ln(P_U/P_V). \quad (28)$$

The RMS error of z , namely σ_x , has been derived and numerically presented in [5], and the performance curves are shown here in Figure 5. The RMS error is dependent only on the number of independent inputs M and the normalized correlation coefficient (ρ) between U_I and V_I , as given in equations (21) through (23). It can be seen that, as the normalized correlation coefficient increases, the RMS error decreases and, in the limit, as $\rho \rightarrow 1$, the RMS error $\rightarrow 0$.

The improvement in performance due to increases in signal-to-noise ratio is related to RMS error through the correlation coefficient. As indicated in (23) and plotted in Figure 6, the normalized correlation coefficient increases as the signal-to-noise ratio increases.

In Figure 7, the results of Figures 5 and 6 are combined. The RMS error of the maximum likelihood estimate is shown as a function of the $\text{SNR} = P_{\text{avg } r} / (N_0 B_F)$ for various values of M . In this system, the pertinent value of M is 10, since there are 5 RFs in the frequency diversity and 2 range gates.

The second step is to obtain the appropriate understanding of $\ln(P_U/P_V)$, which is the quantity being estimated in the maximum likelihood sense by z . Upon substitution of (20) into (28),

$$\ln(P_U/P_V) = \ln \left[\frac{(\Sigma + \Delta)^2 P_{\text{avg } r} + N_0 B_F}{(\Sigma - \Delta)^2 P_{\text{avg } r} + N_0 B_F} \right] = \ln \left[\frac{(1 + \frac{\Delta}{\Sigma})^2 + \frac{N_0 B_F}{\Sigma^2 P_{\text{avg } r}}}{(1 - \frac{\Delta}{\Sigma})^2 + \frac{N_0 B_F}{\Sigma^2 P_{\text{avg } r}}} \right]. \quad (29)$$

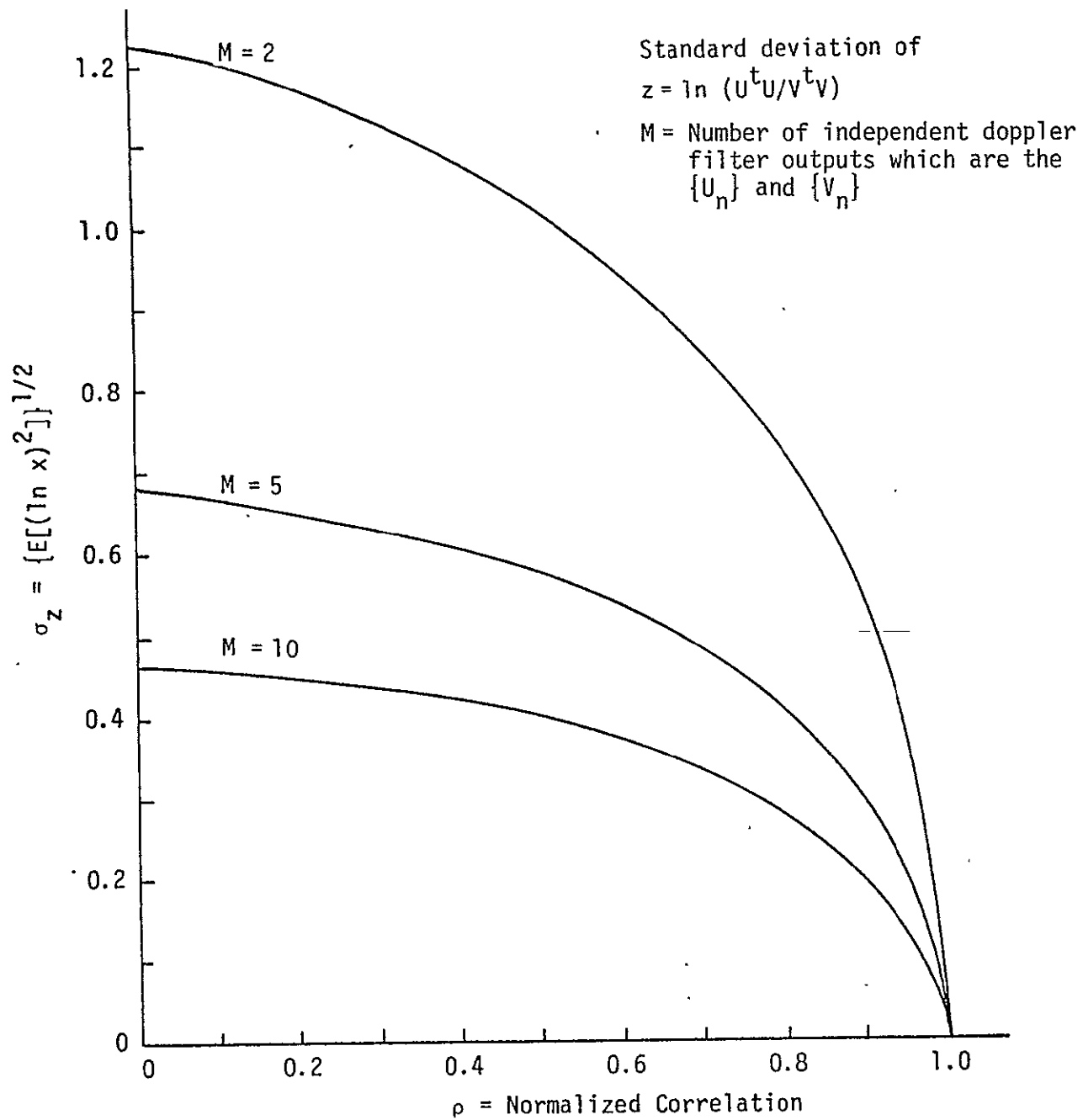


Figure 5. Standard Deviation of the Random Variable z as a Function of Correlation

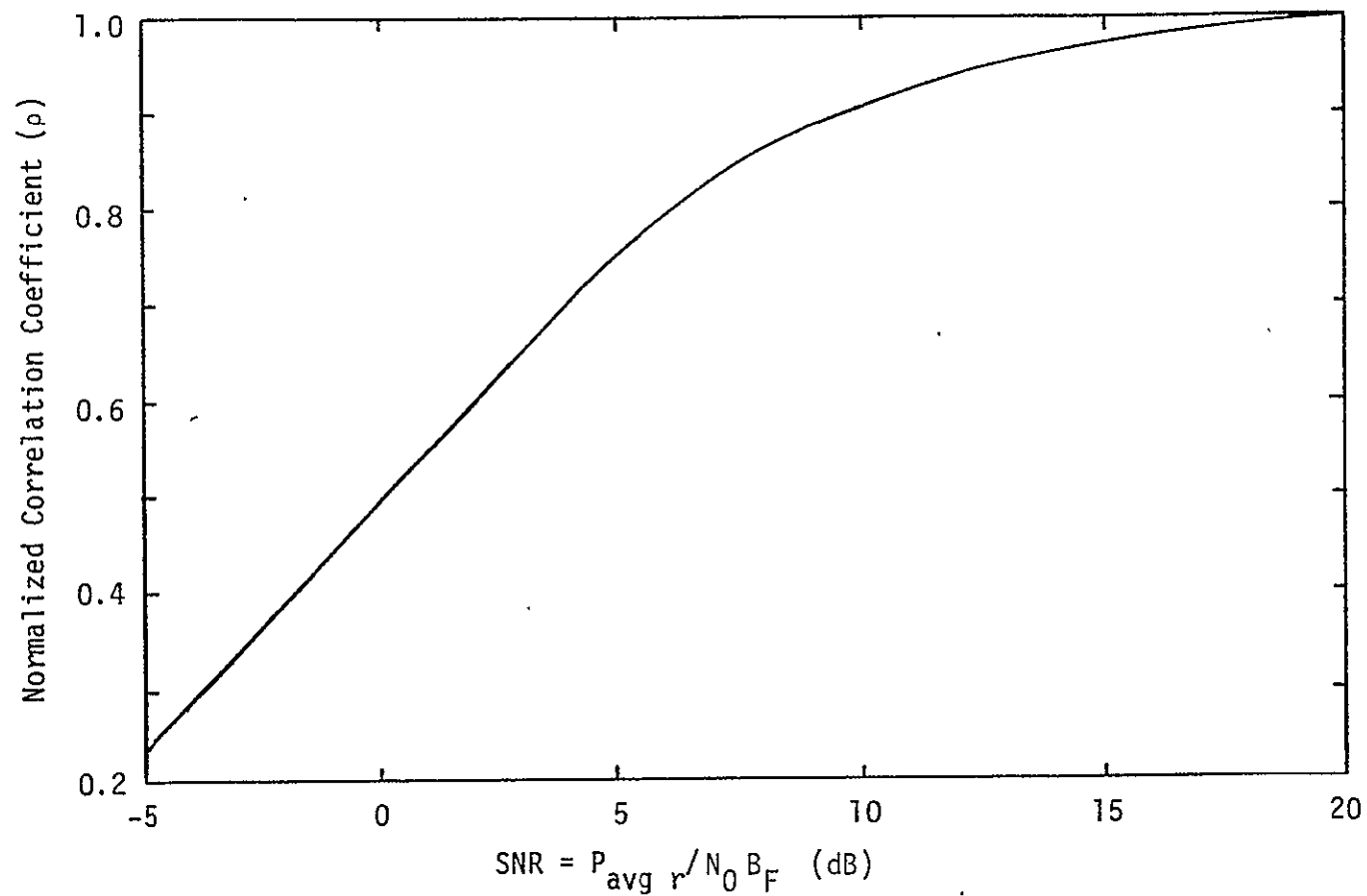


Figure 6. Normalized Correlation Coefficient ρ Versus Signal-to-Noise Ratio $P_{\text{avg}} r/N_0 B_F$, as given by Eq. (23)

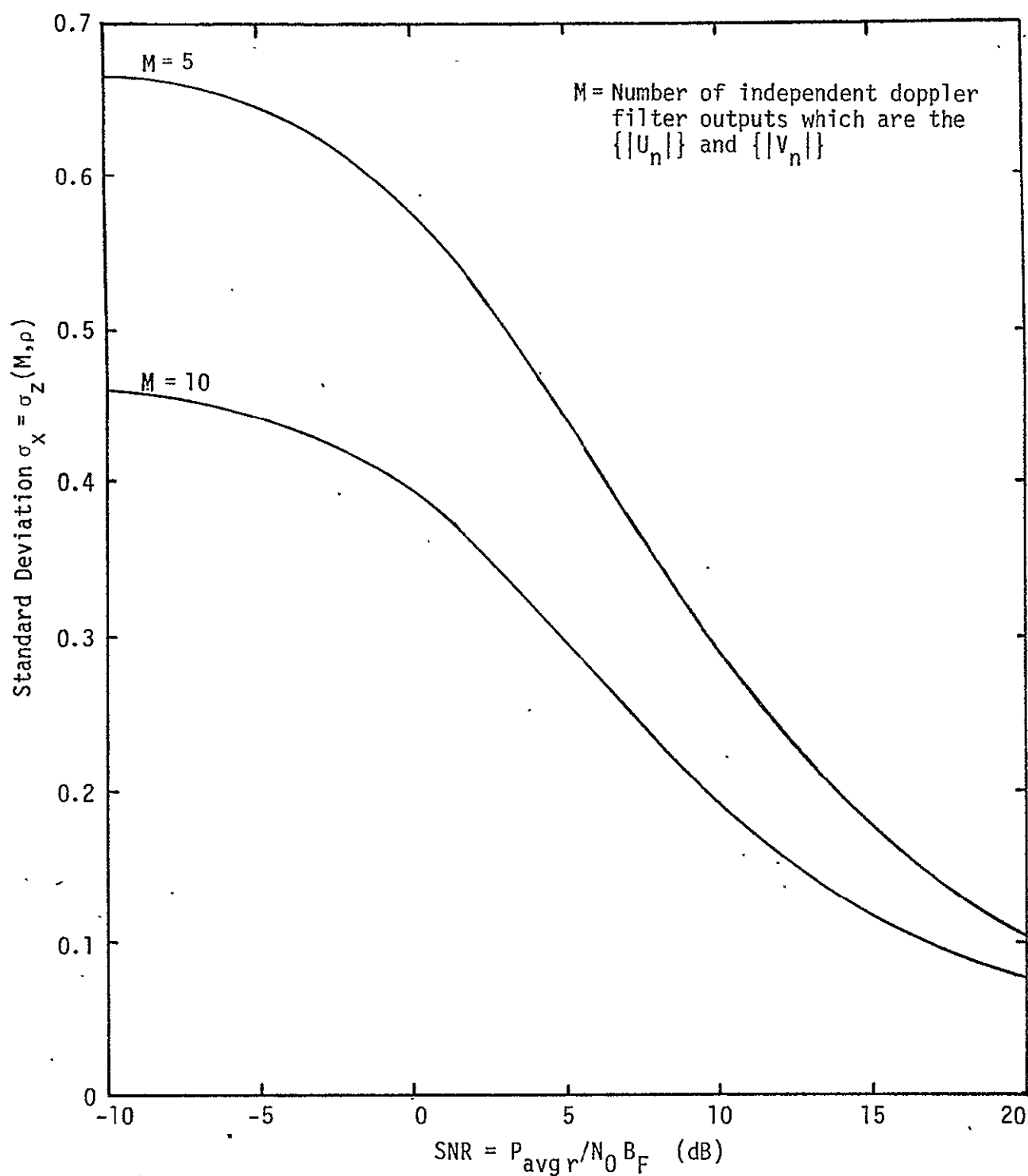


Figure 7. Standard Deviation of the Output of the Logarithm Discriminant Generator Versus Signal-to-Noise Ratio for Certain Values of M

Inspection of (29) indicates that the output of the discriminant generator is a function of the signal-to-noise ratio, as well as the normalized measure of the angle error Δ/Σ .

As indicated in Section 2.0, when the monopulse angle error is small, so that the error voltage is in the linear region, then the desired error voltage is given by

$$\text{Error Voltage} = \frac{E_{\Delta}}{E_S} = \frac{\Delta}{\Sigma} = k_m (\Delta_{\epsilon}/\theta_B) \quad (30a)$$

or, equivalently, the actual angular error is

$$\Delta_{\epsilon} = \theta_B k_m^{-1} \frac{E_{\Delta}}{E_S} = \theta_B k_m^{-1} \left(\frac{\Delta}{\Sigma} \right). \quad (30b)$$

For small values of (Δ/Σ) , corresponding to small values of antenna angular error Δ_{ϵ} , $\ln (P_U/P_V)$ as described in (29) can be expressed as

$$\begin{aligned} \ln (P_U/P_V) &= \ln \left[\frac{1 + \frac{2(\Delta/\Sigma)}{1 + (\text{SNR})^{-1}} + \frac{(\Delta/\Sigma)^2}{1 + (\text{SNR})^{-1}}}{1 - \frac{2(\Delta/\Sigma)}{1 + (\text{SNR})^{-1}} + \frac{(\Delta/\Sigma)^2}{1 + (\text{SNR})^{-1}}} \right] \\ &\approx 4 \left(\frac{\Delta}{\Sigma} \right) \left[\frac{1}{1 + (\text{SNR})^{-1}} \right] = 4\rho \left(\frac{\Delta}{\Sigma} \right), \end{aligned} \quad (31)$$

where

$$\text{SNR} \triangleq \frac{P_{\text{avg}} r}{2 N_0 B_F}, \quad (32)$$

Σ^2 is already normalized to unity, and the approximation $\ln (1+\gamma) \approx \gamma$ for small γ has been employed.

The first moment of the output of the log discriminant generator $\ln (P_U/P_V)$ without the above approximation is shown in Figure 8. It can be observed that, for small values of Δ/Σ , the value of $\ln (P_U/P_V)$ varies almost linearly in Δ/Σ , and that the slope is dependent on SNR. The more drastic variations in $\ln (P_U/P_V)$ occur at larger values of Δ/Σ where the reduction in loop gain is more significant. It is henceforth assumed that the approximation in (31) is satisfactory, and that the

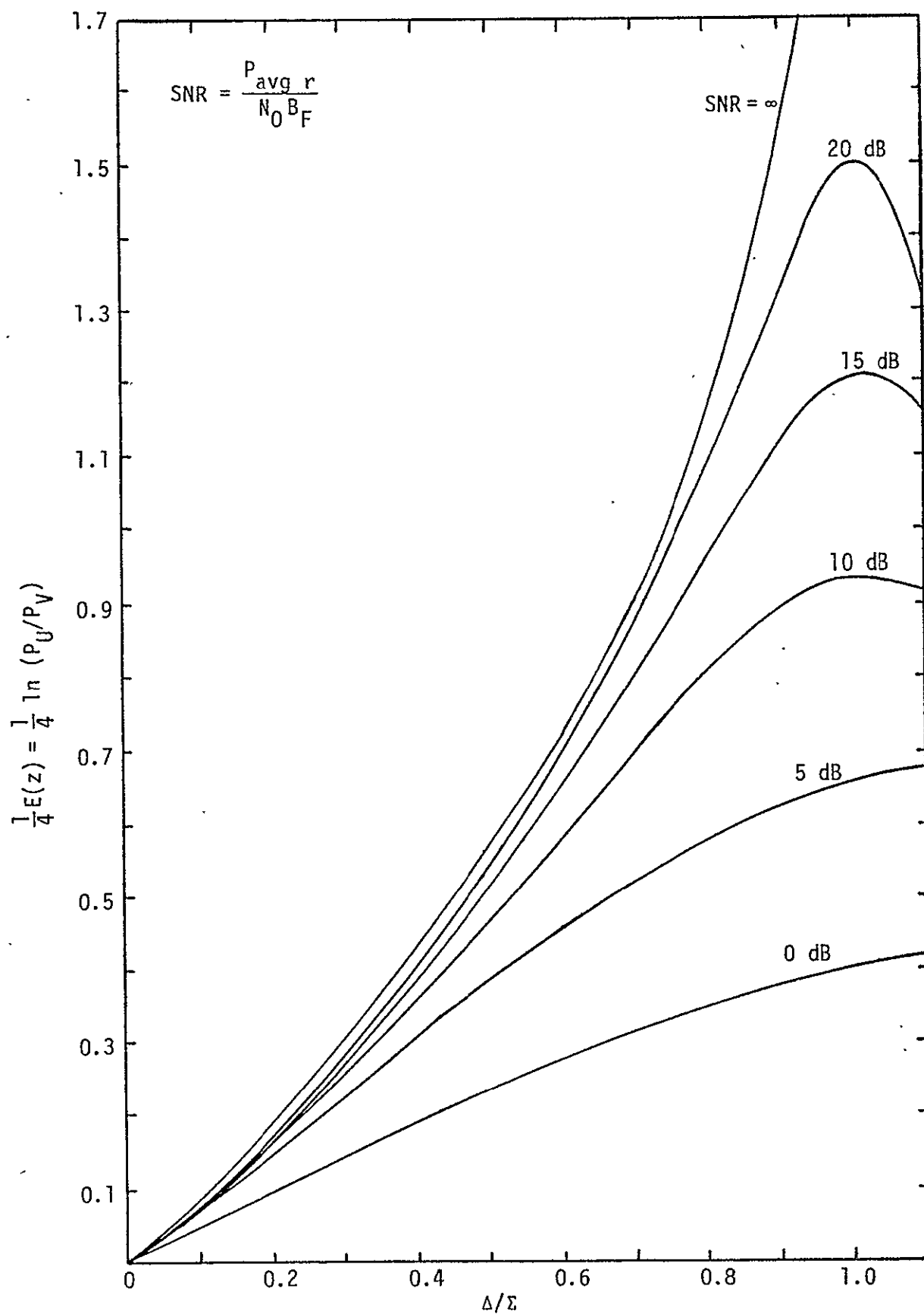


Figure 8. First Moment of Output of Angle Tracking Discriminant Generator as a Function of Normalized Angle Error for Various Signal-to-Noise Ratios

effect of SNR on $\ln (P_U/P_V)$ is through the multiplication of (Δ/Σ) by ρ , thus corresponding to a reduction in loop gain. In an actual implementation, the discriminant output will probably have to be soft-limited in order to offset the increase in loop gain at large values of tracking error.

4.0 PERFORMANCE OF THE AMPLITUDE MONOPULSE ANGLE TRACKING LOOP

The results of the previous sections can now be combined to provide the RMS angle error due to thermal noise and target scintillation when the target is in the linear region of the antenna angle error channels. Only one of the angle errors is considered.

A block diagram of the equivalent model of the antenna tracking loop is shown in Figure 9. The result is a system whose angle tracking performance is identical to that in Figure 1 when the antenna is in the linear region. In Figure 9,

θ_T = relative angle of the target with respect to an arbitrary inertial reference

θ_A = relative angle of the antenna boresight in either the azimuth or elevation direction

$\Delta_e = \theta_T - \theta_A$ = angular error in either the azimuth or elevation directions

k_m/θ_B = scale factor necessary to convert angular error to antenna amplitude monopulse output voltage

4ρ = scale factor in (31) necessary to give $\ln (P_U/P_V)$

x = equivalent noise of the system, taking into account the effects of thermal noise and target scintillation as described in this report and in [5]

$z = \ln (P_U/P_V) + x$ is the output of the log discriminant generator, as given in (26) and diagrammed in Figure 1

K_{eq} = equivalent loop gain of the antenna tracking loop, which takes into account all of the various contributing gains

$F(s)$ = open loop antenna angle control system and inertial stabilization transfer function. A discussion of such transfer functions is given in [6].

In the actual implementation, the output of the open loop filter $f(s)$ is fed back via a mechanical linkage to the antenna servo system to rotate it to a new position, as seen in Figure 1.

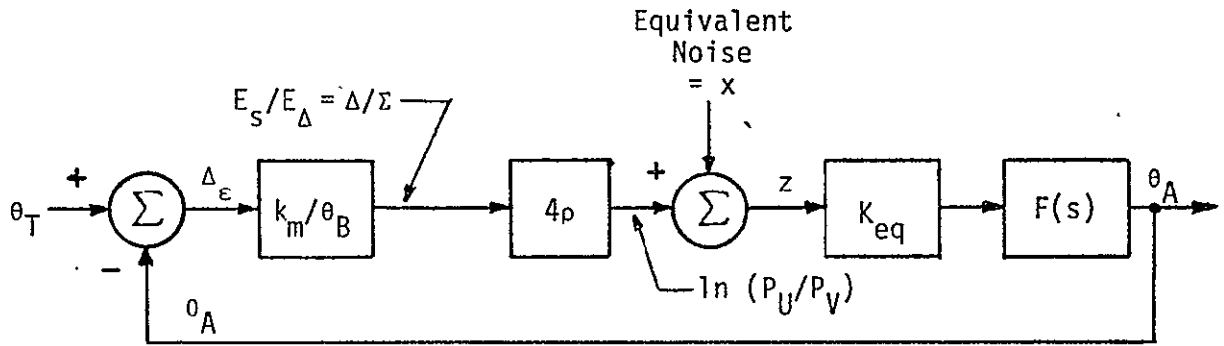


Figure 9. Block Diagram of the Equivalent Model of the Antenna Tracking Loop

Since a transient analysis and a study of the dynamic characteristics of the antenna tracking loop are not a part of this development, the effects of the loop gain and open loop transfer functions are taken into account through the loop noise bandwidth B_N (Hz).

Referring to Figure 9, the closed loop transfer function from θ_T to θ_A is equal to

$$H(j 2\pi f) = \frac{\left(\frac{4\rho k_m}{\theta_B}\right) K_{eq} F(j 2\pi f)}{1 + \left(\frac{4\rho k_m}{\theta_B}\right) K_{eq} F(j 2\pi f)} \quad (33)$$

and the corresponding closed-loop one-sided noise bandwidth is defined as

$$B_N(\rho) \triangleq \int_0^\infty |H(j 2\pi f)|^2 df. \quad (34)$$

The exact structure of the loop filter $F(j\omega)$ in (33) is relatively complex, and accounts for inertial stabilization and Orbiter movement. Block diagrams of the complete angle tracking system are discussed in [6,13]. In an error analysis of this type, the entire open loop transfer function relates to performance primarily through the corresponding closed loop noise bandwidth defined in (34). The coupling of inertial stabilization and tracking errors is expected to be quite small and is therefore neglected in this development.

The dependence of B_N on ρ has been explicitly indicated to emphasize the dependence of noise bandwidth on the signal-to-noise ratio by way of the normalized correlation coefficient ρ . For intermediate and high-gain tracking loops, the dependence of B_N on ρ is approximately given by

$$B_N(\rho) \approx \rho B_N(\rho=1), \quad (35)$$

where $\rho=1$ corresponds to the infinite SNR case. This is the case since, at high values of loop gain, the noise bandwidth varies approximately linearly with the effective loop gain, $4\rho k_m K_{eq}/\theta_B$. This is indeed the case for all loop transfer function that are anticipated for $F(s)$, including first- and second-order tracking loops.

The transfer function from the equivalent noise input x to the angle tracking error Δ_ϵ is given by

$$\Delta_\epsilon = \left(\frac{\theta_B}{4\rho k_m} \right) H(p) x, \quad (36)$$

where p is the Heaviside operator, so that the variance of the angle tracking error is given by

$$\sigma_{\Delta_\epsilon}^2 = \left(\frac{\theta_B}{4\rho k_m} \right)^2 B_N(\rho) T_s \sigma_x^2(N, \rho), \quad (37)$$

where

$\sigma_x^2(N, \rho) = \sigma_x^2$ is the variance of the maximum likelihood estimate of $\ln(P_U/P_V)$, which is also the variance per sample of the noise in the equivalent block diagram of the angle tracking loop. The dependence on the correlation coefficient ρ and the number of RF frequencies N is emphasized in (37).

T_s = time per sample of the random sequence x by the D/A converter and succeeding boxcar detector in Figure 1. In this system,

$$T_s = T_p(N)(4)(N'), \quad (38)$$

$N' = 5$ is the number of RF frequencies. The noise samples (x) are assumed to be statistically independent from frequency to frequency

$N = 16$ is the number of pulses during which $\Sigma + \Delta_J$ is observed (see Figure 2), $J = 1, \dots, 4$

4 = factor corresponding to the number of different angular error measurements (time slots) per frequency dwell time, namely, $\Sigma + \Delta_{AZ}$, $\Sigma - \Delta_{AZ}$, $\Sigma + \Delta_{EL}$, $\Sigma - \Delta_{EL}$

T_p = pulse repetition interval = 335 μ sec, when
PRF = 2987 Hz.

Upon substitution of these values into (38),

$$T_s = 320 T_p = 107.2 \text{ msec.} \quad (39)$$

Upon substitution, the RMS angle tracking error is then given by

$$\sigma_{\Delta_\epsilon} \Big|_{\text{deg}} = \frac{\theta_B}{4 \sqrt{\rho} k_m} \left[B_N(\rho=1) T_s \right]^{1/2} \sigma_x(N, \rho) \quad (40)$$

or, equivalently,

$$\sigma_{\Delta_\epsilon} \Big|_{\text{deg}} = \frac{\theta_B}{4 k_m} \left\{ 1 + \left(\frac{P_{\text{avg}} r}{N_0 B_F} \right)^{-1} \right\}^{1/2} \left[B_N(\rho=1) T_s \right]^{1/2} \sigma_x \left(M, \rho \left(\frac{P_{\text{avg}} r}{N_0 B_F} \right) \right) \quad (41)$$

where $\theta_B = 3$ dB antenna beamwidth in degrees. This result accurately predicts the expected performance of the angle tracking loop in Figure 1. Performance computations are carried out in the next section.

5.0 PERFORMANCE COMPUTATIONS

For the Ku-Band Integrated Radar and Communication Equipment for the Space Shuttle Orbiter Vehicle Proposal [1], the radar parameters needed to compute the RMS angle error in (41) are given as

$$\begin{aligned} M &= 10 \\ \theta_B &= 1.6^\circ \\ k_m &= 1 \text{ ([1], p. 3-47)} \\ B_N &= 1 \text{ Hz ([1], p. 3-47); } B_N = 0.4 \text{ Hz ([10-11])} \\ T_s &= 107.2 \text{ msec [(39)]} \end{aligned}$$

For these values of the system parameters, the performance of the angle tracking loop is shown in Figure 10. The RMS angle tracking error is plotted against the signal-to-noise ratio $P_{\text{avg}} r / (N_0 B_F)$, which is the maximum SNR at the output of the doppler filters, assuming no range gate straddling loss (see Figure 1).

The specification value for the Ku-band radar system is shown in Table 2 as

$$\sigma_{\text{SPEC}} = 0.153 \text{ deg.} \quad (42)$$

This is shown as the dashed line in Figure 10. It is seen that the specification value is met for

$$\frac{P_{\text{avg r}}}{N_0 B_F} > -3.5 \text{ dB}, \quad (43a)$$

when $B_N(\rho = 1) = 1 \text{ Hz}$, and for

$$\frac{P_{\text{avg r}}}{N_0 B_F} > -8 \text{ dB}, \quad (43b)$$

when $B_N(\rho = 1) = 0.4 \text{ Hz}$.

Table 2. Specification Radar Parameter Allowable Measurement Errors

	Random 3σ	Bias 3σ
Angle Rate Error Including Target Effects		
LOS	0.8 mrad	$\pm 2^\circ$
Pitch	0.458 deg	
LOS	0.8 mrad	$\pm 2^\circ$
Azimuth	0.458 deg	
Angle Rate Error Including Target Effects		
LOS	0.14 mrad/sec	$\pm 0.14 \text{ mrad/sec}$
Pitch	0.008 deg/sec	
LOS	0.14 mrad/sec	$\pm 0.14 \text{ mrad/sec}$
Azimuth	0.008 deg/sec	

In order to obtain angle track performance as a function of range, the following radar equation is used to determine $P_{\text{avg r}}/(N_0 B_F)$:

$$\frac{P_{\text{avg r}}}{N_0 B_F} = \frac{[G^2 \sigma \lambda^2][d_t P_p \tau_E]}{(4\pi)^3 L [k T_{\text{sys}}] R^4}, \quad (44)$$

where all of the parameters are defined in Appendix A of [12]. The values used in the computation correspond to those in Table 3, Budget 2,

of Appendix A of [12] or as updated by [9-13], namely,

G = peak antenna gain	=	38.5 dB	
$\bar{\sigma}$ = radar cross-section	=	1 m^2	
λ = wavelength	=	0.0216 m (13.883 GHz)	
d_t = duty factor	=	$\begin{cases} 0.099 & (R > 9.5 \text{ nmi}) \\ 0.116 & (3.8 < R < 9.5) \end{cases}$	
P_p = peak transmitted power	=	60 watts (17.8 dBw)	
τ_E = dwell time corresponding to one computation of the DFT = B_F^{-1}	=	$\begin{cases} 5.36 \text{ msec} & (R > 9.5 \text{ nmi}) \\ 2.29 \text{ msec} & (3.8 < R < 9.5) \end{cases}$	
k = Boltzmann's constant	=	$1.38 \times 10^{-23} \text{ w/Hz-K}$	
T_{sys} = system noise temperature	=	1500°K	
R = range, in meters			
L = losses, itemized as follows for angle track (see [12], Appendix A, for more details):			
Transmit	3.7 dB	(Ref. [13])	
Scan alignment	0		
Lateral scan	0		
Threshold (CFAR)	1.7	(Ref. [13])	
Processor loss	1.0	(Ref. [1])	
Range gate straddling	6.0	Section 3.1	
Doppler mismatch	0.91	Section 3.3	
PDI	1.25	(Ref. [1])	
Pre-sum	$\begin{cases} 0.14 \text{ dB} & (R > 9.5 \text{ nmi}) \\ 0.07 \text{ dB} & (3.8 < R < 9.5) \end{cases}$		Eq. (14a) Eq. (14a)
Signal loss due to coupling	3.0	Section 7.0	
Noise increase due to combining of Σ and Δ channels	-1.2	Section 7.0	
A/D conversion	0.4	Appendix H	
Total losses	$\begin{cases} 16.90 \text{ dB} & (R > 9.5) \\ 16.83 \text{ dB} & (3.8 < R < 9.5) \end{cases}$		

The A/D conversion of 0.4 dB is based on a signal-to-noise ratio of 0.9 dB at the input to the A/D converter. The loss in A/D conversion is analyzed in Appendix H of this report. The SNR at the input to the A/D converter is based on a range of 9.5 nmi, a PRF of 2987, and an LPF of 237 kHz preceding the A/D converter, as shown in Figure 1. The remaining parameters are as in the enclosed power budget.

With these parameters, the RMS angle tracking error is shown in Figure 11 versus range in nautical miles. For all ranges below 20 nmi, the RMS angle error is below the specification value for $B_N = 1 \text{ Hz}$, where

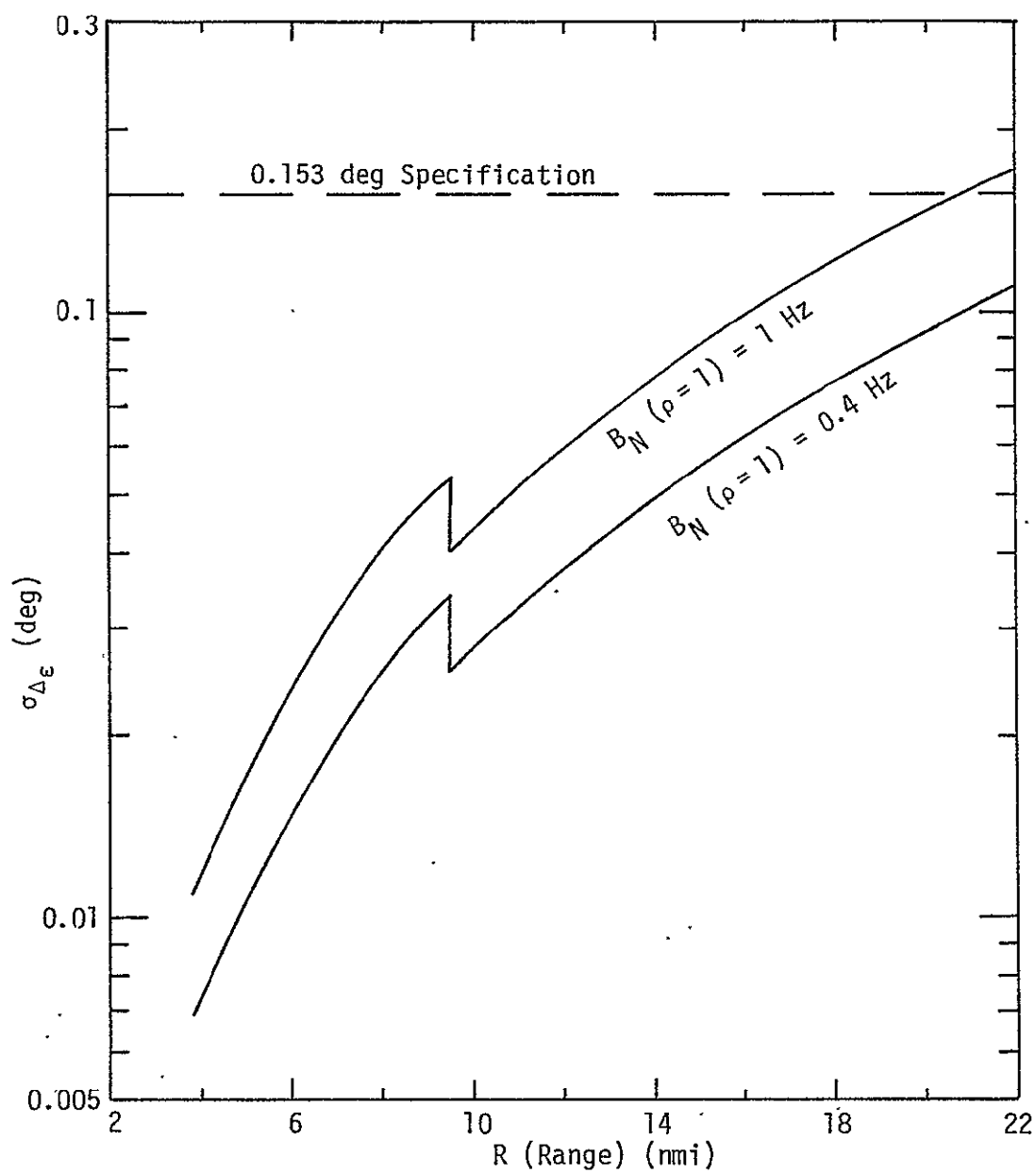


Figure 11. RMS Angle Tracking Error of Passive Radar vs. Range (nmi)

the effects of both thermal noise and target scintillation have been taken into account. The improvement in performance when $B_N = 0.4$ Hz is also observable. The discontinuity at 9.5 nmi is due to the changes in system parameters that have been given above. The performance curves do not take into account any degradation in the angle tracking loops due to errors in the range tracking loop. Errors in the doppler estimation technique have been taken into account, however. With the SNR design margin for angle tracking of passive targets at approximately 9.5 dB at 12 nmi, there is room to allow degradations for these errors.

In summary, the angle tracking specification for passive targets is met with ample design margin (≈ 9.5 dB) by the Ku-band system.

The other angle tracking specification is the estimation of angular rate. Note that the angular rate specification does not require that target effects be taken into account. Therefore, a nonfluctuating target can be assumed, thereby greatly increasing the average signal-to-noise ratio. The performance of angular rate estimation is not taken into account in this report.

6.0 COMMENTS CONCERNING THE FILTER RESPONSE OF THE DISCRETE FOURIER TRANSFORM

In this section, certain additional comments are made concerning the response of a DFT to a coherent pulse train. The particular waveform under discussion is shown in Figure 12. It is a complex baseband signal which is assumed to be ideally range gated as shown. It corresponds to the signal $I + jQ$ in Figure 1. The signal is sampled and pre-summed to form the complex numbers s_1, \dots, s_N , where $N = 16$. These are the inputs to the DFT.

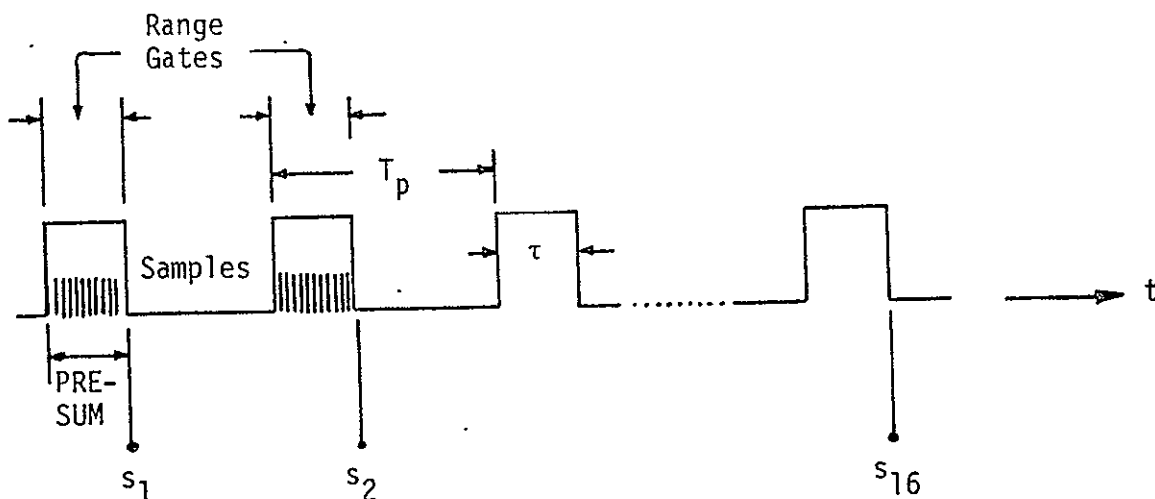


Figure 12. Coherent Pulse Train with Pre-Sum

The time of pre-sum is equal to the pulse width, which is equal to the width of the range gate. During the remainder of the time, the signal does not exist, although implicitly it does, since coherence is maintained from pulse to pulse.

In the frequency domain, the picture is as shown in Figure 13. In the upper part of the figure is the spectrum of the coherent pulse train. The bandwidth to the first crossover is $1/\tau$. The "needles" of the spectrum are spaced by the PRF. The one-sided width of each "needle" is $(NT_p)^{-1}$, where N is the number of pulses observed.

The number of "needles" within the bandwidth $1/\tau$ is d_t^{-1} , where $d_t = \tau/T_p$ is the duty factor. The shift of the entire spectrum due to a doppler frequency shift is also indicated.

In the lower part of Figure 13 is the location of each of the filters in the DFT filter bank. In this instance, the fact that digital filters have periodic frequency domain responses is an advantage and all "needles" in the signal spectrum will fall within one of the filters.

The bandwidth of each filter is $(NT_p)^{-1}$. If the pulse width remains constant and T_p varies, then

- (a) The bandwidth of the signal, $1/\tau$, remains unchanged.
- (b) The bandwidth of each needle varies.
- (c) The bandwidth of each filter varies exactly as that of the needle in the signal spectrum.

Since the filter bandwidth is matched to the bandwidth of each needle in the signal spectrum, the output signal-to-noise ratio at the end of the observation period is approximately optimized. This is what is done, since the samples are made at the end of the observation interval.

Whether in a search or track mode, a coherent radar can extract the maximum energy from the signal by use of the optimal receiver shown in Figure 14. To be truly optimal, all of the necessary ideal assumptions have been made, namely, doppler is assumed known, the range to the target is assumed known, and ideal coherence is maintained. The digital signal processor, which is a slightly suboptimal implementation of the above, is shown in Figure 15. The only difference is the reversal of order of the integrator over the range gate, and the mixing by the

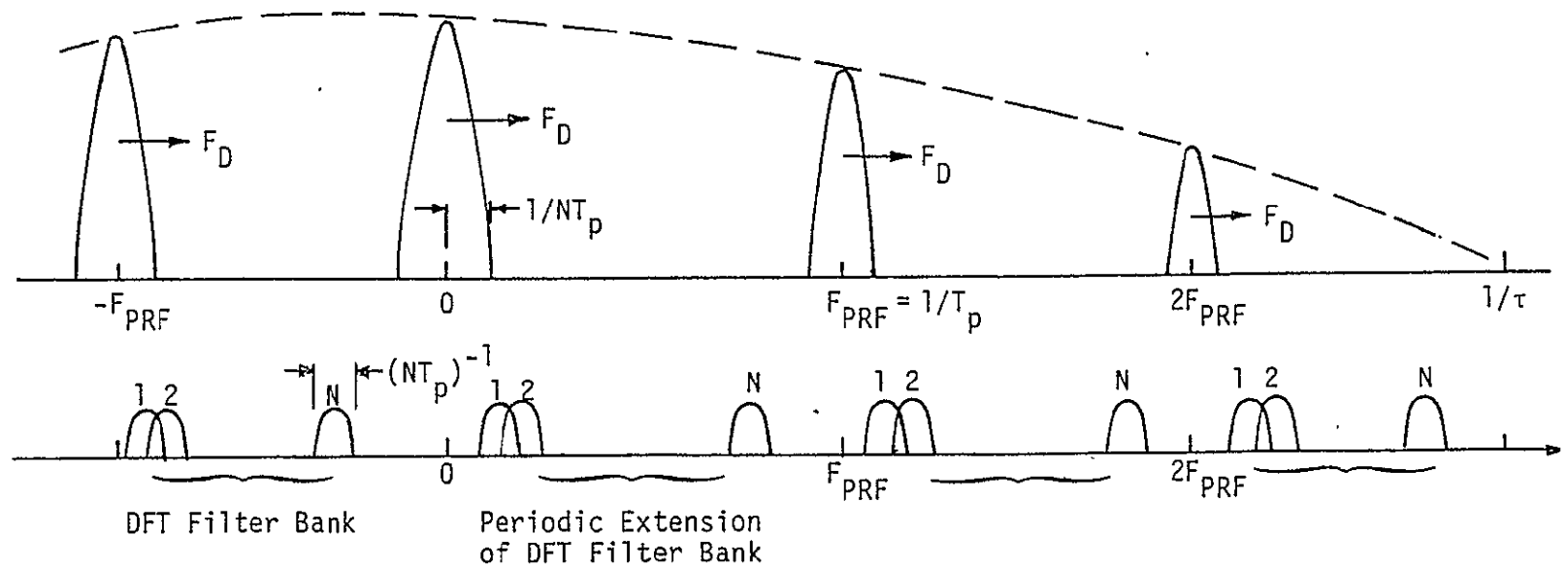


Figure 13. Spectrum of Transmitted Pulse Train and the Bank of Filters Formed by the DFT

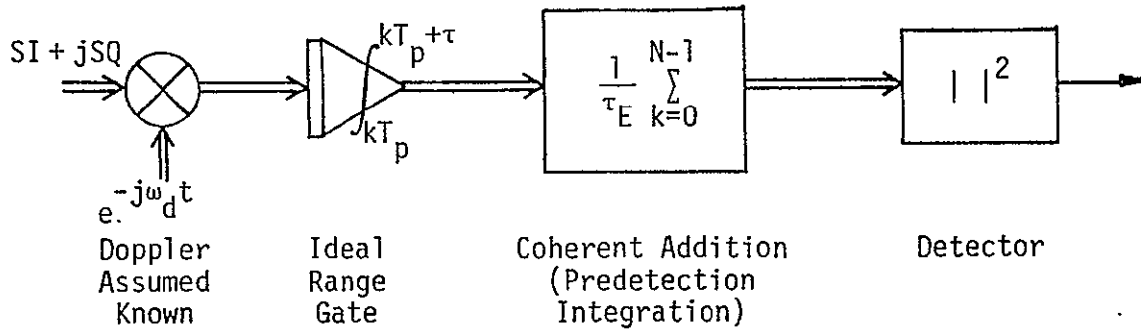


Figure 14. Block Diagram of Optional Coherent Radar Receiver

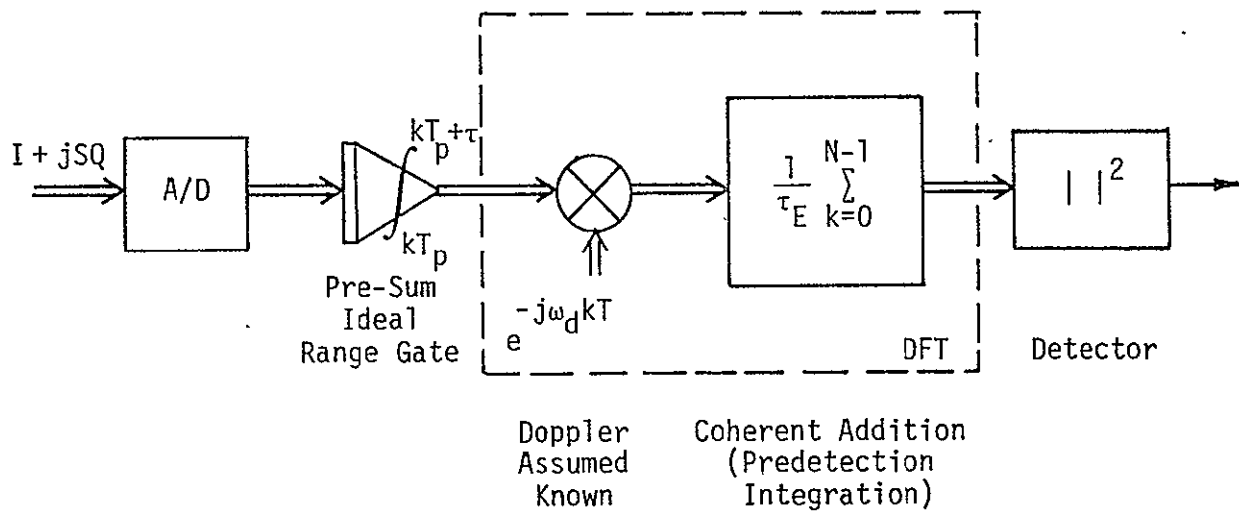


Figure 15. Digital Signal Processor Implementation of the Coherent Radar Receiver

doppler frequency. In most coherent radars, the resulting loss is negligible (in the hundredths of a dB).

In order to see precisely the difference between the optimal coherent radar receiver in Figure 14 and the digital signal processor implementation in Figure 15, they are considered individually in more detail. The input signal for the k th pulse is $SI + jSQ$, as given in (9).

6.1 Optimal Coherent Radar Receiver

When the doppler is not known exactly, the receiver in Figure 12 multiplies the input by $\exp[-j(\omega_d + \Delta\omega_d)t]$, where ω_d is the exact doppler and $\Delta\omega_d$ is the doppler error. After this multiplication and the integration over $[kT_p, kT_p + \tau]$, where an ideal range gate is assumed, the result is

$$\begin{aligned} \text{PSI}(I, J, K) + j\text{PSQ}(I, J, K) &= \int_{kT_p}^{kT_p + \tau} [SI(t) + jSQ(t)] \exp[-j(\omega_d + \Delta\omega_d)t] dt \\ &= (\Sigma + \Delta_J) A_I \tau \exp[j(\theta_I - \Delta\omega_d(kT_p + \tau/2))] \frac{\sin(\Delta\omega_d \tau/2)}{(\Delta\omega_d \tau/2)} \\ &\quad + \int_{kT_p}^{kT_p + \tau} [N_c(t) + jN_s(t)] dt. \end{aligned} \quad (45)$$

In the I and Q channels, the integrated noise processes in (47) have power $N_0\tau/2$ watts.

As shown in Figure 14 for the optimal coherent radar receiver, $N=16$ pulses are coherently added, after which the detector forms the magnitude squared of the resulting complex number.

After coherent integration

$$\begin{aligned} \frac{1}{\tau_E} \sum_{K=0}^{N-1} \{\text{PSI}(I, J, K) + j\text{PSI}(I, J, K)\} &= (\Sigma + \Delta_J) A_I d_t \left[\frac{\sin(\omega_d \tau/2)}{(\omega_d \tau/2)} \right] \left[\frac{\sin(\Delta\omega_d N T_p/2)}{N \sin(\Delta\omega_d T_p/2)} \right] \\ &\quad \cdot \exp\{j[\theta_I - \Delta\omega_d \tau/2 - \Delta\omega_d(N + \frac{1}{2}) T_p/2]\} \\ &\quad + N_{cIJ} + jN_{sIJ}, \end{aligned} \quad (46)$$

where $\tau_E = NT_p$ is the slot time and

$$N_{cIJ} + jN_{sIJ} = \frac{1}{\tau_E} \sum_{k=0}^{N-1} \int_{kT_p}^{kT_p + \tau} [N_c(t) + jN_s(t)] dt. \quad (47)$$

N_{cIJ} and N_{sIJ} are independent zero mean Gaussian random variables, each with variance

$$\sigma^2 = \frac{N_0 \tau N}{2 \tau_E^2} = \frac{N_0 d_t}{2 N T_p} = \frac{N_0 d_t B_F}{2}, \quad (48)$$

where $B_F = \tau_E^{-1}$ is the equivalent bandwidth of the optimal receiver operation.

As verification of these results, consider the signal-to-noise ratio in the absence of doppler error. Using (48),

$$\text{SNR} = \frac{(A_I d_t)^2}{2 \sigma^2} = \frac{P_{pr} d_t \tau_E}{N_0} = \frac{\mathcal{E}_r}{N_0}, \quad (49)$$

where \mathcal{E}_r is the total received signal energy in τ_E seconds. This is the maximum attainable SNR from a matched filter and is therefore an additional verification of the optimality of the receiver in Figure 14 under ideal conditions. The signal power with a doppler mismatch is

$$\text{Signal Power} = P_{pr} d_t^2 \left[\frac{\sin(\Delta\omega_d \tau/2)}{(\Delta\omega_d \tau/2)} \right]^2 \left[\frac{\sin(\Delta\omega_d N T_p/2)}{N \sin(\Delta\omega_d T_p/2)} \right]^2. \quad (50)$$

The first bracketed factor represents the loss due to doppler mismatch over the pulse integration period. The second bracketed factor represents the loss due to doppler mismatch over the predetection summation of N pulses. When $\Delta\omega_d \rightarrow 0$, both bracketed factors go to 1.

These results are now compared to those for the digital signal processor implementation of the coherent radar receiver.

6.2 Digital Signal Processor Implementation of the Coherent Radar Receiver

Referring now to Figure 15, an ideal range gate is again assumed, so that the pre-sum over the pulse width is given by [also shown in (10)]:

$$\begin{aligned}
\text{PSI}(I,J,K) + j\text{PSQ}(I,J,K) &= \int_{kT_p}^{kT_p+\tau} [\text{SI}(t) + j\text{SQ}(t)] dt \\
&= (\Sigma + \Delta_J) A_I \tau \left[\frac{\sin(\omega_d \tau/2)}{(\omega_d \tau/2)} \right] \exp \{j[\theta_I + \omega_d(kT_p + \tau/2)]\} \\
&\quad + \int_{kT_p}^{kT_p+\tau} [N_c(t) + jN_s(t)] dt, \tag{51}
\end{aligned}$$

where the sum of the samples is approximated by analog integration. The bracketed factor in the signal term in (51) is the pre-sum integration loss, and is discussed in Appendix A of [12]. The DFT operation, accounting for a doppler mismatch of $\Delta\omega_d$, can be described as

$$\begin{aligned}
\frac{1}{\tau_E} \sum_{k=0}^{N-1} [\text{PSI}(I,J,K) + j\text{PSQ}(I,J,K)] \exp [-j(\omega_d + \Delta\omega_d)kT_p] \\
= (\Sigma + \Delta_J) A_I d_t \left[\frac{\sin(\omega_d \tau/2)}{(\omega_d \tau/2)} \right] \left[\frac{\sin(\Delta\omega_d T_p N/2)}{N \sin(\Delta\omega_d T_p/2)} \right] \\
\exp \{j[\theta_I + \omega_d \tau/2 - \Delta\omega_d T_p(N-1)/2]\} + N_{cJ} + jN_{sJ}, \tag{52}
\end{aligned}$$

where the statistics of N_{cJ} and N_{sJ} have been given in Section 6.1. The detector removes the phase dependence. It is also noted that the effect of the summation with doppler mismatch in the DFT corresponds to the effect of doppler mismatch in the coherent integration sum of the optimal receiver. When the doppler mismatch is zero, the only difference in the two receivers is the effect due to pre-sum integration loss, since the SNR in the digital signal processor implementation is

$$\text{SNR} = \frac{(A_I d_t)^2}{2\sigma^2} \left[\frac{\sin(\omega_d \tau/2)}{(\omega_d \tau/2)} \right]^2 = \frac{\mathcal{E}_r}{N_0} \left[\frac{\sin(\omega_d \tau/2)}{(\omega_d \tau/2)} \right]^2. \tag{53}$$

The pre-sum loss is taken into account in the power budget. Other than that, the digital signal processor implementation can be considered optimal for angle tracking analysis, so long as ideal range and doppler tracking are assumed.

In this radar, it is shown (in [12], Appendix A) that the loss due to pre-sum is approximately 0.6 dB. The purpose for making the change is that the doppler mixing and predetection integration are then most conveniently carried out by the DFT. The digital implementation is thus essentially the same as the optimal implementation. The time domain representation and the frequency domain representation have the same appearance for both implementations.

7.0 ANGLE TRACKING COUPLING LOSSES

In the power budget of Section 5.0, two coupling losses are noted; these are determined as follows: In Figure 16, the power divide and power combiner for the sum and angle error channels are shown. In the power divide, the signal and noise powers decrease by the coupling factor $A = -3$ dB. The overall power in the $\Sigma + \Delta$ or $\Sigma - \Delta$ combined signal is therefore reduced by 3 dB, since the signal power in the angle error channel is very small. This is the signal loss due to coupling.

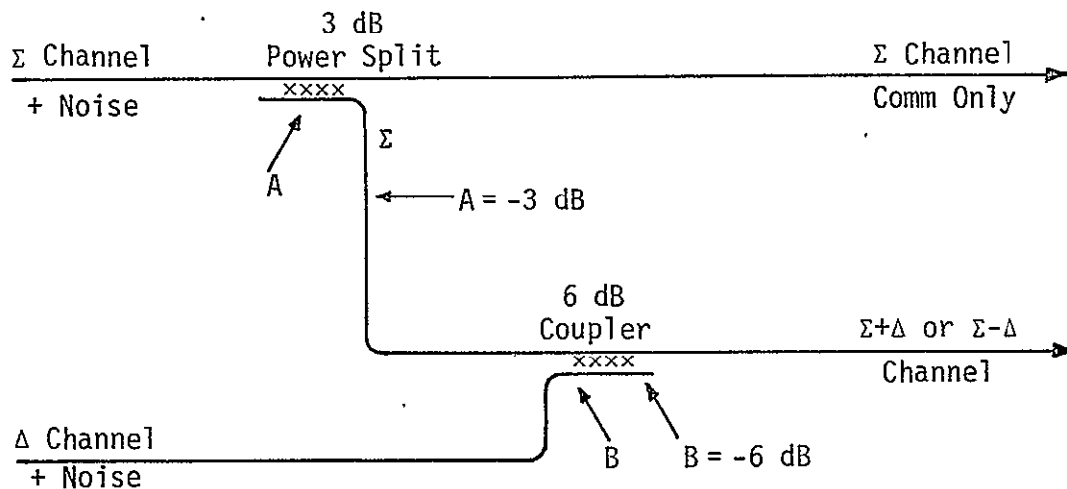


Figure 16. Block Diagram of Coupling Losses

For the noise, the thermal noise spectral density levels in the sum and angle error channels are the same. These two noises are also statistically independent and their spectral density levels can therefore be added. The overall noise level is therefore

$$N_{0|\Sigma+\Delta} = A N_{0|\Sigma} + B N_{0|\Delta} = 0.75 N_0, \quad A = \frac{1}{2}, B = \frac{1}{4} \quad (54)$$

which is an increase in noise spectral density of 0.75 or -1.2 dB.

This is the noise increase due to the thermal noise in the difference channel being combined with that in the sum channel.

In summary, the effect of the power splitter and combiner is:

Net Signal Loss = 3 dB

Net Noise Loss = -1.2 dB

Net Signal-to-
Noise Ratio Loss = 1.8 dB.

REFERENCES

1. Hughes Aircraft Co., "Proposal for Ku-Band Integrated Radar and Communication Equipment for the Space Shuttle Orbiter Vehicle," Volume II, May 1976.
2. D. K. Barton. Radar System Analysis. New York: Prentice-Hall, 1964.
3. P. W. Hannan, "Optimum Feed for All Three Modes of a Monopulse Antenna," IRE Trans. Ant. Prop., Vol. AP-9, No. 5, September 1961, pp. 441-461.
4. S. F. George and A.S. Zannamaker, "Multiple Target Resolution of Monopulse Versus Scanning Radars," Proc. NEC, No. 15, 1959, pp. 814-823.
5. C. L. Weber, "Maximum Likelihood Estimation of the Ratio of Powers in Two Narrowband Processes," Axiomatix Report No. R7701-3, January 31, 1977. Also see Hughes Aircraft Co., "Space Shuttle Ku-Band Integrated Rendezvous Radar/Communications System Study Final Report," No. D4148 SCG 60041R, March 1976, Appendix C.
6. C. L. Weber, "The Orbiter Monopulse Antenna Angular Control System," Axiomatix Report No. R7607-4, July 1976.
7. Hughes Aircraft Co., "Ku-Band Integrated Radar and Communication Equipment for the Space Shuttle Orbiter Vehicle," Monthly Progress Meeting, April 20, 1977.
8. N. E. Nahi. Estimation Theory and Applications. R. E. Kreiger, 1976.
9. Hughes Aircraft Co., "Ku-Band Integrated Radar and Communication Equipment for the Space Shuttle Orbiter Vehicle," Schematic Review, July 19, 1977.
10. D. T. LaFlame, "Ku-Band Forward Link Angle Tracking Loop Performance," Hughes Aircraft Co. IDC, HS237-681, May 17, 1977.
11. D. T. LaFlame, "Angle Tracking Analysis Update," Hughes Aircraft Co. IDC, HS237-885, July 13, 1977.
12. C. L. Weber, S. Udalov, and W. Alem, "Study to Investigate and Evaluate Means of Optimizing the Ku-Band Combined Radar/Communication Functions for the Space Shuttle," Axiomatix Report No. R7705-1, May 31, 1977.
13. Hughes Aircraft Co., "Ku-Band Integrated Radar and Communication Equipment for the Space Shuttle Orbiter Vehicle - EA-2 Design Review," August 15-18, 1977.

APPENDIX D
THE ESTIMATION OF ANGLE RATE
•

APPENDIX D

THE ESTIMATION OF ANGLE RATE

by

Charles L. Weber

Waddah K. Alem

In the digital pulse doppler radar developed in this report, a measure of angle rate is obtained directly from the transfer function used in the angle tracking loop. Angle rate measurement is an estimation process which results from angle tracking; that is, it is estimated only, as opposed to being tracked. Extensive use is made of the development of angle tracking in Appendix C of this report.

A common loop filter transfer function for angle tracking is a lead filter with a perfect integrator, given by

$$F(s) = \frac{1 + \tau s}{s^2} \quad (1)$$

The second integrator represents the operation of the antenna servomotor.

This is a very simplified version of the entire transfer function in the angle tracking loop. When evaluating the estimation capability of angle rate, however, the effects of the motor dynamics, the gyro rate loop, the gimbal pointing loop, and the motor driver can be neglected. The primary components of the transfer function have been maintained and the result is the filter in (1).

For convenience, the block diagram of the equivalent model of the antenna tracking loop is shown in Figure 1. This is a reproduction of Figure 9 of Appendix C, where the equivalent noise x has been scaled and moved as shown. This does not alter performance.

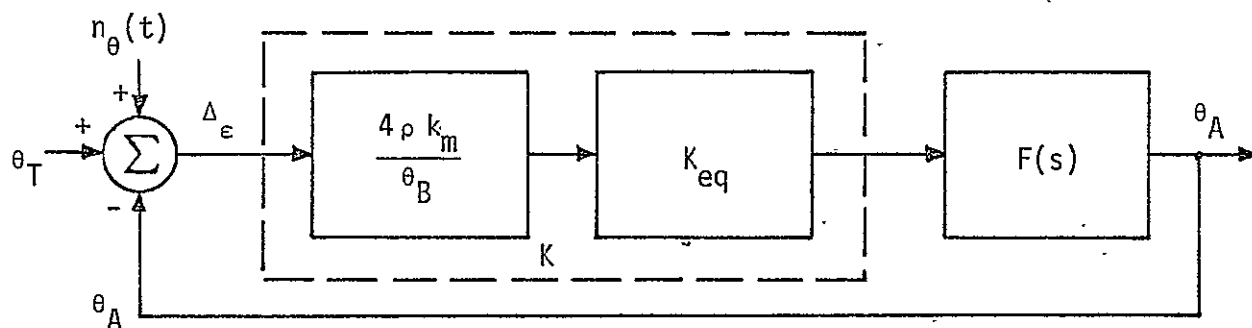


Figure 1.. Block Diagram of the Equivalent Model of the
Antenna Tracking Loop

The equivalent noise $n_\theta(t)$ is related to x by

$$n_\theta = \frac{\theta_B}{4\rho k_m} x. \quad (2)$$

The remaining parameters in Figure 1 are described in Appendix C.

A block diagram of the implementation [1] of the transfer function in (1) is shown in Figure 2, where it can be seen where the angle rate estimation is obtained.

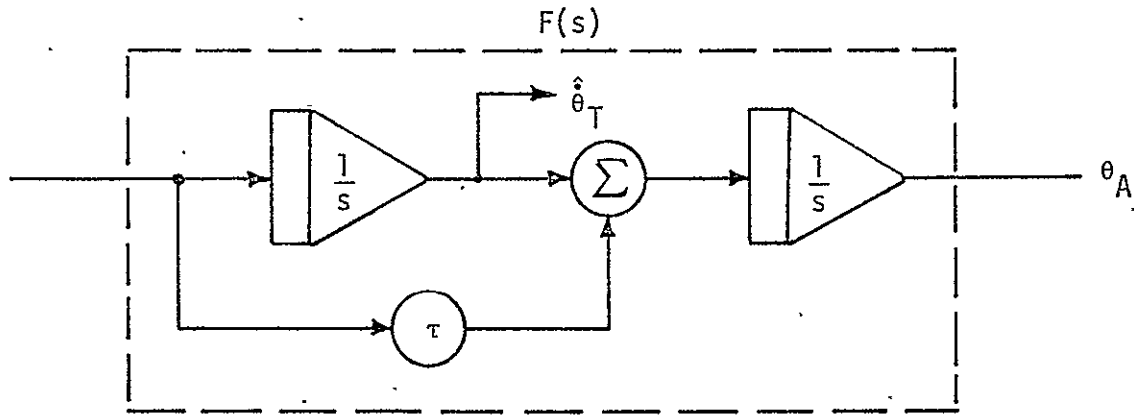


Figure 2. Implementation of Angle Tracking Loop Filter

In this analysis, we are concerned with the convergence time and the RMS error of the angle rate estimator $\hat{\theta}_T$. When the implementation of the angle tracking loop filter in Figure 2 is inserted into Figure 1, the resulting system description is shown in Figure 3. The system is approximately linear. If K is assumed to be constant, and the statistics of the equivalent noise n_θ are assumed to be independent of signal-to-noise ratio (SNR), then the system is linear.

The analysis developed herein assumes a quasi-linear system. By this we mean that the loop gain K and the statistics of n_θ vary with SNR (via ρ) sufficiently slowly that performance can be determined by a linear assumption on the system dynamics. This is an excellent simplifying assumption.

When this is the case, the primary loop parameters are the loop gain,

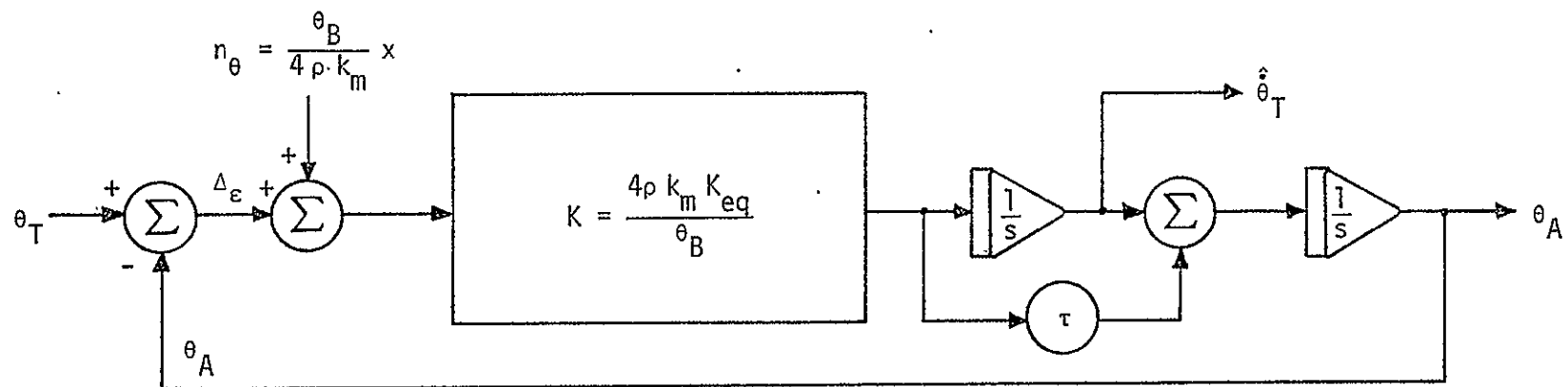


Figure 3. Block Diagram of Equivalent Model of Angle Tracking Loop Showing Angle Rate Estimator

$$K = \frac{4p k_m K_{eq}}{\theta_B} \quad (3)$$

and the time constant τ . The closed loop transfer function from the equivalent noise n_θ in Figure 3 to the angle rate estimate $\hat{\theta}_T$ is given by

$$H_1(s) = \frac{K s}{s^2 + k(\tau s + 1)} \quad (4)$$

The one-sided noise bandwidth B_{N1} corresponding to this filtering operation between n_θ and $\hat{\theta}_T$ is [2]:

$$\begin{aligned} B_{N1} &\triangleq \int_0^\infty |H_1(j 2\pi f)|^2 df \\ &= \frac{K}{4\tau} \end{aligned} \quad (5)$$

The variance of the estimate of angle rate, $\sigma_{\Delta_\epsilon}^2$, is therefore given by

$$\sigma_{\Delta_\epsilon}^2 = N_{n_\theta} B_{N1} \quad (6)$$

where N_{n_θ} is the one-sided power spectral density of the equivalent angle tracking loop noise $n_\theta(t)$. This assumes an analog system operation where, in reality, we are dealing with a digital implementation. The digital implementation provides a variance of each sample of noise, where the update time is T_s seconds (see Appendix C). Using noise bandwidths, a good approximate relationship between the equivalent one-sided power spectral density and the variance per sample is

$$\sigma_{n_\theta}^2 = N_{n_\theta} B \quad (7)$$

where the noise bandwidth $B \approx 1/T_s$, and T_s is the update period. Therefore

$$N_{n_\theta} = T_s \sigma_{n_\theta}^2 \quad (8)$$

Upon substitution of (5) and (8) into (6),

$$\sigma_{\hat{\theta}_T} = \sigma_{\Delta_\epsilon} = \sqrt{\frac{KT_s}{4\tau}} \sigma_{n_\theta}, \quad (9)$$

where all units are in radians and seconds.

It is also of value to consider the transfer function between the equivalent noise n_θ and the angle tracking error Δ_ϵ . If we assume $\theta_T = 0$, this is equivalent to the transfer function between n_θ and θ_A , which is given by

$$H_2(s) = \frac{K(\tau s + 1)}{s^2 + K(\tau s + 1)}. \quad (10)$$

The corresponding one-sided noise bandwidth, B_{N2} , for this transfer function is [2]:

$$\begin{aligned} B_{N2} &\triangleq \int_0^\infty |H_1(j2\pi f)|^2 df \\ &= \frac{K\tau^2 + 1}{4\tau}. \end{aligned} \quad (11)$$

The units of K are sec^{-2} . Therefore, the units of B_{N2} are Hertz.

Following the same development as used for $\hat{\theta}$, the variance of the angle tracking error is given by

$$\sigma_{\Delta_\epsilon}^2 = N_{n_\theta} B_{N2}. \quad (12)$$

Substituting (8) and (11) into (12),

$$\sigma_{\Delta_\epsilon} = \sqrt{\frac{(K\tau^2 + 1) T_s}{4\tau}} \sigma_{n_\theta}, \quad (13)$$

where the units of the square root are dimensionless, and the units of σ_θ are the same as those of σ_{n_θ} . Various equivalent versions of σ_{Δ_ϵ} are also given in Appendix C.

In order to obtain the relationship between σ_{Δ_ϵ} and $\sigma_{\hat{\theta}}$, (13) is divided into (9) with the result that

$$\boxed{\frac{\sigma_{\dot{\Delta}_\epsilon}^*}{\sigma_{\Delta_\epsilon}} = \sqrt{\frac{K}{K\tau^2 + 1}} \sec^{-1}} \quad (14)$$

This describes the relationship that exists between the RMS error of the angle tracking loop and the RMS error of the angle rate estimator. Notice that the ratio is independent of the update time T_s . This is as expected inasmuch as the update time affects the angle tracking loop in exactly the same way as it does the angle rate estimation.

As can be observed from (14), $\sigma_{\dot{\Delta}_\epsilon}^* / \sigma_{\Delta_\epsilon}$ depends only on the loop gain K and the time constant τ . The loop gain is given in terms of other system parameters in (3), where it is observed that K is dependent on ρ , and therefore SNR. Hence the ratio in (14) will vary with range.

The transfer function $H_1(s)$ in (4) relates the angle rate estimate, $\hat{\theta}_T$, to the equivalent angle tracking noise, $n_\theta(t)$. It can be expressed in standard second-order control system form, as

$$H_1(s) = \frac{s}{1 + \tau s + \frac{s^2}{K}} = \frac{s}{1 + \frac{2\zeta}{\omega_n} s + \left(\frac{s}{\omega_n}\right)^2} \quad (15)$$

It is clear that the natural frequency $\omega_n = 2\pi f_n$ and the damping factor ζ are related to K and τ by

$$K = \omega_n^2, \quad \tau = \frac{2\zeta}{\omega_n} \quad (16)$$

The noise bandwidth, B_{N2} , in (11) for the angle tracking loop can be expressed in terms of f_n and ζ as

$$B_{N2} = \frac{K\tau^2 + 1}{4\tau} = (1 + 4\zeta^2) \frac{\pi f_n}{2\zeta} \quad (17)$$

Also, the ratio $\sigma_{\dot{\Delta}_\epsilon}^* / \sigma_{\Delta_\epsilon}$ can be expressed in terms of ζ and f_n as

$$\frac{\sigma_{\dot{\Delta}_\epsilon}^*}{\sigma_{\Delta_\epsilon}} = \frac{2\pi f_n}{\sqrt{4\zeta^2 + 1}} = \begin{cases} \frac{2\pi f_n}{\sqrt{5}}, & \zeta = 1 \\ \frac{2\pi f_n}{\sqrt{3}}, & \zeta = 0.707 \end{cases} \quad (18)$$

A rough but satisfactory measure of the convergence time for the angle rate estimator is given by two time constants of the closed loop transfer function. A convergence time T_{CT} is therefore defined as

$$T_{CT} \triangleq 2\tau = \frac{4\zeta}{2\pi f_n} = \begin{cases} 0.637 f_n^{-1}, & \zeta = 1 \\ 0.450 f_n^{-1}, & \zeta = 0.707 \end{cases} \quad (19)$$

The results in (18) and (19) are shown in Figure 4, where the standard tradeoff between convergence time and RMS performance is shown. These results will be of value in eventually choosing a natural frequency for the angle tracking loop. Before the choice can be carefully made, the absolute RMS error of angle rate estimation must be determined, as well as evaluating deterministic performance in the presence of angular acceleration.

To determine the RMS error of angle rate estimation, we substitute (37) from Appendix C and (17) of this appendix into (18), so that

$$\begin{aligned} \sigma_{\dot{\Delta}_\epsilon} &= \frac{2\pi f_n}{\sqrt{4\zeta^2 + 1}} \sigma_{\Delta_\epsilon} \\ &= \frac{2\pi f_n}{\sqrt{4\zeta^2 + 1}} \left(\frac{\theta_B}{4\rho k_m} \right) \sqrt{B_N(\rho) T_s} \sigma_X(N, \rho) \\ &= \frac{2\pi f_n}{\sqrt{4\zeta^2 + 1}} \left(\frac{\theta_B}{4\rho k_m} \right) \left[(1 + 4\zeta^2) \frac{\pi f_n}{2\zeta} T_s \right]^{1/2} \sigma_X(N, \rho). \end{aligned} \quad (20)$$

With some simplification, we have the result that

$$\boxed{\sigma_{\dot{\Delta}_\epsilon} = \frac{\theta_B}{2\rho k_m} \pi^{3/2} f_n^{3/2} \sqrt{\frac{T_s}{2\zeta}} \sigma_X(N, \rho)}, \quad (21)$$

where the units of $\sigma_{\dot{\Delta}_\epsilon}$ are the same as θ_B times sec^{-1} . If we substitute $\zeta = \pi\tau f_n$ from (16) into (21), then

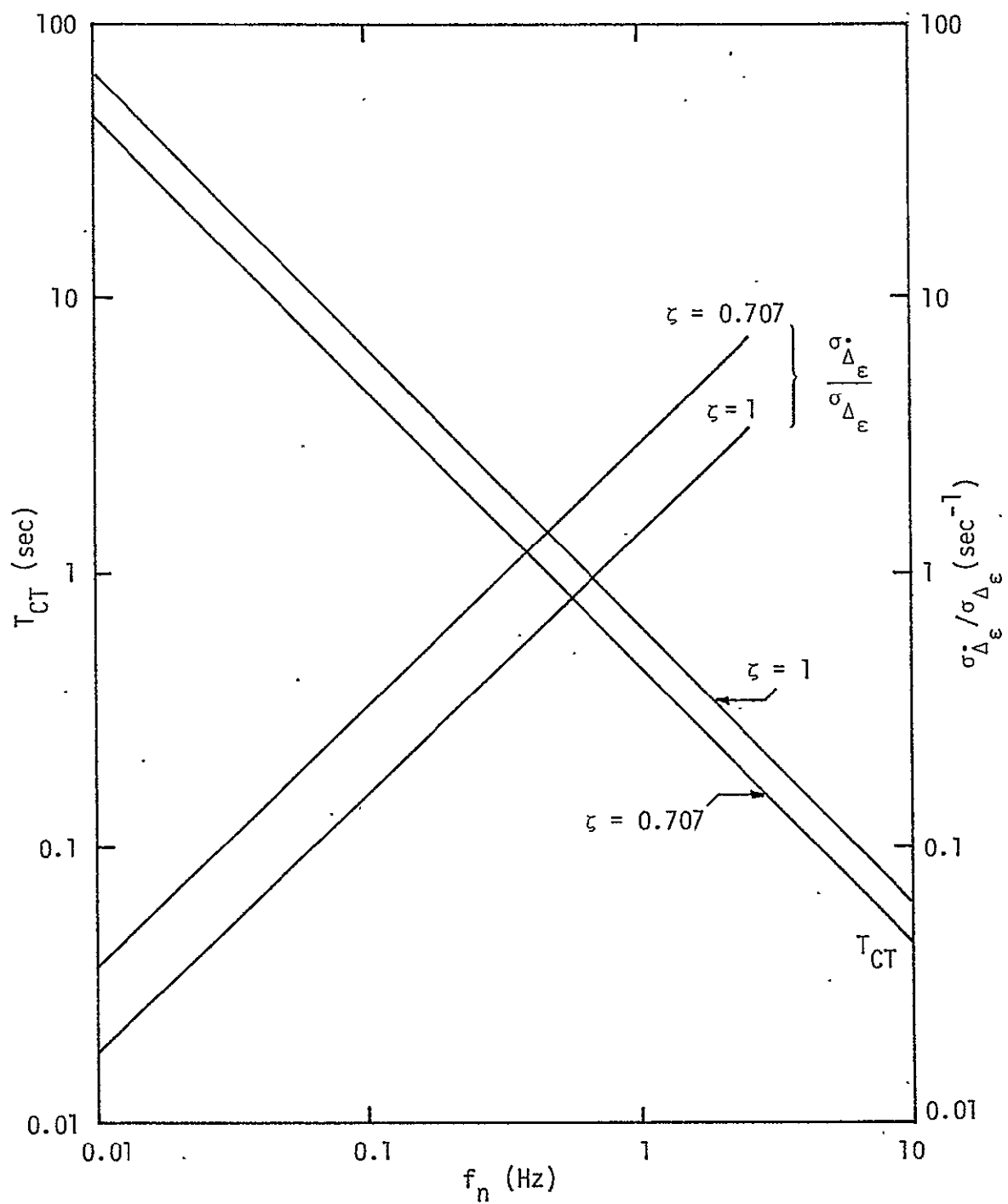


Figure 4. $\sigma_{\Delta_\epsilon}^* / \sigma_{\Delta_\epsilon}$ vs. Natural Frequency for Angle Tracking Loop for Different Damping Ratios

$$\sigma_{\dot{\Delta}_\epsilon} = \frac{\pi \theta_B f_n}{2 \rho k_m} \sqrt{\frac{T_s}{2\tau}} \sigma_X(N, \rho) \quad (22)$$

This result is plotted in Figure 5. All system values employed in the angle tracking performance evaluation in Appendix C are again used. In addition, the values of convergence time and natural frequency that are used at the various ranges are shown. For example, for $R > 9.5$ nmi, the convergence time of $T_{CT} = 24$ sec and the natural frequency of 0.027 Hz are used.

As can be seen by inspection of Figure 5, the angle rate estimation is below the spec value of

$$\sigma_{\dot{\Delta}_\epsilon} = 2.57 \text{ mdeg/sec} \quad (23)$$

This evaluation accounts for target scintillation and receiver front end noise. It is also a steady state evaluation and thereby does not take into account the effects of target acceleration. A mild attempt at this is accomplished by defining a convergence time equal to two loop time constants. The deterministic response of angular accelerations will be taken into account and reported in a subsequent report.

This evaluation has also assumed a point target, and therefore does not address the deterioration in performance that results from glint.

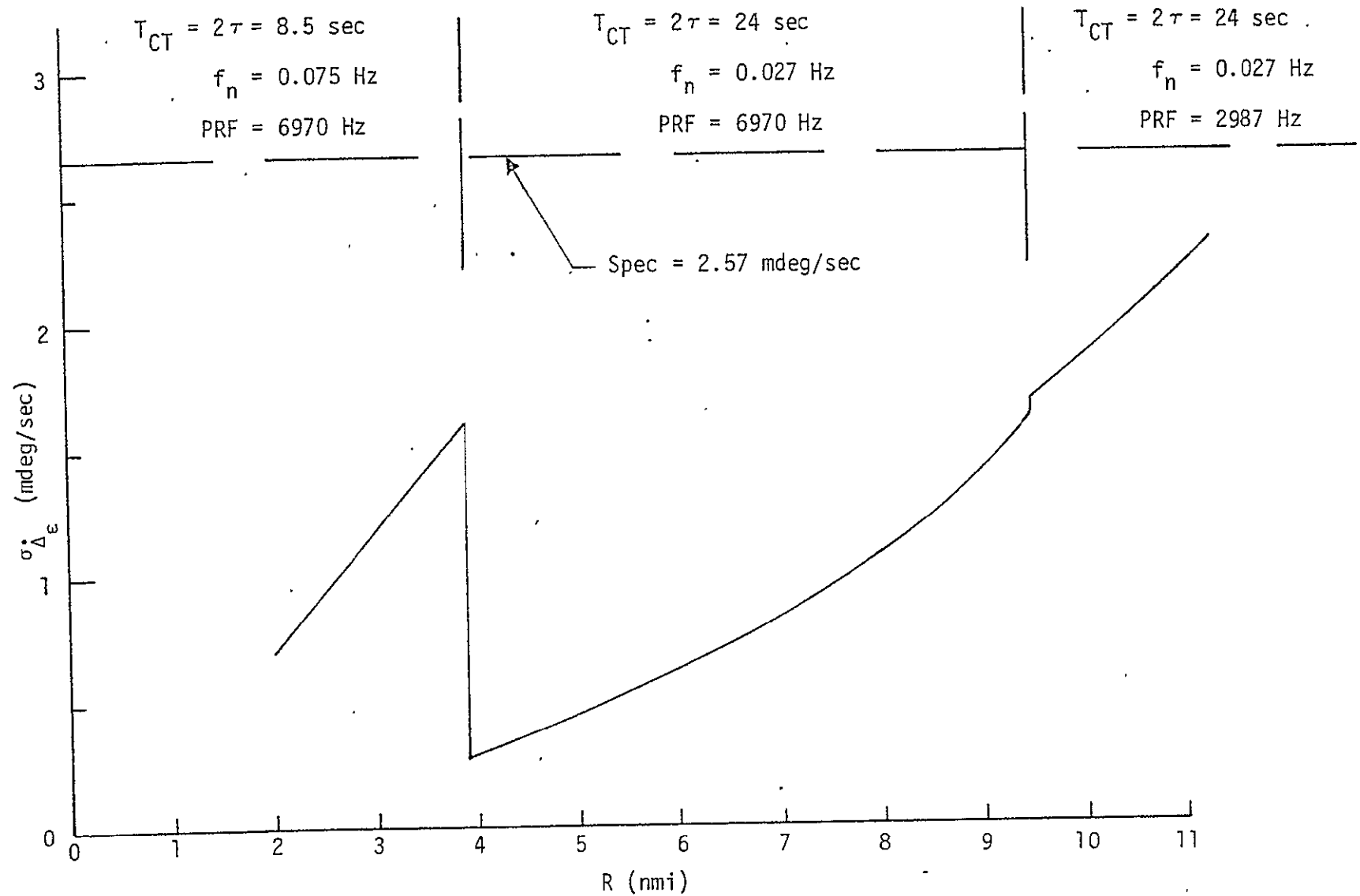


Figure 5. Performance of Angle Rate Estimation vs. Range in Nautical Miles - Pertinent System Parameters as Indicated

REFERENCES

1. Hughes Aircraft Co., "Ku-Band Integrated Radar and Communication Equipment for the Space Shuttle Orbiter Vehicle," Program Status Report, October 13, 1977.
2. I. S. Gradshteyn and M. Y. Tseytlin. Tables of Integrals, Series, and Products. Academic Press, 1965.

APPENDIX E

TIME-MULTIPLEXED SINGLE CHANNEL RANGE TRACKING OF PASSIVE TARGETS

APPENDIX E

TIME-MULTIPLEXED SINGLE CHANNEL RANGE TRACKING OF PASSIVE TARGETS

by

Waddah K. Alem
Charles L. Weber

1.0 INTRODUCTION

Range tracking is carried out by sequential processing of monopulse signals as is the case for angle tracking. Single channel processing is used to generate the error signal. The single channel is time-division-multiplexed between four time slots— $\Sigma + \Delta_{AZ}$, $\Sigma - \Delta_{AZ}$, $\Sigma + \Delta_{EL}$, and $\Sigma - \Delta_{EL}$. In order to form a range error signal, the received pulses are passed through an early gate and a nonoverlapping late gate which are located around the predicted estimate of the range from a previous calculation. The width of the gate is equal to the pulse width. The signals are then processed through a bank of doppler filters and then through the post-detection integration process before the logarithmic discriminant forms the range errors [1]. In this appendix, the range tracking accuracies in the passive mode are calculated.

2.0 DESCRIPTION OF SINGLE-CHANNEL MONOPULSE TRACKING BLOCK DIAGRAM

The single-channel monopulse was described in Appendix C where angle tracking errors are analyzed. The description is repeated here for convenience.

The amplitude monopulse feed of the Ku-band antenna system outputs three channels of data—the sum channel Σ , the azimuth error channel Δ_{AZ} , and the elevation error channel Δ_{EL} , as shown in Figure 1. As described in more detail in Appendix B of [1], the elevation and azimuth error channels time-share the single signal processing channel. The modulation by ± 1 either passes the error signal unchanged or inverts the RF phase. After recombining the error channel with the sum channel, the time-sharing is as shown in Figure 2.

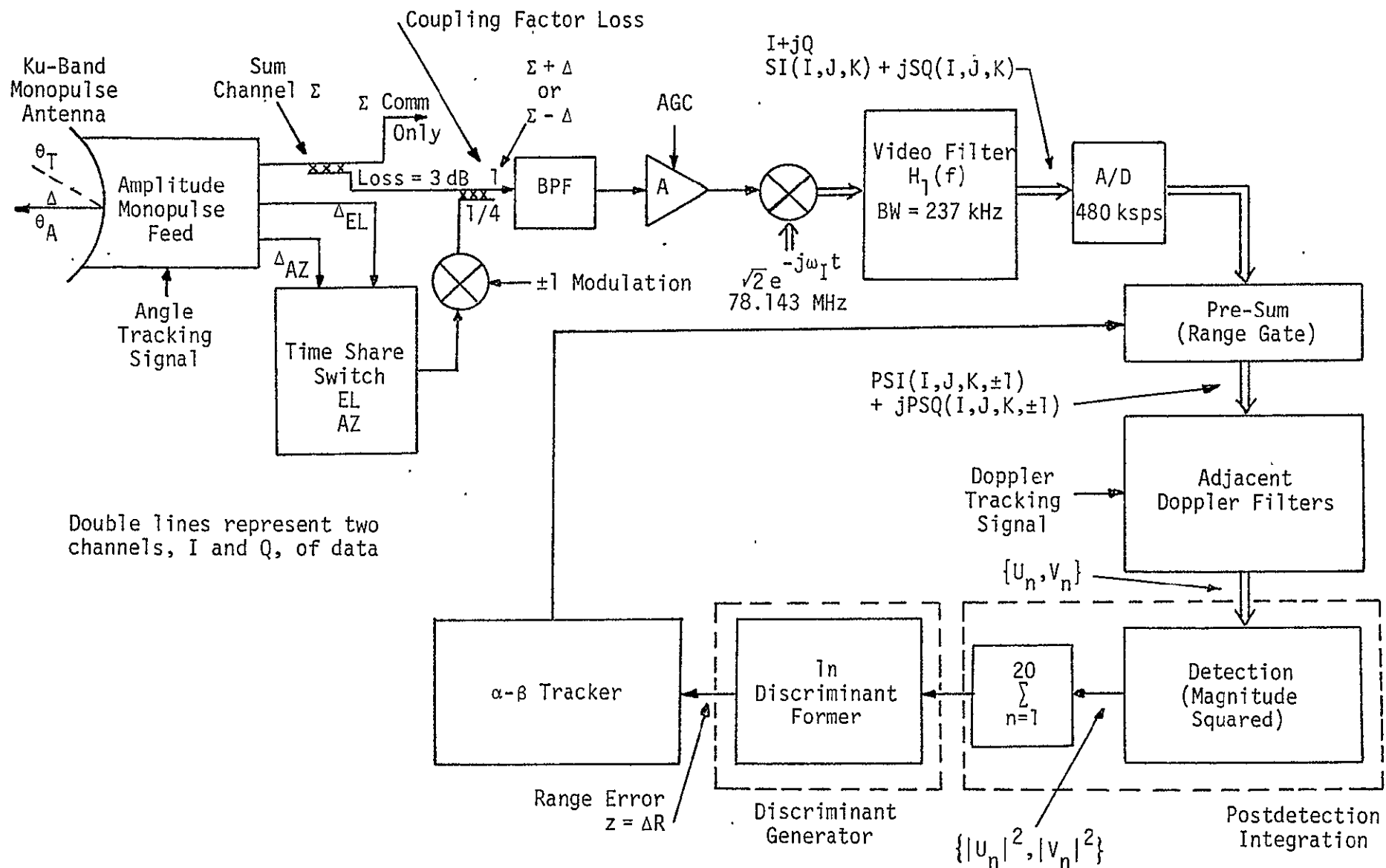


Figure 1. Block Diagram of Single Channel Monopulse Range Tracking Loop

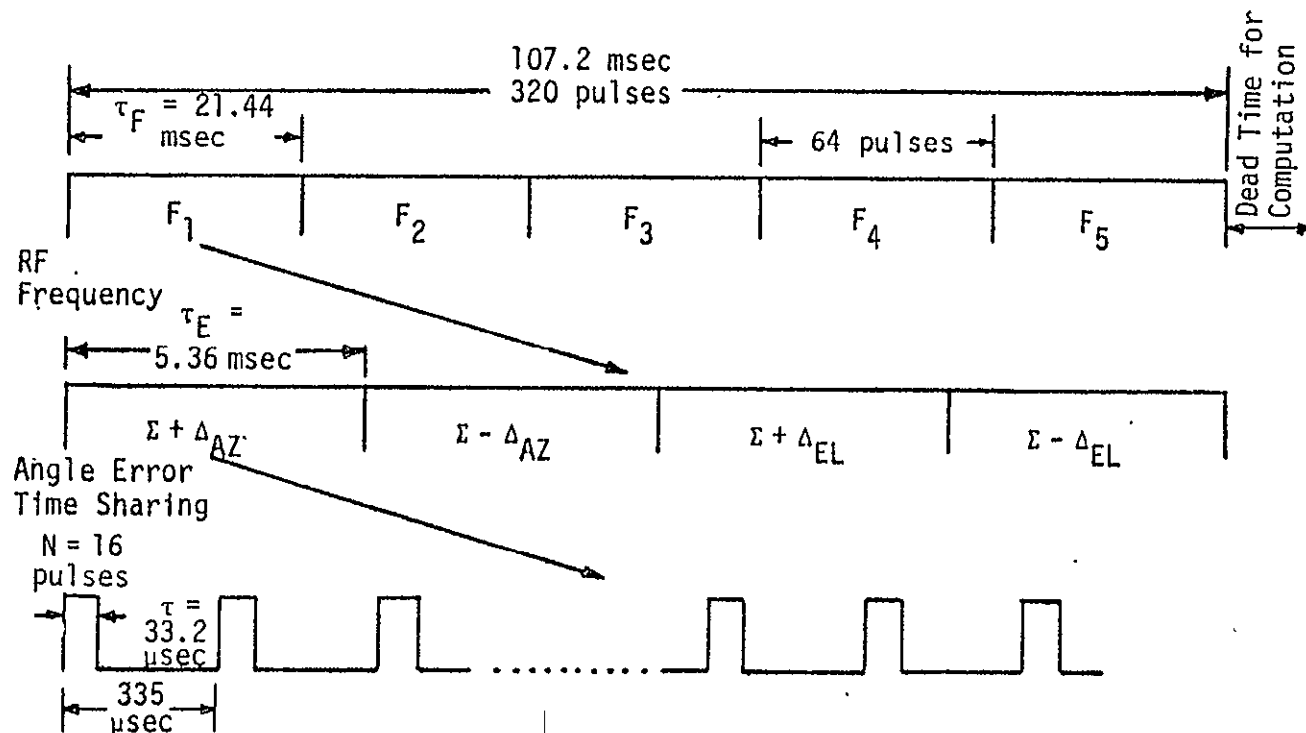


Figure 2. Timing for Single-Channel Time-Shared Monopulse Tracking, PRF = 2987 Hz

During the track mode of operation, the frequency diversity consists of 5 RFs, each of which operates for $\tau_F = 21.44$ msec. During each RF frequency, the single channel processing is equally time-shared among the four signals— $\Sigma + \Delta_{AZ}$, $\Sigma - \Delta_{AZ}$, $\Sigma + \Delta_{EL}$, $\Sigma - \Delta_{EL}$ —in the four time slots. Each of these is processed for $\tau_E = 5.36$ msec (designated the slot time), during which time 16 pulses are transmitted and received. Throughout this description, the system parameters corresponding to the largest range interval of interest are being employed. In particular [4],

$$\text{PRI} = T_p = \text{pulse repetition interval} = 335 \mu\text{sec}$$

$$\text{PRF} = 2987$$

$$\text{Pulse Width} = \tau = 33.2 \mu\text{sec}$$

$$\text{Frequency Dwell Time} = \tau_F = 21.44 \text{ msec/RF}.$$

τ_E is the dwell time of $\Sigma + \Delta_{AZ}$, which is one of the four time slots for each frequency dwell, and the range interval for this set of parameters is 9.5 to 18.9 nmi. The equivalent coherent integration time/frequency is defined as $\tau_c \triangleq 16\tau$.

Referring again to Figure 1, the various stages of IF and AGC are simplified and consolidated into one bandpass filter (BPF) and AGC. The AGC is shown but not taken into account in the range track performance analysis, since for range tracking purposes, the logarithmic discriminant is already self-normalizing. The primary purpose of the AGC is to maintain satisfactory signal level in the receiver and to avoid receiver saturation. The AGC is herein assumed to be performing its operation, so that all normalization can be accounted for in the discriminant.

The final stage of IF converts the sum plus error narrowband signals to I and Q (complex) baseband waveforms. The video filter before the A/D is a 2-pole Butterworth with transfer function

$$|H_1(f)|^2 = \left[1 + \left(\frac{f}{f_c} \right)^4 \right]^{-1},$$

where $f_c = 237$ kHz. At these longer ranges, $R > 9.5$ nmi, where the pulse width is $33.2 \mu\text{sec}$, the signal can be assumed to be undistorted by $H_1(f)$.

The sampling frequency of the A/D is 480 ksps, which corresponds to 16 samples over each pulse width τ . This is a sufficiently large

number so that the pre-sum can be accurately approximated by analog integration.

The notation developed in the previous report [1] is maintained. In particular,

$I = 1, \dots, 5$ corresponds to RF frequency

$J = 1, \dots, 4$ corresponds to time slot;

$J = 1$ implies $\Sigma + \Delta_{AZ} (\alpha)$

$J = 2$ implies $\Sigma - \Delta_{AZ} (-\alpha)$

$J = 3$ implies $\Sigma + \Delta_{EL} (\beta)$

$J = 4$ implies $\Sigma - \Delta_{EL} (-\beta)$

$K = 1, \dots, 16$ corresponds to the pulse number for a given I and J .

There are actually additional pulses transmitted periodically to allow time for signal processing, register resets, etc. Without loss of generality, only those signals which contribute to the range tracking operation and performance are taken into account.

Now consider the complex baseband waveforms before the pre-sum for a given time slot J ,

$$SI(I, J, K) = \left\{ \sqrt{2} (\Sigma + \Delta_J) A_I P(t - kT_p) \cos [(\omega_I + \omega_d)t + \theta_I] + n(t) \right\} \sqrt{2} \cos(\omega_I t) \quad (1a)$$

and

$$SQ(I, J, K) = \left\{ \sqrt{2} (\Sigma + \Delta_J) A_I P(t - kT_p) \cos [(\omega_I + \omega_d)t + \theta_I] + n(t) \right\} \sqrt{2} \sin(\omega_I t) \quad (1b)$$

for the I and Q channel, respectively. The peak received signal power is given by

$$P_{pr} = E[A_I^2], \quad (2)$$

where it is assumed that $(\Sigma + \Delta_J)$, for all J 's, are normalized to 1. The average received power is then

$$P_{avg \ r} = d_t P_{pr} \quad (3)$$

where d_t is the duty factor of the radar pulse train. The duty factor is constant for a given designated range but varies for different range

designations. Table 1 lists the values of the duty factor for various ranges in the passive tracking mode.

Table 1. Duty Factors d_t for Various Designated Ranges

	Designated Range (nmi)					
	> 9.5	9.5-3.8	3.8-1.9	1.9-0.95	0.95-0.42	< 0.42
Pulse width (μsec)	33.2	16.5	8.3	4.15	2.07	0.122
PRF (Hz)	2987	6970	6970	6970	6970	6970
d_t	0.099	0.116	0.058	0.029	0.0144	0.00085

Since, for illustration, only the largest range is under consideration in this appendix, $d_t = 0.1$. Since the target is assumed to be Swerling I, the amplitudes A_I are assumed to be Rayleigh random variables. The random phase θ_I is assumed to be uniformly distributed over $(0, 2\pi)$. The Rayleigh and uniform variables A_I and θ_I , respectively, are independent. The pulse $P(t)$ has a magnitude of unity over the transmitted pulse width $\tau = 33.2 \mu\text{sec}$.

The doppler frequency shift is represented by ω_d .

The receiver noise $n(t)$ after the bandpass filter has the narrow-band representation

$$n(t) = \sqrt{2} [N_c(t) \cos \omega_I t - N_s(t) \sin \omega_I t] \quad (4)$$

where N_c and N_s are independent zero mean narrowband Gaussian processes with one-sided power spectral density of N_0 watts/Hz, and one-sided noise bandwidth approximately equal to f_c ($f_c = 237$ kHz), which is the 3 dB bandwidth of $H_1(f)$. Before the A/D, the complex waveform is given by

$$\begin{aligned} SI + jSQ &= \left[\sqrt{2} (\Sigma + \Delta_J) A_I P(t - kT_p) \cos [(\omega_I + \omega_d)t - \theta_I] + n(t) \right] \sqrt{2} e^{-j\omega_I t} \\ &= (\Sigma + \Delta_J) A_I P(t - kT_p) \exp [j(\omega_d t + \theta_I)] + N_c(t) + jN_s(t). \end{aligned} \quad (5)$$

3.0 PRE-SUM (RANGE GATES)

After the A/D, each received pulse is pre-summed over the pulse width. The timing of this pre-sum is dependent on the setting of the range gates in the range tracking loop. Two range gates were used for every pulse, an early gate and a late gate, as shown in Figure 3, where it is noted that, for tracking, the gates are nonoverlapping. Recall that, in the GPC Designate Search mode, two wider and overlapping range gates are employed.

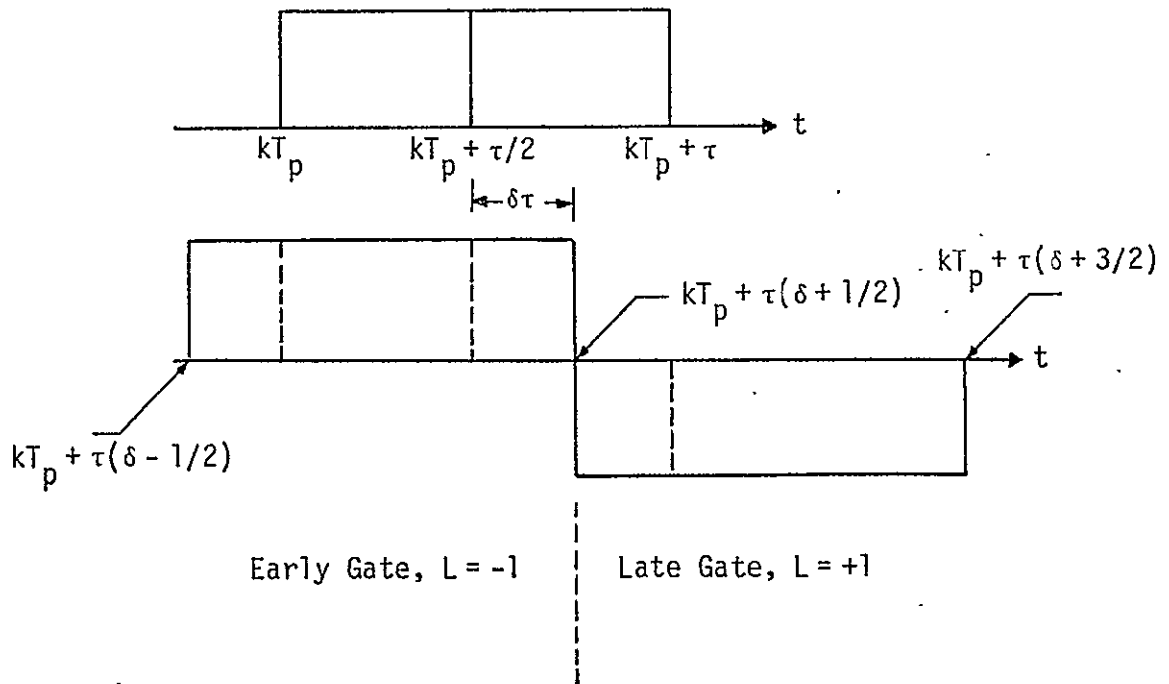


Figure 3. Early and Late Gates Alignment . .

The early and late gates will be represented by an additional index $L = -1, +1$, respectively. If the relative offset in the range gate setting is δ , then the output of the early gate is given by

$$P(I, J, K, -1) = \int_{kT_p + \tau(\delta - 1/2)}^{kT_p + \tau(\delta + 1/2)} (SI + j SQ) dt \quad (6)$$

and the output of the late gate is

$$P(I, J, K, +1) = \int_{kT_p + \tau(\delta + 1/2)}^{kT_p + \tau(\delta + 3/2)} (SI + j SQ) dt, \quad (7)$$

where the digital sum of the pre-sum is being approximated by analog integration.

The limits of the relative offset δ are given by

$$|\delta| < \frac{1}{2}.$$

This is due to the fact that the range gates are adjusted in such a way that the signal energy is divided between them. Under ideal tracking conditions, the outputs of the gates will have an equal amount of energy. The location of the gates is adjusted via the time processing unit which is used to calculate the predicted range estimate. When $\delta = 1/2$, the early gate extracts all the signal energy while the late gate gets no signal energy. The opposite happens when $\delta = -1/2$.

The actual timing error (ΔT), which is the time difference between the actual signal return and the estimated signal return, is thus equal to $\delta\tau$.

4.0 DOPPLER FILTERS (RANGE RATE TRACKING)

During search, 16 doppler filters are used. For convenience, these are numbered 1,3,5,...,31. During track, these same 16 doppler filters are used but, in addition, the even-numbered filters are also formed, numbered 2,4,...,32. For doppler tracking, filters F_n and F_{n+2} are used, during which time the output of F_{n+1} is used for angle and range track. These filters are not adjusted, so that the center of filter F_{n+1} corresponds to the doppler frequency received. Alternatively, the center frequency of all of these filters remains fixed until the error gets sufficiently large to shift filters. At the maximum offset of the center doppler filter, the loss incurred for not shifting is 1.1 dB. This is accounted for in the power budget for range tracking in Section 8.0. This doppler processing tracking technique is discussed in more detail in Appendices B, C, and G.

Assuming that the center frequency of the doppler filter closest to ω_d is denoted by $\omega_d - \Delta\omega_1$, where $\Delta\omega_1$ represents the error in doppler tracking, the effect of this DFT filtering can be accurately approximated

by multiplying $S_I + jSQ$ by $\exp[-j(\omega_d - \Delta\omega_1)]$ before the pre-sum integration and extending the equivalent integration over the length of a time slot ($\tau_E = 5.36$ msec). This corresponds to the single-sided bandwidth of the doppler filter of approximately $\tau_E^{-1} = 187$ Hz.

The actual implementation where pre-summing precedes doppler filtering results in an effective power loss of not more than 0.6 dB, which will be taken into consideration when calculating the tracking error in subsequent sections. The trade-offs between the two implementations are discussed in Appendix C.

5.0 STATISTICAL PARAMETERS OF DOPPLER FILTERS OUTPUTS

The outputs of the center doppler filters M_1 will be denoted by $W(I, J, M_1, \pm 1)$, where -1 corresponds to the early gate and $+1$ corresponds to the late gate. There are two outputs to be considered; each has a signal part W_s and a noise part W_n .

Again approximating the pre-sum by an analog integration, the signal part of the output of the doppler filter is found by examining the location of the signal with respect to the range gates which adjust the limits of the integrals under consideration. The output for the early gate is

$$W_s(I, J, M_1, -1) = (\Sigma + \Delta_J) A_I \frac{1}{\tau_E} \sum_{k=0}^{N-1} \int_{kT_p}^{kT_p + \tau(\delta+1/2)} \exp[j(\theta_I + \Delta\omega_1 t)] dt \quad (8)$$

and for the late gate

$$W_s(I, J, M_1, +1) = (\Sigma + \Delta_J) A_I \frac{1}{\tau_E} \sum_{k=0}^{N-1} \int_{kT_p + \tau(\delta+1/2)}^{kT_p + \tau} \exp[j(\theta_I + \Delta\omega_1 t)] dt. \quad (9)$$

$N=16$ is the number of received pulses in every time slot. Carrying out the integration and summation results in

$$W_s(I, J, M_1, -1) = (\Sigma + \Delta_J) A_I e^{j(\theta_I + \Delta\omega_1 \tau(1/2+\delta)/2)} \frac{\sin[\Delta\omega_1 \tau(1/2+\delta)/2]}{\Delta\omega_1 \tau(1/2+\delta)/2} \\ \times \frac{\sin(\Delta\omega_1 \tau_E/2)}{N \sin(\Delta\omega_1 T_p/2)} e^{j(\tau_E - T_p)\Delta\omega_1/2} \left(\frac{1}{2} + \delta\right) d_t \quad (10)$$

and

$$W_S(I, J, M_1, +1) = (\Sigma + \Delta_J) A_I e^{j(\theta_I + \Delta\omega_1 \tau(\delta+3/2)/2)} \frac{\sin [\Delta\omega_1 \tau(1/2-\delta)/2]}{\Delta\omega_1 \tau(1/2-\delta)/2} \times \frac{\sin (\Delta\omega_1 \tau_E/2)}{N \sin (\Delta\omega_1 T_p/2)} e^{j(\tau_E - T_p)\Delta\omega_1/2} d_t(\frac{1}{2} - \delta) \quad (11)$$

To further analyze the range tracking accuracy, two simplifying assumptions are made:

1. Doppler is exactly known, which results in $\Delta\omega_1 = 0$. As mentioned earlier, the maximum power loss due to doppler mismatch is 1.1 dB. This is taken into account in the calculation of the power budget.
2. The angle tracking circuit is functioning ideally, that is, $\Delta_J = 0$ for $J = 1, 2, 3, 4$.

The outputs of filter M_1 of the doppler filter bank become

$$W_S(I, J, M_1, -1) = \Sigma A_I e^{j\theta_I} d_t(\frac{1}{2} + \delta) \quad (12)$$

for the early gate and

$$W_S(I, J, M_1, +1) = \Sigma A_I e^{j\theta_I} d_t(\frac{1}{2} - \delta) \quad (13)$$

for the late gate. The outputs of the doppler filter (M_1) for a given time slot J and a given RF frequency I can be written as

$$U(I, J) = \Sigma A_I e^{j\theta_I} d_t(\frac{1}{2} + \delta) + N_U(I, J) \quad (14)$$

and

$$V(I, J) = \Sigma A_I e^{j\theta_I} d_t(\frac{1}{2} - \delta) + N_V(I, J), \quad (15)$$

where the subscripts I, J are used to indicate that both U and V are functions of a given IF frequency and time slot, respectively. N_U and N_V represent the equivalent noise at the output of the doppler filter (M_1) due to the early gate signal and the late gate signal, respectively. Since the doppler tracking loop is assumed to be working ideally, $N_U(I, J)$ and $N_V(I, J)$ are Gaussian random variables with zero means and equal variances σ^2 .

$N_U(I,J)$ is the sum of two independent components from the I and Q channels, namely, N_{Us} and N_{Uc} , given by

$$N_{Us} = \frac{1}{\tau_E} \sum_{k=0}^{N-1} \int_{kT_p}^{kT_p + \tau} N_c(t) dt \quad (16)$$

and

$$N_{Uc} = \frac{1}{\tau_E} \sum_{k=0}^{N-1} \int_{kT_p}^{kT_p + \tau} N_s(t) dt. \quad (17)$$

Since the integrals for various k 's result in Gaussian independent variables, the variance of both N_{Uc} and N_{Us} is given by

$$\sigma^2 = \frac{1}{2} N \tau \frac{N_0}{\tau_E} = \frac{N_0 d_t}{2 \tau_E} = \frac{d_t N_0 B_F}{2}, \quad (18)$$

where $B_F = \tau_E^{-1}$ is the one-sided bandwidth of the DFT filters, namely, $B_F = (5.36 \text{ msec})^{-1} = 187 \text{ Hz}$. Since N_{Uc} and N_{Us} are independent, the variance of N_U becomes

$$\sigma_{N_U}^2 = d_t N_0 B_F. \quad (19a)$$

A similar argument follows for N_V , which results in

$$\sigma_{N_V}^2 = d_t N_0 B_F. \quad (19b)$$

As was the case in angle tracking, the statistical parameters of the doppler filters outputs are now determined for a given RF frequency I and a time slot J. In particular, the power in $U(I,J)$ is

$$P_U \triangleq E[|U(I,J)|^2] = d_t^2 E(A_I^2) \left(\frac{1}{2} + \delta\right)^2 \Sigma^2 + d_t N_0 B_F. \quad (20)$$

The power in $V(I,J)$ is

$$P_V \triangleq E[|V(I,J)|^2] = d_t^2 E(A_I^2) \left(\frac{1}{2} - \delta\right)^2 \Sigma^2 + d_t N_0 B_F \quad (21)$$

and the unnormalized correlation is

$$\begin{aligned} P_{UV} &\triangleq E[U(I,J) V^*(I,J)] \\ &= d_t^2 E(A_I^2) \left(\frac{1}{2} + \delta\right) \left(\frac{1}{2} - \delta\right) \Sigma^2, \end{aligned} \quad (22)$$

where * is used to denote complex conjugate. There is no noise term in P_{UV} because U and V are independent. In general, P_{UV} is a complex quantity. This might be due to a variety of reasons, such as an unaccounted-for RF phase shift in the antenna, DMA or DEA or a doppler mismatch which results in a phase error between U and V. When this occurs, P_{UV} becomes complex. In this development, P_{UV} is assumed real.

Recalling that the average received signal power is given by

$$P_{\text{avg } r} = d_t P_{\text{pr}} = d_t E(A_I)^2$$

and since Σ^2 is normalized to unity,

$$P_U = d_t P_{\text{avg } r} \left(\frac{1}{2} + \delta\right)^2 + d_t N_0 B_F$$

$$P_V = d_t P_{\text{avg } r} \left(\frac{1}{2} - \delta\right)^2 + d_t N_0 B_F$$

$$P_{UV} = d_t P_{\text{avg } r} \left(\frac{1}{2} + \delta\right) \left(\frac{1}{2} - \delta\right). \quad (23)$$

As discussed previously, when $\delta = 1/2$, it is obvious that P_U , which represents the early gate, has all the signal power and P_V , which represents the late gate, has no signal power. The opposite happens when $\delta = -1/2$.

Define the normalized correlation coefficient between U and V as

$$\rho^2 \triangleq \frac{|P_{UV}|^2}{P_U P_V}, \quad (24)$$

then

$$\rho^2 = \frac{d_t^2 P_{\text{avg } r}^2 \left(\frac{1}{2} + \delta\right)^2 \left(\frac{1}{2} - \delta\right)^2}{(d_t P_{\text{avg } r} \left(\frac{1}{2} + \delta\right)^2 + d_t N_0 B_F) (d_t P_{\text{avg } r} \left(\frac{1}{2} - \delta\right)^2 + d_t N_0 B_F)}, \quad (25)$$

when the range tracking loop is performing correctly, that is, when the range error is small ($\delta \approx 0$), the normalized correlation coefficient becomes

$$\rho = \frac{1}{1 + 4/\text{SNR}}, \quad (26)$$

where the signal-to-noise ratio (SNR) is defined as

$$\text{SNR} \triangleq \frac{P_{\text{avg}} r}{N_0 B_F} = \frac{P_{\text{avg}} r^T E}{N_0} \quad (27)$$

Note that, in general, the normalized correlation coefficient () is a function of δ . However, the variations of ρ with δ become negligible when the latter is small, as shown in (26). It is important to observe that the normalized correlation coefficient is dependent on SNR as given in (26) such that, as $\text{SNR} \rightarrow \infty$, then $\rho \rightarrow 1$, and as $\text{SNR} \rightarrow 0$, then $\rho \rightarrow 0$.

Instead of using two subscripts for U and V , namely, I and J , one subscript (n) will be used in the subsequent discussion. The subscript n takes the values 1 - 20 because there are four time slots ($j=1,4$) for every RF frequency ($I=1,5$). With these statistical parameters of U_n and V_n , the remainder of the range tracking loop can be described and the performance analyzed.

6.0 RANGE TRACKING DISCRIMINANT GENERATOR

Referring to Figure 1, the detector forms the magnitude squared:

$$|U_n|^2; \quad n=1, \dots, 20$$

$$|V_n|^2; \quad n=1, \dots, 20$$

This comes about by summing the outputs of doppler filters for each of the four time slots and for each of the five RF frequencies, all at the center doppler frequency and the early range gate. These outputs are the $|U_n|$. The same is done for the late gate, and these are designated $|V_n|$.

In the actual implementation, $|U_n|$ and $|V_n|$ are formed, whereas in this performance analysis, because of the resulting simplification, $|U_n|^2$ and $|V_n|^2$ are used. The difference in performance is only a few tenths of a dB.

As noted in the previous section, the statistical parameters of the complex Gaussian random variables $\{U_n, V_n\}$ are independent of n . The post-detection integration forms

$$\sum_{n=1}^N |U_n|^2, \quad \sum_{n=1}^N |V_n|^2$$

where $N = 20$.

Finally, the logarithmic discriminant generates

$$z = \ln \left[\frac{\sum_{n=1}^N |U_n|^2}{\sum_{n=1}^N |V_n|^2} \right]. \quad (28)$$

The random variable z is the maximum likelihood (M.L.) estimate [2] of the logarithm of the ratio of power in U_n to the power in V_n , i.e.,

$$z = \widehat{\ln [P_U/P_V]}, \quad (29)$$

where $(\hat{})$ denotes the maximum likelihood estimate.

In order to see how z is a measure of the target range error, note that z is an unbiased estimate of $\ln (P_U/P_V)$, namely [3],

$$z = \ln (P_U/P_V) + x \quad (30)$$

where [2] $E(x) = 0$ and $\sigma_x^2 = \sigma_z^2$ is the variance of the estimate of P_U/P_V . Equivalently stated,

$$E(z) = \ln (P_U/P_V). \quad (31)$$

The standard deviation (RMS error) of z has been derived in [2] and the performance curves are shown in Figure 4 for $N=2,5,10,20$. The RMS error is dependent on two variables, the number of independent samples (N) and the normalized correlation coefficient (ρ) between U_n and V_n . The figure shows that, for all N , as the normalized correlation coefficient increases, the RMS error decreases and tends to zero as $\rho \rightarrow 1$.

The improvements in the normalized correlation coefficient (ρ) and hence in the performance due to the increase in signal-to-noise ratio is indicated in (26) and plotted in Figure 5.

Figure 6 combines Figures 4 and 5, where the standard deviation (σ_x) is shown as a function of signal-to-noise ratio ($\text{SNR} = P_{\text{avg}} r / (N_0 B_F)$) for various numbers of samples N .

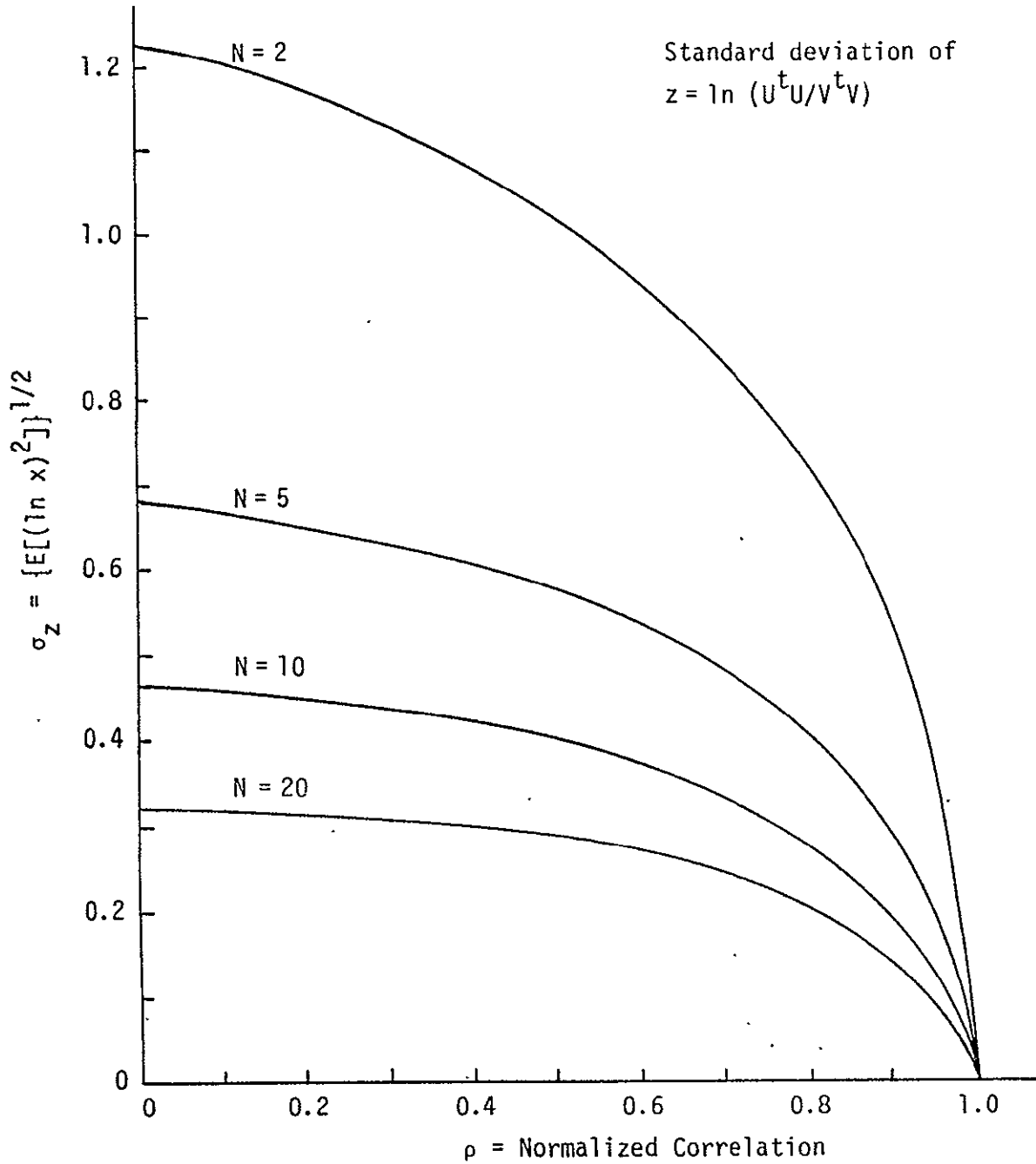


Figure 4. Standard Deviation of the Random Variable z as a Function of Correlation

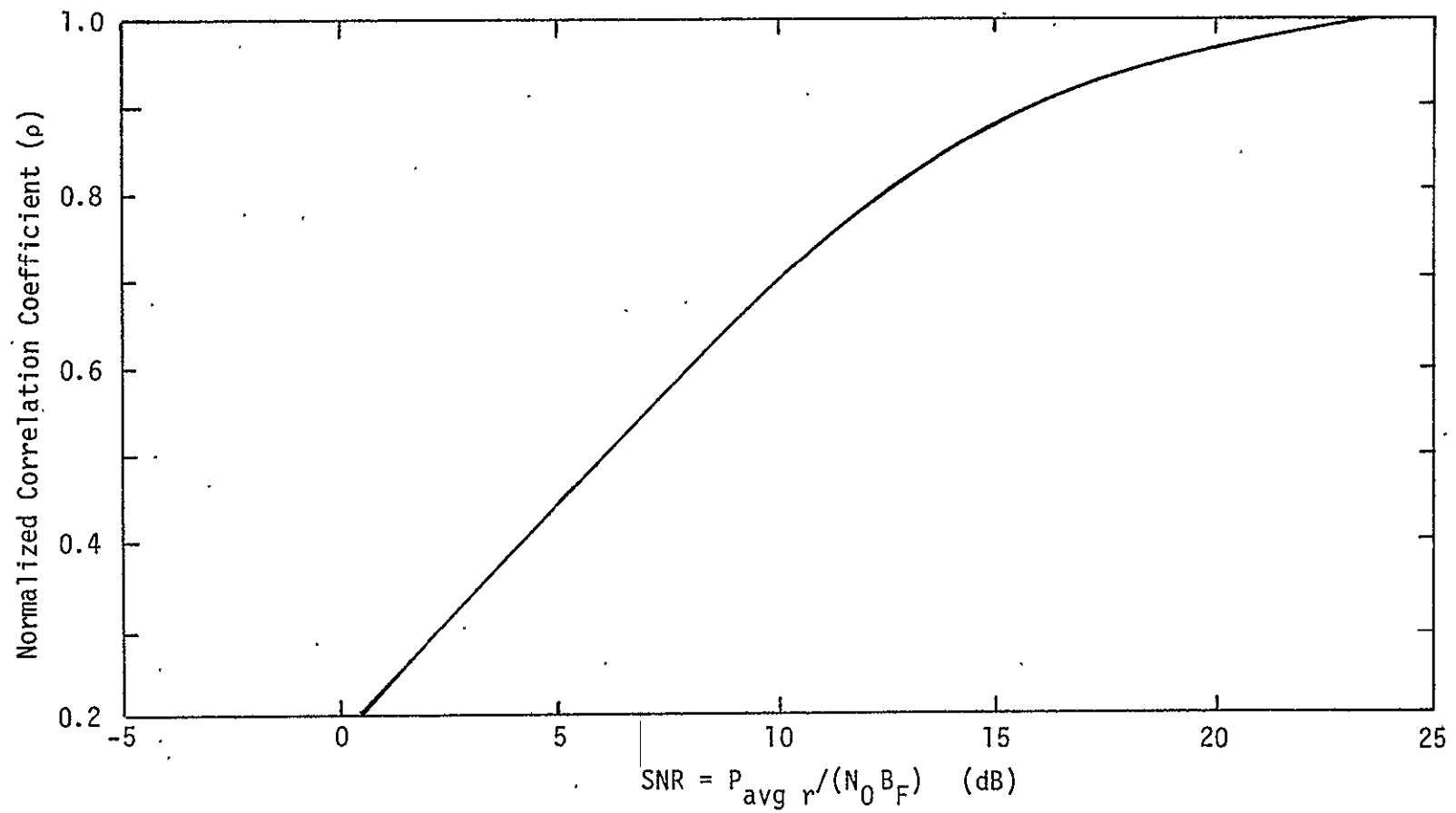


Figure 5. Normalized Correlation Coefficient ρ vs. Signal-to-Noise Ratio $P_{\text{avg}} r / (N_0 B_F)$

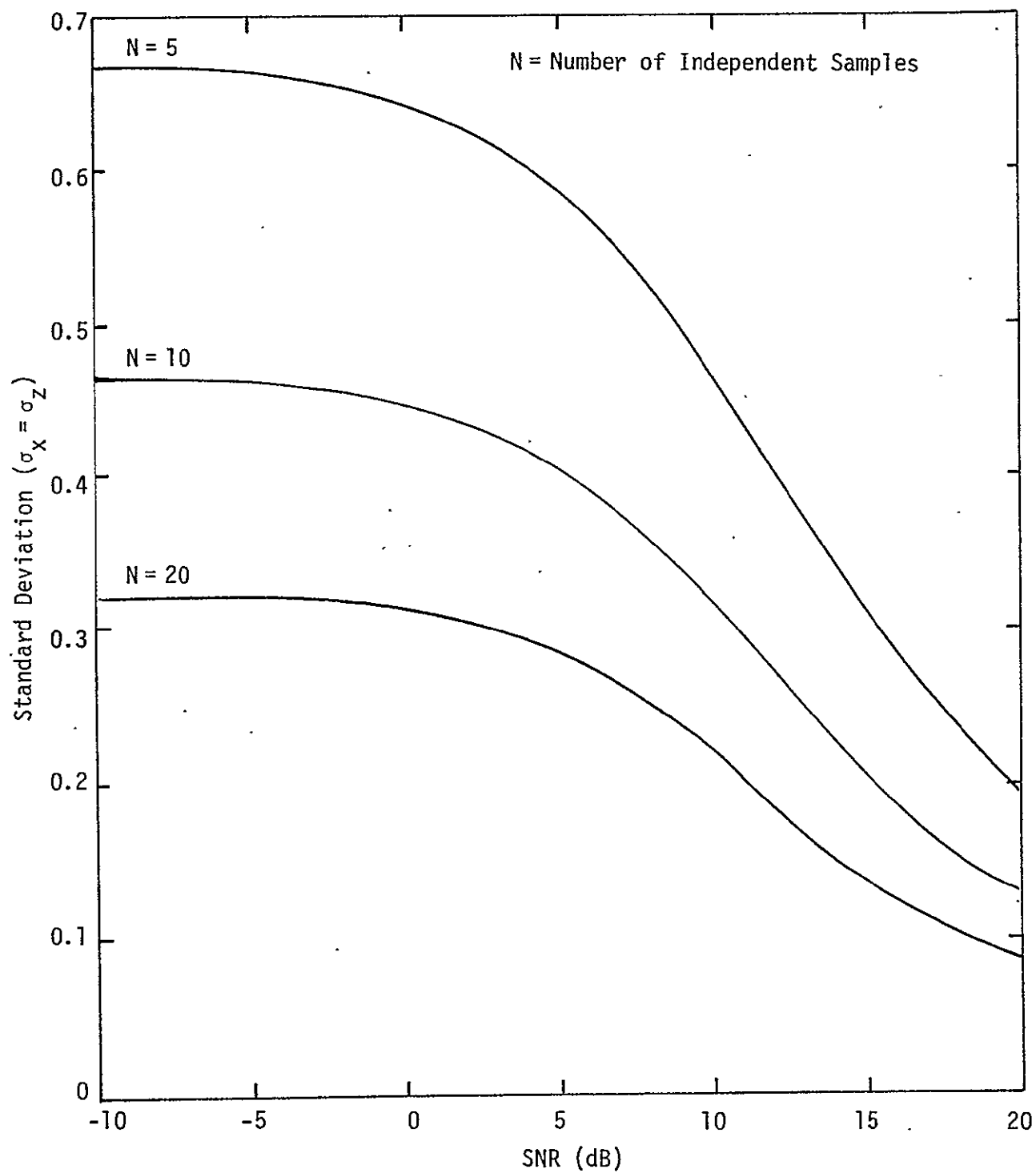


Figure 6. Standard Deviation of the Output of the Logarithmic Discriminant Generator vs. Signal-to-Noise Ratio at the Output of the Doppler Filters for Certain Values of N

0.5

The next step is to relate the maximum likelihood estimate z to the quantity being estimated, which is the range error (δ). Upon substituting (23) into (31),

$$\begin{aligned} E(z) = \ln (P_U/P_V) &= \ln \left[\frac{P_{\text{avg}} r \left(\frac{1}{2} + \delta\right)^2 + N_0 B_F}{P_{\text{avg}} r \left(\frac{1}{2} - \delta\right)^2 + N_0 B_F} \right] \\ &= \ln \left[\frac{(1 + 2\delta)^2 + (4/\text{SNR})}{(1 - 2\delta)^2 + (4/\text{SNR})} \right], \end{aligned} \quad (32)$$

which indicates that the mean of the output of the logarithmic discriminant is a function of the signal-to-noise ratio, as well as the normalized range gate error δ . The normalized range gate error δ corresponds to the range error ΔR in such a way that

$$\delta \tau = 2\Delta R/c$$

where c is the velocity of light ($c = 3 \times 10^8$ m/sec = 9.84×10^8 ft/sec) and τ is the pulse width (for long ranges, $\tau = 33.2$ μ sec); then,

$$\delta = \frac{2\Delta R}{\tau c}. \quad (33)$$

For small values of δ which correspond to small values of range error ΔR , $\ln (P_U/P_V)$ can be expressed as

$$\ln (P_U/P_V) = \ln \left[\frac{1 + \frac{4\delta}{1 + 4/\text{SNR}}}{1 - \frac{4\delta}{1 + 4/\text{SNR}}} \right], \quad (34)$$

where second-order terms have been dropped. Using the approximation that $\ln (1 + \alpha) = \alpha$ for small α , (32) becomes

$$E(z) = \ln (P_U/P_V) = \frac{8\delta}{1 + 4/\text{SNR}} = 8\delta \rho. \quad (35)$$

Thus, the mean of the output of the logarithmic discriminant generator for small values of δ is a linear function of δ and the normalized correlation coefficient ρ . The slope of $E(z)$ as a function of δ is dependent on the signal-to-noise ratio through the multiplication of δ by ρ , which corresponds to a reduction in the effective loop gain. Figure 7 illustrates the actual behavior of $\ln (P_U/P_V)$ as a function

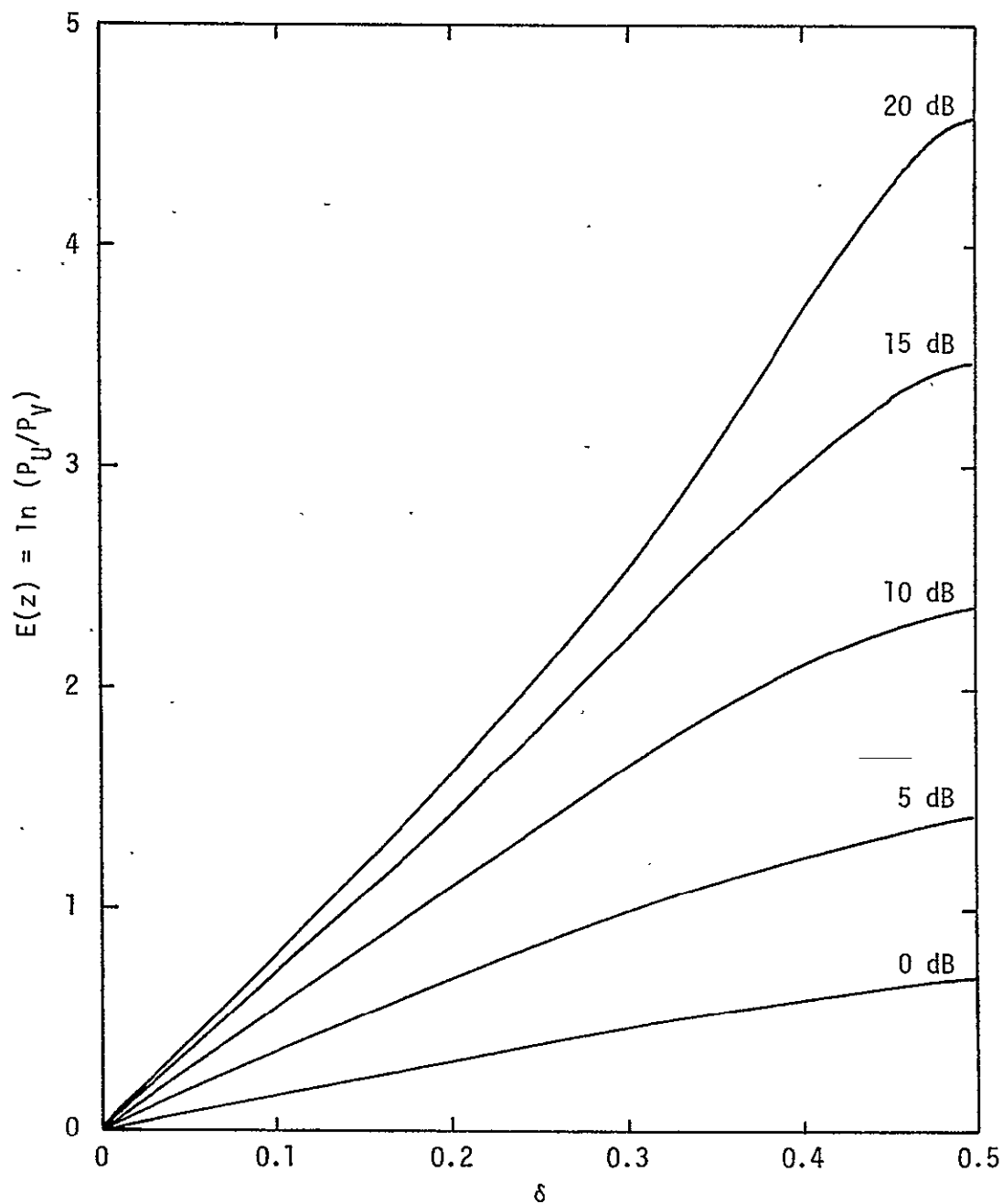


Figure 7. First Moment of the Output of the Range Tracking Discriminant Generator as a Function of Normalized Range Error for Various Signal-to-Noise Ratios

of δ (without any of the above approximations) with signal-to-noise ratio as a parameter. The figure is drawn for positive δ only since $E(z)$ in (32) is an odd function of δ . It is obvious that, for small values of δ , the function is linear.

7.0 PERFORMANCE OF RANGE TRACKING LOOP

The purpose of this section is to incorporate all the results of the previous sections so as to provide the RMS range (timing) error due to thermal noise. A block diagram of the equivalent range tracking loop is shown in Figure 8.

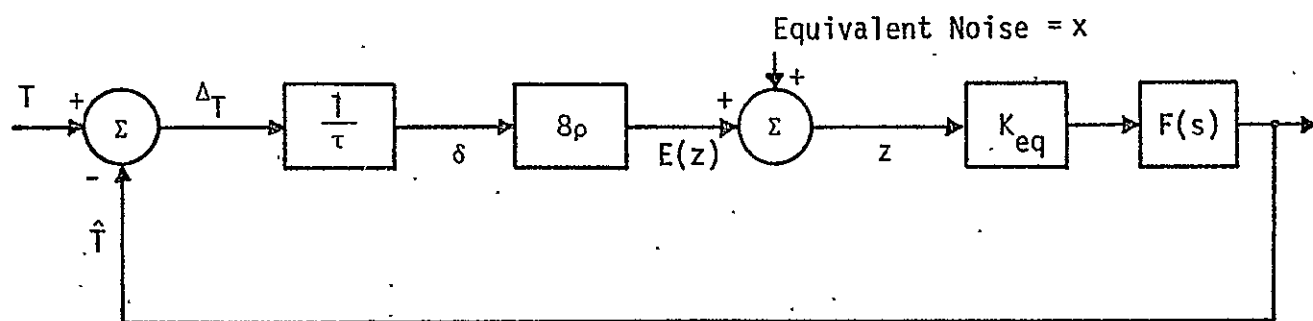


Figure 8. Block Diagram of the Equivalent Range Tracking Loop

The loop represents the linearized model of the actual range tracking block diagram shown in Figure 1. In Figure 8,

T = the actual time delay between the transmission and the reception of a given pulse. For a passive target at a range R , $T = 2R/c$, where c is the velocity of light in free space.

\hat{T} = the loop estimate of the actual delay T .

$\Delta_T = T - \hat{T}$ = the timing error.

τ = the pulse width, which is given in Table 1 for various range designations. It is used as a scale factor to convert the actual timing error into a normalized error δ as defined in Section 3.0.

8ρ = scale factor in (35) necessary to give $E(z) = \ln(P_U/P_V)$.

x = equivalent noise of the system due to the thermal noise.

$z = \ln(P_U/P_V) + x$ is the output of the logarithmic discriminant generator as given in (30) and diagrammed in Figure 1.

K_{eq} = the equivalent loop gain of the tracking loop which represents the various contributing gains.

$F(s)$ = the open loop range tracking transfer function. $F(s)$ represents the α - β tracker [5] in the loop. The analysis of the α - β tracker is presented in Appendix F of this report, where the transfer function is derived as a function of the parameters α and β .

Since the transient analysis and the dynamic characteristics of the range tracking loop are not a part of this development, the effects of the loop gain and open loop transfer functions are taken into account through the single closed loop noise bandwidth B_N (Hz).

The closed loop transfer function from T to \hat{T} , as seen in Figure 8, is equal to

$$H(j 2\pi f) = \frac{\left(\frac{8\rho}{\tau}\right) K_{eq} F(j 2\pi f)}{1 + \left(\frac{8\rho}{\tau}\right) K_{eq} F(j 2\pi f)} \quad (36)$$

and the corresponding single-sided loop noise bandwidth is defined as

$$B_N(\rho) = \int_0^{\infty} |H(j 2\pi f)|^2 df. \quad (37)$$

The dependence of B_N on ρ has been explicitly indicated to emphasize the dependence of noise bandwidth on the signal-to-noise ratio by way of the normalized correlation coefficient ρ . For intermediate and high gain tracking loops, the dependence of B_N on ρ is approximately given by

$$B_N(\rho) \approx \rho B_N(\rho = 1), \quad (38)$$

where $\rho = 1$ corresponds to the infinite SNR case. This is the case since, at high values of loop gain, the noise bandwidth varies approximately linearly with the equivalent loop gain $(8\rho/\tau)$. This is indeed the case for all loop transfer functions that are anticipated for $F(s)$, including first and second order tracking loops.

The transfer function from the equivalent noise input x to the timing tracking error Δ_T is given by

$$\Delta_T = \left(\frac{\tau}{8\rho}\right) H(p) x, \quad (39)$$

where p denotes the Heaviside operator, so that the variance of the timing error in range tracking is given by

$$\sigma_{\Delta_T}^2 = \left(\frac{\tau}{8\rho}\right)^2 B_N(\rho) T_S \sigma_x^2(N, \rho), \quad (40)$$

where

$\sigma_x^2(N, \rho) = \sigma_x^2$ is the variance of the maximum likelihood estimate of $\ln(P_U/P_V)$, which is also the variance per sample of the noise in the equivalent block diagram of the range tracking loop. The dependence on the correlation coefficient ρ and the number of independent samples N is emphasized in (40)

T_S = time per sample of the random sequence x by the D/A converter in Figure 1. In this system,

$$T_S = T_p(16)(4)(I), \text{ where} \quad (41)$$

$I = 5$ is the number of RF frequencies. The noise samples x are assumed to be statistically independent in each time slot

16 = number of pulses during which $\Sigma + \Delta_J$ is observed (see Figure 2); $J = 1, \dots, 4$.

4 = factor corresponding to the number of different angular error measurements per frequency dwell time, namely, $\Sigma + \Delta_{AZ}$, $\Sigma - \Delta_{AZ}$, $\Sigma + \Delta_{EL}$, and $\Sigma - \Delta_{EL}$.

T_p = pulse repetition interval = 335 μ sec, when PRF = 2987 Hz and 143 μ sec when PRF = 6970 Hz.

Upon substitution of these values into (41),

$$T_S = 320 T_p = 107.2 \text{ msec, when PRF} = 2987 \text{ Hz} \quad (42a)$$

$$T_S = 320 T_p = 45.9 \text{ msec, when PRF} = 6970 \text{ Hz.} \quad (42b)$$

Substituting the above into (40) yields the following expression for the RMS timing error in range tracking,

$$\sigma_{\Delta_T} = \frac{\tau}{8} \left(1 + \frac{4}{\text{SNR}}\right)^{1/2} (B_N(\rho = 1) T_S)^{1/2} \sigma_x(N, \text{SNR}), \quad (43)$$

where τ is the pulse width and SNR is defined in (27) as $P_{\text{avg}} r / (N_0 B_F)$. The RMS of range tracking error is thus given as

$$\sigma_R = \frac{c}{2} \sigma_{\Delta_T}. \quad (44)$$

8.0 PERFORMANCE COMPUTATIONS

The radar parameters needed to compute the RMS range error in (44) are given as

$$\begin{aligned}\tau &= 33.2 \text{ } \mu\text{sec} ; R > 9.5 \text{ nmi} \\ &= 16.6 \text{ } \mu\text{sec} ; 3.8 < R < 9.5 \text{ nmi} \quad [\text{Table 1}]\end{aligned}$$

$$B_N = 0.4, 1, 3 \text{ Hz}$$

$$\begin{aligned}T_S &= 107.2 \text{ msec} ; R > 9.5 \text{ nmi} \quad [\text{Eq. (42a)}] \\ &= 45.9 \text{ msec} ; R < 9.5 \text{ nmi} \quad [\text{Eq. (42b)}]\end{aligned}$$

The specification values for the Ku-band radar system are shown in Figure 9. There is no required specification in the passive mode for $R > 10$ nmi. For the range $4.9 \leq R \leq 10$ nmi, the RMS of the range error is given by

$$\sigma_R = 100 \text{ ft} = 30.47 \text{ m}. \quad (45)$$

In order to obtain the range tracking performance as a function of range, the following radar equation is used to determine the signal-to-noise ratio $[P_{\text{avg}} r / (N_0 B_F)]$ as a function of range

$$\frac{P_{\text{avg}} r}{N_0 B_F} = \frac{[G^2 \bar{\sigma} \lambda^2][d_t P_p \tau_E]}{(4\pi)^3 L[kT_{\text{sys}}] R^4}, \quad (46)$$

where all the parameters in (46) are described in [1]. The values used in the computation are

$$\begin{aligned}G &= \text{peak antenna gain} &= 38.5 \text{ dB} \\ \bar{\sigma} &= \text{radar cross-section} &= 1 \text{ m}^2 \\ \lambda &= \text{wavelength} &= 0.0216 \text{ m} \\ d_t &= \text{duty factor} &= \begin{cases} 0.099 & (R > 9.5 \text{ nmi}) \\ 0.125 & (3.8 < R < 9.5) \end{cases} \\ P_p &= \text{peak transmitted power} &= 60 \text{ watts} \\ \tau_E &= \text{dwell time corresponding to} \\ &\quad \text{one computation of the DFT} = B_F^{-1} &= \begin{cases} 5.36 \text{ msec} & (R > 9.5 \text{ nmi}) \\ 2.29 \text{ msec} & (3.8 < R < 9.5) \end{cases} \\ k &= \text{Boltzmann's constant} &= 1.38 \times 10^{-23} \text{ w/Hz-K} \end{aligned}$$

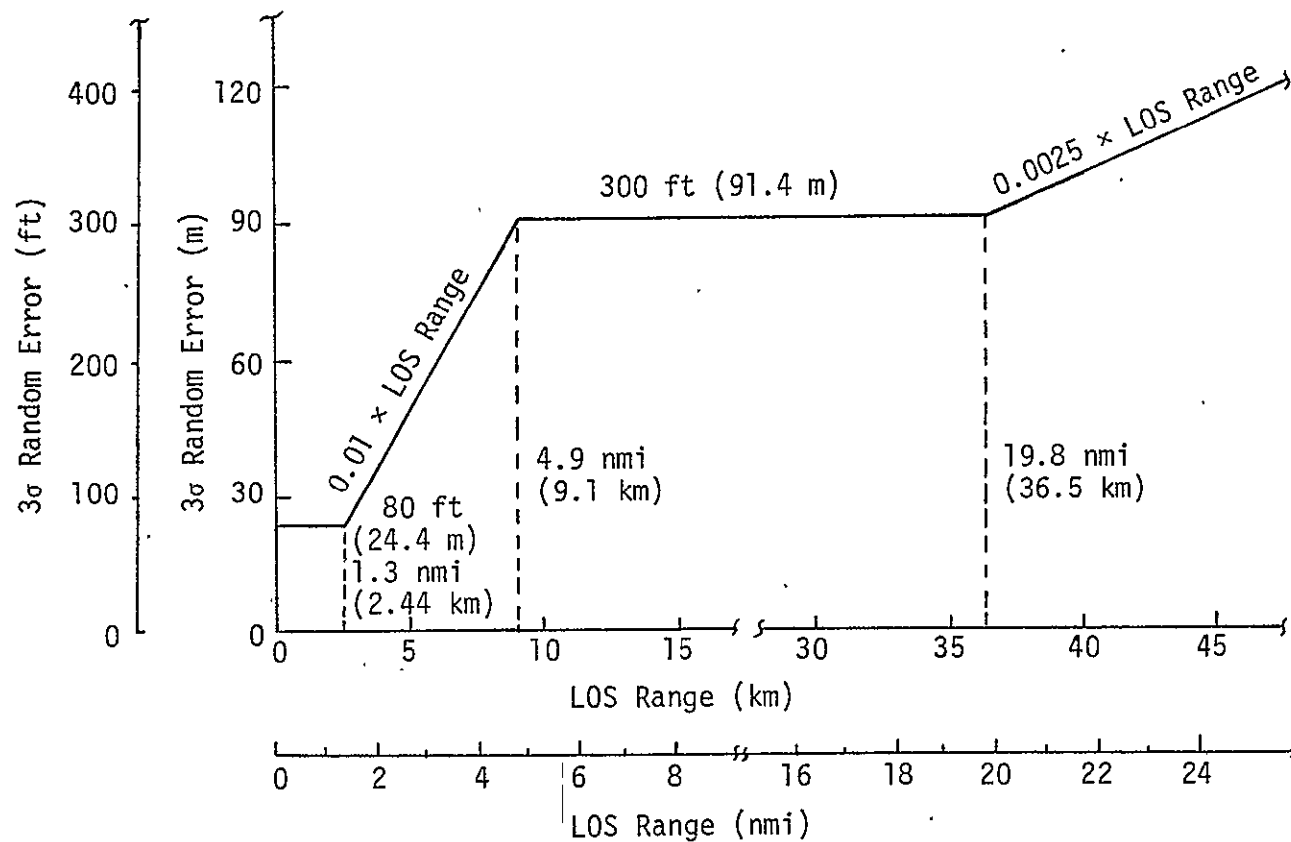


Figure 9. Specification for Three-Sigma Random Range Error vs. LOS Range

T_{sys} = system noise temperature = 1500°K

R = range, in meters

L = losses, itemized as follows for range track:

Transmit	3.7 dB
Scan alignment	0
Lateral scan	0
Threshold	0.5
Processor loss	1.0
Doppler mismatch	1.1
PDI	1.25
Pre-Sum	$\begin{cases} 0.14 & (R > 9.5 \text{ nmi}) \\ 0.07 & (3.8 < R < 9.5) \end{cases}$
Coupling loss	1.8
Total Losses	$\begin{cases} 9.49 \text{ dB} & (R > 9.5 \text{ nmi}) \\ 9.12 \text{ dB} & (3.8 < R < 9.5) \end{cases}$

Quantization loss has not been taken into account because, as is discussed in Appendix H, the quantization loss is small for the signal-to-noise ratios under consideration.

With these parameters, the RMS range tracking error is shown in Figure 10 versus range in nautical miles for $B_N = (0.4, 1, 3)$ Hz or, alternatively, $\alpha = (0.05, 0.1, 0.15)$ (see Appendix F). The design margin, at $R = 10$ nmi, as a function of the loop noise bandwidth is shown in Table 2.

Table 2. Design Margin for Range Tracking

Loop Bandwidth (Hz)	0.4	1.0	3.0
Design Margin (dB)	1.4	-1.6	-8.5

9.0 SIGNAL-TO-NOISE RATIO COUPLING LOSS

In the power budget of Section 8.0, a coupling loss of 1.8 dB is noted. This is obtained via noting the power divider and combiner as seen in Figure 11. In the power divide, the signal and noise powers decrease by a factor of 3 dB. This is due to the fact that the Σ -channel power is divided equally between the communication and radar receivers. The power in the Σ -channel is then combined with that of the Δ -channel after the latter is reduced by a factor of 1/4.

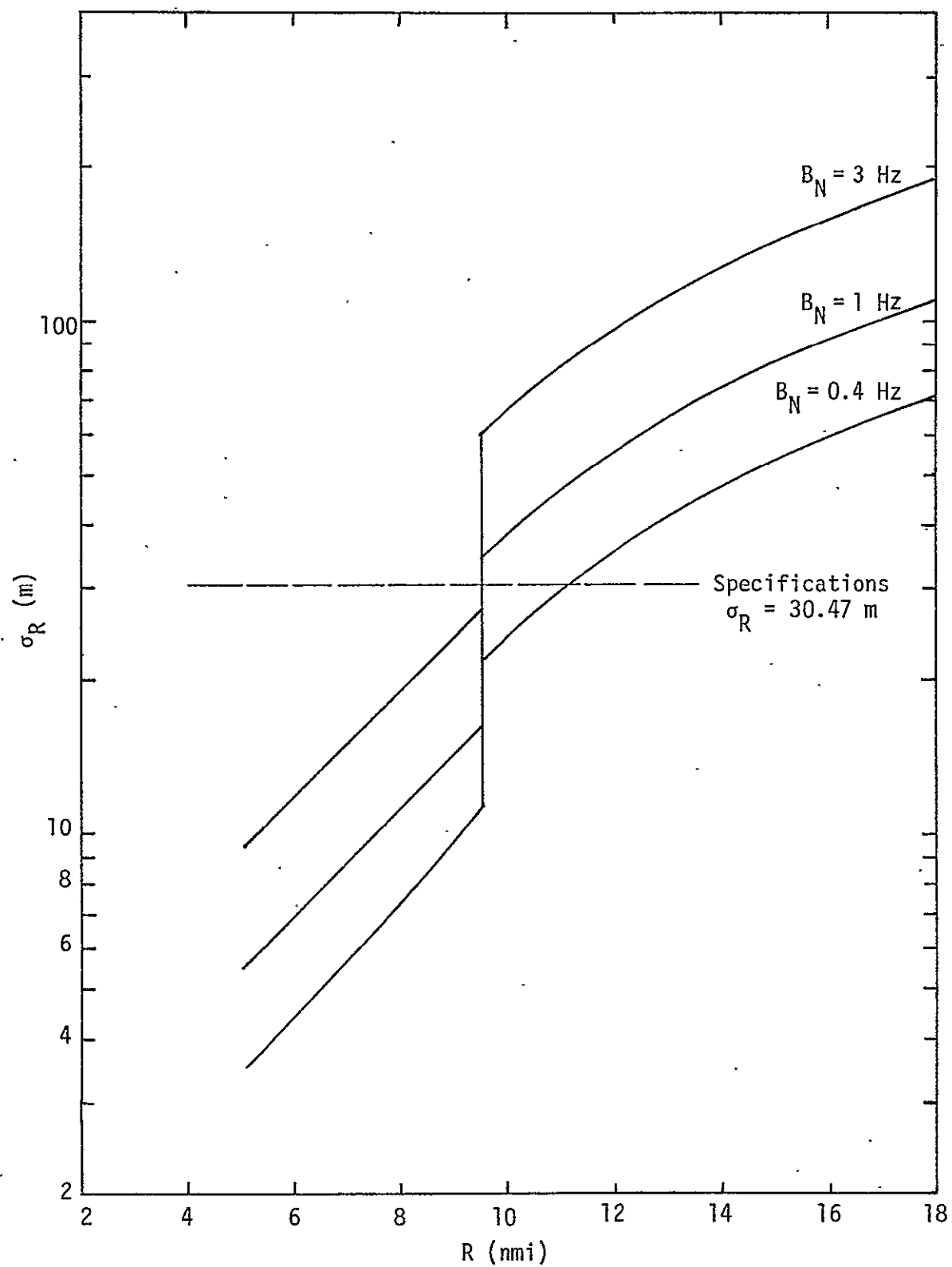


Figure 10. RMS Range Tracking Error of Passive Targets Versus Range (nmi)

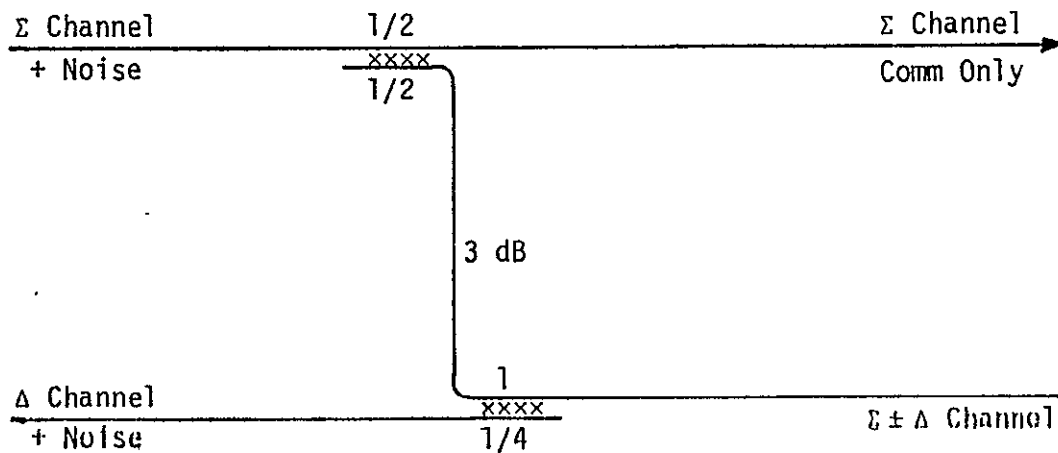


Figure 11. Block Diagram of the Coupling Loss

Since the power in the channel is small compared to that in the Σ -channel and since the noises in the two channels are statistically independent with equal spectral density levels, the signal-to-noise ratio in the $(\Sigma \pm \Delta)$ channel becomes

$$\left. \frac{\text{Signal Power}}{\text{Noise Spectral Density}} \right|_{\Sigma \pm \Delta} = \frac{(\text{Signal Power in } \Sigma\text{-Channel})/2}{\left(\frac{\text{Noise Spectral Density in } \Sigma\text{-Channel}}{2} \right) + \left(\frac{\text{Noise Spectral Density in } \Delta\text{-Channel}}{4} \right)}$$

If we denote the signal power in the Σ -channel by P_s and the noise spectral density by N_0 , then

$$\left. \frac{\text{Signal Power}}{\text{Noise Spectral Density}} \right|_{\Sigma \pm \Delta} = \frac{P_s/2}{N_0/2 + N_0/4} = \frac{2P_s}{3N_0} = \frac{2}{3} \frac{P_s}{N_0}$$

The loss factor $(2/3)$ is equal to 1.8 dB degradation in the signal-to-noise ratio due to coupling loss.

REFERENCES

1. C. L. Weber, S. Udalov, and W. K. Alem. "Study to Investigate and Evaluate Means of Optimizing the Ku-Band Combined Radar/Communication Functions for the Space Shuttle," Axiomatix Report No. R7705-1, May 31, 1977.
2. C. L. Weber. "Maximum Likelihood Estimation of the Ratio of Powers in Two Narrowband Processes," Axiomatix Report No. R7701-3, January 31, 1977.
3. N. E. Nahi. Estimation Theory and Applications. R. E. Kreiger, 1976.
4. Hughes Aircraft Co. "Ku-Band Integrated Radar and Communication Equipment for the Space Shuttle Orbiter Vehicle," Schematic Review Vol. 1, July 1977.
5. C. L. Weber. "The Estimation of Range Rate for Noncoherent Radar," Axiomatix Report No. R7511-3, November 24, 1975.
6. Hughes Aircraft Co. "Proposal for Ku-Band Integrated Radar and Communication Equipment for the Space Shuttle Orbiter Vehicle," Vol. 2, May 1976.
7. B. C. Kuo. Analysis and Synthesis of Sampled Data Control Systems. Prentice-Hall, Inc., 1963.
8. J. Skalansky. "Optimizing the Dynamic Parameters of a Track-While-Scan System," RCA Laboratories, Princeton, N.J., N.d.

APPENDIX F

CONTINUOUS TIME α - β TRACKER MODEL FOR RANGE TRACKING

APPENDIX F

CONTINUOUS TIME α - β TRACKER MODEL FOR RANGE TRACKING

by

Charles L. Weber
Waddah K. Alem

1.0 INTRODUCTION

The subject of the α - β tracker has been discussed in [1-3]. The common type of track-while-scan system which is characterized by two dynamic parameters corresponding to the range error and the range rate error is analyzed in [1], while the performance measures which reflect both noise reduction and maneuver-following capability are described in [2]. An "optimal" relationship between α and β is derived in [2] which insures a certain degree of damping in the dynamic system for all α without significantly degrading the noise performance. An adaptive α - β - γ tracker is discussed in [3], where the constants of the tracker are varied in each step to minimize the mean squared tracking error in that step.

The choice of α is one of bandwidth, which is dependent on the system application. In this appendix, an equivalent continuous time representation of the α - β tracker is presented and incorporated in the range tracking loop (discussed extensively in Appendix E). An equivalent noise bandwidth for the range tracking loop as a function of α is also discussed.

2.0 EQUIVALENT CONTINUOUS α - β TRACKER TRANSFER FUNCTION

The α - β tracker is used in the range tracking loop of the Ku-band radar after the range discriminant estimate is obtained to improve that estimate and to obtain two additional estimates. If the range error signal at the output of the logarithmic discriminant at a given sampling time is $\Delta R(n)$, then the three estimates at the output of the tracker are:

- (1) A predicted range estimate $\hat{R}_p(n+1)$, used to set the new position of the early and late gates.
- (2) A smoothed range estimate $\hat{R}_s(n)$, used for display.
- (3) A smoothed range rate estimate $\hat{\dot{R}}_s(n)$, used to remove doppler ambiguity in velocity measurements [4].

A block diagram of the α - β tracker is shown in Figure 1. T_s denotes the time between two consecutive samples.

The operation of the α - β tracker as seen in Figure 1 can be expressed using the following set of equations:

1. Smoothing Equations

$$\hat{R}_s(n) = \hat{R}_p(n) + \alpha \Delta R(n) \quad (1)$$

$$\hat{\hat{R}}_s(n) = \hat{\hat{R}}_p(n) + \frac{\beta}{T_s} \Delta R(n) \quad (2)$$

2. Prediction Equations

$$\hat{\hat{R}}_p(n+1) = \hat{\hat{R}}_s(n) \quad (3)$$

$$\hat{R}_p(n+1) = \hat{R}_s(n) + T_s \hat{\hat{R}}_s(n) \quad (4)$$

In order to incorporate the α - β tracker in an overall closed range tracking loop, it is essential to find the transfer function of the α - β tracker between the input ΔR and the predicted output $\hat{R}_p(n+1)$ which is used to set the early and late gate position. Defining the z-transform as [5]:

$$G(z) \triangleq \sum_{n=0}^{\infty} g(n) z^{-n}$$

and taking the transforms of (1) through (4) results in :

$$\hat{R}_s(z) = \hat{R}_p(z) + \alpha \Delta R(z) \quad (5)$$

$$\hat{\hat{R}}_s(z) = \hat{\hat{R}}_p(z) + \frac{\beta}{T_s} \Delta R(z) \quad (6)$$

$$z(\hat{\hat{R}}_p(z) - \hat{\hat{R}}_p(n=0)) = \hat{\hat{R}}_s(z) \quad (7)$$

$$z(\hat{R}_p(z) - \hat{R}_p(n=0)) = \hat{R}_s(z) + T_s \hat{\hat{R}}_s(z) \quad (8)$$

where $\hat{R}_s(z)$, $\hat{R}_p(z)$, $\Delta R(z)$, $\hat{\hat{R}}_s(z)$ and $\hat{\hat{R}}_p(z)$ are the z-transforms of $\hat{R}_s(n)$, $\hat{R}_p(n)$, $\Delta R(n)$, $\hat{\hat{R}}_s(n)$, and $\hat{\hat{R}}_p(n)$, respectively, and $\hat{\hat{R}}_p(n=0)$ and $\hat{R}_p(n=0)$ represent the first predicted estimate at time $t = (n=0)$. Solving for $\hat{R}_p(z)$ in terms of $\Delta R(z)$ results in

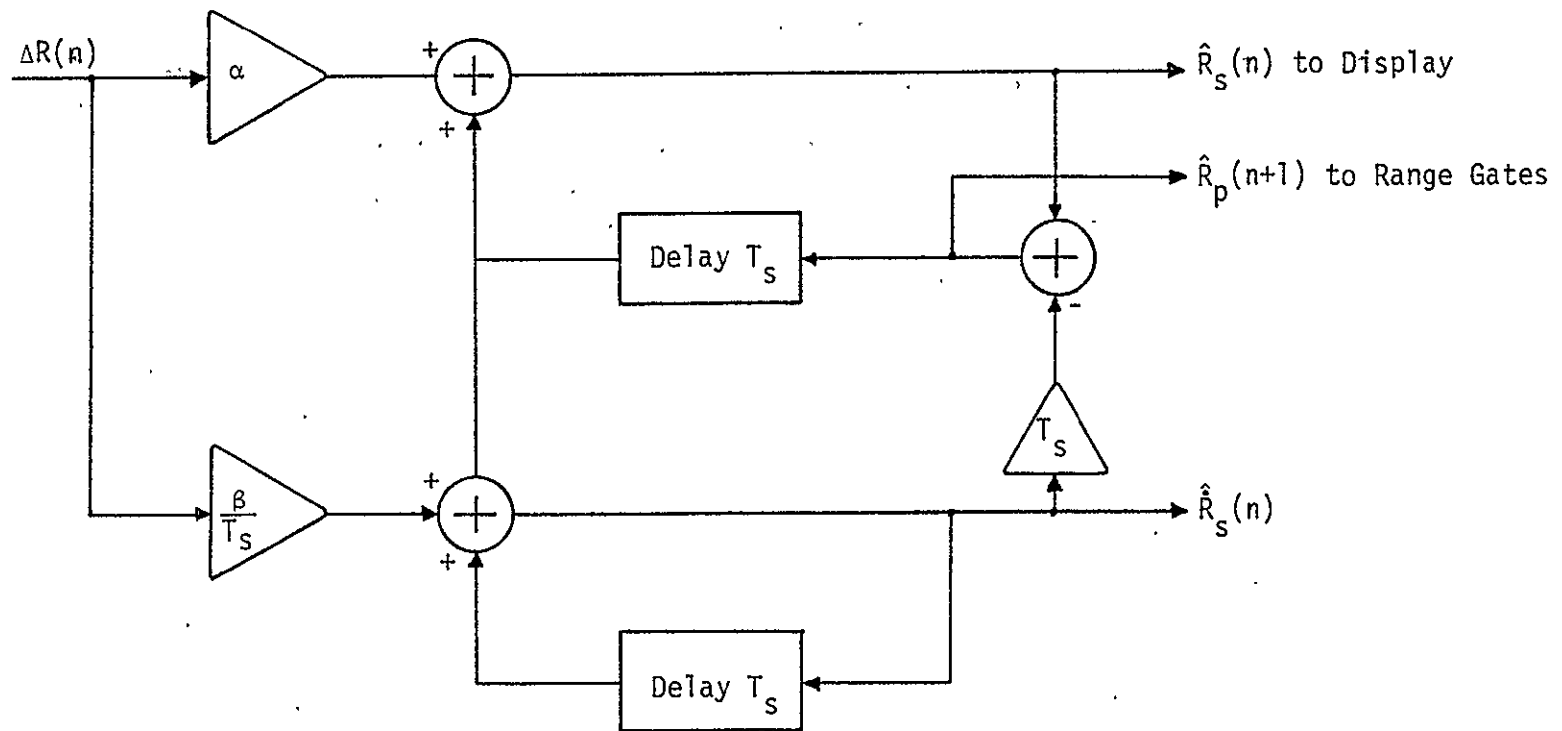


Figure 1. α - β Tracker Block Diagram

$$\hat{R}_p(z) = \frac{\hat{R}_p(n=0) T_s z}{(z-1)^2} + \left(\frac{z}{z-1}\right) \hat{R}_p(n=0) + \left[\frac{\alpha(z-1) + \beta z}{(z-1)^2} \right] \Delta R(z). \quad (9)$$

Since it is assumed that the α - β tracker is operating in a steady-state mode and since $n=0$ represents the initial estimate before any input, $\hat{R}_p(n=0)$ and $\dot{\hat{R}}_p(n=0)$ are set equal to zero. Thus,

$$\hat{R}_p(z) = \frac{\alpha(z-1) + \beta z}{(z-1)^2} \Delta R(z) \quad (10)$$

or
$$\hat{R}_p(z) = G(z) \Delta R(z),$$

where

$$G(z) = \frac{\alpha(z-1) + \beta z}{(z-1)^2} \quad (11)$$

represents the open loop transfer function of the α - β tracker in the complex field. From the basic definition of a z -transform, $G(z)$ can be written as

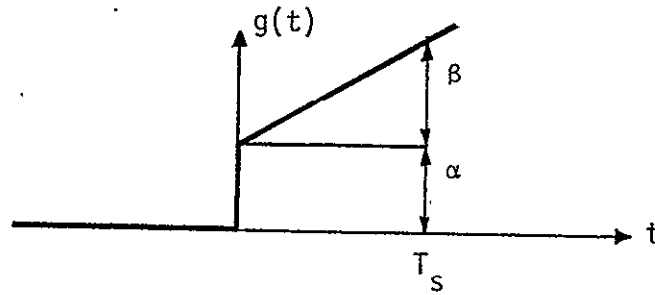
$$G(z) = \sum_{n=1}^{\infty} [(\alpha + \beta n) z^{-n}]. \quad (12)$$

The summation in (12) starts from $n=1$ rather than $n=0$ because this is when the first input sample occurs and because the estimate in each new sampling period is proportional to the range error at the end of the previous sampling period and not to the error at the beginning of the new period [1]. Equation (12) can be written in terms of the related Laplace transform as

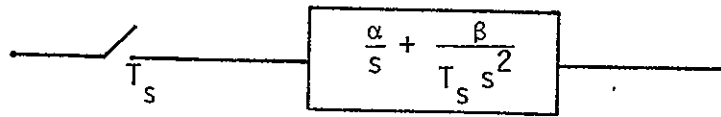
$$G(s) = \frac{\alpha}{s} + \frac{\beta}{T_s s^2}. \quad (13)$$

The equivalent block diagram and the continuous time response of the α - β tracker are shown in Figure 2. It can be seen that the constants of proportionality, α and β , used in estimating the range and velocity completely characterize the performance of the α - β tracker. Obviously, the behavior of the system varies with the values of the constants α and β .

(a) Time Response



(b) Equivalent block diagram

Figure 2. Open Loop α - β Tracker Transfer Function

A plot of the "optimum" β , as obtained in [2] and quoted in [6], namely,

$$\beta = \frac{\alpha^2}{2 - \alpha} \quad (14)$$

is shown in Figure 3 as a function of α .

3.0 RANGE TRACKING LOOP NOISE BANDWIDTH

The range tracking loop was derived in Appendix E with an equivalent loop gain (K_{eq}) and a loop filter transfer function $F(s)$. In this section, the noise bandwidth (B_L) of the loop is derived as a function of α and β , and evaluated for some currently suggested values of α using the "optimum" value of β given in (14). Figure 4 shows a block diagram of the equivalent range tracking loop with the α - β tracker as its open loop filter (Figure 8 of Appendix E). In Figure 4,

T = actual time delay between the transmission and reception of a given pulse. For a passive target at range R , $T = 2R/c$, where c is the velocity of light in free space.

\hat{T} = loop estimate of the actual delay T .

$\Delta_T = T - \hat{T}$ = timing error.

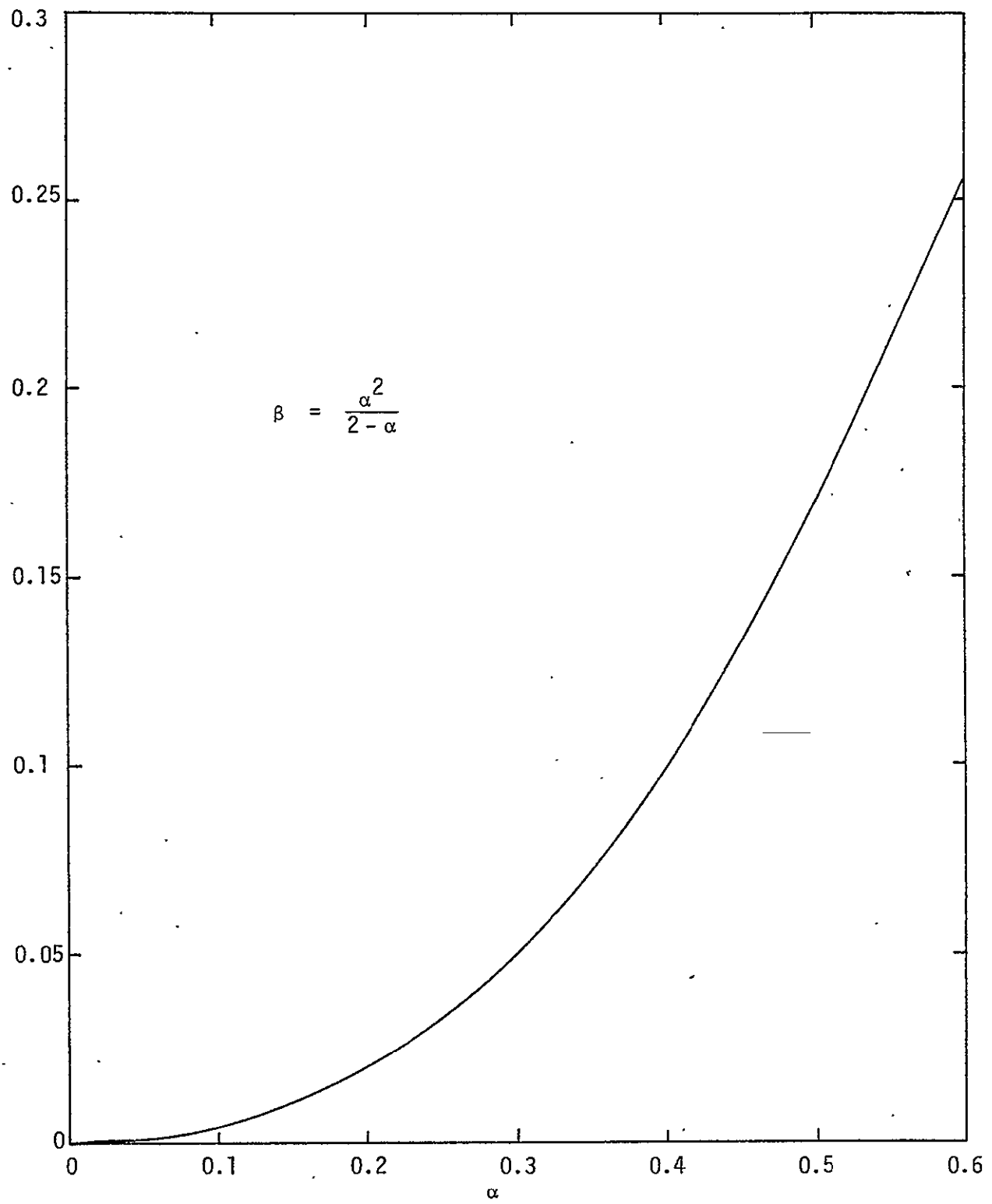


Figure 3. The "Optimum" Value of β vs. α

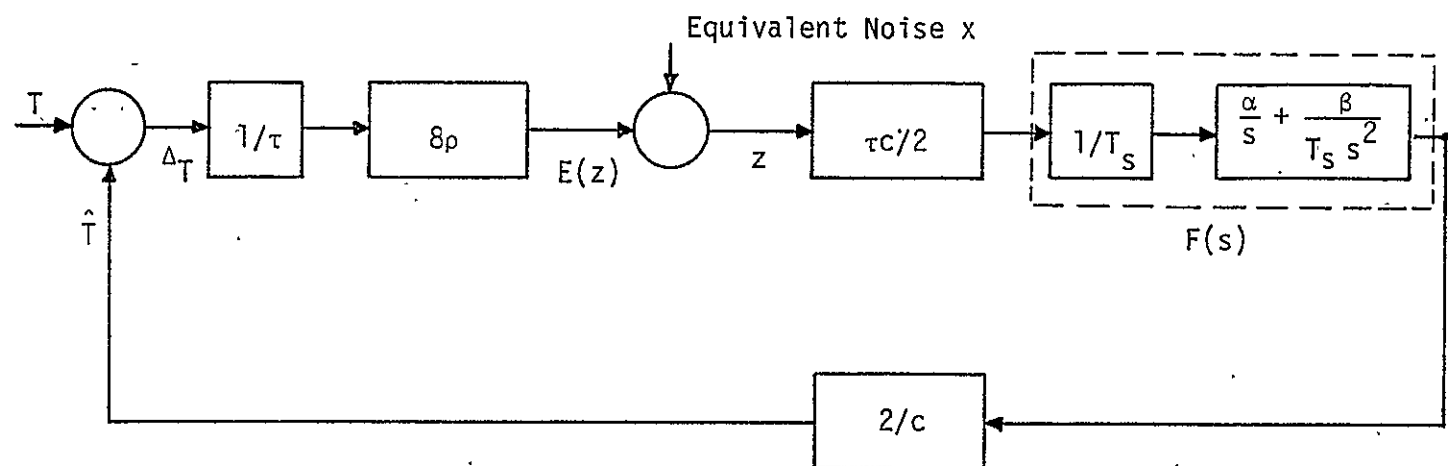


Figure 4. Block Diagram of the Equivalent Range Tracking Loop

τ = the pulse width which is equal to 33.2 μ sec for $R > 9.5$ nmi and 16.5 μ sec for $3.8 < R < 9.5$ nmi. $1/\tau$ is used as a scale factor to convert the timing error into a normalized error δ as defined in Appendix E, Section 3.0.

8ρ = scale factor necessary to give $E(z) = \ln(P_U/P_V)$. The normalized correlation coefficient ρ is given by [(26), Appendix E]

$$\rho = \frac{1}{1 + 4/\text{SNR}},$$

where SNR is the signal-to-noise ratio at the output of the doppler filters.

x = equivalent noise of the system due to thermal noise.

$z = \ln(P_U/P_V) + x$ is the normalized output of the logarithmic discriminant generator.

$\frac{\tau C}{2}$ = scale factor used to convert the normalized output of the logarithmic generator (z) into a range error.

$\frac{2}{C}$ = scale factor used to convert the output of the loop filter $F(s)$ to a timing estimate of \hat{T} .

$F(s)$ = open loop range tracking transfer function of the loop filter given by

$$F(s) = \frac{1}{T_s} \left[\frac{\alpha}{s} + \frac{\beta}{T_s s^2} \right]. \quad (15)$$

The factor $1/T_s$ multiplying the α - β tracker function in (15) is used because the block diagram in Figure 4 is a continuous time equivalent tracking loop of the actually implemented discrete time loop. Since $1/s$ represents an integration in the time domain, the scale factor $1/T_s$ is essential to make the open loop filter an averaging filter over the computation time T_s per sample of the random sequence x . T_s is given by

$$T_s = 107.2 \text{ msec, when PRF} = 2987 \text{ Hz} \quad (16a)$$

$$T_s = 45.9 \text{ msec, when PRF} = 6970 \text{ Hz.} \quad (16b)$$

Defining

$$\alpha' \triangleq \frac{8\rho}{T_s} \alpha \quad (17a)$$

$$\beta' \triangleq \frac{8\rho}{T_s} \beta, \quad (17b)$$

the closed loop transfer function can be written as

$$H(s) = \frac{\alpha' (s + \beta' / (\alpha' T_s))}{s^2 + \alpha' s + \beta' / T_s} \quad (18)$$

The noise bandwidth of the loop is defined as

$$B_N(\rho) \triangleq \int_0^\infty |H(j 2\pi f)|^2 df$$

which, when evaluated, results in [7]:

$$B_N(\rho) = \frac{8\rho\alpha^2 + \beta}{4\alpha T_s} \quad (19)$$

For $\beta = \alpha^2 / (2 - \alpha)$, Equation (19) becomes

$$B_N(\rho) = \frac{8\rho\alpha(2 - \alpha) + \alpha}{4 T_s (2 - \alpha)} \quad (20)$$

Table 1. summarizes the values of $B_N(\rho=1)$ for various values of α .

Table 1. Noise Bandwidth (Hz) as a Function of α
 $\rho = 1$, $\beta = \alpha^2 / (2 - \alpha)$, $T_s = 106.2$ msec

α	0.05	0.1	0.15	0.2
$B_N(\rho=1)$, Hz	1.01	2.07	3.19	4.35

The RMS of the range error (timing error) is computed using [Equations (43) and (44), Appendix E]:

$$\sigma_R = \frac{\tau_C}{4} \left(1 + \frac{4}{\text{SNR}}\right)^{1/2} (B_N(\rho=1) T_s)^{1/2} \sigma_x(N, \text{SNR}), \quad (21)$$

where N is the number of independent samples used to obtain σ_x (for range tracking, $N = 20$). Substituting (20) into (21) yields

$$\sigma_R = \frac{\tau_C}{4} \left(1 + \frac{4}{\text{SNR}}\right)^{1/2} \frac{\alpha(17 - \alpha)}{4(2 - \alpha)} \sigma_x(N, \text{SNR}), \quad (22)$$

which is the required equation for finding the RMS range error at a given range as a function of the parameter α .

Using Equation (46) of Appendix E, namely,

$$\text{SNR} = \frac{[G^2 \sigma \lambda^2][d_t P_p \tau_E]}{(4\pi)^3 L [k T_{\text{sys}}] R^4},$$

the RMS range error can be calculated as a function of range. The results are plotted in Figure 5, where the range error is shown as a function of range for $\alpha = 0.05$ and $\alpha = 0.1$. Similar computations with the noise bandwidth B_N as a parameter are illustrated in Figure 10 of Appendix E.

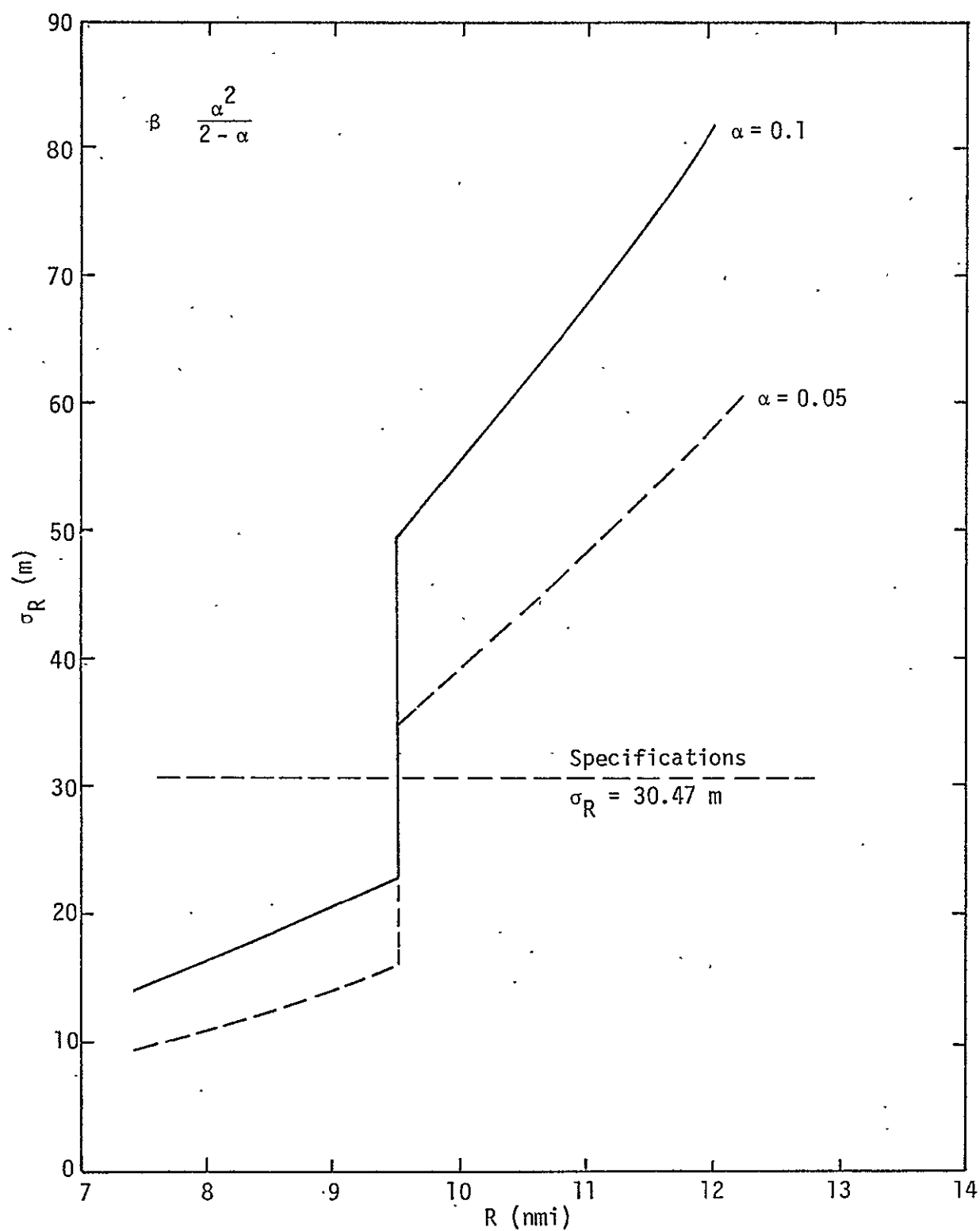


Figure 5. Range RMS Error vs. Range with α as a Parameter

REFERENCES

1. J. Sklansky. "Optimizing the Dynamic Parameters of a Track-While-Scan System," RCA Review, Vol. 18, June 1957, pp. 163-185.
2. T. R. Benedict and G. W. Bordner. "Synthesis of an Optimal Set of Radar Track-While-Scan Smoothing Equations," IRE Transactions on Automatic Control, July 1962, pp. 27-32.
3. C. L. Weber. "The Estimation of Range Rate for Noncoherent Radar," Axiomatix Report No. R75100-3, Appendix D, November 24, 1975.
4. C. L. Weber, S. Udalov, and W. K. Alem. "Study to Investigate and Evaluate Means of Optimizing the Ku-Band Combined Radar/Communication Functions for the Space Shuttle," Axiomatix Report No. R7705-1, Appendix B, May 1977.
5. B. C. Kuo. Analysis and Synthesis of Sampled-Data Control Systems. Prentice-Hall, Inc., Englewood Cliffs, N.J., 1963.
6. "Space Shuttle Ku-Band Integrated Rendezvous Radar/Communications System Study," Final Report,
7. A. J. Viterbi. Principles of Coherent Communication. McGraw-Hill Book Company, N.Y., 1966.

APPENDIX G

TIME MULTIPLEXED SINGLE CHANNEL RANGE RATE TRACKING OF PASSIVE TARGETS

APPENDIX G

TIME MULTIPLEXED SINGLE CHANNEL RANGE RATE TRACKING OF PASSIVE TARGETS

by

Charles L. Weber
Waddah K. Alem

1.0 INTRODUCTION

Range rate tracking is carried out in a way similar to range tracking by sequential processing of monopulse signals. The single channel sequential processing is carried out by time division multiplexing between four signals— $\Sigma + \Delta_{AZ}$, $\Sigma - \Delta_{AZ}$, $\Sigma + \Delta_{EL}$, and $\Sigma - \Delta_{EL}$ —each occupying a separate time slot. In order to form a range rate error the signals are first passed through early and late timing gates which are used for range tracking. Pre-summing is performed at the range gates. Each received pulse results in two signals, one from each range gate. The signals are then processed through a bank of doppler filters (DFT). The outputs of the doppler filter which is centered at a higher frequency than the actual doppler (high filter) and that which is centered at a lower frequency (low filter) are then processed through a post-integration stage before a logarithmic discriminant forms the range rate error [1].

As discussed in Appendices B and C, there is also a filter between the high filter and low filter which is used for angle and range tracking. If the filters are indexed F_n , F_{n+1} , F_{n+2} , then filters F_n and F_{n+2} are used in forming the logarithmic discriminant for doppler filtering, and filter F_{n+1} , whose center frequency is closest to the actual doppler frequency, is used for range and angle tracking.

The center frequencies of the filters in the bank of doppler filters do not move during the tracking process. When an error becomes sufficiently large so that it is better to use different high and low filters for the formation of the logarithmic discriminant, the change to the new set is carried out.

At long ranges, $R > 9.5$ nmi, the time between outputs of the log discriminant is 107.2 msec, as shown in Appendix C. This opens the possibility that, during an acceleration mode, the velocity could change

sufficiently that there is loss of lock. As described in more detail in Appendix C, this conservatively might occur if there is a doppler frequency shift of approximately 93 Hz. This converts to an acceleration of approximately 30 ft/sec^2 , or about 1 g. This is an order of magnitude greater than the maximum acceleration anticipated. Therefore, loss of lock due to acceleration is quite remote.

Due to the periodic nature of the filtering operation, doppler ambiguity might result. This is resolved by comparing the obtained doppler estimate to that from the α - β tracker. In this appendix, the range rate tracking accuracies in the passive mode are calculated.

2.0 DESCRIPTION OF SINGLE CHANNEL MONOPULSE TRACKING SYSTEM

The single channel monopulse block diagram was described in Appendix B of this report. The description is repeated here for convenience.

The amplitude monopulse feed of the Ku-band antenna system outputs three channels of data—the sum channel Σ , the azimuth error channel Δ_{AZ} , and the elevation error channel Δ_{EL} , as shown in Figure 1. As described in more detail in Appendix B of [1], the elevation and azimuth error channels time-share the single signal processing channel. The modulation by ± 1 either passes the error signal unchanged or inverts the RF phase. After recombining the error channel with the sum channel, the time-sharing is as shown in Figure 2.

During the track mode of operation, the frequency diversity consists of 5 RFs, each of which operates for $\tau_F = 21.44 \text{ msec}$. During each RF frequency, the single channel processing is equally time-shared among the four signals— $\Sigma + \Delta_{AZ}$, $\Sigma - \Delta_{AZ}$, $\Sigma + \Delta_{EL}$, $\Sigma - \Delta_{EL}$ —in the four time slots. Each of these is processed for $\tau_E = 5.36 \text{ msec}$ (designated the slot time), during which time 16 pulses are transmitted and received. Throughout this description, the system parameters corresponding to the largest range interval of interest are being employed. In particular [4]:

$$\text{PRI} = T_p = \text{pulse repetition interval} = 335 \text{ } \mu\text{sec}$$

$$\text{PRF} = 2987$$

$$\text{Pulse width} = \tau = 33.2 \text{ } \mu\text{sec}$$

$$\text{Frequency Dwell Time} = \tau_F = 21.44 \text{ msec/RF.}$$

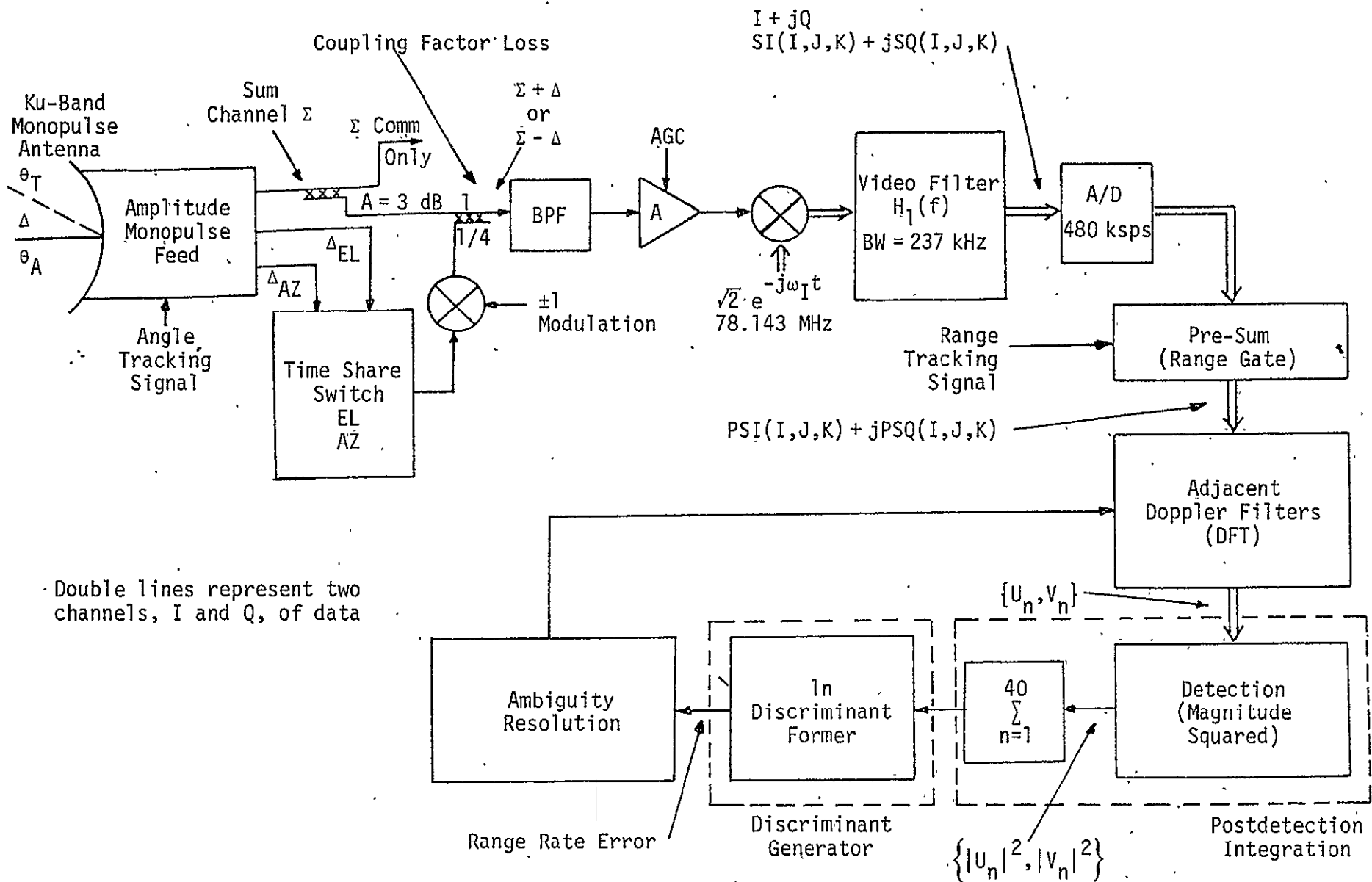


Figure 1. Block Diagram of Single-Channel Monopulse Range Rate Tracking Loop

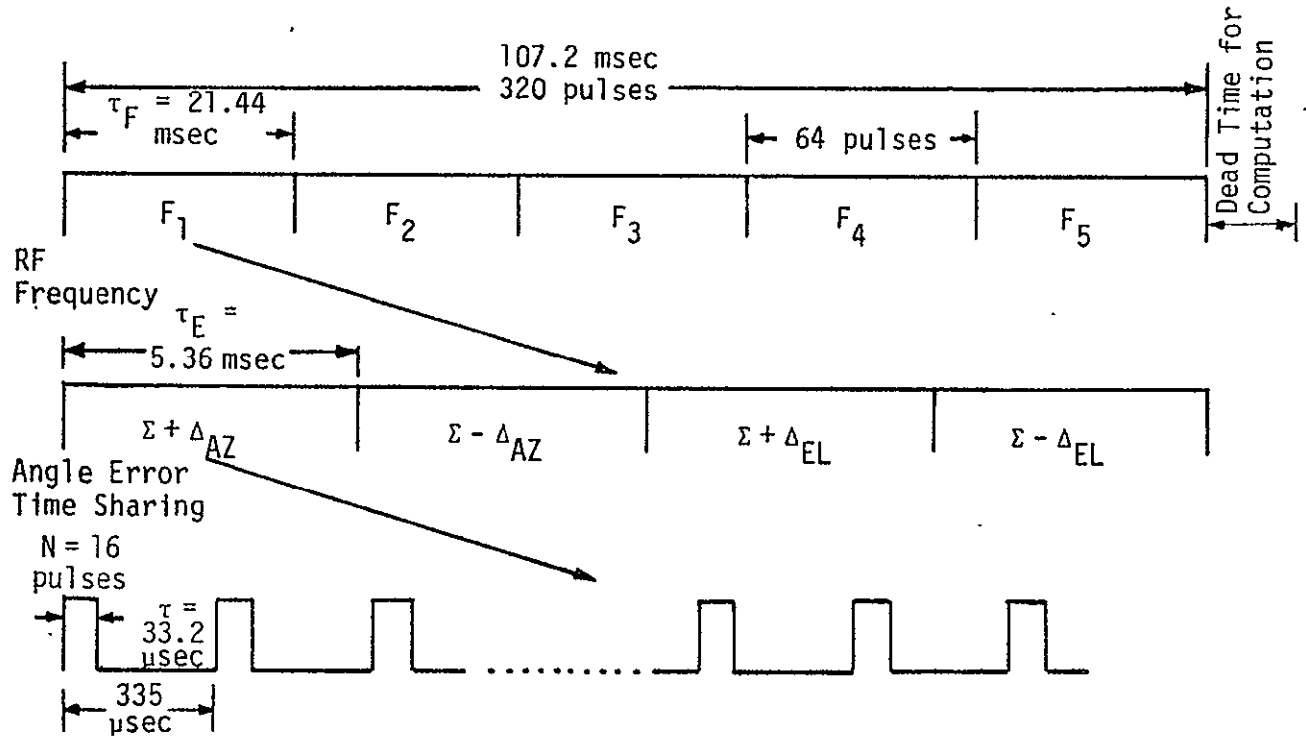


Figure 2. Timing for Single-Channel Time-Shared Monopulse Tracking, PRF = 2987 Hz

τ_E is the dwell time of $\Sigma + \Delta_{AZ}$, which is one of the four time slots for each frequency dwell; the range interval for this set of parameters is 9.5 to 18.9 nmi. The equivalent coherent integration time/frequency is defined as $\tau_c \triangleq 16\tau$.

Referring again to Figure 1, the various stages of IF and AGC are simplified and consolidated into one bandpass filter (BPF) and AGC. The AGC is shown but not taken into account in the tracking performance analysis, since for tracking purposes, the logarithmic discriminant is already self-normalizing. The primary purpose of the AGC is to maintain satisfactory signal level in the receiver and avoid receiver saturation. The AGC is herein assumed to be performing its operations so that all normalization can be accounted for in the discriminant.

The final stage of IF converts the sum plus error narrowband signals to I and Q (complex) baseband waveforms. The video filter before the A/D is a 2-pole Butterworth with transfer function

$$|H_1(f)|^2 = \left[1 + \left(\frac{f}{f_c} \right)^4 \right]^{-1},$$

where $f_c = 237$ kHz. At these longer ranges, $R > 9.5$ nmi, where the pulse width is $33.2 \mu\text{sec}$, the signal can be assumed to be undistorted by $H_1(f)$.

The sampling frequency of the A/D is 480 ksps, which corresponds to 16 samples over each pulse width τ . This is a sufficiently large number so that the pre-sum can be accurately approximated by analog integration.

The notation developed in the previous report [1] is maintained; in particular,

$I = 1, \dots, 5$ corresponds to RF frequency

$J = 1, \dots, 4$ corresponds to time slot;

$J = 1$ implies $\Sigma + \Delta_{AZ}$

$J = 2$ implies $\Sigma - \Delta_{AZ}$

$J = 3$ implies $\Sigma + \Delta_{EL}$

$J = 4$ implies $\Sigma - \Delta_{EL}$

$K = 1, \dots, 16$ corresponds to the pulse number for a given I and J .

There are actually additional pulses transmitted periodically to allow time for signal processing, register resets, etc. Without loss of generality, only those signals which contribute to the range rate tracking operation and performance are taken into account.

Now consider the complex baseband waveforms before the pre-sum for a given time slot J ;

$$SI(I, J, K) = \{ \sqrt{2} (\Sigma + \Delta_J) A_I P(t - kT_p) \cos [(\omega_I + \omega_d)t + \theta_I] + n(t) \} \sqrt{2} \cos (\omega_I t) \quad (1a)$$

and

$$SQ(I, J, K) = \{ \sqrt{2} (\Sigma + \Delta_J) A_I P(t - kT_p) \cos [(\omega_I + \omega_d)t + \theta_I] + n(t) \} \sqrt{2} \sin (\omega_I t) \quad (1b)$$

for the I and Q channel, respectively. The peak received signal power is given by

$$P_{pr} = E[A_I^2], \quad (2)$$

where it is assumed that $(\Sigma + \Delta_J)$, for all J's, is normalized to 1. The average received power is then

$$P_{avg\ r} = d_t P_{pr}, \quad (3)$$

where d_t is the duty factor of the radar pulse train. The duty factor is constant for a given designated range but varies for different range designations. (For values of d_t as a function of the designated range, see Table 1, Appendix C.)

Since the target is assumed to be Swerling I, the amplitudes A_I are assumed to be Rayleigh random variables. The random phase θ_I is assumed to be uniformly distributed over $(0, 2\pi)$. The Rayleigh and uniform variables, A_I and θ_I , respectively, are independent. The pulse $P(t)$ has a magnitude of unity over the transmitted pulse width $\tau = 33.2 \mu\text{sec}$. The doppler frequency shift is represented by ω_d .

The receiver noise $n(t)$ after the bandpass filter has the narrow-band representation

$$n(t) = \sqrt{2} [N_c(t) \cos \omega_I t - N_s(t) \sin \omega_I t], \quad (4)$$

where N_c and N_s are independent zero mean narrowband Gaussian processes with one-sided power spectral density of N_0 watts/Hz, and one-sided noise bandwidth approximately equal to f_c . ($f_c = 237 \text{ kHz}$), which is the 3 dB bandwidth of $H_1(f)$. Before the A/D, the complex waveform is given by

$$\begin{aligned} SI + jSQ &= [\sqrt{2} (\Sigma + \Delta_J) A_I P(t - kT_p) \cos [(\omega_I + \omega_d)t + \theta_I] + n(t)] \sqrt{2} e^{-j\omega_I t} \\ &= (\Sigma + \Delta_J) A_I P(t - kT_p) \exp [j(\omega_d t + \theta_I)] + N_c(t) + jN_s(t). \end{aligned} \quad (5)$$

3.0 PRE-SUM (RANGE GATES)

After the A/D, each received pulse is pre-summed over the pulse width. The timing of this pre-sum is dependent on the setting of the range gates in the range tracking loop. Two range gates were used for every pulse, an early gate and a late gate, as shown in Figure 3. The early and late gates will be represented by an additional index $L = -1, +1$, respectively. If the relative offset in the range gate setting is δ , then the output of the early gate is given by

$$ZP(I, J, K, -1) = \int_{kT_p + \tau(\delta - 1/2)}^{kT_p + \tau(\delta + 1/2)} (SI + jSQ) dt \quad (6)$$

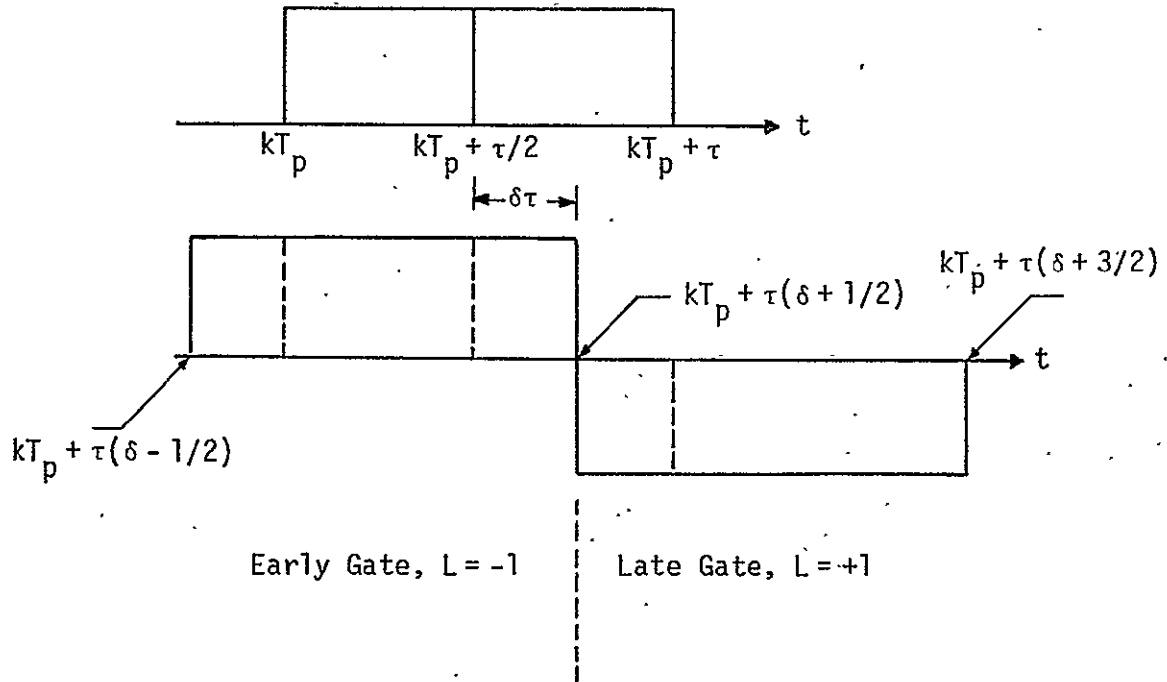


Figure 3. Early and Late Gates Alignment

and the output of the late gate is

$$ZP(I, J, K, +1) = \int_{kT_p + \tau(\delta + 1/2)}^{kT_p + \tau(\delta + 3/2)} (SI + j SQ) dt, \quad (7)$$

where the digital sum of the pre-sum is being approximated by analog integration.

4.0 DOPPLER FILTERING

A bank of 16 doppler filters are used for range rate tracking, as shown in Figure 4a. The numbers in parentheses represent the values for designated ranges less than 9.5 nmi when PRF = 6970 Hz, whereas the other numbers are those pertaining to $R > 9.5$ nmi, where PRF = 2987 Hz. These PRFs correspond to the third IF frequency and are chosen because they represent the middle frequency. For more details, see Appendix B.

The filters are uniformly spaced over the frequency range $[f_c, f_c + f_{PRF}]$. The spacing between two adjacent doppler filters is designated as B_F , which is equal to 186 Hz for $R > 9.5$ nmi and 448 Hz for $R < 9.5$ nmi. B_F is equal to the one-sided 3 dB bandwidth of the doppler filters.

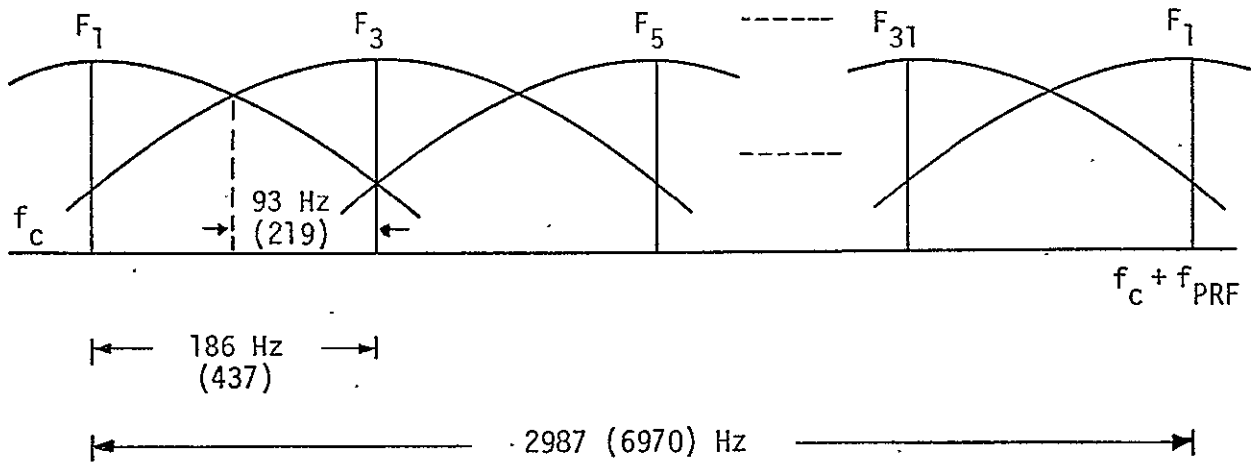


Figure 4a. The Doppler Filters Bank

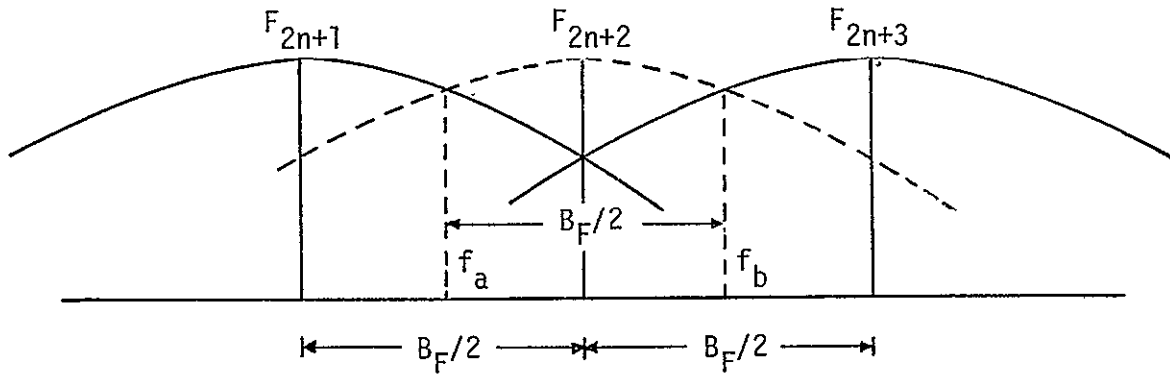


Figure 4b. Doppler Filter Configuration in the Track Mode

In the actual implementation of the track mode, the 16 doppler filters are designated F_{2n+1} , where $n=0,1,\dots,15$. In addition, even-numbered filters (F_{2n+2} , $n=0,\dots,15$) are also formed. The even filters which are identical to the odd filters are located between the odd filters in such a way that the center frequencies of the new configuration are $(B_F/2)$ Hz apart, as seen in Figure 4b.

Instead of continuously adjusting the location of the filters as a result of a new range rate estimate, the filters are kept fixed as long as the error is small. This means that, if F_{2n+1} and F_{2n+3} are used for range rate error calculations, then F_{2n+2} will be used to obtain the actual doppler reading as long as the doppler frequency is between f_a and f_b . If the doppler frequency exceeds f_b , the filter F_{2n+4} is used and if it becomes less than f_a , filter F_{2n} is used.

Assuming that the actual doppler in the received signal is equal to ω_d and denoting the frequency offset between the actual doppler and the low (high) doppler filters by ω_1 (ω_2), then the center frequencies of the low and high filters can be expressed as $\omega_d - \omega_1$ and $\omega_d + \omega_2$, respectively. Figure 5 illustrates the various parameters under consideration.

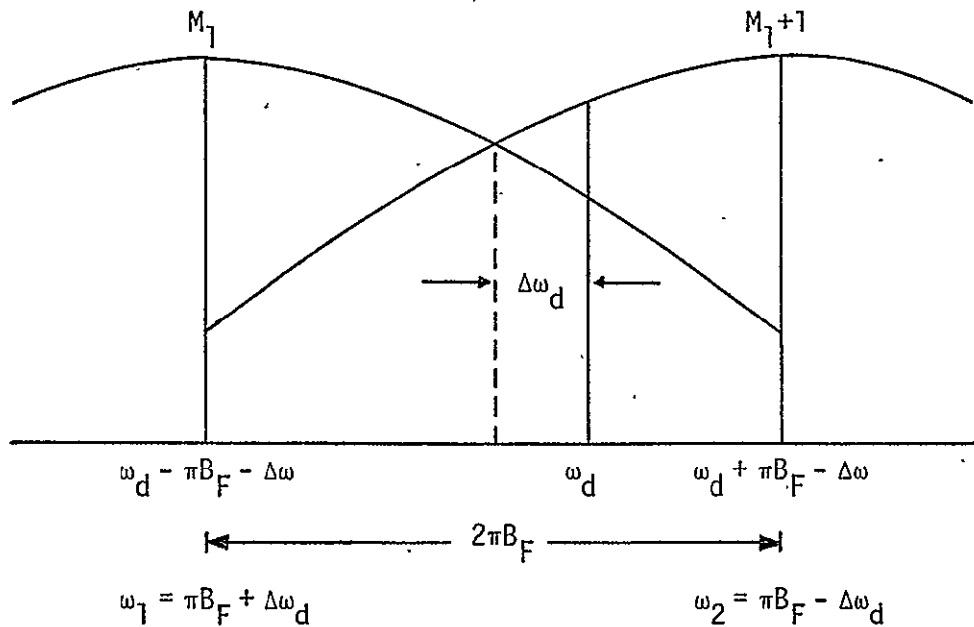


Figure 5. Doppler Frequency Location

The parameter $\Delta\omega_d$ denotes the doppler offset relative to the center location between the low and high filters. As can be easily seen in Figure 5,

$$\omega_1 = \pi B_F + \Delta\omega_d \quad (8a)$$

$$\omega_2 = \pi B_F - \Delta\omega_d \quad (8b)$$

The effect of DFT filtering can be approximated by multiplying $SI + jSQ$ by $\exp[-j(\omega_d - \omega_1)]$ and $\exp[-j(\omega_d + \omega_2)]$ before the pre-sum integration and extending the equivalent integration over the length of a time slot ($\tau_E = 5.36$ msec). This corresponds to the single-sided bandwidth of each doppler filter.

The actual implementation where pre-summing precedes doppler filtering results in an effective power loss of not more than 0.6 dB, which will be taken into consideration when calculating the tracking error in subsequent sections. The trade-offs between the two implementations are discussed in Appendix C.

5.0 STATISTICAL PARAMETERS IN DOPPLER FILTER OUTPUTS

Referring to Figure 5, the outputs of the two adjacent doppler filters (M_1 and M_1+1) will be denoted by $W(I, J, M_1, \pm 1)$ and $W(I, J, M_1+1, \pm 1)$ where -1 corresponds to the early gate and $+1$ corresponds to the late gate. Since the outputs of both the early and late gates and the high and low doppler filters are being processed to obtain the range rate accuracies, there are four outputs to be considered; each has a signal part W_s and a noise part W_n . Approximating the pre-sum by an analog integration, the signal part of the output of the doppler filters is found by examining the location of the signal with respect to the range gates which adjust the limits of the integrals under consideration. For the low filter (M_1),

$$W_s(I, J, M_1, -1) = (\Sigma + \Delta_J) A_I \frac{1}{\tau_E} \sum_{k=0}^{N-1} \int_{kT_p}^{kT_p + \tau(\delta+1/2)} \exp[j(\theta_I + \omega_1 t)] dt \quad (9)$$

and

$$W_s(I, J, M_1, +1) = (\Sigma + \Delta_J) A_I \frac{1}{\tau_E} \sum_{k=0}^{N-1} \int_{kT_p + \tau(\delta+1/2)}^{kT_p + \tau} \exp[j(\theta_I + \omega_1 t)] dt \quad (10)$$

for the early and late gates, respectively. $N=16$ is the number of received pulses per time slot (J). Carrying out the integration and summation results in

$$W_S(I, J, M_1, -1) = (\Sigma + \Delta_J) A_I e^{j(\theta_I + \omega_1 \tau(1/2 + \delta)/2)} \frac{\sin [\omega_1 \tau(1/2 + \delta)/2]}{\omega_1 \tau(1/2 + \delta)/2} \\ \times \frac{\sin \omega_1 \tau_E/2}{N \sin (\omega_1 T_p/2)} e^{j(\tau_E - T_p)\omega_1/2} \left(\frac{1}{2} + \delta\right) d_t \quad (11)$$

and

$$W_S(I, J, M_1, +1) = (\Sigma + \Delta_J) A_I e^{j(\theta_I + \omega_1 \tau(3/2 + \delta)/2)} \frac{\sin [\omega_1 \tau(1/2 - \delta)/2]}{\omega_1 \tau(1/2 - \delta)/2} \\ \times \frac{\sin (\omega_1 \tau_E/2)}{N \sin (\omega_1 T_p/2)} e^{j(\tau_E - T_p)\omega_1/2} \left(\frac{1}{2} - \delta\right) d_t \quad (12)$$

Assuming that the range tracking loop is performing ideally, which implies that $\delta = 0$, the outputs of the low filter can be written as:

$$W_S(I, J, M_1, -1) = (\Sigma + \Delta_J) A_I e^{j[\theta_I + \omega_1 \tau/4]} \frac{d_t}{2} \frac{\sin [\omega_1 \tau/4]}{\omega_1 \tau/4} \\ \times \frac{\sin (\omega_1 \tau_E/2)}{N \sin (\omega_1 T_p/2)} e^{j(\tau_E - T_p)\omega_1/2} \quad (13)$$

$$W_S(I, J, M_1, +1) = (\Sigma + \Delta_J) A_I e^{j[\theta_I + 3\omega_1 \tau/4]} \frac{d_t}{2} \frac{\sin [\omega_1 \tau/4]}{\omega_1 \tau/4} \\ \times \frac{\sin (\omega_1 \tau_E/2)}{N \sin (\omega_1 T_p/2)} e^{j(\tau_E - T_p)\omega_1/2} \quad (14)$$

Since $\omega_1 \tau/4 \ll 1$, the term involving $\sin (\omega_1 \tau/4)/(\omega_1 \tau/4)$ is set equal to unity. Also, assuming that the angle tracking loop is performing ideally, Δ_J is set to equal zero. Since, in Section 2, $(\Sigma + \Delta_J)$ is normalized to unity, the outputs of the low filter can now be written as

$$W_S(I, J, M_1, -1) = A_I \frac{d_t}{2} \frac{\sin (\omega_1 \tau_E/2)}{N \sin (\omega_1 T_p/2)} \exp [j(\theta_I + \omega_1 (\frac{\tau}{2} + \tau_E - T_p)/2)] \quad (15)$$

and

$$W_S(I, J, M_l, \pm 1) = A_I \frac{d_t}{2} \frac{\sin(\omega_1 \tau_E/2)}{N \sin(\omega_1 T_p/2)} \exp [j(\theta_I + \omega_1(\frac{3\tau}{2} + \tau_E - T_p)/2)]. \quad (16)$$

The noise term W_n added to each of the outputs can be found as in Appendix E. The variance of W_n for the four outputs under consideration is found to be [Eq. (19), Appendix E],

$$\sigma_{W_n}^2 = d_t N_0 B_F. \quad (17)$$

The outputs of the high filter are obtained in a similar manner by substituting $(-\omega_2)$ for (ω_1) in (15) and (16).

Post-detection integration takes place at the output of the doppler filter bank where magnitudes squared of all the outputs of the low (high) doppler filters are summed over the four time slots ($J=1, \dots, 4$), the five RF frequencies ($I=1, \dots, 5$) and the two range gates ($L=\pm 1$).

For convenience, U_n and V_n will be used to denote the outputs of the high and low filters, respectively, where the subscript n varies from 1 to 40 [$40 = 4$ (time slots) $\times 5$ (RF frequencies) $\times 2$ (gates)]. Thus, as was the case in angle tracking, the statistical parameters of the doppler filter outputs are now determined. In particular, the power in U_n is

$$P_U \triangleq E[|U_n|^2] = \frac{1}{4} d_t^2 E(A_I)^2 \left(\frac{\sin(\omega_1 \tau_E/2)}{N \sin(\omega_1 T_p/2)} \right)^2 + d_t N_0 B_F \quad (18)$$

and the power in V_n is

$$P_V \triangleq E[|V_n|^2] = \frac{1}{4} d_t^2 E(A_I)^2 \left(\frac{\sin(\omega_2 \tau_E/2)}{N \sin(\omega_2 T_p/2)} \right)^2 + d_t N_0 B_F \quad (19)$$

and the unnormalized correlation is

$$P_{UV} \triangleq E[U_n V_n^*] = \frac{1}{4} d_t^2 E(A_I)^2 \frac{\sin(\omega_1 \tau_E/2)}{N \sin(\omega_1 T_p/2)} \frac{\sin(\omega_2 \tau_E/2)}{N \sin(\omega_2 T_p/2)} \quad (20)$$

where (*) is used to denote complex conjugate. As apparent from (20), there is no noise term in P_{UV} because U and V are independent. In addition to that, the actual P_{UV} is a complex quantity involving a complex exponential term of the form $\exp(j\Delta\omega_d(\tau_E + \frac{\tau}{2} - T_p))$ for the early gate and $\exp(j\Delta\omega_d(\tau_E + \frac{3\tau}{2} - T_p))$ for the late gate. These terms have been dropped

in (20) because, in the tracking mode, $\Delta\omega_d\tau_E = \Delta\omega_d/B_F \ll 1$ and both τ and T_p are small with respect to τ_E . Another source which might make P_{UV} a complex number might be an unaccounted-for RF phase shift in the mono-pulse antenna. In this development, P_{UV} will be assumed real.

It is worth noting that the factor 1/4 in equations (18), (19) and (20) is a 6 dB loss in signal power due to the use of both range gates in calculating U_n and V_n . This loss factor is frequently referred to as the range gate straddling loss. In this appendix, no straddling loss will appear in the power budget because it is directly accounted for in the previous development.

Define the normalized correlation coefficient between U_n and V_n as

$$\rho^2 \triangleq \frac{|P_{UV}|^2}{P_U P_V} \quad (21)$$

Recalling that the average received signal power is given by

$$P_{\text{avg } r} = d_t P_{\text{pr}} = d_t E(A_I)^2, \quad (22)$$

the normalized correlation coefficient becomes

$$\rho^2 = \frac{P_{\text{avg } r}^2 \left(\frac{\sin(\omega_1 \tau_E/2)}{N \sin(\omega_1 T_p/2)} \right)^2 \left(\frac{\sin(\omega_2 \tau_E/2)}{N \sin(\omega_2 T_p/2)} \right)^2}{\left(P_{\text{avg } r} \left(\frac{\sin(\omega_1 \tau_E/2)}{N \sin(\omega_1 T_p/2)} \right)^2 + 4 N_0 B_F \right) \left(P_{\text{avg } r} \left(\frac{\sin(\omega_2 \tau_E/2)}{N \sin(\omega_2 T_p/2)} \right)^2 + 4 N_0 B_F \right)}$$

which simplifies to

$$\rho^2 = \frac{1}{\left[1 + \frac{4}{\text{SNR} \left(\frac{\sin(\omega_1 \tau_E/2)}{N \sin(\omega_1 T_p/2)} \right)^2} \right] \left[1 + \frac{4}{\text{SNR} \left(\frac{\sin(\omega_2 \tau_E/2)}{N \sin(\omega_2 T_p/2)} \right)^2} \right]} \quad (23)$$

where the signal-to-noise ratio (SNR) is defined as

$$\text{SNR} \triangleq \frac{P_{\text{avg } r}}{N_0 B_F} = \frac{P_{\text{avg } r} \tau_E}{N_0} \quad (24)$$

Note that ρ^2 is a function of $(\omega_1 = \pi B_F + \Delta\omega_d)$ and $(\omega_2 = \pi B_F - \Delta\omega_d)$ or, alternatively, ρ^2 is a function of the doppler error $\Delta\omega_d$. Note, however,

that

$$\frac{\sin(\omega_i \tau_E/2)}{N \sin(\omega_i T_p/2)} = \frac{\sin(\pi B_F \tau_E/2 \pm \Delta\omega_d \tau_E/2)}{N \sin(\pi B_F T_p/2 \pm \Delta\omega_d T_p/2)}; \quad i=1,2, \quad (25)$$

where the plus sign corresponds to $i=1$ and the minus sign corresponds to $i=2$. Since $\tau_E B_F = 1$ and since $\sin(\frac{\pi}{2} \pm x) = \pm \cos x$, then (25) becomes

$$\left(\frac{\sin(\omega_i \tau_E/2)}{N \sin(\omega_i T_p/2)} \right)^2 = \left(\frac{\cos(\Delta\omega_d/(2B_F))}{N \sin\left(\frac{\pi}{2N} \left(1 \pm \frac{\Delta\omega_d}{\pi B_F}\right)\right)} \right)^2$$

which, for small values of $\Delta\omega_d/(2B_F)$ becomes $(N \sin \pi/2N)^{-2}$. Since $N=16$, $\sin \pi/2N$ can be approximated by $\pi/2N$; hence,

$$\left(\frac{\sin(\omega_i \tau_E/2)}{N \sin(\omega_i T_p/2)} \right)^2 = \left(\frac{2}{\pi} \right)^2; \quad i=1,2, \quad \frac{\Delta\omega_d}{2B_F} \ll 1. \quad (26)$$

Substituting (26) into (23), the normalized correlation coefficient becomes

$$\rho = \frac{1}{1 + \frac{\pi^2}{\text{SNR}}}. \quad (27)$$

It is important to observe that the normalized correlation coefficient is dependent on the signal-to-noise ratio as given in (27) such that, as $\text{SNR} \rightarrow \infty$, then $\rho \rightarrow 1$, and as $\text{SNR} \rightarrow 0$, then $\rho \rightarrow 0$. It is worth noting that, if the spacing between the filters is doubled, then ρ becomes zero for small values of $\Delta\omega_d$ and range rate tracking becomes impossible.

6.0 RANGE RATE TRACKING DISCRIMINANT GENERATOR

Referring to Figure 1, the detector forms the magnitude squared

$$|U_n|^2; \quad n=1, \dots, 40$$

$$|V_n|^2; \quad n=1, \dots, 40.$$

The number $n=40$ results from the sum of doppler filter outputs over the five RF frequencies for each of the four angle tracking time slots for both the early and late range gates. This occurs for both the low and high doppler tracking filters.

As noted in the previous section, the statistical parameters of the complex Gaussian random variables $\{U_n, V_n\}$ are independent of n .

The post-detection integration forms

$$\sum_{n=1}^{40} |U_n|^2, \quad \sum_{n=1}^{40} |V_n|^2.$$

Finally, the logarithmic discriminant generates

$$z = \ln \left[\frac{\sum_{n=1}^{40} |U_n|^2}{\sum_{n=1}^{40} |V_n|^2} \right] \quad (28)$$

The random variable z is the maximum likelihood (M.L.) estimate [2] of the logarithm of the ratio of powers U_n to the powers in V_n , i.e.,

$$z = \widehat{\ln [P_U/P_V]}, \quad (29)$$

where $(\widehat{})$ denotes the maximum likelihood estimate.

In order to see z as a measure of the target range rate error, note that z is an unbiased estimate of $\ln [P_U/P_V]$ (see Ref. [3]), namely,

$$z = \ln (P_U/P_V) + x, \quad (30)$$

where [2], $E(x) = 0$ and $\sigma_x^2 = \sigma_z^2$ is the variance of the estimate of P_U/P_V . Equivalently,

$$E(z) = \ln [P_U/P_V]. \quad (31)$$

The standard deviation (RMS error) of z has been derived in [2] and the performance curves are shown in Figure 6 for $N = 20, 40$. The RMS error is dependent on two variables, the number of independent samples (N) and the normalized correlation coefficient (ρ) between U_n and V_n . Figure 6 shows that, for all N , as the normalized correlation coefficient increases, the RMS error decreases and tends to zero as $\rho \rightarrow 1$.

The improvement in the normalized correlation coefficient (ρ) and hence in the performance due to the increase in signal-to-noise ratio is indicated in (27) and plotted in Figure 7.

Figure 8 combines Figures 6 and 7, where the standard deviation (σ_x) is shown as a function of signal-to-noise ratio ($\text{SNR} = P_{\text{avg}} r / (N_0 B_F)$) for a various number of samples N .

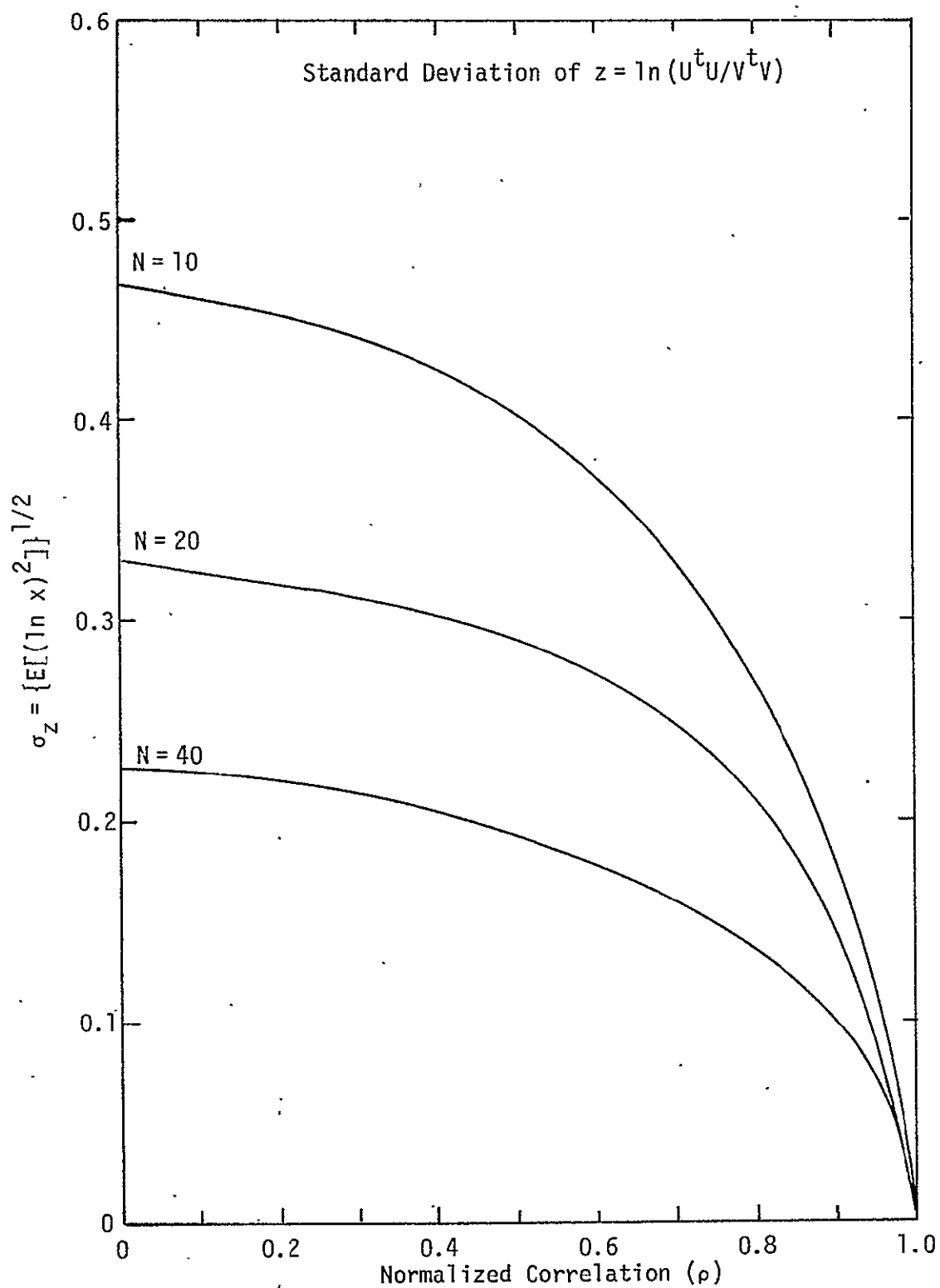


Figure 6. Standard Deviation of the Random Variable z as a Function of Correlation Coefficient ρ

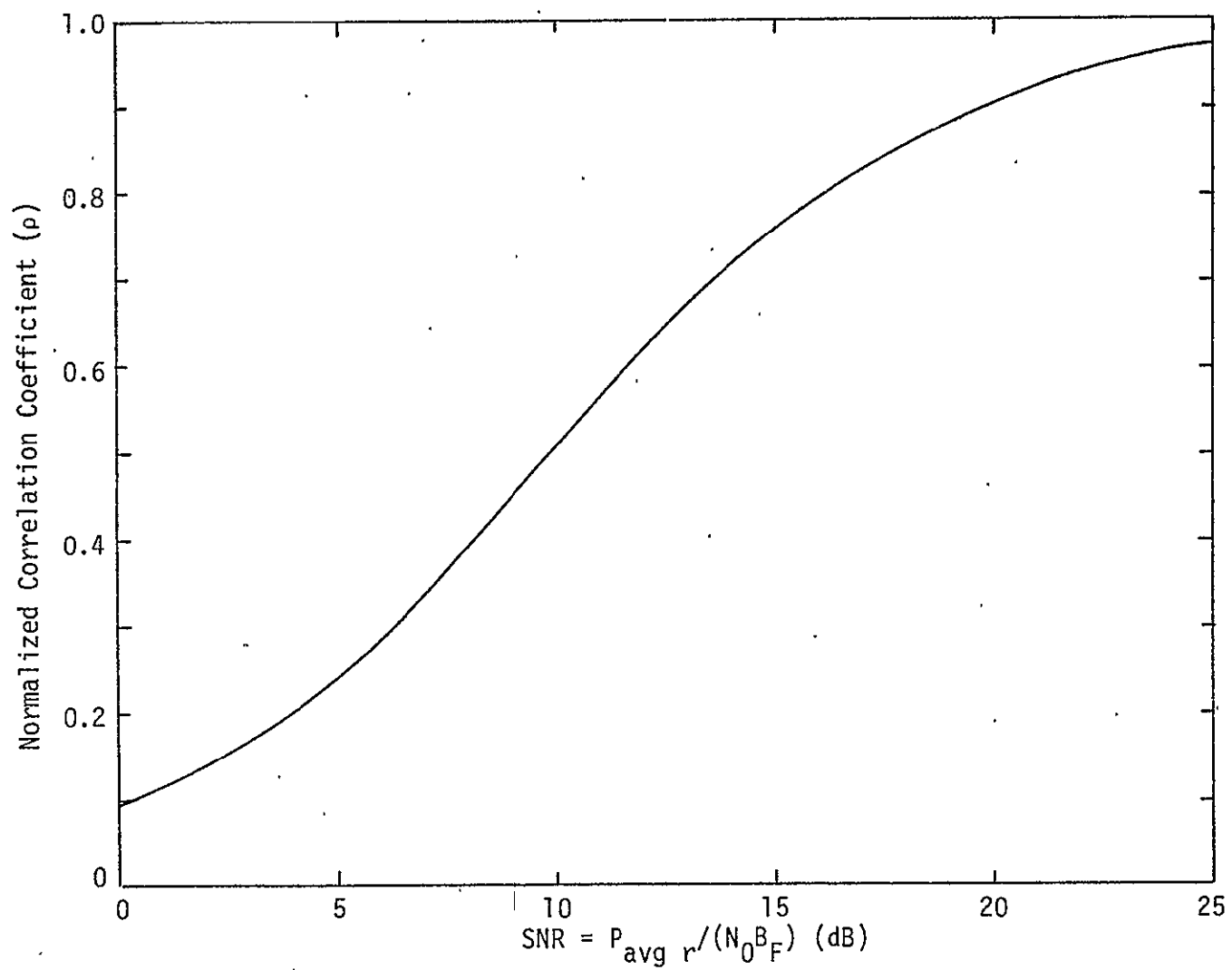


Figure 7. Normalized Correlation Coefficient ρ Versus Signal-to-Noise Ratio $P_{\text{avg}} r / (N_0 B_F)$

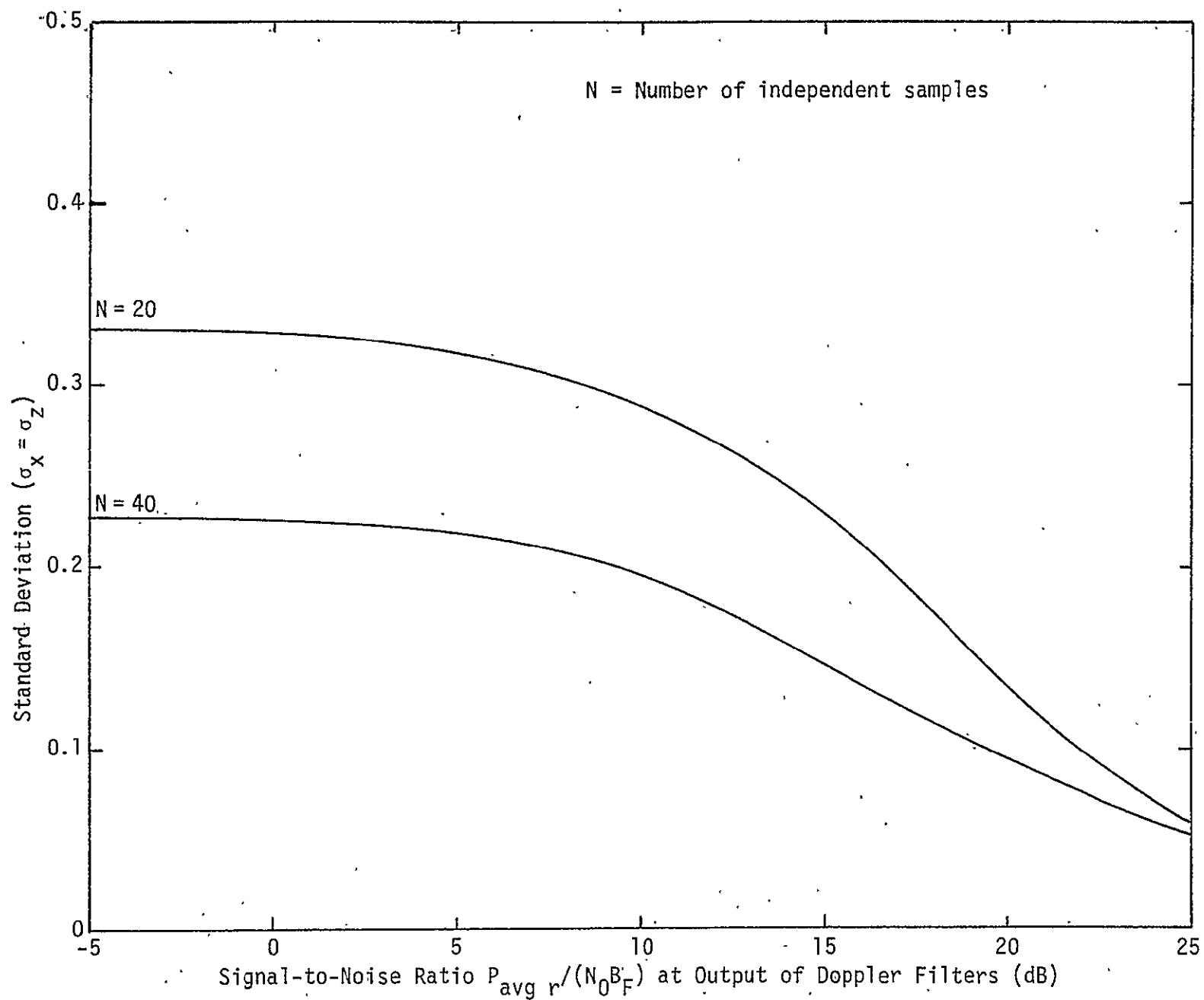


Figure 8. Standard Deviation of the Output of the Logarithmic Discriminant Generator Versus Signal-to-Noise Ratio for N = 20, 40

It is possible now to relate the maximum likelihood estimate z to the quantity being estimated, which is the doppler error ($\Delta\omega_d$). Upon substituting (18) and (19) into (31),

$$E(z) = \ln \frac{P_U}{P_V} = \ln \frac{\left(\frac{\sin(\omega_2 \tau_E/2)}{N \sin(\omega_2 \tau_p/2)} \right)^2 + 4 \text{SNR}^{-1}}{\left(\frac{\sin(\omega_1 \tau_E/2)}{N \sin(\omega_1 \tau_p/2)} \right)^2 + 4 \text{SNR}^{-1}} \quad (32)$$

Upon making similar assumptions to those made in deriving (27), namely, $\Delta\omega_d/2B_F \ll 1$ and $\frac{\pi}{2N} \ll 1$, $E(z)$ becomes

$$E(z) = \ln \frac{\frac{1}{N^2 \left[\frac{\pi}{2N} \left(1 + \frac{\Delta\omega_d}{\pi B_F} \right)^2 \right]} + 4 \text{SNR}^{-1}}{\frac{1}{N^2 \left[\frac{\pi}{2N} \left(1 + \frac{\Delta\omega_d}{\pi B_F} \right)^2 \right]} + 4 \text{SNR}^{-1}}$$

Simplifying and dropping the second-order terms,

$$E(z) = \ln \frac{1 + \frac{2\Delta\omega_d}{\pi B_F} (1 + \pi^2 \text{SNR}^{-1})^{-1}}{1 - \frac{2\Delta\omega_d}{\pi B_F} (1 + \pi^2 \text{SNR}^{-1})^{-1}},$$

which indicates that the mean of the output of the logarithmic discriminant is a function of the signal-to-noise ratio, as well as the doppler error ($\Delta\omega_d$). The doppler error can be directly transformed into a range rate error via the well-known relation

$$\Delta \dot{R} = \frac{1}{2} \frac{\Delta\omega_d}{2\pi} \frac{c}{f_c} = \frac{\Delta\omega_d}{4\pi} \frac{c}{f_c}, \quad (33)$$

where c is the velocity of light in free space ($c = 3 \times 10^8$ m/sec = 9.84×10^8 ft/sec) and f_c is the carrier frequency which, for the Ku-band radar, is approximately equal to 13.7 GHz. Substituting these numbers into (33) results in

$$\Delta \dot{R} = 0.00174 \Delta\omega_d \text{ m/sec} \quad (34)$$

For small values of $\frac{\Delta\omega_d}{B_F}$, the mean becomes

$$E(z) = \ln \frac{P_U}{P_V} = \frac{4\Delta\omega_d}{\pi B_F} (1 + (\pi)^2 \text{SNR}^{-1})^{-1}, \quad (35)$$

where the approximation $\ln(1+x) = x$ for small x has been used. Substituting (27) into (35) results in

$$\ln \frac{P_U}{P_V} = \frac{4\Delta\omega_d}{\pi B_F} \rho. \quad (36)$$

Defining a normalized doppler error with respect to the frequency spacing between two doppler filters as

$$\zeta \triangleq \frac{\Delta\omega_d}{2\pi B_F}, \quad (37)$$

the mean becomes

$$E(z) = \ln \frac{P_U}{P_V} = 8\zeta \rho. \quad (38)$$

Thus, the mean of the output of the logarithmic discriminant generator for small values of ζ is a linear function of ζ and the normalized correlation coefficient (ρ). The slope of $E(z)$ as a function of ζ is dependent on the signal-to-noise ratio through the multiplication of ρ , which corresponds to a reduction in the effective loop gain. Figure 9 illustrates the actual behavior of $\ln(P_U/P_V)$ as a function of ζ without any simplifying assumptions with the signal-to-noise ratio as a parameter. The figure is drawn for positive ζ only, since $E(z)$ in equation (32) is an odd function of ζ . It is clear that, for small values of ζ , the function is linear, as was apparent in (38).

7.0 PERFORMANCE OF RANGE RATE TRACKING LOOP

The purpose of this section is to incorporate all the results of the previous sections so as to provide the RMS range rate (doppler) error due to thermal noise. A block diagram of the equivalent range rate tracking loop is shown in Figure 10. The loop represents the linearized model of the actual range rate tracking block diagram shown in Figure 1.

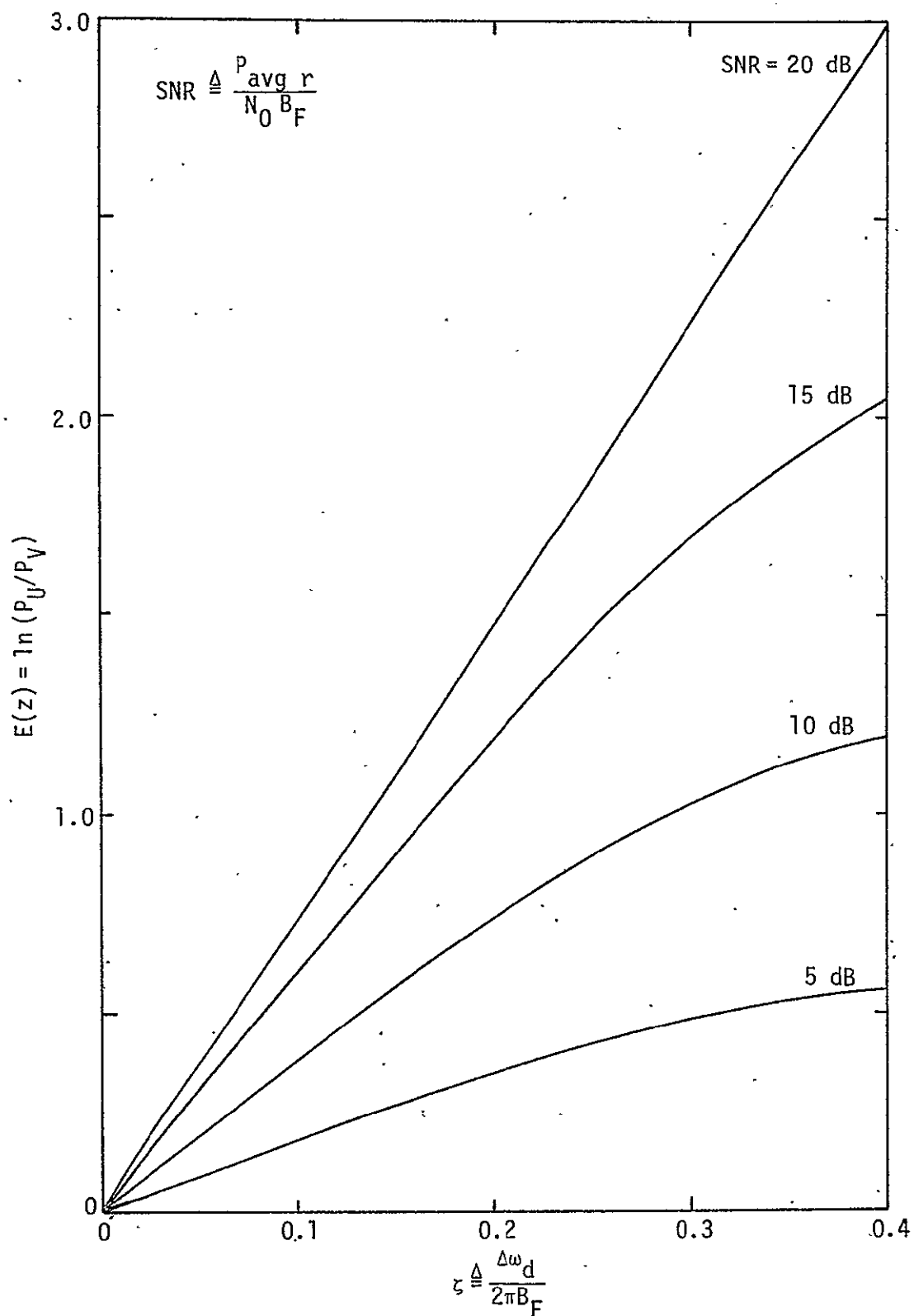


Figure 9. First Moment of the Output of the Range Rate Tracking Discriminant Generator as a Function of Normalized Angle Error for Various Signal-to-Noise Ratios

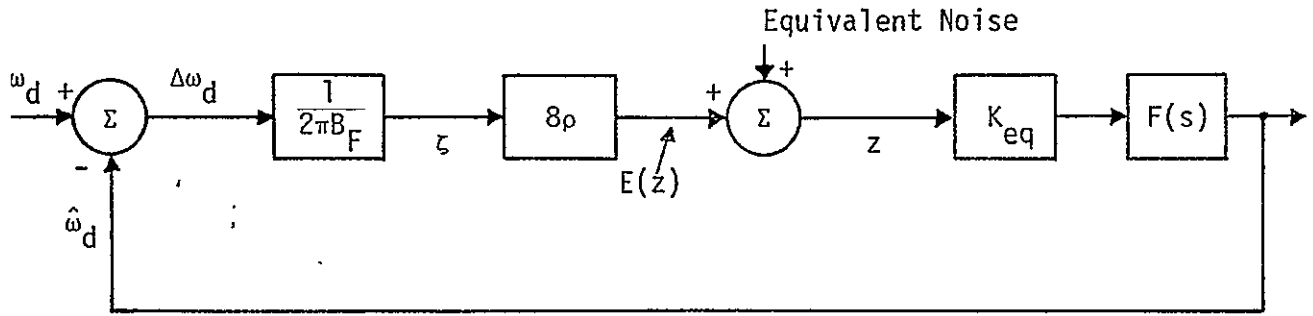


Figure 10. Block Diagram of Equivalent Range Rate Tracking Loop

In Figure 10, ω_d is the actual doppler in the received signal. For a passive target at range R and range rate \dot{R} ,

$$\omega_d = 4\pi \frac{\dot{R}}{c} f_c,$$

where c is the velocity of light in free space and f_c is the carrier frequency.

$\hat{\omega}_d$ = loop estimate of the actual doppler ω_d

$\Delta\omega_d = \omega_d - \hat{\omega}_d$ = doppler tracking error

B_F = one-sided 3 dB bandwidth of the doppler filters

$B_F = 186$ Hz for $R > 9.5$ nmi

$B_F = 437$ Hz for $R < 9.5$ nmi

8ρ = scale factor in (38) necessary to give $E(z) = \ln(P_U/P_V)$

x = equivalent noise of the system due to thermal noise

$z = \ln(P_U/P_V) + x$ is the output of the logarithmic discriminant generator, as given in (30) and diagrammed in Figure 1

K_{eq} = equivalent loop gain of the tracking loop which represents the various contributing gains

$F(s)$ = open loop range tracking transfer function. It represents the sliding window averaging process which takes place in the range rate tracking loop where m discriminant estimates are averaged before being fed back to the doppler filters bank.

Since the transient analysis and the dynamic characteristics of the range rate tracking loop are not a part of this development, the effects of the loop gain and open loop transfer functions are taken into account through the single-sided loop noise bandwidth B_N (Hz).

The closed loop transfer function from ω_d to $\hat{\omega}_d$, as seen in Figure 9, is equal to

$$H(j 2\pi f) = \frac{\left(\frac{8\rho}{2\pi B_F}\right) K_{eq} F(2\pi j f)}{1 + \left(\frac{8\rho}{2\pi B_F}\right) K_{eq} F(2\pi j f)}, \quad (39)$$

and the corresponding single-sided loop bandwidth is defined as

$$B_N(\rho) = \int_0^\infty |H(j 2\pi f)|^2 df. \quad (40)$$

The dependence of B_N on ρ has been explicitly indicated to emphasize the dependence of noise bandwidth on the signal-to-noise ratio by way of the normalized correlation coefficient ρ . For intermediate and high gain tracking loops, the dependence of B_N on ρ is approximately given by

$$B_N(\rho) \approx \rho B_N(\rho = 1), \quad (41)$$

where $\rho = 1$ corresponds to the infinite SNR case. This is the case since, at high values of loop gain, the noise bandwidth varies approximately linearly with the effective loop gain $(8\rho/2\pi B_F)$. This is indeed the case for all loop transfer functions that are anticipated for $F(s)$, including first- and second-order tracking loops.

The transfer function from the equivalent noise input x to the doppler tracking error $\Delta\omega_d$ is given by

$$\Delta\omega_d = \left(\frac{2\pi B_F}{8\rho}\right) H(p) x, \quad (42)$$

where p is the Heaviside operator, so that the variance of the angle tracking error is given by

$$\sigma_{\Delta\omega_d}^2 = \left(\frac{2\pi B_F}{8\rho}\right)^2 B_N(\rho) T_s \sigma_x^2(N, \rho), \quad (43)$$

where

$\sigma_x^2(N, \rho) = \sigma_x^2$ is the variance of the maximum likelihood estimate of $\ln(P_U/P_V)$, which is also the variance per sample of the noise in the equivalent block diagram of the range rate tracking loop. The dependence on the correlation coefficient ρ and the number of independent samples N is emphasized in (43).

T_s = time per sample of the random sequence x by the D/A converter in Figure 1. In this system,

$$T_s = T_p(16)(4)(I), \text{ where} \quad (44)$$

$I = 5$ is the number of RF frequencies. The noise samples x are assumed to be statistically independent.

16 = number of pulses during which $\Sigma + \Delta_J$ is observed (see Figure 2), $J = 1, \dots, 4$.

4 = factor corresponding to the number of different angular error measurements per frequency dwell time, namely, $\Sigma + \Delta_{AZ}$, $\Sigma - \Delta_{AZ}$, $\Sigma + \Delta_{EL}$, $\Sigma - \Delta_{EL}$.

T_p = pulse repetition interval = 335 μ sec, when PRF = 2987 Hz and $T_p = 143$ μ sec, when PRF = 6970 Hz.

Upon substitution of these values into (44),

$$T_s = 320 T_p = 107.2 \text{ msec, when PRF} = 2987 \text{ Hz,} \quad (45a)$$

$$T_s = 320 T_p = 45.9 \text{ msec, when PRF} = 6970 \text{ Hz.} \quad (45b)$$

Substituting the above into equation (43) yields the following expression for the RMS doppler (range rate) error in range rate tracking:

$$\sigma_{\Delta\omega_d} = \frac{\pi B_F}{4} \left(1 + \frac{\pi^2}{\text{SNR}}\right)^{1/2} (B_N(\rho=1) T_s)^{1/2} \sigma_x(N, \text{SNR}), \quad (46)$$

where B_F is the single-sided 3 dB bandwidth of the doppler filters and SNR is defined in (24) as $P_{\text{avg}} r / (N_0 B_F)$.

The RMS of the range rate tracking error is thus given as

$$\sigma_{\dot{R}} = \left(\frac{c}{4\pi f_c}\right) \sigma_{\Delta\omega_d}. \quad (47)$$

8.0 PERFORMANCE CALCULATIONS

The radar parameters needed to compute the RMS range rate error in (47) are given as:

$$\begin{aligned} B_F &= 186 \text{ Hz} & R > 9.5 \text{ nmi} \\ &= 437 \text{ Hz} & R < 9.5 \text{ nmi} \end{aligned}$$

$$\begin{aligned} B_N &= 9.4, 4.7 \text{ or } 2.35 \text{ Hz} & R > 9.5 \text{ nmi} \\ &= 22.4, 11.2, \text{ or } 5.6 \text{ Hz} & R < 9.5 \text{ nmi} \end{aligned}$$

These values of loop bandwidth B_N are chosen so as to correspond to averaging 4, 2 and 1 samples. If every sample required T_S msec to compute, then the bandwidth B_N is equal to $1/mT_S$, where m is the number of samples being averaged.

$$\begin{aligned} T_S &= 107.2 \text{ msec} & R > 9.5 \text{ nmi, Eq. (45a)} \\ &= 45.9 \text{ msec} & R < 9.5 \text{ nmi, Eq. (45b)} \end{aligned}$$

The specification values for the Ku-band range rate tracking [4] state that $\sigma_R < 0.1 \text{ m/sec}$ (or $3\sigma_R = 0.3 \text{ m/sec}$) for ranges less than 10 nmi. In order to obtain the range tracking performance as a function of range, the following radar equation is used to determine the signal-to-noise ratio $P_{avg} r / (N_0 B_F)$ as a function of range,

$$\frac{P_{avg} r}{N_0 B_F} = \frac{[G^2 \bar{\sigma} \lambda^2][d_t P_p \tau_E]}{(4\pi)^3 L [k T_{sys}] R^4}, \quad (48)$$

where all of the parameters in (48) are described in [1]. The values used in the computation are

$$\begin{aligned} G &= \text{peak antenna gain} &= 38.5 \text{ dB} \\ \bar{\sigma} &= \text{radar cross-section} &= 1 \text{ m}^2 \\ \lambda &= \text{wavelength} &= 0.0216 \text{ m} \\ d_t &= \text{duty factor} &= \begin{cases} 0.099 & (R > 9.5 \text{ nmi}) \\ 0.115 & (3.8 < R < 9.5 \text{ nmi}) \end{cases} \\ P_p &= \text{peak transmitted power} &= 60 \text{ watts} \\ \tau_E &= \text{dwell time corresponding to} &= \begin{cases} 5.36 \text{ msec} & (R > 9.5 \text{ nmi}) \\ 2.29 \text{ msec} & (3.8 < R < 9.5 \text{ nmi}) \end{cases} \\ &\quad \text{one computation of the DFT} = B_F^{-1} \\ k &= \text{Boltzmann's constant} &= 1.38 \times 10^{-23} \text{ w/Hz-K} \\ T_{sys} &= \text{system noise temperature} &= 1500^\circ\text{K} \\ R &= \text{range, in meters} \end{aligned}$$

L = losses, itemized as follows for range rate track

Transmit	3.7	dB
Scan alignment	0	
Lateral scan	0	
Threshold	0.5	
Processor loss	1.0	
Doppler mismatch	0	
PDI	1.25	
Pre-sum	{ 0.14 (R > 9.5 nmi)	
	{ 0.07 (3.8 < R < 9.5 nmi)	
Coupling loss	1.8	
Total losses	{ 8.39 dB (R > 9.5 nmi)	
	{ 8.32 dB (3.8 < R < 9.5 nmi)	

With these parameters, the RMS range rate tracking error is shown in Figure 11 versus range in nautical miles for $m=1,2,4$ samples. In the present state of the range rate loop design, the number of samples used is $m=2$ for $R > 10$ nmi and $m=4$ for $R < 10$ nmi [4]. This results in a design margin of 2.5 dB at 9.5 nmi.

9.0 DOPPLER AMBIGUITY RESOLUTION

The doppler discriminant and resulting estimation will give a value between $[0, \text{PRF}]$. The maximum closing velocity is +148 fps and the maximum opening velocity is -75 fps. At 13.9 GHz, this corresponds to approximately 28 Hz/fps doppler. The maximum opening doppler is therefore -2100 Hz and maximum closing doppler is +4144 Hz, as shown in Figure 12.

When the high PRF of 6970 is used, there is no doppler ambiguity from the doppler estimation from the α - β tracker. For the low PRF at longer ranges, namely, 2987, there is a doppler ambiguity as indicated in Figure 12. The resolution is easily obtained from the coarser estimation of range rate from the α - β tracker [1] by noting the following:

(a) If the coarse estimation from the α - β tracker ($\hat{R}_s(n)$) is larger than zero (opening), then the fine estimation $\hat{R}_{sc}(n)$ will be in Region 3', whereas the actual estimate should be in Region 3. In this case, $\hat{R}_{sc}(n)$ is adjusted by subtracting the PRF equal to 2987 Hz.

(b) If the coarse estimation $\hat{R}_s(n)$ is longer than 2987 Hz (high closing velocity), then the estimate $\hat{R}_{sc}(n)$ will be in Region 2'. In this case, $\hat{R}_{sc}(n)$ is adjusted by adding the PRF.

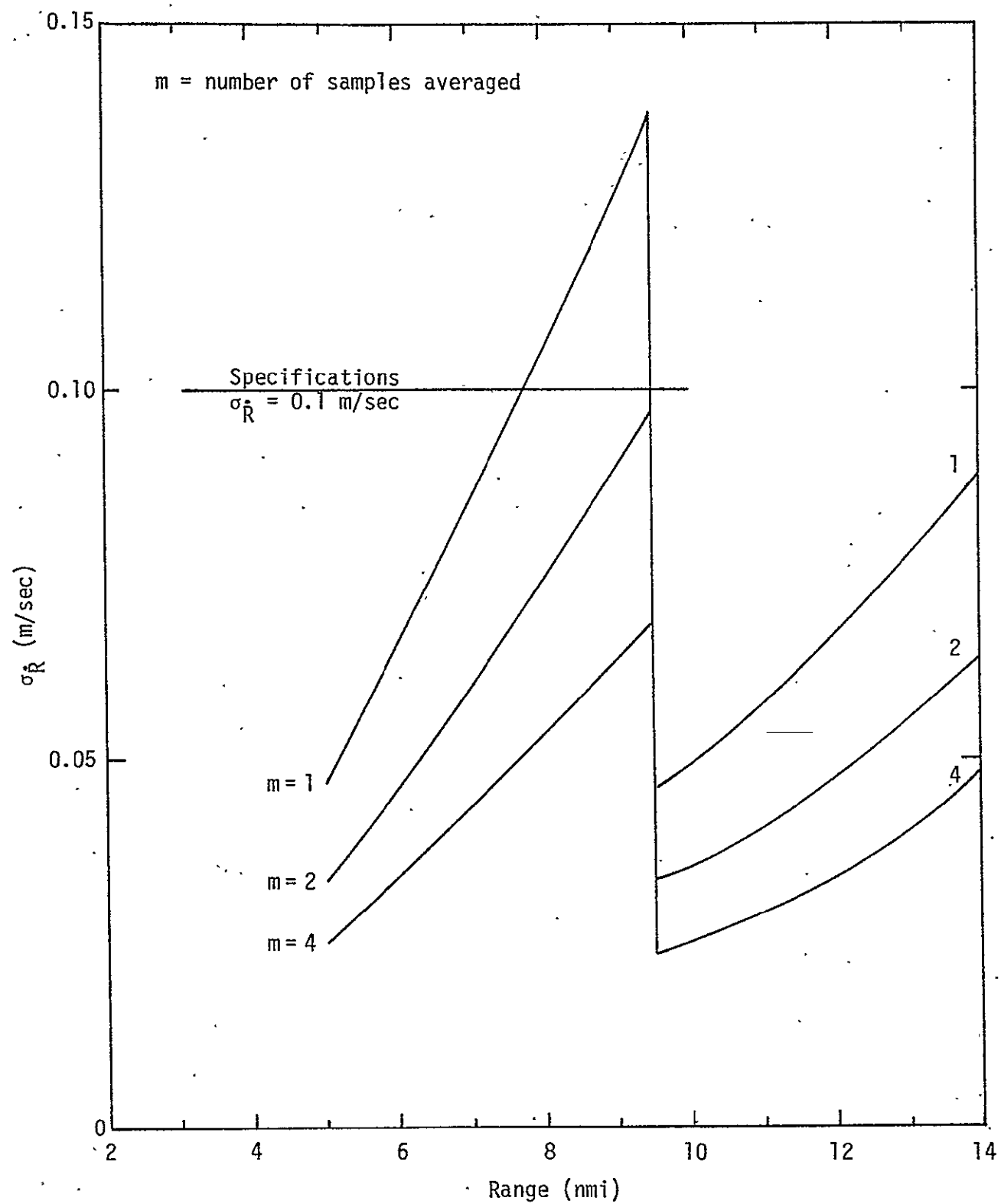


Figure 11. RMS Range Rate Tracking Error of Passive Targets Vs. Range

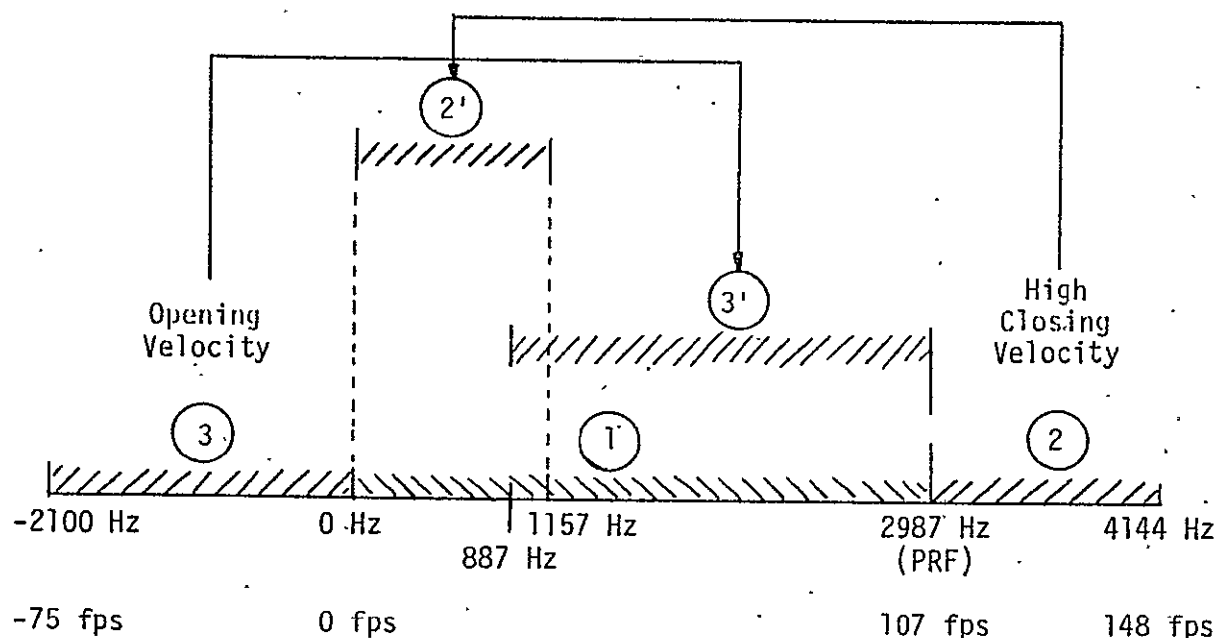


Figure 12. Resolution of Doppler Ambiguity

(c) If the coarse estimate is between 0 and 2987 Hz, the fine estimate is not altered.

It is assumed that the resolution of the ambiguity is carried out ideally, so that it does not contribute to the RMS tracking error.

10.0 SIGNAL-TO-NOISE RATIO COUPLING LOSS

In the power budget of Section 8.0, a coupling loss of 1.8 dB is noted. This is obtained by noting the power divider and combiner as seen in Figure 13. In the power divide, the signal and noise powers decrease by a factor of 3 dB. This is due to the fact that the Σ channel power is divided equally between the communication and radar receivers. The power in the Σ channel is then combined with that of the Δ channel after the latter is reduced by a factor of 1/4.

Since the power in the Δ channel is small compared to that in the Σ channel and since the noises in the two channels are statistically independent with equal spectral density levels, the signal-to-noise ratio in the $(\Sigma \pm \Delta)$ channel becomes

$$\left. \frac{\text{Signal Power}}{\text{Noise Spectral Density}} \right|_{\Sigma \pm \Delta} = \frac{(\text{Signal Power in } \Sigma \text{ Channel})/2}{\left(\frac{(\text{Noise Spectral Density in } \Sigma \text{ Channel})}{2} \right) + \left(\frac{(\text{Noise Spectral Density in } \Delta \text{ Channel})}{4} \right)}$$

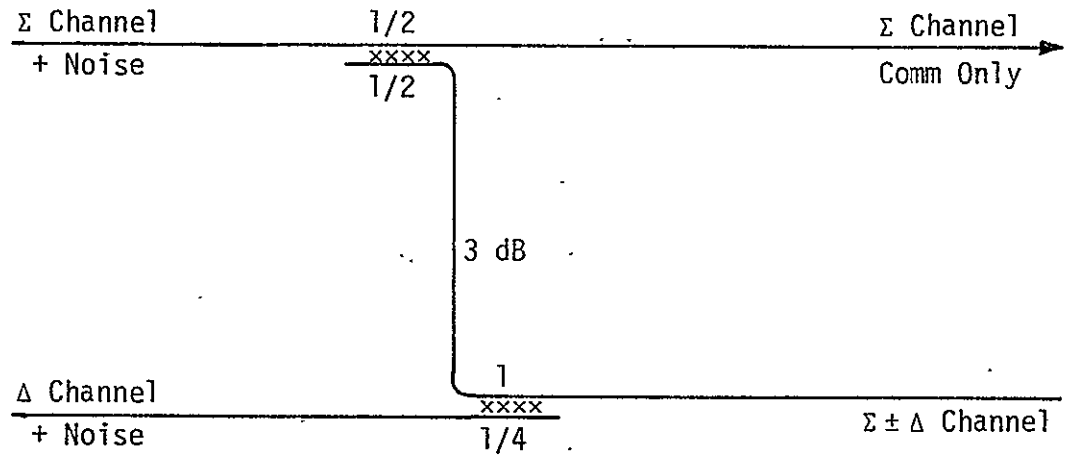


Figure 13. Block Diagram of the Coupling Loss

If we denote the signal power in the Σ channel by P_s and the noise spectral density by N_0 , then

$$\left. \frac{\text{Signal Power}}{\text{Noise Spectral Density}} \right|_{\Sigma \pm \Delta} = \frac{P_s/2}{N_0/2 + N_0/4} = \frac{2P_s}{3N_0} = \frac{2}{3} \frac{P_s}{N_0}.$$

The loss factor $(2/3)$ is equal to 1.8 dB degradation in the signal-to-noise ratio due to coupling loss.

REFERENCES:

1. C. L. Weber, S. Udalov, and W. K. Alem. "Study to Investigate and Evaluate Means of Optimizing the Ku-Band Combined Radar/Communication Functions for the Space Shuttle, First Report," Axiomatix Report No. R7705-1 (under Contract No. NAS 9-14614, Exhibit D), May 31, 1977.
2. C. L. Weber. "Maximum Likelihood Estimation of the Ratio of Powers in Two Narrowband Processes," Axiomatix Report No. R7701-3 (under Contract No. NAS 9-14614), January 31, 1977.
3. N. E. Nahi. Estimation Theory and Applications. R. E. Kreiger, 1976.
4. Hughes Aircraft Co. "Ku-Band Integrated Radar and Communication Equipment for the Space Shuttle Orbiter Vehicle," Schematic Review, Vol. 1, July 19, 1977.
5. Rockwell International/Space Division Specification. "Integrated Communication and Radar Equipment, Ku-Band," February 6, 1976.

APPENDIX H

REDUCTION IN SIGNAL-TO-NOISE RATIO DUE TO QUANTIZATION
AND SATURATION NOISE IN A/D CONVERSION

APPENDIX H

REDUCTION IN SIGNAL-TO-NOISE RATIO DUE TO QUANTIZATION AND SATURATION NOISE IN A/D CONVERSION

by

Charles L. Weber

1.0 INTRODUCTION

The reduction in signal-to-noise ratio due to quantization and saturation noise in A/D conversion is determined. The results of the derivations [1-3] are included in this development.

The voltage at the input to the A/D converter is assumed to be a sample from a zero mean Gaussian random variable. This is a valid assumption, particularly in the radar environment. To see this, note that the complex baseband signal, at an arbitrary instant of time before A/D conversion, is of the form

$$I + jQ = S + N, \quad (1)$$

where the desired signal, S , is of the form

$$S = R e^{j\theta} \quad (2)$$

and the noise N is a complex Gaussian random variable represented by

$$N = N_I + jN_Q. \quad (3)$$

A block diagram illustrating the reduction of an IF waveform to a complex baseband signal is shown in Figure 1.

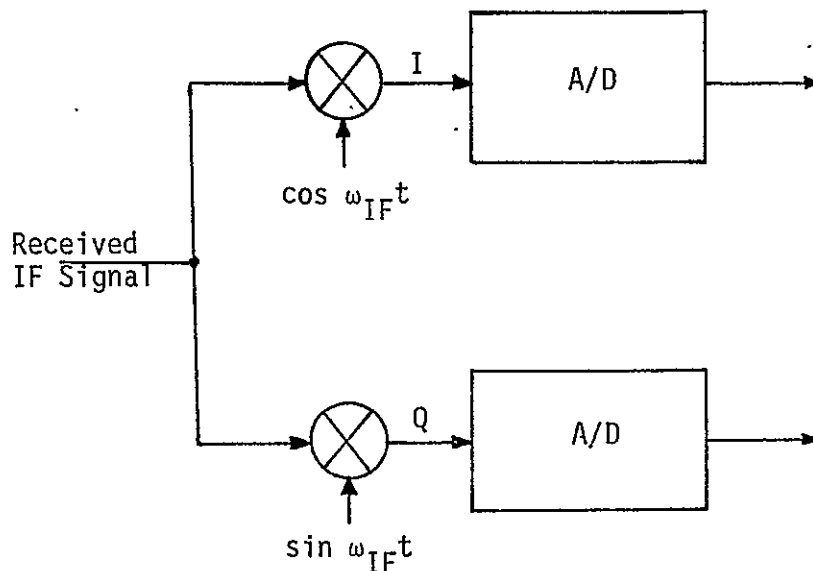


Figure 1. Reduction of IF Signal to a Sampled Complex Baseband Signal

Both I and Q are individually sampled, so that

$$I = R \cos \theta + N_I \quad (4a)$$

$$Q = R \sin \theta + N_Q \quad (4b)$$

For most radars which are searching and/or tracking passive targets, R is a Rayleigh random variable and the random phase θ is uniformly distributed over $(0-2\pi)$ and independent of R. At any sampling instant, θ will be uniformly distributed independent of the magnitude of the doppler frequency shift. When this is the case, both $R \cos \theta$ and $R \sin \theta$ are zero mean Gaussian random variables.

The input to the A/D converter is therefore assumed to be of the form

$$x = s + n, \quad (5)$$

where s and n are real zero-mean Gaussian random variables with variances σ_s^2 and σ_n^2 , respectively. They are also assumed to be independent. The signal-to-noise ratio at the input to the A/D converter is defined as

$$(\text{SNR})_{\text{in}} \triangleq \frac{\sigma_s^2}{\sigma_n^2} \quad (6)$$

and the total input power is

$$\sigma_x^2 = \sigma_s^2 + \sigma_n^2. \quad (7)$$

With the above assumptions, the quantization and saturation noise powers are developed in the next section.

2.0 QUANTIZATION AND SATURATION NOISE

Figure 2 indicates notation for the input and output of the A/D converter.

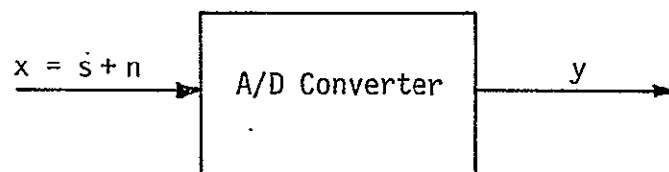


Figure 2. Box Representing the A/D Function

In Figure 3, the characteristics of the A/D converter are depicted. The number of bits of quantization is designated by M . In Figure 3, the case of $M=4$ is shown, where it is assumed one bit is used for the sign of the input. The input is quantized to some magnitude $k\sigma_x$, where σ_x is the standard deviation of the input and k represents the number of standard deviations (not necessarily an integer) to be quantized on either side of zero.

The number of output levels is 2^{M-1} for $x \geq 0$, and 2^{M-1} for $x \leq 0$, where the zero level output can occur for both $x > 0$ and $x < 0$. The number of quantization spaces (or intervals) for $x > 0$ is $2^{M-1}-1$, namely, one less than the number of output levels. These parameters are therefore related by the relationship

$$k\sigma_x = Q[2^{M-1} - 1], \quad (8)$$

where Q is the quantization step size, as shown in Figure 3a. The quantization step size is therefore given by

$$Q = \frac{k\sigma_x}{2^{M-1} - 1}. \quad (9)$$

The corresponding error signal

$$\varepsilon(x) \triangleq x - y \quad (10)$$

is shown in Figure 3b, where that part of $\varepsilon(x)$ between $[-k\sigma_x, k\sigma_x]$ is designated quantization error, and the remaining contribution is called the saturation error.

The probability density function (PDF) of the input is shown in Figure 3c, and is analytically given by

$$p(x) = g(x) \triangleq \frac{\exp[-\frac{1}{2}(x/\sigma_x)^2]}{\sqrt{2\pi}\sigma_x}. \quad (11)$$

The input and A/D converter are now sufficiently described so that the quantization and saturation errors can be determined. Following [3], the total noise power P_N due to quantization and saturation is given by

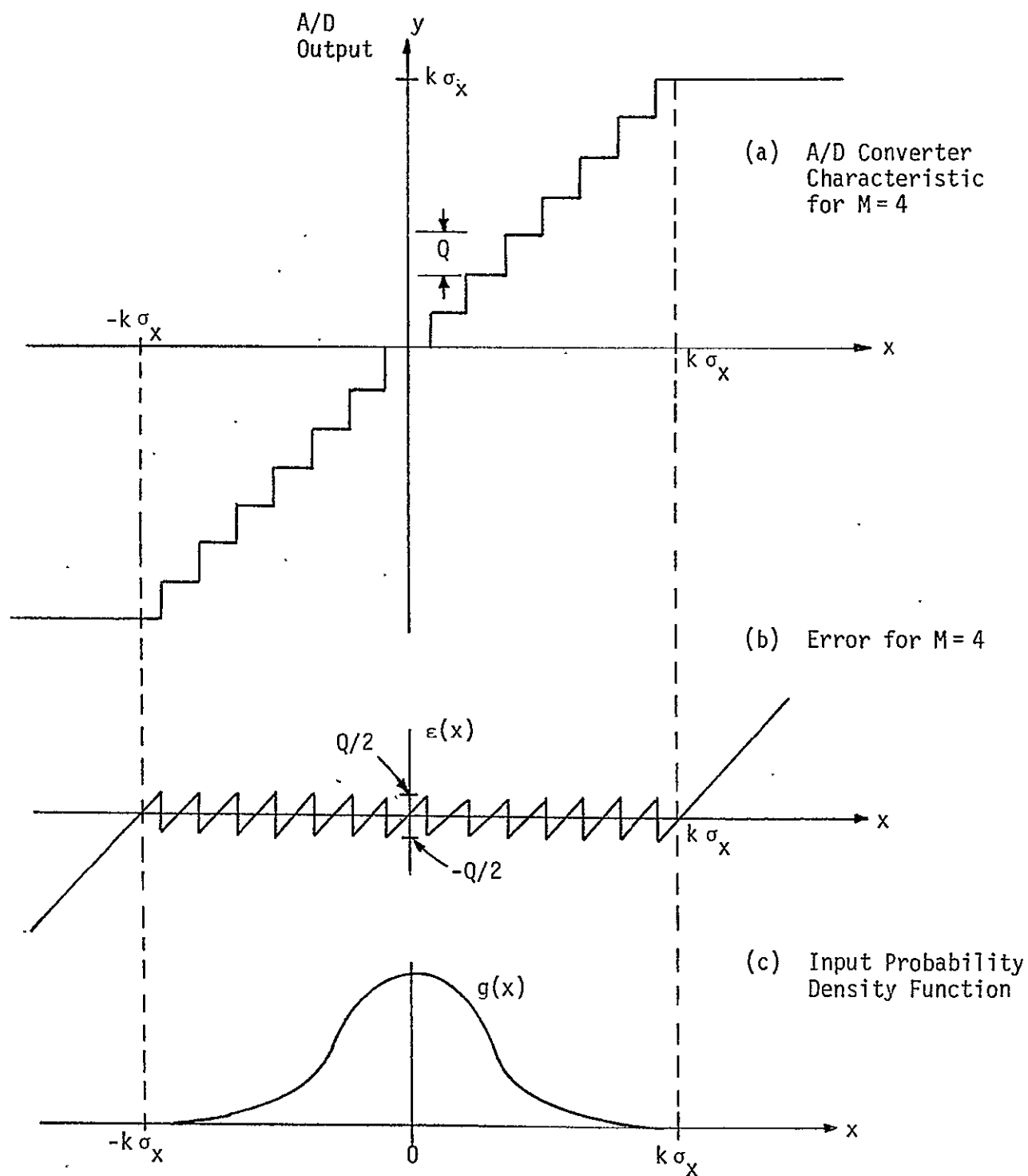


Figure 3. Characteristics of A/D Converter

$$\begin{aligned}
 P_N &\triangleq E[\epsilon^2(x)] \\
 &= \int_{-\infty}^{\infty} \epsilon^2(x) g(x) dx .
 \end{aligned}$$

Since the integrand is an even function of x , P_N can be written as

$$\begin{aligned}
 P_N &= 2 \int_0^{\infty} \epsilon^2(x) g(x) dx \\
 &= QN + SN ,
 \end{aligned} \tag{12}$$

where

$$QN \triangleq 2 \int_0^{k\sigma_x} \epsilon^2(x) g(x) dx \tag{13}$$

is the quantization noise contribution and

$$SN \triangleq 2 \int_{k\sigma_x}^{\infty} \epsilon^2(x) g(x) dx \tag{14}$$

is the saturation noise contribution.

The quantization noise contribution can be approximated by

$$\begin{aligned}
 QN &= 2 \sum_{n=0}^N \int_{(n-\frac{1}{2})Q}^{(n+\frac{1}{2})Q} (x - nQ)^2 g(x) dx \\
 &\approx 2 \sum_{n=0}^N g(nQ) \int_{-Q/2}^{Q/2} x^2 dx \\
 &\approx 2 \left(\frac{Q^2}{12} \right) \sum_{n=0}^N g(nQ) Q \\
 &\approx 2 \left(\frac{Q^2}{12} \right) \int_0^{k\sigma_x} g(x) dx \\
 &\approx 2 \left(\frac{Q^2}{12} \right) \left[\frac{1}{2} - \operatorname{erfc}(k) \right] ,
 \end{aligned} \tag{15}$$

where each term in the sum has been simplified by replacing $g(x)$ with its value at the midpoint of the interval. Also $\text{erfc}(u)$ is the complementary error function, defined as

$$\text{erfc}(u) \triangleq \int_u^{\infty} \frac{\exp(-\frac{1}{2}v^2)}{\sqrt{2\pi}} dv. \quad (16)$$

By substituting (9) into (15), a normalized representation for the quantization error is obtained, namely,

$$\frac{QN}{\sigma_x^2} \approx 2 \left\{ \frac{k^2}{12(N-1)^2} \left[\frac{1}{2} - \text{erfc}(k) \right] \right\} \quad (17)$$

where

$$N \triangleq 2^{M-1}. \quad (18)$$

The saturation noise can be computed from

$$\begin{aligned} SN &= 2 \int_{k\sigma_x}^{\infty} (x - k\sigma_x)^2 g(x) dx \\ &= 2\sigma_x^2 \int_k^{\infty} (z - k)^2 \frac{\exp(-\frac{1}{2}z^2)}{\sqrt{2\pi}} dz \\ &= 2\sigma_x^2 \left\{ (k^2 + 1) \text{erfc}(k) - \frac{2k \exp(-\frac{1}{2}k^2)}{\sqrt{2\pi}} \right\}. \end{aligned} \quad (19)$$

The normalized version of the saturation noise becomes

$$\frac{SN}{\sigma_x^2} = 2 \left\{ (k^2 + 1) \text{erfc}(k) - \frac{2k \exp(-\frac{1}{2}k^2)}{\sqrt{2\pi}} \right\}. \quad (20)$$

The total normalized noise power is given by

$$\frac{PN}{\sigma_x^2} = \frac{QN}{\sigma_x^2} + \frac{SN}{\sigma_x^2} \equiv h(M, k), \quad (21)$$

where the dependence is only a function of the number of bits of quantization, M , and the normalized saturation parameter, k .

In Figure 4 (taken from [3]), the normalized total noise power, P_N/σ_x^2 is plotted as a function of k for various values of M . It is noted that, for each M , there is an optimum value of k and a corresponding minimum value of saturation plus quantization noise. In Table 1 (taken from [3]), the optimum values of k and the corresponding values of QN/σ_x^2 , SN/σ_x^2 , and P_N/σ_x^2 are shown for various values of M .

Table 1: Optimum k and Noise Powers for Various Values of M

M	k_{opt}	$\frac{QN}{\sigma^2}$	$\frac{SN}{\sigma^2}$	$\frac{P_N}{\sigma^2} = h(M, k)$	$SNR_{A/D}$ (dB)
3	1.9	3.15×10^{-2}	1.50×10^{-2}	4.65×10^{-2}	13.3
4	2.5	1.05×10^{-2}	0.24×10^{-2}	1.29×10^{-2}	18.9
5	2.9	3.1×10^{-3}	0.6×10^{-3}	3.7×10^{-3}	24.3
6	3.26	0.92×10^{-3}	0.13×10^{-3}	1.05×10^{-3}	29.8
7	3.6	2.7×10^{-4}	0.4×10^{-4}	3.1×10^{-4}	35.1
8	3.9	7.9×10^{-5}	1.0×10^{-5}	8.9×10^{-5}	40.5
9	4.24	2.3×10^{-5}	0.2×10^{-5}	2.5×10^{-5}	46.0
10	4.5	6.5×10^{-6}	0.5×10^{-6}	7.0×10^{-6}	51.5

Referring back to Figure 4, note that, near the optimum k , the curves are relatively flat. For the values of M shown, a $\pm 10\%$ change in k will result in a very small change in total noise power. Therefore, the A/D converter input power need not be very closely controlled. In general, it will have to be controlled via an AGC loop, which will take place before A/D conversion.

Also note that, at the optimum k , QN/σ_x^2 is always several times larger than SN/σ_x^2 .

3.0 PERFORMANCE

By using the results of the previous section, the effect that quantization and saturation noise have on the overall system performance can now be determined.

The input signal-to-noise ratio was defined in (6). The output signal-to-noise ratio of the A/D converter is defined as

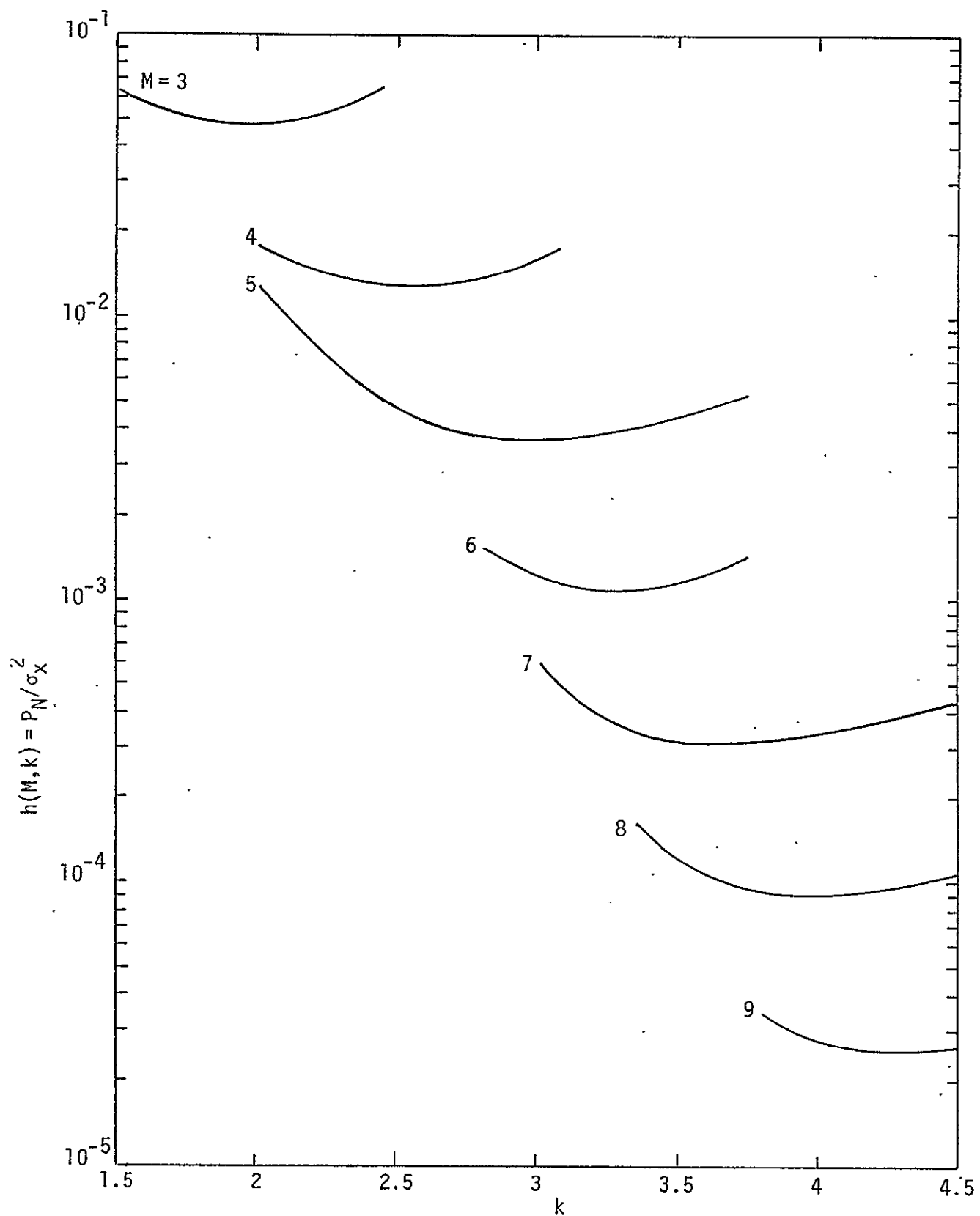


Figure 4. Normalized Quantization and Saturation Noise vs. k for Various Values of the Number of Bits of Quantization, M

$$(\text{SNR})_{\text{OUT}} \triangleq \frac{\sigma_s^2}{\sigma_n^2 + p_N}, \quad (22)$$

where the denominator consists of the sum of the input noise, σ_n^2 , and the quantization and saturation noise, p_N , introduced by A/D conversion. Substituting (21) and (7) into (22), the output SNR of the A/D converter can be expressed as

$$(\text{SNR})_{\text{OUT}} = \frac{\sigma_s^2}{\sigma_n^2 + (\sigma_s^2 + \sigma_n^2) h(M, k)}. \quad (23)$$

An SNR which describes the A/D operation can be defined as the ratio of the total input power divided by the sum of the quantization and saturation noise powers, namely,

$$(\text{SNR})_{\text{A/D}} \triangleq \frac{\sigma_x^2}{p_N} = [h(M, k)]^{-1}. \quad (24)$$

Substituting (24) into (23),

$$(\text{SNR})_{\text{OUT}} = \left[\frac{1}{1 + [1 + (\text{SNR})_{\text{IN}}] (\text{SNR})_{\text{A/D}}^{-1}} \right] (\text{SNR})_{\text{IN}}, \quad (25)$$

which relates output SNR in terms of input SNR and the SNR associated with the A/D conversion. The loss due to the A/D conversion can now be defined as

$$L_{\text{A/D}} \triangleq 1 + \frac{[1 + (\text{SNR})_{\text{IN}}]}{(\text{SNR})_{\text{A/D}}}. \quad (26)$$

This is plotted in Figure 5 for various values of the number of bits of quantization, M . The values of $(\text{SNR})_{\text{A/D}} = h^{-1}(M, k)$ used in the computations are the optimal values taken from Table 1. As expected, observation of Figure 5 indicates that, as the number of bits of quantization increases, the loss in SNR incurred by use of the A/D conversion decreases rapidly. It is also noted that the loss increases as the input signal-to-noise ratio increases. This is also to be expected since, at higher values of input signal-to-noise ratio, the signal quality is good. Hence, introducing the distortion caused by the A/D converter will

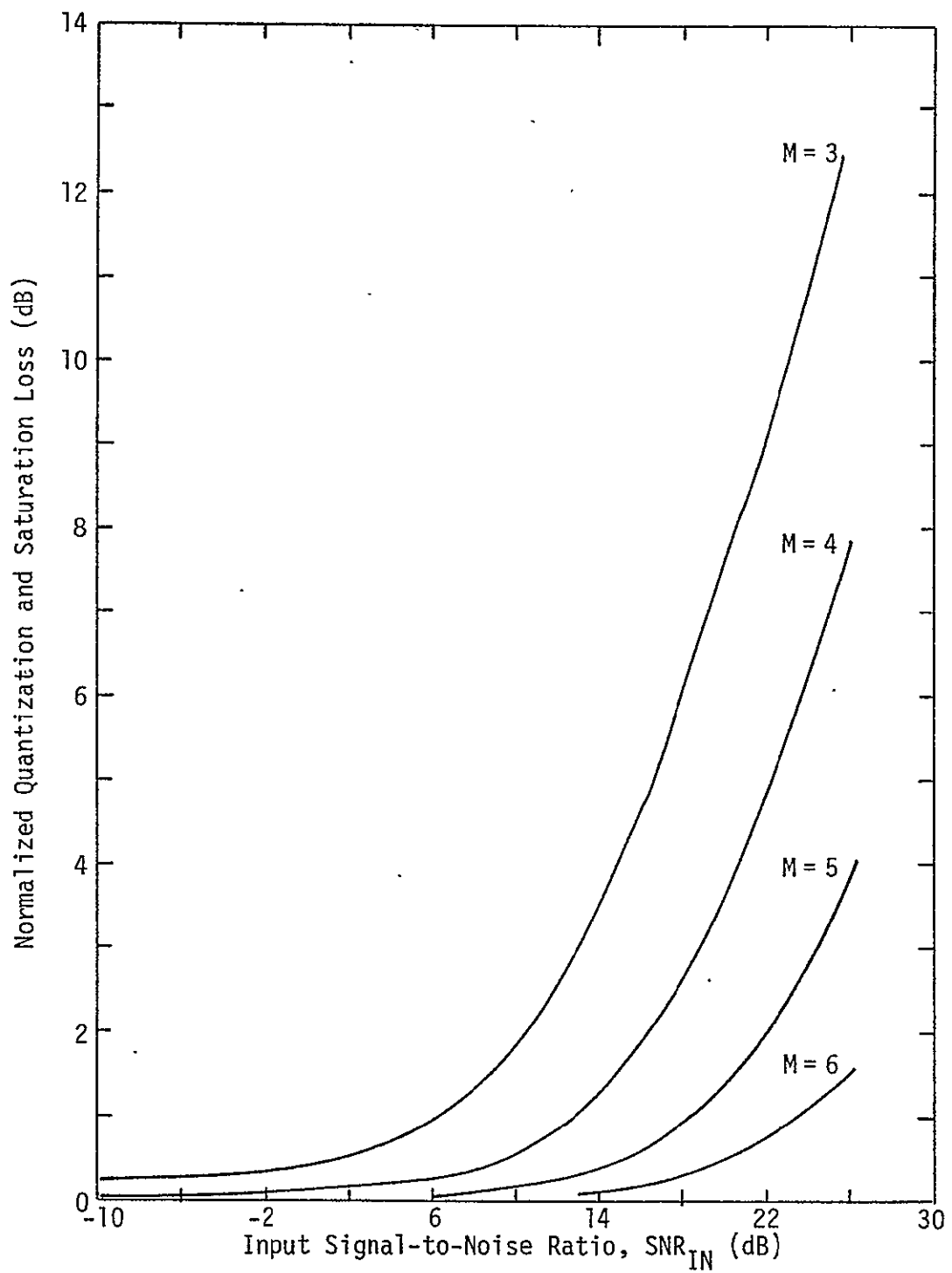


Figure 5. Normalized Quantization and Saturation Loss Versus Input Signal-to-Noise Ratio for $M=3$ to $M=6$ Bits of Quantization

substantially increase the total noise power. At low values of input signal-to-noise ratio, however, the signal quality is poor, and the introduction of distortion caused by A/D conversion does not appreciably increase the total noise power.

For these same values of $(\text{SNR})_{A/D}$, the output signal-to-noise ratio $(\text{SNR})_{OUT}$, as given in (25), is plotted versus the input signal-to-noise ratio $(\text{SNR})_{IN}$ in Figure 6 for various values of the number of bits of quantization M . Here again, at low values of input SNR, the quantization and saturation losses are negligible, whereas at large values of $(\text{SNR})_{IN}$, the effect of the A/D loss is a saturation effect in output SNR. This can analytically be seen to be the case in (26) when the second term dominates at large values of $(\text{SNR})_{IN}$. The A/D loss then increases linearly in input signal-to-noise ratio.

As the input $(\text{SNR})_{IN}$ increases, the output signal-to-noise ratio saturates at $(\text{SNR})_{A/D}$, i.e.,

$$\lim_{(\text{SNR})_{IN} \rightarrow \infty} (\text{SNR})_{OUT} = (\text{SNR})_{A/D} . \quad (27)$$

For example, for $M=4$ bits of quantization, the output SNR saturates at 18.9 dB.

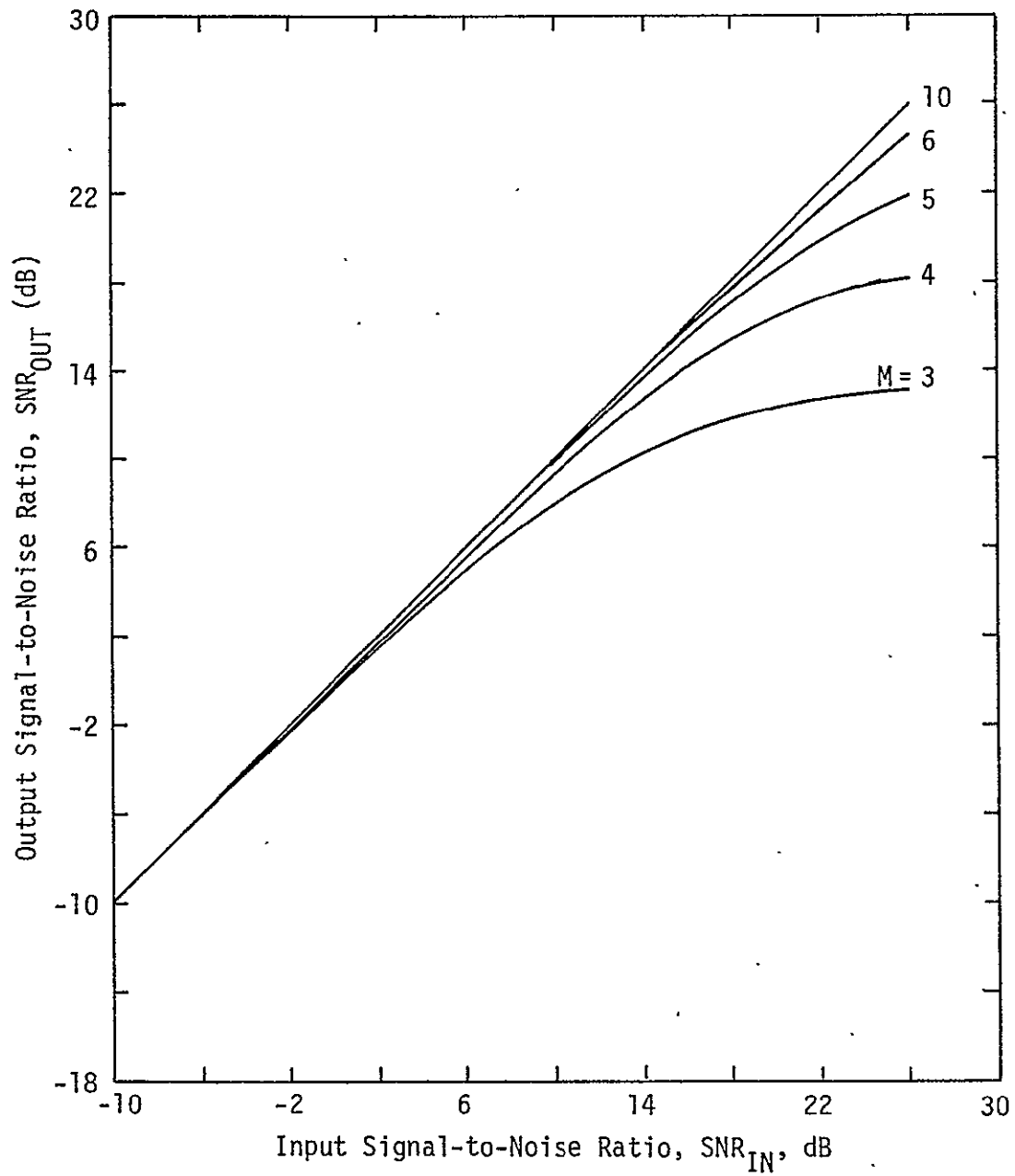


Figure 6. Output Signal-to-Noise Ratio Versus Input Signal-to-Noise Ratio for $M=3$ to $M=10$ Bits of Quantization

REFERENCES

1. G. A. Gray and G. W. Zeoli. "Quantization and Saturation Noise Due to Analog-to-Digital Conversion," IEEE Transactions on Aerospace and Electronic Systems, January 1971, pp. 222-223.
2. L. E. Brennan and I. S. Reed. "Quantization Noise in Digital Moving Target Indication Systems," IEEE Transactions on Aerospace and Electronic Systems, Vol. AES-2, November 1966.
3. J. Max. "Quantizing for Minimum Distortion," IEEE Transactions on Information Theory, Vol. PGIT-6, March 1960.

APPENDIX I

SHORT RANGE POWER BUDGET FOR THE KU-BAND RADAR PASSIVE SEARCH

APPENDIX I

SHORT RANGE POWER BUDGET FOR THE KU-BAND RADAR PASSIVE SEARCH

by

Waddah K. Alem
Charles L. Weber

1.0 INTRODUCTION

A power budget for the Ku-band Orbiter radar at short ranges ($R < 0.42$ nmi) is presented in this appendix. The various implementation losses at short ranges are also examined individually. Since the signal processing at these ranges is different from longer ranges ($R > 0.42$ nmi), the detection procedure is first examined. Only passive automatic search is considered.

2.0 DETECTION PROCEDURE AT SHORT RANGES

The basic difference between target detection for long range and short range lies in the fact that, while 16 pulses are coherently added (pre-summing) and passed through a bank of doppler filters in the first case, a single pulse detection without doppler filtering is implemented in the second case. The transmitted signal consists of 5 RF frequencies which are cycled, as is the case in long-range detection [1]. Within each frequency, a total of 16 pulses are transmitted. The width of each pulse is $\tau = 0.122$ μ sec and the PRF is equal to 6970 Hz. The transmitted power is not the same for all the pulses. As shown in Figure 1, the first eight pulses, P_0 through P_7 , are transmitted with the TWT completely bypassed, which results in a power of 7 dBm (5 mw). P_8 through P_{11} are transmitted with the TWT amplification and a series attenuation of 24 dB. The power in this case is equal to 23 dBm (200 mw). The last four pulses, P_{12} through P_{15} , are transmitted with a full power of 47 dBm (50 w). The power cycle is started with the least amount of power to avoid saturation of the receiver when the target is at a very short range.

The detection procedure is shown in Figure 2 [2]. After the second IF stage, the signal is passed through an I-Q stage to convert it to baseband. The lowpass arm filters used in this stage are two-pole Butterworth filters with single-sided cutoff frequency of 4.1 MHz. The complex baseband signal at the output of the I/D channel is sampled via an A/D

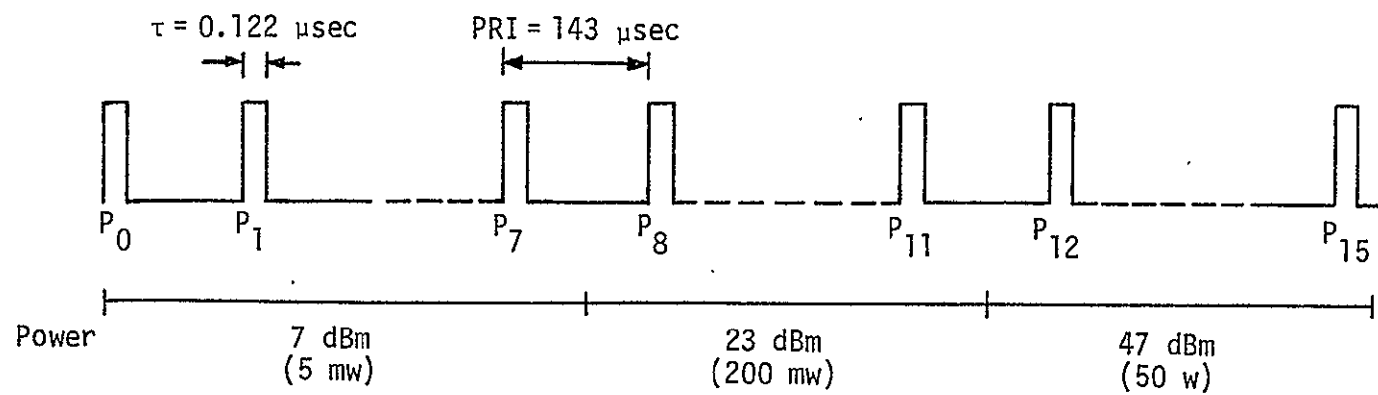


Figure 1. Signal Format for Short-Range Passive Search

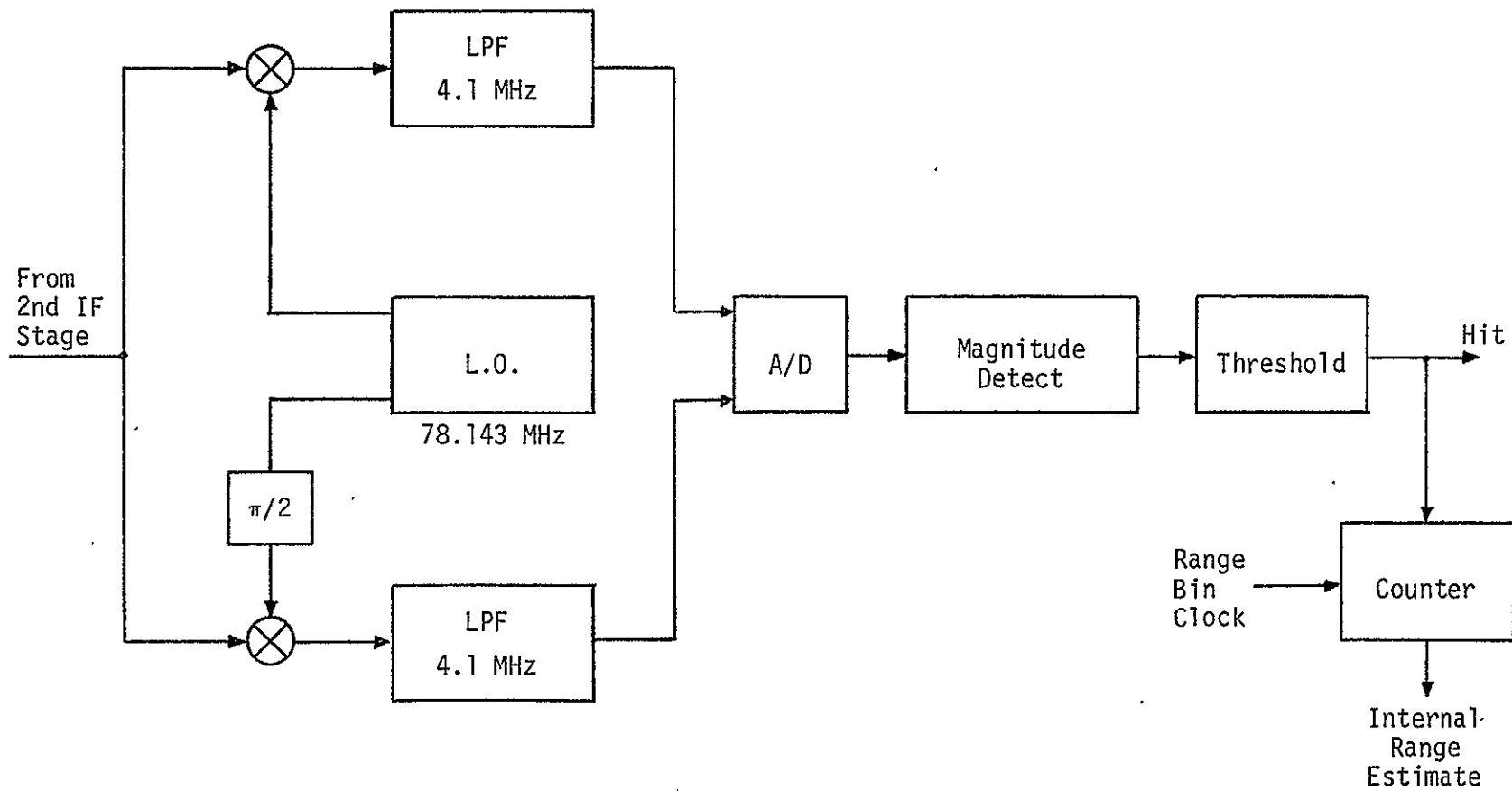


Figure 2. Single Pulse Short Range Detection

converter with a sampling frequency of 8.2 MHz, which corresponds to $1/\tau$ or one sample per pulse width. Each sample of the complex signal is magnitude-detected and compared to a threshold. Once the threshold is exceeded, a hit is declared. Detection is based on five hits to give an accumulative detection probability of 0.99. A maximum of 50 samples (range bins) are taken for each pulse return. This corresponds to a maximum range

$$\begin{aligned} R_{\max} &= 0.122 (\mu\text{sec/pulse}) \times 50 (\text{pulses}) \times 0.16187 (\text{nmi}/\mu\text{sec})/2 \\ &= 0.494 \text{ nmi} \\ &\approx 3000 \text{ feet.} \end{aligned}$$

The range bin clock and the counter are used to find the particular sample (range bin) for which the threshold was exceeded in order to calculate an internal range estimate to initiate the track mode.

3.0 RADAR EQUATION

The radar equation that is appropriate for short-range passive mode detection of a monopulse radar which is essentially using an optimal receiver [3-5] is given by

$$\bar{R}_p = \frac{2E_p}{N_0} = \frac{[G^2 \bar{\sigma} \lambda^2][2 P_p \tau]}{[(4\pi)^3 R^4][k T_s][L]},$$

where \bar{R}_p = ensemble averaged peak SNR required per pulse for a given probability of detection P_d and false alarm probability P_{fa} .

E_p = peak signal energy received per pulse.

N_0 = equivalent one-sided noise power spectral density of the entire receiver system = kT_s

$\bar{\sigma}$ = average target cross-section

λ = radar RF wavelength

G = peak antenna power gain

P_p = peak transmit power = P_{avg}/d_t

P_{avg} = average transmit power

d_t = transmitter duty factor

τ = transmitted pulse width

R = range

k = Boltzmann constant = 1.38×10^{-23} Joules/°K

T_s = system noise temperature, °K

L = total system losses.

4.0 SEARCH RADAR SYSTEM PARAMETERS

Each of the above parameters is now considered in regard to the Ku-band radar for the Space Shuttle Orbiter Vehicle. The reasoning and/or source of the choice of each parameter value is indicated.

4.1 Required Peak Signal-to-Noise Ratio Per Pulse

$$\bar{R}_p = \frac{2E_p}{N_0}$$

This value is dependent on the assumptions made about the mode of detection. The assumptions to be used in these power budgets are among the following cases. The overall probability of detection is 0.99 and the false alarm probability is 5.5×10^{-10} . The 0.99 value is a specification requirement and the $P_{fa} = 5.5 \times 10^{-10}$ value is approximately equivalent to one false alarm per hour, which is the specified value. The value of \bar{R}_p is relatively insensitive to the choice of P_{fa} . Hence, the choice is not critical. Since five scans of the target are used to declare detection, the probability of false detection per scan is 0.6.

In computing the required peak signal-to-noise ratio for short range, a Swerling III model will be used. In this model, the pulse amplitude is assumed to be a random variable with one dominant plus Rayleigh probability density function [4]. This model offers more conservative signal-to-noise ratios than the other Swerling models.

In order to use the results in [4], the following definition is used:

n' = false alarm number

$$P_{fa} = \ln 2/n'$$

Figure 3 is used to compute the required \bar{R}_p for $n' = 1.26 \times 10^{-9}$ and $P_d = 0.60$. This value is equal to 17.6 dB.

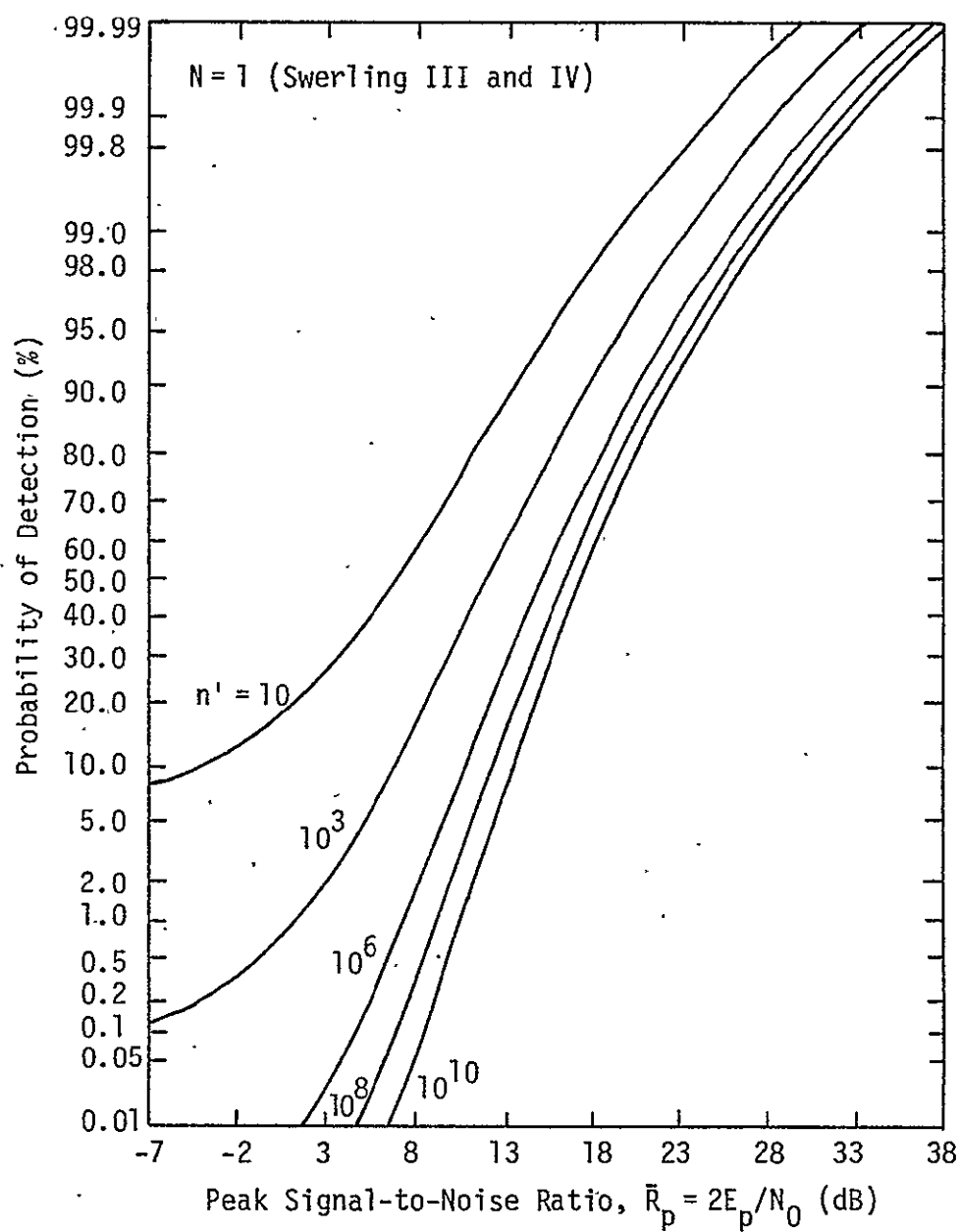


Figure 3. Probability of Detecting a Fluctuating Target, $N=1$ (Swerling III and IV). [N =number of pulses incoherently integrated; $P_{fa} = 0.693/n'$].

4.2 Average Target Cross-Section

$$\begin{aligned}\bar{\sigma} &= 1 \text{ m}^2, \text{ as in specification} \\ &= 0 \text{ dB}\end{aligned}$$

It is possible to use a target cross-section of 1 m^2 at short ranges up to 250 feet because, as is seen in Table 1 and Figure 4, the field of view in meters for a 3 dB antenna beam of 1.6° is equal to 2.13 m at 250 ft. This corresponds to an area of 3.56 m^2 , which justifies the fact that a 1 m^2 target can be totally illuminated within the main lobe of the antenna.

Table 1. Field of View of the Antenna With 3 dB Beamwidth $\theta_B = 1.6^\circ$

R (ft)	250	500	750	1000	1500	2000	2500
Field of View (m)	2.13	4.26	6.39	8.52	12.78	17.04	21.29
Illuminated Area (m^2)	3.56	14.25	32.07	57.01	128.28	228.05	355.99

In addition, the far field of an antenna is given in [10] by $2d^2/\lambda$, where d is the maximum linear dimension of the antenna (in this case, $d = 36'' = 0.914 \text{ m}$) and λ is the wave length. Substituting, it is found that the far field for the Ku-band antenna starts from 250 ft, which means that all the calculations beyond that range are done in the far field.

4.3 Radar RF Wavelength

The RF for the radar is 13.775 GHz. This corresponds to

$$\lambda = 0.0216 \text{ m}$$

$$\lambda^2 = -33.31 \text{ dB}.$$

4.4 Peak Antenna Power Gain

The antenna diameter has been specified as $d = 36'' = 0.914 \text{ m}$. Based on the rule of thumb,

$$\theta_B \text{ (deg)} \approx (180/\pi)(d/\lambda),$$

the 3 dB beamwidth is $\theta_B = 1.32 \text{ deg}$. The 3 dB beamwidth quoted in [7]

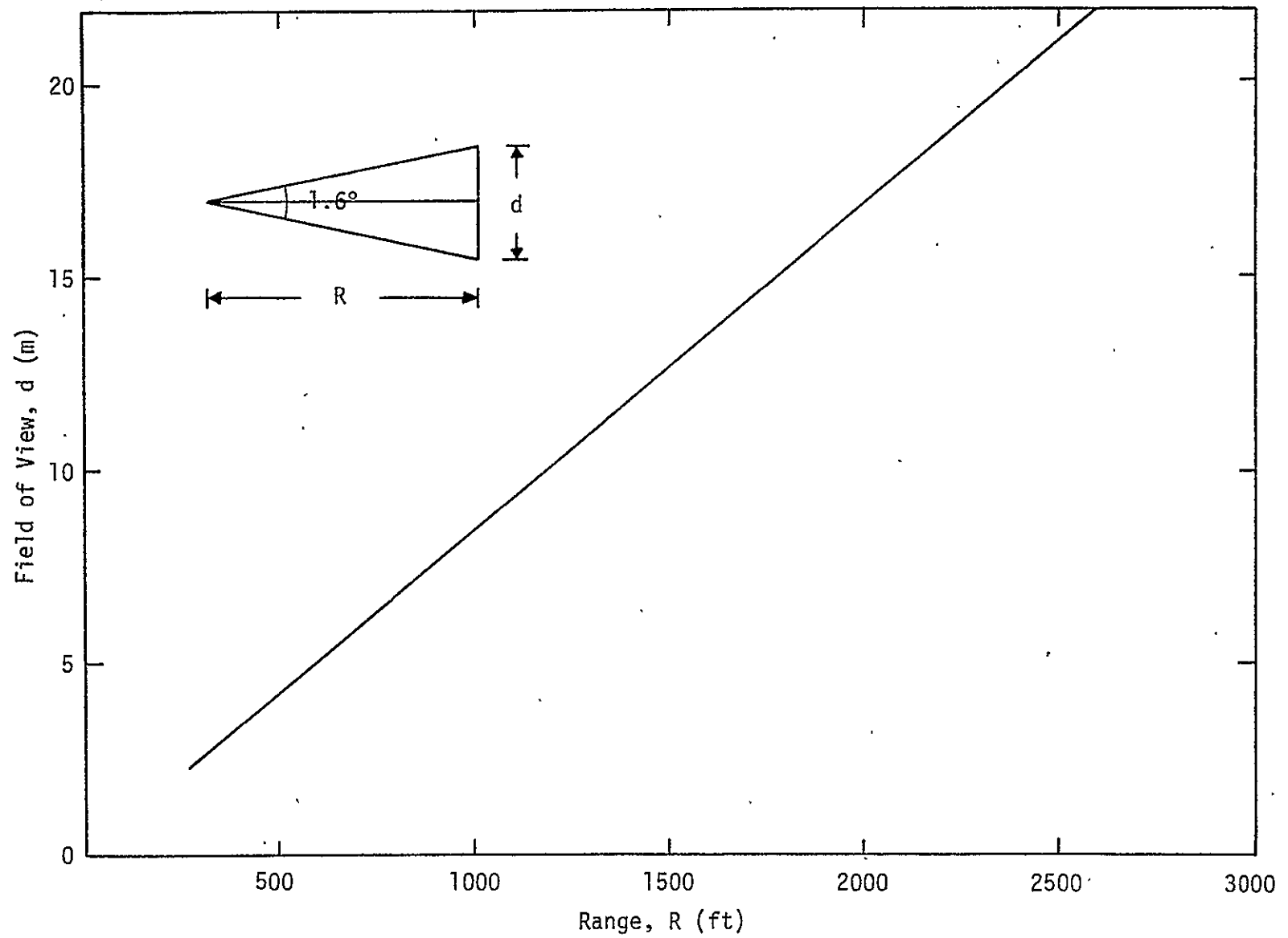


Figure 4. Field of View, d (m) versus Range, R (ft).

is 1.6 deg. Based on the rule of thumb [10],

$$G \approx \frac{32,000}{(\theta_B)^2} \quad (\theta_B \text{ in deg}),$$

the peak power gain of the antenna is

$$G \approx 41 \text{ dB}.$$

The peak power gain in [7] is 38.9 dB, so that

$$G^2 = 77.8 \text{ dB}.$$

More recently, however, the peak power gain is given as 38.5 dB [5], so that

$$G^2 = 77.0 \text{ dB}.$$

The latter value is used in the power budgets in this appendix.

4.5 Transmitted Signal Characteristics

P_p = peak transmitter power

Given all other parameters and assumptions in the radar equation, the required peak transmitter power will then be obtained. The pulse width is

$$\tau = 0.122 \text{ } \mu\text{sec}.$$

For the automatic search mode of a passive target at short range, the PRF is set at 6970 Hz, so that the pulse repetition interval (PRI) is

$$\text{PRI} = T_p = 143 \text{ } \mu\text{sec};$$

so the transmitter duty factor is

$$d_t = 8.5 \times 10^{-4}.$$

4.6 Range

The above signal characteristics are implemented for $R \leq 0.42 \text{ nmi}$ (2550 ft). The power budget will be calculated for the following ranges:

$$R = 2550, 800, 250 \text{ ft},$$

which correspond to

$$R^4 = 115.64, 95.49, 75.28 \text{ dB-meter}^4.$$

4.7 Receiver Noise Parameters

The receiver noise parameters were calculated in [6]. The calculations are included here for convenience.

The equivalent one-sided power spectral density of the receiver noise is

$$N_0 = kT_s \text{ watts/Hz},$$

where k = Boltzmann constant = 1.38×10^{-23} Joules/K°
= -228.6 dB.

T_s = overall system noise temperature.

The components in the overall system noise temperature can be computed from the diagram in Figure 5.



Figure 5. Simplified Diagram of Losses for Ku-Band Radar Receiver.

The receiver is assumed to have a noise figure of 5 dB. All component losses [7] between the antenna and the receiver add to 2.8 dB.

When the first stage of a receiver is an attenuator, as is the case here, it can be shown [8] that the system noise temperature, computed at the antenna, is

$$T_s = T_A + T_c + (L-1)T_0 + LT_e,$$

where T_A = antenna temperature.

T_c = additional antenna temperature due to clutter

L = total attenuation from all lossy components between the antenna and receiver input

T_e = receiver noise temperature = $(F_n - 1)T_0$

F_n = receiver noise figure

T_0 = standard room temperature = 290°K.

The design in [7] assumes the receiver noise figure is $F_n = 5.0$ dB or, equivalently, $T_e = 627^\circ\text{K}$, and the attenuation from all lossy components

between the antenna and receiver front end is $L = 2.8$ dB. The antenna temperature is assumed to be $T_A = 5.5^\circ\text{K}$ and the additional antenna temperature due to earth clutter when looking horizontally is $T_C = 36.5^\circ\text{K}$. Then,

$$\begin{aligned} T_S &= T_A + T_C + (L-1)T_0 + LT_e \\ &= 5.5 + 36.5 + 263 + 1195 \\ &= 1500^\circ\text{K} \\ &= 31.76 \text{ dB} . \end{aligned}$$

This is increased somewhat as the look angle increases. When looking directly toward the earth, the clutter temperature increases to 263.5°K and T_S increases to

$$T_S = 1727^\circ\text{K} = 32.27 \text{ dB} .$$

4.8 Losses

In this section, the pertinent losses are listed, along with the references where the values were derived or where losses were specified.

4.8.1 Transmit Losses

The RFP and the response [7] have specified the transmit losses at 3.7 dB. At this point, no attempt is being made to dispute this value, so it is accepted and used in the computations.

4.8.2 Scan Alignment Loss and Lateral Scan Loss

The specification calls for a total beam shape loss of 2 dB. In [4], it is shown that scan alignment loss is 1.03 dB each way and the lateral scan loss is 0.58 dB each way, when the antenna movement from one circle to the next in the spiral scan is $0.6 \theta_B$. The spiral scan described in [7] calls for an antenna movement of $0.7 \theta_B$. The difference in scan alignment loss and lateral scan loss between adjacent antenna paths of $0.6 \theta_B$ and $0.7 \theta_B$ is negligible. Thus, the two-way loss due to beam shape which includes scan alignment loss and lateral scan loss is set at $2(1.03 + 0.58) = 3.2$ dB.

4.8.3 Threshold Loss (Constant FAP)

The specification calls for a threshold loss of 1 dB due to maintaining a constant false-alarm probability by monitoring the system

noise level. This value is used in the computation, realizing that it should be possible to reduce this value to a few tenths of a dB.

4.8.4 Range Gate Straddling

The range gate straddling is due to the fact that a single sample is taken per pulse width ($\tau = 0.122 \mu\text{sec}$) after the pulse is passed through a two-pole Butterworth filter with a one-sided cutoff frequency of 4.1 MHz. Figure 6 shows the shape of the filtered pulse at the output of the two-pole Butterworth filter [9]. Since the sampling can occur any time within the pulse width ($0.122 \mu\text{sec}$) a maximum straddling loss of 6.5 dB is included in the calculation of the power budget.

5.0 POWER BUDGET FOR SHORT RANGE PASSIVE SEARCH

Table 2 summarizes the power budget calculations at the indicated ranges. Comparing the required peak powers to the existing available powers of 47 dBm, 23 dBm, and 7 dBm, it is found that

- (1) Design margin at 2550 ft compared to the available
47 dBm = 12.06 dB.
- (2) Design margin at 800 ft compared to the available
23 dBm = 8.22 dB.
- (3) Design margin at 250 ft compared to the available
7 dBm = 12.44 dB.

It is obvious from the derived design margins that the search for passive target at short ranges has a wide design margin; therefore, no problem in the Ku-band short-range passive target detection is anticipated.

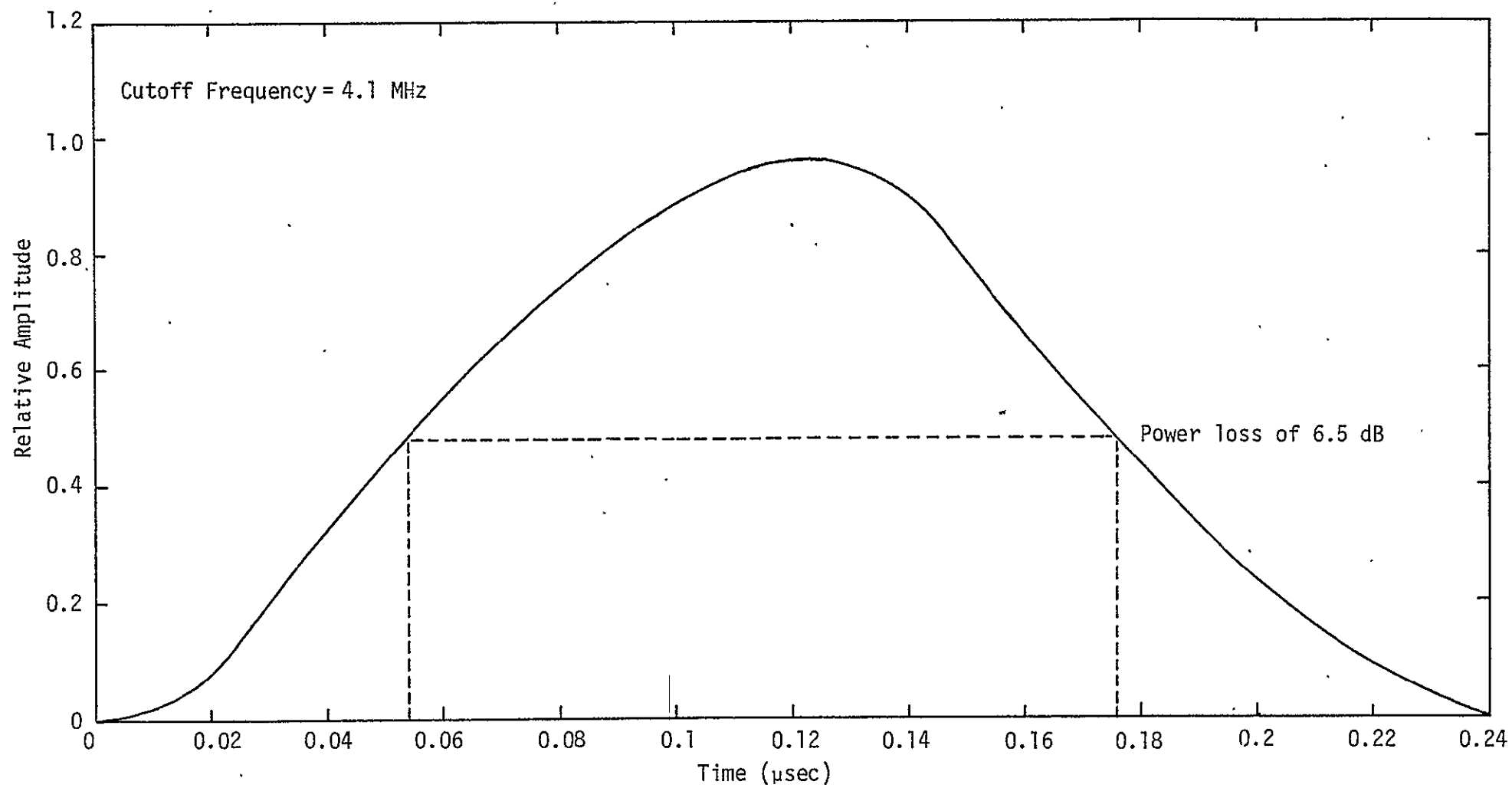


Figure 6. Two-Pole Butterworth Response to a Pulse of 0.122 μsec

Table 2. Power Budget for Short Range

Term	Value	Budget (dB)			
\bar{R}_p	Required peak SNR	17.6			
G^2	$G = 38.5$ dB	-77.0			
λ^2	$\lambda = 0.0216$ m	33.31			
$\bar{\sigma}$	1 m^2	0.0			
$(4\pi)^3$	---	32.98			
R^4	$R = 2550, 800, 250$ ft	115.65,	95.49,	75.28	
k	3.8×10^{-23} Joules/ $^{\circ}\text{K}$	-228.6			
T_s	1500°K	31.76			
τ	Pulsewidth = $0.122 \text{ } \mu\text{sec}$	-69.14			
	Factor of 2	-3.0			
<u>Losses</u>					
Transmit	REP	3.7			
Beam Shape	Scan Alignment	2.0			
Threshold	Constant FAP	1.0			
Straddling	Spreading of pulse	6.5			
P_p	Required peak powers	4.94 (34.94)	-15.22 (14.78)	-35.44 (-5.44)	dBw dBm

REFERENCES

1. Hughes Aircraft Co., "Ku-Band Integrated and Communication Equipment for the Space Shuttle Orbiter Vehicle," Schematic Review, Vol. II, July 20, 1977.
2. Hughes Aircraft Co., "Ku-Band Integrated and Communication Equipment for the Space Shuttle Orbiter Vehicle," Schematic Review, Vol. I, July 19, 1977.
3. S. Udalov. "Power Budgets for Passive Target Detection - Pulse Doppler Radar," Appendix N of "Study to Investigate and Evaluate Means of Optimizing the Radar Function for the Space Shuttle," Axiomatix Report No. R7607-4, July 1976.
4. C. L. Weber. "Optimization of Proposed Radar for the Integrated Ku-Band Radar Communication System," Axiomatix Report No. R7408-5, August 1974.
5. J. V. DiFranco and W. L. Rubin. Radar Detection. Prentice-Hall, 1968.
6. C. L. Weber, S. Udalov, and W. K. Alem. "Study to Investigate and Evaluate Means of Optimizing the Ku-Band Combined Radar/Communication Functions for the Space Shuttle," Axiomatix Report No. R7705-1, May 31, 1977.
7. Hughes Aircraft Co. "Ku-Band Integrated Radar and Communication Equipment for the Space Shuttle Orbiter Vehicle," Ref. No. D7738-SCG76076V, HS237-202, Conceptual Design Review, January 31, 1977.
8. A. B. Carlson. Communication Systems - An Introduction to Signals and Noise in Electrical Communication. McGraw-Hill, 1968.
9. K. W. Henderson and W. H. Kautz. "Transient Responses of Conventional Filters," IRE Transactions on Circuit Theory, 1958, pp. 333-347.
10. M. Skolnik. Radar Handbook. McGraw-Hill, 1970.

APPENDIX J

MAXIMUM LIKELIHOOD ESTIMATION OF THE RATIO OF POWERS IN TWO NARROWBAND PROCESSES

APPENDIX J..

MAXIMUM LIKELIHOOD ESTIMATION OF THE RATIO OF POWERS IN TWO NARROWBAND PROCESSES

by

Charles L. Weber

1.0 INTRODUCTION

In this appendix, we consider the maximum likelihood (M.L.) estimate of the ratio of the power in two narrowband processes. These processes are assumed to be Gaussian and, in general, will be correlated. The in-phase and quadrature-phase components of each process are sampled N times, where the time between samples is assumed to be large enough so that the samples are statistically independent.

The estimate of this ratio and its performance play a fundamental role for all types of tracking in the radar described in [1].

2.0 THE MAXIMUM LIKELIHOOD ESTIMATE OF POWER RATIO

Consider the narrowband Gaussian process $u(t)$, which we describe as

$$u(t) = u_c(t) \cos \omega_0 t + u_s(t) \sin \omega_0 t, \quad (1)$$

where $u_c(t)$ and $u_s(t)$ are baseband, zero mean, stationary, and Gaussian random processes.

The in-phase and quadrature-phase samples of $u(t)$ are represented as the real and imaginary components of a sequence of complex Gaussian random variables, namely,

$$U_i = u_{ci} + j u_{si}, \quad i = 1, \dots, N. \quad (2)$$

The expected value of $|U_i|^2$ is denoted by

$$P_U = E[|U_i|^2] = E[u_{ci}^2 + u_{si}^2] \quad \text{for all } i, \quad (3)$$

which is twice the average power in $u(t)$, $u_c(t)$, and $u_s(t)$. Equivalently,

$$E[u^2(t)] = E[u_c^2(t)] = E[u_s^2(t)] = \frac{P_U}{2}. \quad (4)$$

The same notation can be established for the other narrowband Gaussian process,

$$v(t) = v_c(t) \cos \omega_0 t + v_s(t) \sin \omega_0 t,$$

with average power $P_V/2$. With this notation, we can restate the estimation problem as follows:

Let \underline{U} and \underline{V} be N -dimensional complex Gaussian vectors whose N complex components U_i, V_i ($i=1, \dots, N$) have magnitudes and phases equal to the magnitudes and phases of a sequence of statistically independent samples of the narrowband processes $u(t)$ and $v(t)$, respectively.

Given these observations, the maximum likelihood estimate of P_U/P_V and $\ln(P_U/P_V)$ are desired, as well as the RMS error of the estimates.

In Addendum A, we show that the M.L. estimate of $\ln(P_U/P_V)$ is given by

$$\widehat{\ln[P_U/P_V]} = \ln \widehat{[P_U/P_V]} = \ln \left[\frac{||\underline{U}||^2}{||\underline{V}||^2} \right] \quad (5)$$

where

$$||\underline{U}||^2 \triangleq \sum_{i=1}^N |U_i|^2 \quad (6)$$

and

$$||\underline{V}||^2 \triangleq \sum_{i=1}^N |V_i|^2. \quad (7)$$

The estimator in (5) says that the M.L. estimate of $\ln(P_U/P_V)$ is equal to the natural logarithm of the M.L. estimate of P_U/P_V . In Addendum A, this is shown to be the case for any strictly monotonically increasing function of the estimate.

3.0 STATISTICAL CHARACTERISTICS OF THE OBSERVATIONS

At time t_i , when the i th sample of $u_c(t)$, $u_s(t)$, $v_c(t)$, and $v_s(t)$ are observed, the covariance matrix of the resulting four-dimensional Gaussian vector will be of the form

$$M_4 = \begin{bmatrix} P_U/2 & a & c & d \\ a & P_U/2 & -d & c \\ \hline c & -d & P_V/2 & b \\ d & c & b & P_V/2 \end{bmatrix}. \quad (8)$$

In Addendum B, the statistical characteristics of two narrowband Gaussian processes are considered. In particular, it is shown that the narrowband processes $u(t)$ and $v(t)$ that are observed in each of the tracking modes of the radar are "spherically symmetric." The physical meaning of a spherically symmetric random process is also described in Addendum B. The result is that $a = b = 0$ in (8). In addition, the conditions under which $d = 0$ are also enumerated, and it is noted that these conditions are met by the narrowband processes $u(t)$ and $v(t)$.

The covariance matrix M_4 in (8) therefore simplifies to

$$M_4 = \begin{bmatrix} P_U/2 & 0 & c & 0 \\ 0 & P_U/2 & 0 & c \\ \hline c & 0 & P_V/2 & 0 \\ 0 & c & 0 & P_V/2 \end{bmatrix}. \quad (9)$$

With this covariance matrix, all in-phase components are statistically independent of all quadrature components. As a result, each complex sample of $u(t)$ and $v(t)$ can be interpreted as two consecutive real samples.

Stated equivalently, the observations can be thought of as $2N$ independent samples of the real baseband Gaussian processes $u_c(t)$ and $v_c(t)$, where these zero mean processes for each sample have covariance matrix

$$M_2 = \begin{bmatrix} P_U/2 & c \\ c & P_V/2 \end{bmatrix}, \quad i = 1, \dots, 2N. \quad (10)$$

The maximum likelihood estimate of P_U/P_V is now given by

$$\widehat{P_U/P_V} \triangleq x_a^2 = \frac{\sum_{i=1}^{2N} u_{ci}^2}{\sum_{k=1}^{2N} v_{ck}^2}. \quad (11)$$

The performance of this estimator, as well as $z = \ln \widehat{P_U/P_V}$ is developed in the next section.

4.0 PERFORMANCE OF M.L. ESTIMATE OF POWER RATIO

In order to develop most directly the pdf of x_a defined in (11), the following notation is used.

The normalized correlation between u_{ci} and v_{ci} is given by

$$\rho = \frac{2c}{\sqrt{P_U P_V}}, \quad |\rho| \leq 1. \quad (12)$$

The inverse of the covariance matrix M_2 is denoted as

$$W_2 \triangleq M_2^{-1} = \begin{bmatrix} w_{11} & w_{12} \\ w_{12} & w_{22} \end{bmatrix}. \quad (13)$$

With this notation, the pdf of x_a in (11) is given by ([2, p. 50] or [5]):

$$q(x_a) = \frac{2 [\det(W_2)]^{n/2} x_a^{n-1} [w_{11} x_a^2 + w_{22}]}{B(\frac{n}{2}, \frac{n}{2}) [(w_{11} x_a^2 + w_{22})^2 - (2 x_a w_{12})^2]^{(n+1)/2}}, \quad (14)$$

where

$$n = \text{total number of independent samples} = 2N \quad (15)$$

$$B(\alpha, \beta) = \text{Beta Function} \triangleq \frac{\Gamma(\alpha) \Gamma(\beta)}{\Gamma(\alpha + \beta)} \quad (16)$$

$$\Gamma(\alpha) = \text{Gamma Function} = (\alpha - 1)! \text{ if } \alpha \text{ is an integer} \quad (17)$$

$$\det W_2 = \text{determinant of } W_2. \quad (18)$$

Substituting (12), (13) and (15) through (18) into (14), the pdf of x_a can be written as

$$q(x_a) = \frac{2 [\sigma_U^2 \sigma_V^2 (1 - \rho^2)]^{-N} x_a^{2N-1} \left[\frac{x_a^2}{\sigma_U^2 (1 - \rho^2)} + \frac{1}{\sigma_V^2 (1 - \rho^2)} \right]}{\frac{[(N-1)!]^2}{(2N-1)!} \left[\left(\frac{x_a^2}{\sigma_U^2 (1 - \rho^2)} + \frac{1}{\sigma_V^2 (1 - \rho^2)} \right)^2 - \left(\frac{2 x_a \rho}{\sigma_U \sigma_V (1 - \rho^2)} \right)^2 \right]^{(2N+1)/2}} \quad (19)$$

$$\text{where } \sigma_U^2 = P_U/2, \sigma_V^2 = P_V/2. \quad (20)$$

The estimate of P_U/P_V is

$$\widehat{P_U/P_V} \triangleq z_a = x_a^2 \quad (21)$$

Carrying out this transformation,

$$z_a = x_a^2$$

$$dz_a = 2x_a dx_a$$

The Jacobian of the transformation is

$$|J| = \frac{1}{2\sqrt{z_a}}$$

and the pdf of z_a , after some algebraic manipulation, is given by

$$p(z_a) = \frac{(2N-1)! \left[\frac{\sigma_U^2}{\sigma_V^2} \right]^N (1-\rho^2)^N z_a^{N-1} \left(z_a + \frac{\sigma_U^2}{\sigma_V^2} \right)}{[(N-1)!]^2 \left[\left(z_a + (\sigma_U^2/\sigma_V^2)(1-2\rho^2) \right)^2 + 4(\sigma_U/\sigma_V)^4 \rho^2(1-\rho^2) \right]^{N+\frac{1}{2}}} \quad (22)$$

The form of this pdf can be substantially simplified if we normalize z_a by setting

$$z_a \triangleq \frac{P_U}{P_V} x \quad (23)$$

Then,*

$$p(x) = A \frac{(x+1) x^{N-1}}{[(x+1)^2 - 4\rho^2 x]^{N+\frac{1}{2}}} \quad (24)$$

where

$$A = (1-\rho^2)^N (2N-1)! / [(N-1)!]^2 \quad (25)$$

The performance of the estimate of

$$\ln \widehat{P_U/P_V} = \ln \widehat{P_U/P_V} = z = \ln z_a \triangleq \ln (P_U/P_V) + \ln x \quad (26)$$

*The pdf of $p(x)$ in (24) agrees exactly with that developed in [1, p. C-9].

is evaluated by determining the RMS error.

The first moment is initially evaluated and is given by

$$E \left[\widehat{\ln (P_U/P_V)} \right] = \ln (P_U/P_V) + E (\ln x) . \quad (27)$$

By making the change of variable $x = e^y$,

$$\begin{aligned} E \left[(\ln x)^k \right] &= A \int_0^\infty \frac{(\ln x)^k (x+1) x^{N-1} dx}{[(x+1)^2 - 4\rho^2 x]^{N+\frac{1}{2}}} \\ &= A \int_{-\infty}^\infty \frac{y^k 2 \cosh (y/2)}{[2 \cosh y + 2 - 4\rho^2]^{N+\frac{1}{2}}} dy . \end{aligned} \quad (28)$$

When $k=1$ in (28), the integrand is an odd function over even limits and therefore vanishes. Hence,

$$E \left(\widehat{\ln P_U/P_V} \right) = \ln (P_U/P_V) \quad (29)$$

and $\widehat{\ln P_U/P_V}$ is an unbiased estimate of $\ln (P_U/P_V)$.

The variance of error is

$$\text{Var} \left[\widehat{\ln P_U/P_V} \right] \triangleq \sigma_z^2 = E \{ [\ln x]^2 \} . \quad (30)$$

Letting $k=2$ in (28),*

$$\begin{aligned} \sigma_z^2 = E [(\ln x)^2] &= 4A \int_0^\infty \frac{y^2 \cosh (y/2)}{[2 \cosh y + 2 - 4\rho^2]^{N+\frac{1}{2}}} dy \\ &= 2A \int_0^\infty \frac{y^2 [1 + e^{-y}] e^{-Ny}}{[e^{-2y} + (2 - 4\rho^2) e^{-y} + 1]^{N+\frac{1}{2}}} dy . \end{aligned} \quad (31)$$

The RMS error, σ_z , has been computed, the results of which are shown in [1, p. B-4] for $N=1,2,4,6,10$.

*Equation (31) agrees with the performance result in [1, p. C-10].

REFERENCES

1. "Space Shuttle Ku-Band Integrated Rendezvous Radar/Communications System Study," Hughes Aircraft Co., Report No. D4148 SCG60041R, for NASA-JSC under Contract NAS 9-14595, March 1976.
2. K. S. Miller, Multidimensional Gaussian Distributions, Wiley, 1964.
3. K. S. Miller, Complex Stochastic Processes, Addison-Wesley, 1974.
4. T. L. Grettenberg, "A Representation Theorem for Complex Normal Processes," IEEE Trans. on Info. Theory, Vol. IT-11, No. 2, April 1965, pp. 305-306.
5. J. Omura and T. Karlath, "Some Useful Probability Distributions," Stanford Electronics Lab Report 7050-6, September 1965.
6. H. Cramer, Mathematical Methods of Statistics, Princeton Press, 1946.
7. C. M. Thomas, "Maximum Likelihood Estimation of Signal-to-Noise Ratio," Ph.D. Dissertation, Department of Electrical Engineering, University of Southern California, June 1967.

ADDENDUM A

MAXIMUM LIKELIHOOD ESTIMATE OF POWER RATIO

MAXIMUM LIKELIHOOD ESTIMATE

The maximum likelihood estimate of the ratio of power in two complex Gaussian vectors is developed. If \underline{U} and \underline{V} are random vectors and α is a parameter of the probability density function (pdf), $p(\underline{U}, \underline{V}; \alpha)$, then the M.L. estimate of α is defined as that α which is

$$\max_{\alpha} p(\underline{U}, \underline{V}; \alpha) \triangleq p(\underline{U}, \underline{V}; \hat{\alpha}) \quad (\text{A-1})$$

If the pdf is unimodal, then $\hat{\alpha}$ is that α which is the solution to

$$\frac{\partial p(\underline{U}, \underline{V}; \alpha)}{\partial \alpha} = 0 \quad (\text{A-2})$$

or equivalently, that α which is the solution to

$$\frac{\partial \ln p(\underline{U}, \underline{V}; \alpha)}{\partial \alpha} = 0 \quad (\text{A-3})$$

If there is more than one unknown parameter, whether or not it is to be estimated, the M.L. estimate is given by the following. Suppose α and β are unknown parameters and α is to be estimated. The M.L. estimate for α and β is formed by simultaneously solving [6-7] the following:

$$\begin{aligned} \frac{\partial \ln p(\underline{U}, \underline{V}; \alpha, \beta)}{\partial \alpha} &= 0 \\ \frac{\partial \ln p(\underline{U}, \underline{V}; \alpha, \beta)}{\partial \beta} &= 0 \end{aligned} \quad (\text{A-4})$$

for α and β . The solutions are the M.L. estimates for α and β . If only one of the parameters is to be estimated, the estimate does not change.

We also note that: The maximum likelihood estimate of any strictly monotonically increasing function of a parameter is equal to that same function of the M.L. estimate of the parameter.

For example, if we have $p(\underline{U}; \alpha)$, and we desire the M.L. estimate of

$$\gamma = \ln \alpha, \quad (\text{A-5})$$

then we form

$$\frac{\partial p(\underline{U}, e^\gamma)}{\partial \gamma} = 0 \quad (\text{A-6})$$

and solve for $\hat{\gamma}$. By the chain scale for differentiation, however,

$$\frac{\partial p(\underline{U}, e^\gamma)}{\partial \gamma} = \frac{\partial p(\underline{U}, \alpha)}{\partial \alpha} \frac{\partial \alpha}{\partial \gamma}. \quad (\text{A-7})$$

Since

$$\frac{\partial \alpha}{\partial \gamma} = e^\gamma > 0 \quad \text{for all } \gamma, \quad (\text{A-8})$$

the only way (A-7) can equal zero is for

$$\frac{\partial p(\underline{U}, \alpha)}{\partial \alpha} = 0, \quad (\text{A-9})$$

since e^γ never vanishes.

Therefore, when determining the M.L. estimate of $\ln (P_U/P_V)$, we need only consider the M.L. estimate of P_U/P_V .

THE MAXIMUM LIKELIHOOD ESTIMATE OF POWER RATIOS

The M.L. estimate of power ratios is developed in steps. Consider first real uncorrelated Gaussian samples. The pdf $p(\underline{U}, \underline{V})$ is given by

$$p(\underline{U}, \underline{V}) = \left[\frac{1}{\sqrt{2\pi} \sigma_U} \right]^N \exp \left[\frac{-1}{2\sigma_U^2} ||\underline{U}||^2 \right] \left[\frac{1}{\sqrt{2\pi} \sigma_V} \right]^N \exp \left[\frac{-1}{2\sigma_V^2} ||\underline{V}||^2 \right]. \quad (\text{A-10})$$

The M.L. estimate of

$$R \triangleq \left[\frac{\sigma_U}{\sigma_V} \right]^2 \quad (\text{A-11})$$

is desired. The second parameter in $p(\underline{U}, \underline{V})$ is chosen to be σ_U , so that $p(\underline{U}, \underline{V})$ can be written as

$$p(\underline{U}, \underline{V}) = \left[\frac{1}{2\pi\sigma_u^2} \right]^N R^{N/2} \exp \left\{ \frac{-1}{2\sigma_u^2} \left[||\underline{U}||^2 + R ||\underline{V}||^2 \right] \right\}. \quad (A-12)$$

The M.L. estimates are solutions to

$$\begin{aligned} \frac{\partial \ln p(\underline{U}, \underline{V})}{\partial R} &= 0 \\ \frac{\partial \ln p(\underline{U}, \underline{V})}{\partial \sigma_u^2} &= 0. \end{aligned} \quad (A-13)$$

Without difficulty, the M.L. estimate for R is shown to be given by

$$\hat{R} = \left[\frac{\hat{\sigma}_u^2}{\hat{\sigma}_v^2} \right]^2 = \frac{||\underline{U}||^2}{||\underline{V}||^2}. \quad (A-14)$$

Also,

$$\hat{\sqrt{R}} = \left[\frac{\hat{\sigma}_u}{\hat{\sigma}_v} \right] = \frac{||\underline{U}||}{||\underline{V}||}, \quad (A-15)$$

since the square root is a strictly monotonically increasing function.

In the case of power ratios, it is noted that

$$\left[\frac{\hat{\sigma}_u^2}{\hat{\sigma}_v^2} \right] = \frac{\hat{\sigma}_u^2}{\hat{\sigma}_v^2} \quad (A-16)$$

when the random vectors are uncorrelated. We shall see that this is also the case when $u(t_i)$ and $v(t_i)$ are correlated.

CORRELATED SAMPLES

Correlated Gaussian samples are now considered. Since the extension from one sample of u and v to N samples is direct, we restrict attention to one sample of u and v . The joint pdf is given by

$$p(u,v) = \frac{1}{2\pi \sigma_u \sigma_v \sqrt{1-\rho^2}} \exp \left\{ \frac{-1}{2(1-\rho^2)} \left[\frac{u^2}{\sigma_u^2} + \frac{v^2}{\sigma_v^2} - \frac{2uv\rho}{\sigma_u \sigma_v} \right] \right\} \quad (A-17)$$

where ρ is the normalized correlation coefficient between u and v , defined by

$$\rho = \frac{E(uv)}{\sigma_u \sigma_v} \quad (A-18)$$

With the definition of R given in (A-11), $p(u,v)$ can be written as

$$p(u,v) = \frac{1}{2\pi \sigma_v^2 [(1-\rho^2)R]^{1/2}} \exp \left\{ \frac{-1}{2(1-\rho^2)} \left[\frac{u^2}{\sigma_v^2 R} + \frac{v^2}{\sigma_v^2} - \frac{2uv\rho}{\sigma_v^2 \sqrt{R}} \right] \right\} \quad (A-19)$$

There are now three parameters, so that the M.L. estimates are given by the solutions of

$$\frac{\partial \ln p(u,v)}{\partial R} = 0 \quad (A-20)$$

$$\frac{\partial \ln p(u,v)}{\partial \rho} = 0 \quad (A-21)$$

$$\frac{\partial \ln p(u,v)}{\partial (\sigma_v^2)} = 0 \quad (A-22)$$

Performing the indicated operations, we obtain

$$R = \frac{1}{(1-\rho^2)\sigma_v^2} [u^2 - uv\rho\sqrt{R}] \quad (A-23)$$

$$\sigma_v^2 = \frac{1}{2} \left(\frac{1}{1-\rho^2} \right) \left[\frac{u^2}{R} + v^2 - \frac{2uv\rho}{\sqrt{R}} \right] \quad (A-24)$$

and

$$\sigma_v^2 = \left(\frac{1}{1-\rho^2} \right) \left(\frac{u^2}{R} + v^2 \right) - \frac{uv}{\sqrt{R}} \left[\frac{1+\rho^2}{\rho(1-\rho^2)} \right] \quad (A-25)$$

from (A-20), (A-21), and (A-22), respectively.

✓
C

From (A-23), (A-24), and (A-25), the M.L. estimate of R is

$$\hat{R} = \frac{u^2}{v^2}$$

or equivalently,

$$\widehat{\ln R} = \ln [u^2/v^2] . \quad (A-26)$$

The key point is that when the random variables become correlated, the M.L. estimate for σ_u^2/σ_v^2 does not change.

The extension of these results to complex correlated Gaussian vectors is straightforward, although somewhat more cumbersome, with the result as shown in (5). With the simpler development that is shown here, the M.L. estimate in (5) is the expected estimate.

ADDENDUM B

STATISTICAL CONSIDERATIONS OF TWO NARROWBAND
GAUSSIAN PROCESSES

Preliminary statistical considerations of the two narrowband Gaussian processes are presented which are necessary before the performance of the maximum likelihood estimate can be determined.

The processes used in this estimation are marginally and jointly "spherically symmetric." Spherically symmetric means that an arbitrary phase shift of the carrier frequency will not change the statistical characteristics of the in-phase and quadrature-phase components of either process.

For spherically symmetric complex Gaussian vector processes, we can invoke Grettenberg's Theorem [3-4], an extension of which is quoted for this application.

Grettenberg's Theorem. Let $\underline{W}(t)$ be a complex (column) vector Gaussian process with mean zero. Then a necessary and sufficient condition that

$$E [\underline{W}(t) \underline{W}^T(s)] = 0 \quad (B-1)$$

for all s, t is that $w(t)$ and $e^{j\theta} w(t)$ be identically distributed for all real θ (i.e., spherically symmetric). The T in (B-1) means "transpose."

Mutually spherically symmetric for vector complex Gaussian processes implies that the information is in the phase differences, and an arbitrary but same phase shift in all components of the vector process produces no change in the joint statistics.

As pointed out above, the processes $u(t)$ and $v(t)$ are such that they are jointly spherically symmetric. It has already been assumed that the successive samples of $\{u(t), v(t)\}$ are sufficiently separated in time so as to be independent. The utility of Grettenberg's Theorem here is when $s = t$, for which

$$E [u^2(t)] = 0 \quad (B-2)$$

$$E [v^2(t)] = 0 \quad (B-3)$$

$$E [u(t) v(t)] = 0 \quad (B-4)$$

From (B-2),

$$E[u^2(t)] = E(u_{ci}^2) - E(u_{si}^2) + 2j E(u_{ci} u_{si}) = 0. \quad (B-5)$$

Hence,

$$E(u_{ci}^2) = E(u_{si}^2) \quad (B-6)$$

and

$$E(u_{ci} u_{si}) = 0. \quad (B-7)$$

Therefore, u_{ci} and u_{si} are statistically independent and identically distributed.

A similar statement can be made about $v(t)$ from (B-3).

From (B-4),

$$0 = E[u(t)v(t)] = E[u_{ci} v_{ci} - u_{si} v_{si}] + j E[u_{ci} v_{si} + u_{si} v_{ci}]. \quad (B-8)$$

Hence,

$$E(u_{ci} v_{ci}) = E(u_{si} v_{si}) \triangleq c \quad (B-9)$$

$$E(u_{ci} v_{si}) = -E(u_{si} v_{ci}) \triangleq d \quad (B-10)$$

where c and d are real.

The cross-correlation of $u(t)$ and $v(t)$ is defined as

$$\begin{aligned} P_{UV} &\triangleq E[u^*(t)v(t)] \\ &= E[u_{ci} v_{ci} + u_{si} v_{si}] + j E[u_{ci} v_{si} - u_{si} v_{ci}]. \end{aligned} \quad (B-11)$$

For spherically symmetric processes,

$$P_{UV} = 2c \quad (B-12)$$

and is real.

The covariance matrix of $[u_{ci}, u_{si}, v_{ci}, v_{si}]^T$ can now be written as

$$M_4 = \left[\begin{array}{cc|cc} P_U/2 & 0 & c & d \\ 0 & P_U/2 & -d & c \\ \hline c & -d & P_V/2 & 0 \\ d & c & 0 & P_V/2 \end{array} \right] \quad (B-13)$$

Next consider $u(t)$ and $v(t)$ expressed in terms of envelope and phase variations:

$$\begin{aligned} u(t) &= R_1(t) \cos [\omega_0 t - \theta_1(t)] \\ v(t) &= R_2(t) \cos [\omega_0 t - \theta_2(t)] \end{aligned} \quad (B-14)$$

Then,

$$\begin{aligned} E[u_c v_c] &= E[R_1 R_2 \cos \theta_1 \cos \theta_2] = c \\ E[u_s v_s] &= E[R_1 R_2 \sin \theta_1 \sin \theta_2] = c \\ E[u_c v_s] &= E[R_1 R_2 \cos \theta_1 \sin \theta_2] = d \\ E[u_s v_c] &= E[R_1 R_2 \sin \theta_1 \cos \theta_2] = -d \end{aligned} \quad (B-15)$$

Let $\phi \triangleq \theta_2 - \theta_1$, where ϕ represents the "phase difference information" between $u(t)$ and $v(t)$. Then,

$$\begin{aligned} E(u_c v_c) &= \frac{1}{2} E \left\{ R_1 R_2 (\cos \phi + \cos (\phi + 2\theta_1)) \right\} = c \\ E(u_s v_s) &= \frac{1}{2} E \left\{ R_1 R_2 (\cos \phi - \cos (\phi + 2\theta_1)) \right\} = c \end{aligned} \quad (B-16)$$

$$\begin{aligned} E(u_c v_s) &= \frac{1}{2} E \left\{ R_1 R_2 (\sin \phi + \sin (\phi + 2\theta_1)) \right\} = d \\ E(u_s v_c) &= \frac{-1}{2} E \left\{ R_1 R_2 (\sin \phi - \sin (\phi + 2\theta_1)) \right\} = -d \end{aligned} \quad (B-17)$$

For spherically symmetric processes, θ_1 is uniformly distributed over $(-\pi, \pi)$. When this is incorporated into (B-16) and (B-17),

$$E[u_c v_c] = -E[u_s v_s] = \frac{1}{2} E[R_1 R_2 \cos \phi] = c \quad (B-18)$$

$$E(u_c v_s) = E(u_s v_c) = \frac{1}{2} E[R_1 R_2 \sin \phi] = d \quad (B-19)$$

Finally, if the phase difference ϕ has a symmetric pdf about 0, then $E(\sin \phi) = 0$, and $d = 0$. In the applications anticipated with this estimator, the statistics of the estimator are independent of phase. In addition, the assumption that ϕ has a symmetric pdf is a very reasonable one for most applications. This assumption is therefore made and, hence, $d = 0$.

The covariance matrix M_4 in (B-13) now simplifies to

$$M_4 = \begin{bmatrix} P_U/2 & 0 & c & 0 \\ 0 & P_U/2 & 0 & c \\ \hline c & 0 & P_V/2 & 0 \\ 0 & c & 0 & P_V/2 \end{bmatrix} \quad (B-20)$$

Inspection of the covariance matrix in (B-20) shows that the only dependence is between the real part of $u(t)$ and the real part of $v(t)$, and the imaginary part of $u(t)$ and the imaginary part of $v(t)$. These correlations are also identical. Since everything else is uncorrelated (and therefore independent, since all processes are Gaussian), the observations could equally well be modeled as $2N$ samples of two real baseband processes $u_c(t)$ and $v_c(t)$.

When the pdf of the estimator is determined, we assume that $2N$ samples of $u_c(t)$ and $v_c(t)$ are observed. The resulting pdf of the estimator is identical to that when N complex samples are assumed to be observed from $u(t)$ and $v(t)$ with the covariance matrix given by (B-20).

APPENDIX K

POWER ALLOCATION PROPERTIES AND COSTAS LOOP SUBCARRIER TRACKING
PERFORMANCE ASSOCIATED WITH A DIGITAL PHASE SHIFT IMPLEMENTATION
OF THE THREE-CHANNEL ORBITER KU-BAND MODULATOR

APPENDIX K

POWER ALLOCATION PROPERTIES AND COSTAS LOOP SUBCARRIER TRACKING PERFORMANCE ASSOCIATED WITH A DIGITAL PHASE SHIFT IMPLEMENTATION OF THE THREE-CHANNEL ORBITER KU-BAND MODULATOR

by

Marvin K. Simon

INTRODUCTION

In a previous report [1], the author initiated a study to determine the feasibility of employing on the Space Shuttle Orbiter (SSO) a particular implementation of the three-channel Ku-band modulator wherein the two lower data rate channels are combined by digitally phase modulating their joint information on a single squarewave subcarrier. Such an implementation has been proposed by Hughes Aircraft Corporation (HAC) and will herein be referred to as the HAC version of the three-channel modulator. Others [2] have also considered such a possibility as an alternate means of transmitting an unbalanced quadri-phase shift keyed (UQPSK) signal. Prior to this suggestion, the accepted means of transmitting the information on the two lower data rate channels was to biphase modulate the two data streams onto quadrature squarewave (or sinusoidal) subcarriers. This version of the three-channel modulator will herein be referred to as the NASA version.

The purpose of this report is to continue the feasibility study begun in [1] with the hope of reaching a conclusion as to the desirability of the Hughes approach relative to a modification of it which incorporates a bandpass filter at the subcarrier modulator output. This modification has the effect of retaining only the fundamental of the digitally phase modulated squarewave subcarrier, thus making the modulator output signal identical in form to that of the NASA version with sinusoidal subcarriers.

We shall begin by rewriting the presentation made in [1] in a form which is more intuitively satisfying and more suitable from the standpoint of understanding the suggested modification mentioned above. Following this, we shall give careful attention to the feasibility of using an in-phase-quadrature type demodulator to extract the data on the two lower data rate channels from the composite modulator output. The performance of a subcarrier reconstruction loop, i.e., a Costas loop,

which incorporates this in-phase-quadrature demodulator in its input will also be investigated. Its tracking performance in response to an input from the HAC version, the modified HAC version, and the NASA version of the three-channel modulator output will be evaluated and compared.

Before concluding this introduction, it should be pointed out that the author in [1] made the statement that when the digital phase modulator implementation is used in the absence of a bandpass filter preceding the subcarrier demodulator, a simple in-phase-quadrature type demodulator of the Costas loop type will not produce a valid loop error signal at the loop filter input. In this regard, credit is due R. Cager of HAC for pointing out, through his analyses [3], that this statement was incorrect. In fact, much of the analysis presented in this report parallels that in [3] in a slightly simpler notation. Also, some additional effects, e.g., finite arm filter bandwidth distortions, which were not accounted for in [3] are hereing taken into account, along with numerical evaluations of system performance.

POWER ALLOCATION PROPERTIES OF THE HAC VERSION OF THE THREE-CHANNEL MODULATOR

In a host of previous studies [4-10], much consideration has been given to implementation of the three-channel Orbiter modulator, whose purpose is to generate a signal for simultaneous transmission of three channels of information on the Ku-band return link. Two of the more common structures for Mode 1 are referred to as the Three-Channel Interplex Modulator and the Three-Channel Quadrature Multiplex Modulator, the latter having the advantage that a linear phase modulator at the carrier frequency is not required. In principle, the quadrature multiplex modulator is of the in-phase-quadrature type wherein the high data rate channel (50 Mbps) is biphase modulated on the in-phase carrier and the two lower data rate channels (192 kbps and up to 2 Mbps), after being biphase modulated onto quadrature squarewave subcarriers and summed, are amplitude modulated onto the quadrature carrier (Figure 1). The disadvantage of this configuration is that the signal which is modulated onto the quadrature carrier is multi-level. Thus, when the in-phase and quadrature modulated carriers are summed and hard-limited, the resulting two-level signal suffers a limiter suppression effect

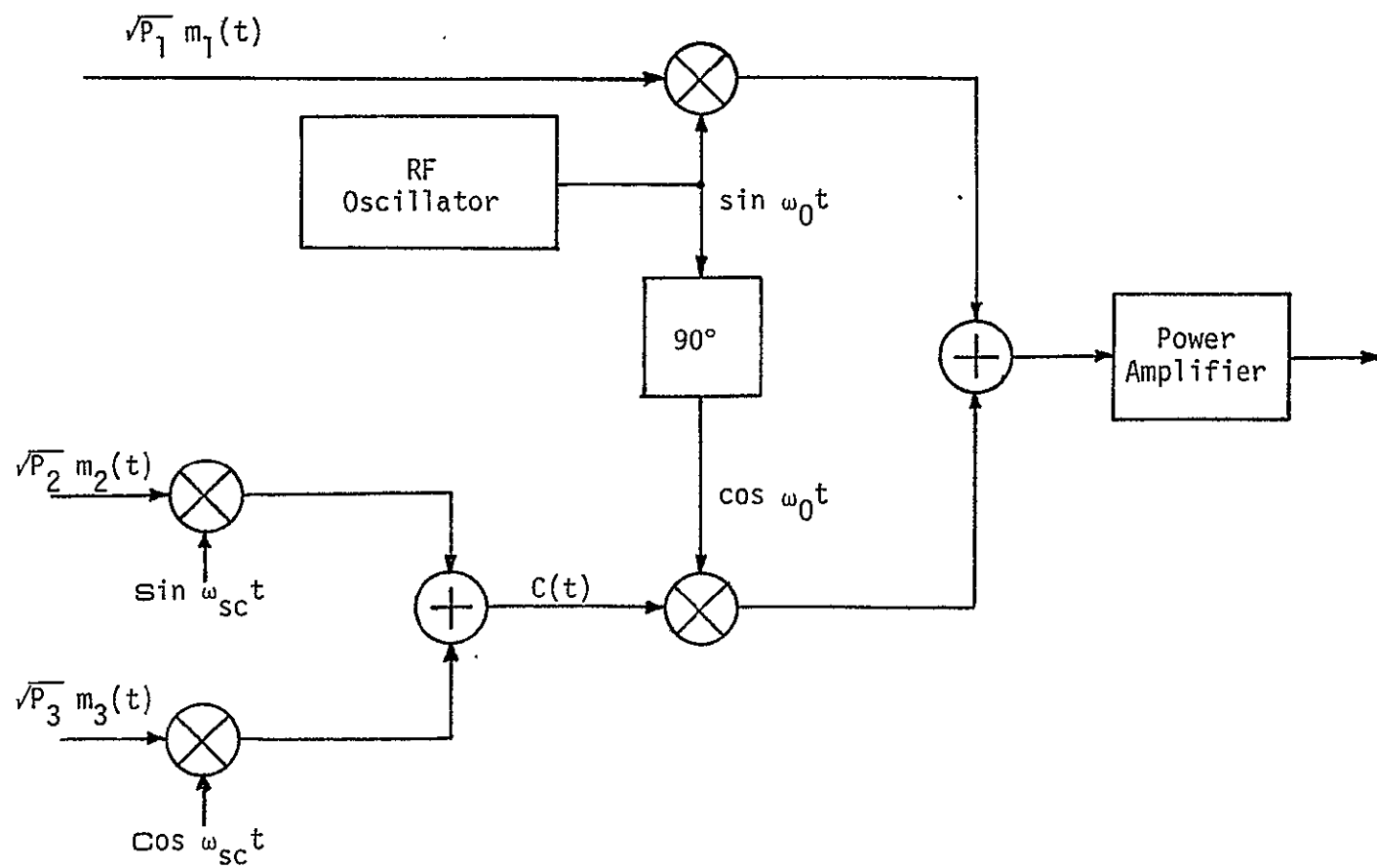


Figure 1. Three-Channel Quadrature Multiplex Modulator - Mode 1

and a redistribution of the power among the three channels, together with the generation of a triple cross-modulation product.

An alternate approach to combining the two lower rate data channels is to digitally phase modulate the joint information on these two channels onto a single squarewave subcarrier (Figure 2). If $m_2(t)$ and $m_3(t)$ respectively denote the lower rate modulations corresponding to channels 2 and 3, then the output of the digital phase modulator in Figure 2 can be expressed in the form

$$C(t) = \sqrt{P_s} \sin [\omega_{sc} t + \theta(t)] , \quad (1)$$

where $\sin x$ is a squarewave subcarrier with radian frequency ω_{sc} , P_s is the total power in this subcarrier, and the digital phase modulation $\theta(t)$ is given by (Figure 3):

$$\theta(t) = m_2(t) m_3(t) \theta_0 - \left(\frac{m_2(t) - 1}{2} \right) \pi . \quad (2)$$

The digital data streams $m_2(t)$ and $m_3(t)$ are ± 1 waveforms of rates R_2 and R_3 , respectively.* Notice from (2) that the digital phase modulation $\theta(t)$ takes on one of the four values $\pm \theta_0$, $\pi \pm \theta_0$, depending on the ± 1 polarity of the modulations $m_2(t)$ and $m_3(t)$. Thus, (1) represents an unbalanced QPSK modulated subcarrier. If $\theta_0 = \pi/4$, then (1) becomes a balanced QPSK modulated subcarrier.

As in Figure 1, the total three-channel signal generated by the modulator is

$$s(t) = \sqrt{2} \{C(t) \cos \omega_0 t + S(t) \sin \omega_0 t\} , \quad (3)$$

where ω_0 is the carrier radian frequency and

$$S(t) = \sqrt{P_1} m_1(t) \quad (4)$$

represents the high data rate channel.

Expanding (1) in a Fourier series gives

$$C(t) = \sqrt{P_s} \sum_{n=1,3,5,\dots}^{\infty} \frac{4}{n\pi} \sin \{n[\omega_{sc} t + \theta(t)]\} \quad (5)$$

*Throughout the remainder of this report, we shall assume that $R_2 > R_3$, e.g., $R_2 = 2$ Mbps, $R_3 = 192$ kbps.

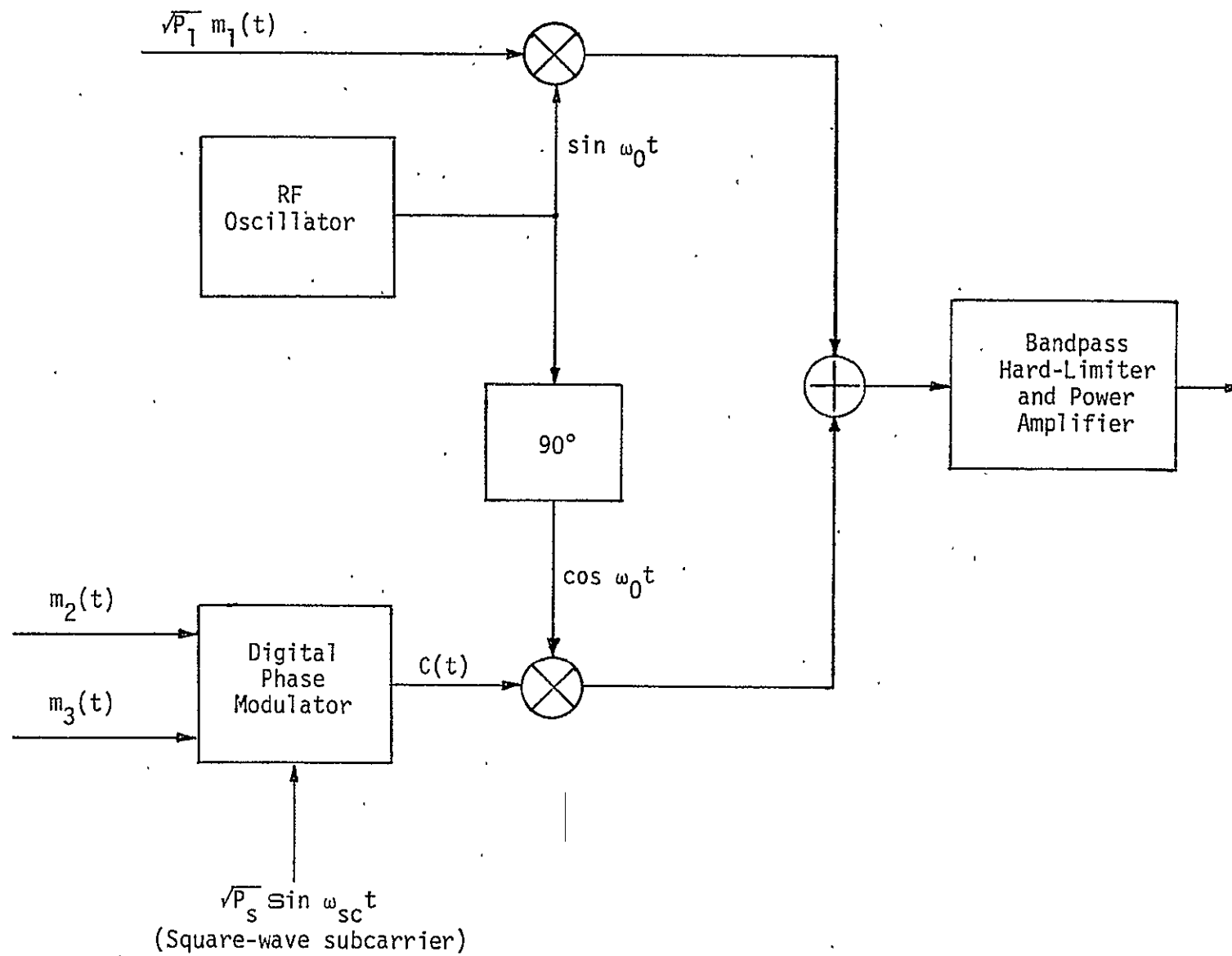


Figure 2. Digital Phase Shift Implementation of Three-Channel Modulator - Mode 1

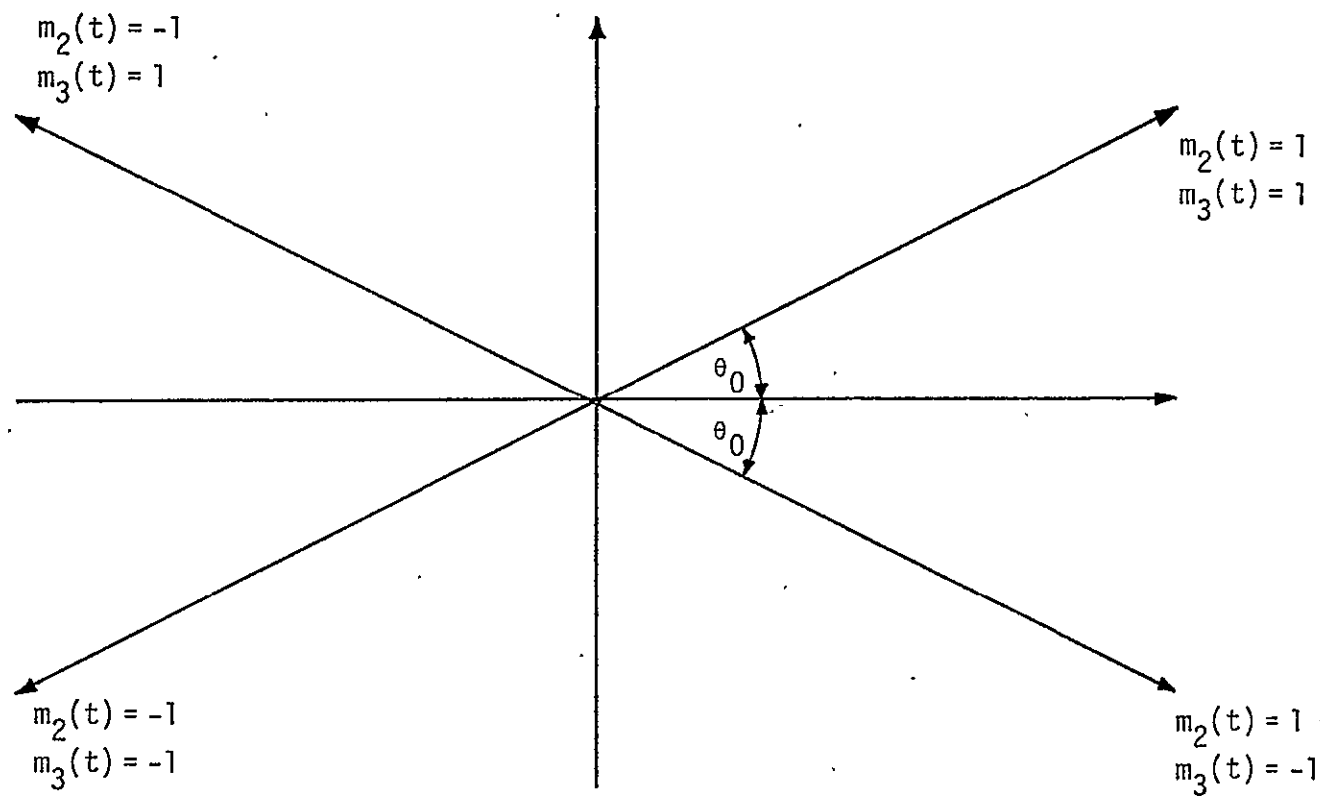


Figure 3. Phasor Representation of Digital Phase Modulator Output

$$\begin{aligned}
\text{or } C(t) &= \sqrt{P_s} \sum_{n=1,3,5,\dots}^{\infty} \frac{4}{n\pi} \sin n\omega_{sc} t \cos n\theta(t) \\
&+ \sqrt{P_s} \sum_{n=1,3,5,\dots}^{\infty} \frac{4}{n\pi} \cos n\omega_{sc} t \sin n\theta(t). \quad (6)
\end{aligned}$$

From (2), we find that, for n odd,

$$\begin{aligned}
\cos n\theta(t) &= \cos [m_2(t) m_3(t) n\theta_0] \cos \left[\left(\frac{m_2(t) - 1}{2} \right) n\pi \right] \overset{= m_2(t)}{} \\
&+ \sin [m_2(t) m_3(t) n\theta_0] \sin \left[\left(\frac{m_2(t) - 1}{2} \right) n\pi \right] \overset{= 0}{} \\
&= m_2(t) \cos n\theta_0 \\
\sin n\theta(t) &= \sin [m_2(t) m_3(t) n\theta_0] \cos \left[\left(\frac{m_2(t) - 1}{2} \right) n\pi \right] \\
&+ \cos [m_2(t) m_3(t) n\theta_0] \sin \left[\left(\frac{m_2(t) - 1}{2} \right) n\pi \right] \\
&= m_2^2(t) m_3(t) \sin n\theta_0 = m_3(t) \sin n\theta_0. \quad (7)
\end{aligned}$$

Thus, substituting (7) into (6) gives

$$\begin{aligned}
C(t) &= \sqrt{P_s} m_2(t) \sum_{n=1,3,5,\dots}^{\infty} \frac{4}{n\pi} \cos n\theta_0 \sin n\omega_{sc} t \\
&+ \sqrt{P_s} m_3(t) \sum_{n=1,3,5,\dots}^{\infty} \frac{4}{n\pi} \sin n\theta_0 \cos n\omega_{sc} t, \quad (8)
\end{aligned}$$

which is an in-phase-quadrature type representation where the "effective" subcarriers have Fourier series with coefficients $(4/n\pi) \cos n\theta_0$ and $(4/n\pi) \sin n\theta_0$.

To determine these effective subcarriers in terms of known functions, we use the trigonometric identities

$$\begin{aligned}
\cos n\theta_0 \sin n\omega_{sc} t &= \frac{1}{2} \sin n(\omega_{sc} t + \theta_0) + \frac{1}{2} \sin n(\omega_{sc} t - \theta_0) \\
\sin n\theta_0 \cos n\omega_{sc} t &= \frac{1}{2} \sin n(\omega_{sc} t + \theta_0) - \frac{1}{2} \sin n(\omega_{sc} t - \theta_0). \quad (9)
\end{aligned}$$

Then, since the squarewave subcarrier $\sin \omega_{sc} t$ has the Fourier series

$$\sin \omega_{sc} t = \sum_{n=1,3,5,\dots}^{\infty} \frac{4}{n\pi} \sin n\omega_{sc} t, \quad (10)$$

it is obvious from (8), (9) and (10) that $C(t)$ can be written in the form

$$C(t) = \sqrt{P_s} m_2(t) S^+(\omega_{sc} t; \theta_0) + \sqrt{P_s} m_3(t) S^-(\omega_{sc} t; \theta_0) \quad (11)$$

where

$$\begin{aligned} S^+(\omega_{sc} t; \theta_0) &\triangleq \frac{1}{2} \sin(\omega_{sc} t + \theta_0) + \frac{1}{2} \sin(\omega_{sc} t - \theta_0) \\ S^-(\omega_{sc} t; \theta_0) &\triangleq \frac{1}{2} \sin(\omega_{sc} t + \theta_0) - \frac{1}{2} \sin(\omega_{sc} t - \theta_0). \end{aligned} \quad (12)$$

Figure 4 illustrates $S^-(\omega_{sc} t; \theta_0)$ and $S^+(\omega_{sc} t; \theta_0)$ versus $\omega_{sc} t$. Note from this figure or the definitions in (12) that

$$\begin{aligned} S^+(\omega_{sc} t; \theta_0) S^-(\omega_{sc} t; \theta_0) &= 0 \\ \langle [S^+(\omega_{sc} t; \theta_0)]^2 \rangle &= 1 - \frac{2\theta_0}{\pi} \\ \langle [S^-(\omega_{sc} t; \theta_0)]^2 \rangle &= \frac{2\theta_0}{\pi}, \end{aligned} \quad (13)$$

where $\langle \rangle$ denotes time average. The first equation in (13) is interesting in that the product of the two effective subcarriers is identically zero rather than the time average of their product. This is a somewhat stronger condition than the usual orthogonality between in-phase and quadrature subcarriers.

It is now a simple matter to compute the power in each of the two lower rate channels at the output of the modulator. Thus, from (11) and (13), we have that

$$\begin{aligned} P_2 &= P_s \langle [S^+(\omega_{sc} t; \theta_0)]^2 \rangle = P_s \left(1 - \frac{2}{\pi} \theta_0\right) \\ P_3 &= P_s \langle [S^-(\omega_{sc} t; \theta_0)]^2 \rangle = P_s \left(\frac{2}{\pi} \theta_0\right). \end{aligned} \quad (14)$$

Thus, the ratio η_{23} of the transmitted power in channel 2 to that in channel 3 is, from (14),

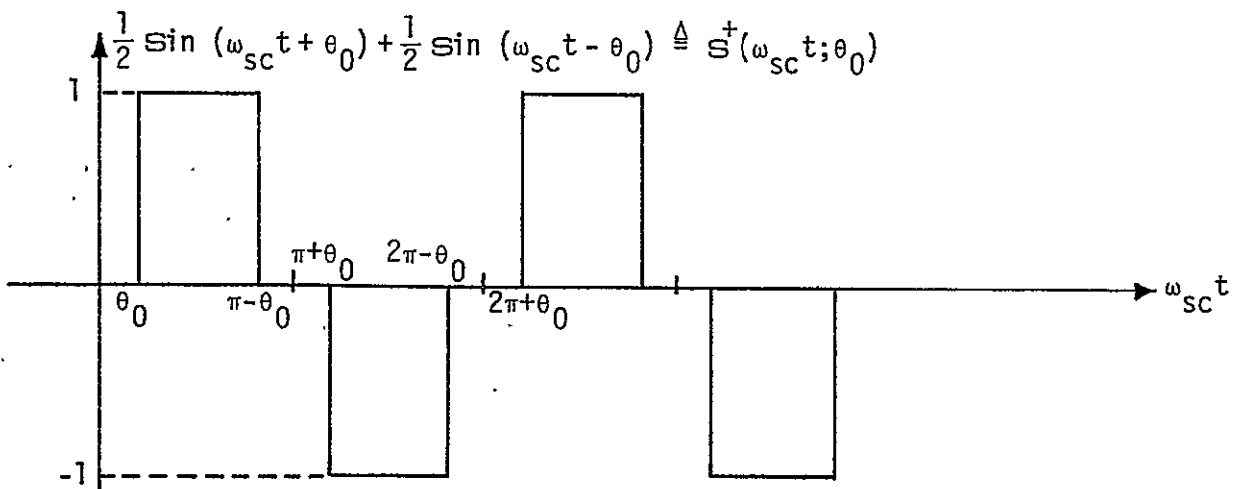
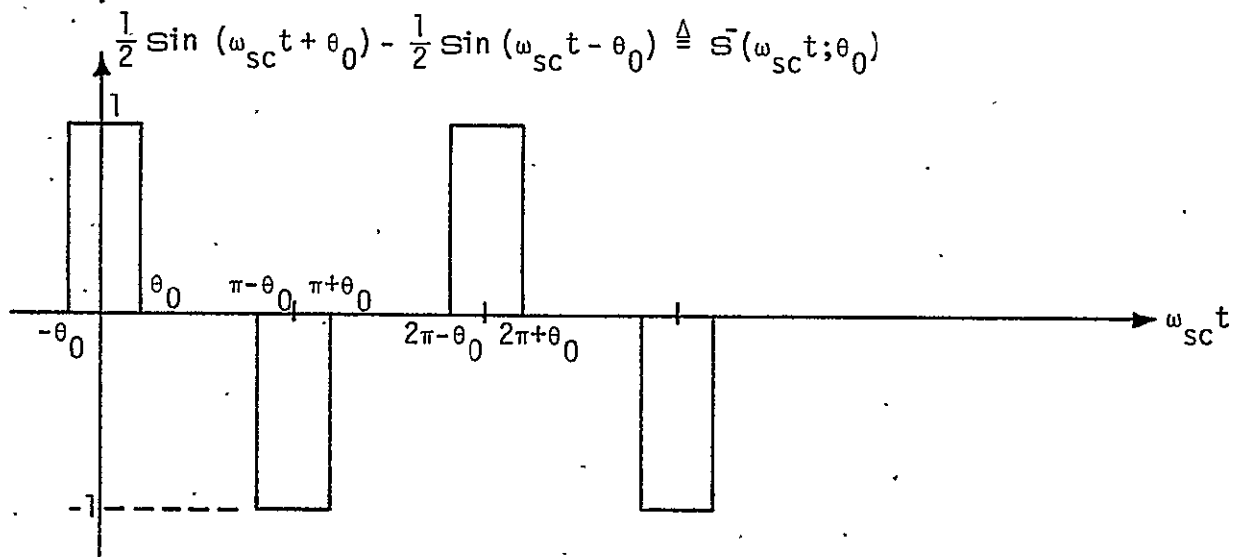
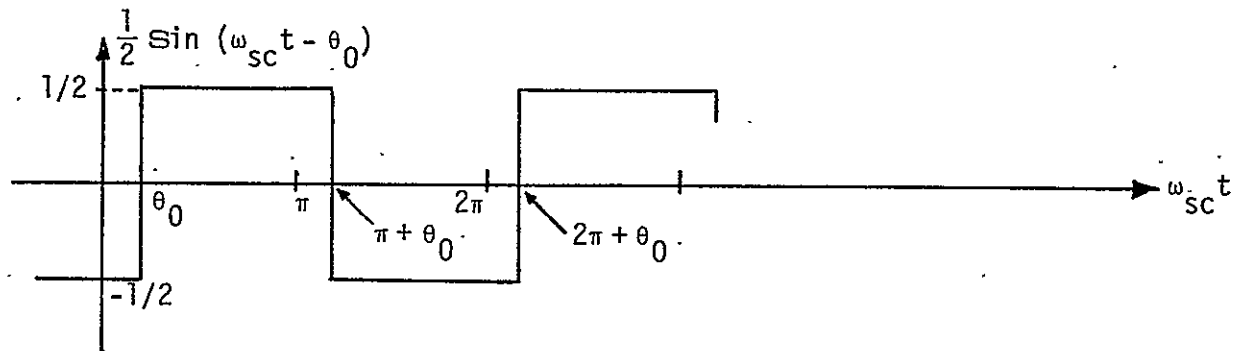
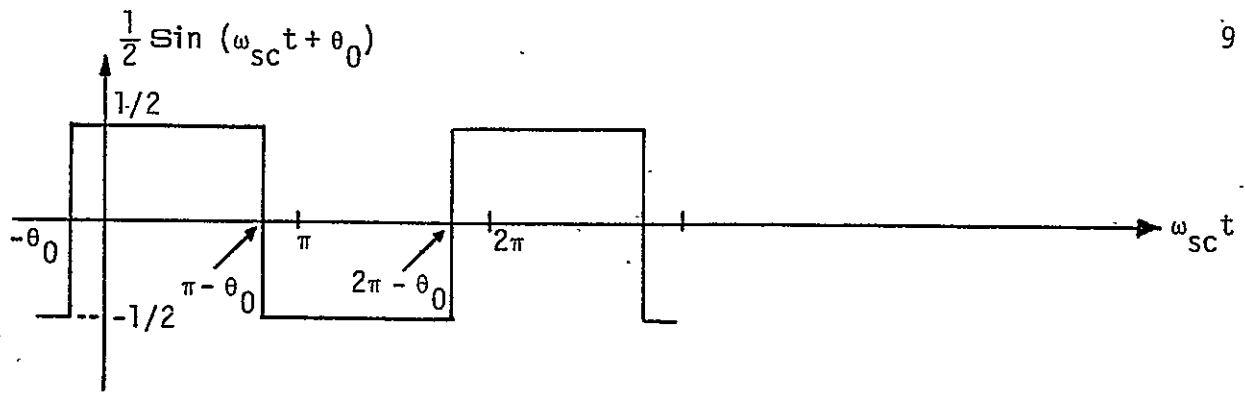


Figure 4. Effective In-Phase and Quadrature Subcarrier Waveforms

$$\eta_{23} \triangleq \frac{P_2}{P_3} = \frac{1 - \frac{2}{\pi} \theta_0}{\frac{2}{\pi} \theta_0} = \frac{\pi}{2\theta_0} - 1 \quad (15)$$

or, equivalently, solving for θ_0 in terms of η_{23} ,

$$\theta_0 = \frac{\pi}{2} \left(\frac{1}{1 + \eta_{23}} \right). \quad (16)$$

A modified version of the HAC three-channel modulator of Figure 2 incorporates a bandpass filter at the digital phase modulator output which allows passage of only the fundamental in this waveform. Also, since this filter output would no longer be digital, the multiplier which puts this signal on the quadrature carrier $\cos \omega_0 t$ would now have to be of the four-quadrant analog type rather than a switching multiplier.

Filtering out the first harmonic in (1) gives

$$\begin{aligned} C_1(t) &= \frac{4}{\pi} \sqrt{P_s} \sin [\omega_{sc} t + \theta(t)] \\ &= \frac{4}{\pi} \sqrt{P_s} \cos \theta(t) \sin \omega_{sc} t + \sqrt{P_s} \sin \theta(t) \cos \omega_{sc} t \end{aligned} \quad (17)$$

or, in view of (7),

$$C_1(t) = \frac{4}{\pi} \sqrt{P_s} m_2(t) \cos \theta_0 \sin \omega_{sc} t + \frac{4}{\pi} \sqrt{P_s} m_3(t) \sin \theta_0 \cos \omega_{sc} t. \quad (18)$$

From (18), we immediately see that the ratio of transmitted powers in data channels 2 and 3 is now

$$\eta_{23} = \frac{P_2}{P_3} = \frac{\frac{1}{2} \left(\frac{4}{\pi} \right)^2 P_s \cos^2 \theta_0}{\frac{1}{2} \left(\frac{4}{\pi} \right)^2 P_s \sin^2 \theta_0} = \cot^2 \theta_0 \quad (19)$$

or, equivalently,

$$\theta_0 = \cot^{-1} \sqrt{\eta_{23}} \quad (20)$$

To compare the relation between θ_0 and η_{23} of (16) or (20) with that of the quadrature multiplex implementation of Figure 1 (the NASA version of the three-channel modulator), we observe that, for the latter, we can immediately write

$$C(t) = \sqrt{P_2} m_2(t) \sin \omega_{sc} t + \sqrt{P_3} m_3(t) \cos \omega_{sc} t, \quad (21)$$

where $\cos x$ denotes a squarewave subcarrier in phase quadrature with $\sin x$. Assuming that the total power in $C(t)$ is again denoted by P_s , then from (21),

$$P_s = P_2 + P_3. \quad (22)$$

If $C(t)$ is bandpass filtered so that only its fundamental harmonic is passed, then from (21) and the Fourier series for $\sin \omega_{sc} t$ and $\cos \omega_{sc} t$, we have that

$$\begin{aligned} C_1(t) &= \frac{4}{\pi} \sqrt{P_2} m_2(t) \sin \omega_{sc} t + \frac{4}{\pi} \sqrt{P_3} m_3(t) \cos \omega_{sc} t \\ &= \frac{4}{\pi} \sqrt{P_s} \sin [\omega_{sc} t + \theta(t)], \end{aligned} \quad (23)$$

where

$$\theta(t) = \cot^{-1} \frac{\sqrt{P_2} m_2(t)}{\sqrt{P_3} m_3(t)}. \quad (24)$$

Comparing (24) with (2), we immediately see that θ_0 is given by (20). Thus, (17) and (21) are identical; or, equivalently, the filtered HAC and filtered NASA versions of the three-channel modulator give the same output signal with the same power allocation between the two lower data rate channels. Alternately, if the NASA version uses direct modulation of quadrature sinusoidal subcarriers rather than squarewave subcarriers, i.e., replace $\sin \omega_{sc} t$ and $\cos \omega_{sc} t$ in Figure 1 by $\sqrt{2} \sin \omega_{sc} t$ and $\sqrt{2} \cos \omega_{sc} t$, respectively, then the combined two-channel output would be given by (23) with the factor $4/\pi$ replaced by $\sqrt{2}$.

Figure 5 illustrates θ_0 (in degrees) versus n_{23} as determined from (16) and (20). To review, the result of (16) corresponds to the unfiltered digital phase modulator implementation (HAC version), whereas θ_0 of (20) corresponds to the unfiltered digital phase modulator (modified HAC version), the filtered quadrature multiplex with squarewave subcarriers (NASA version) or the quadrature-multiplex with sinusoidal subcarriers. Note that, for a transmitted power ratio $n_{23} = 4$, $\theta_0 = 18^\circ$ for the HAC version, whereas $\theta_0 = 26.57^\circ$ for the quadrature-multiplex or

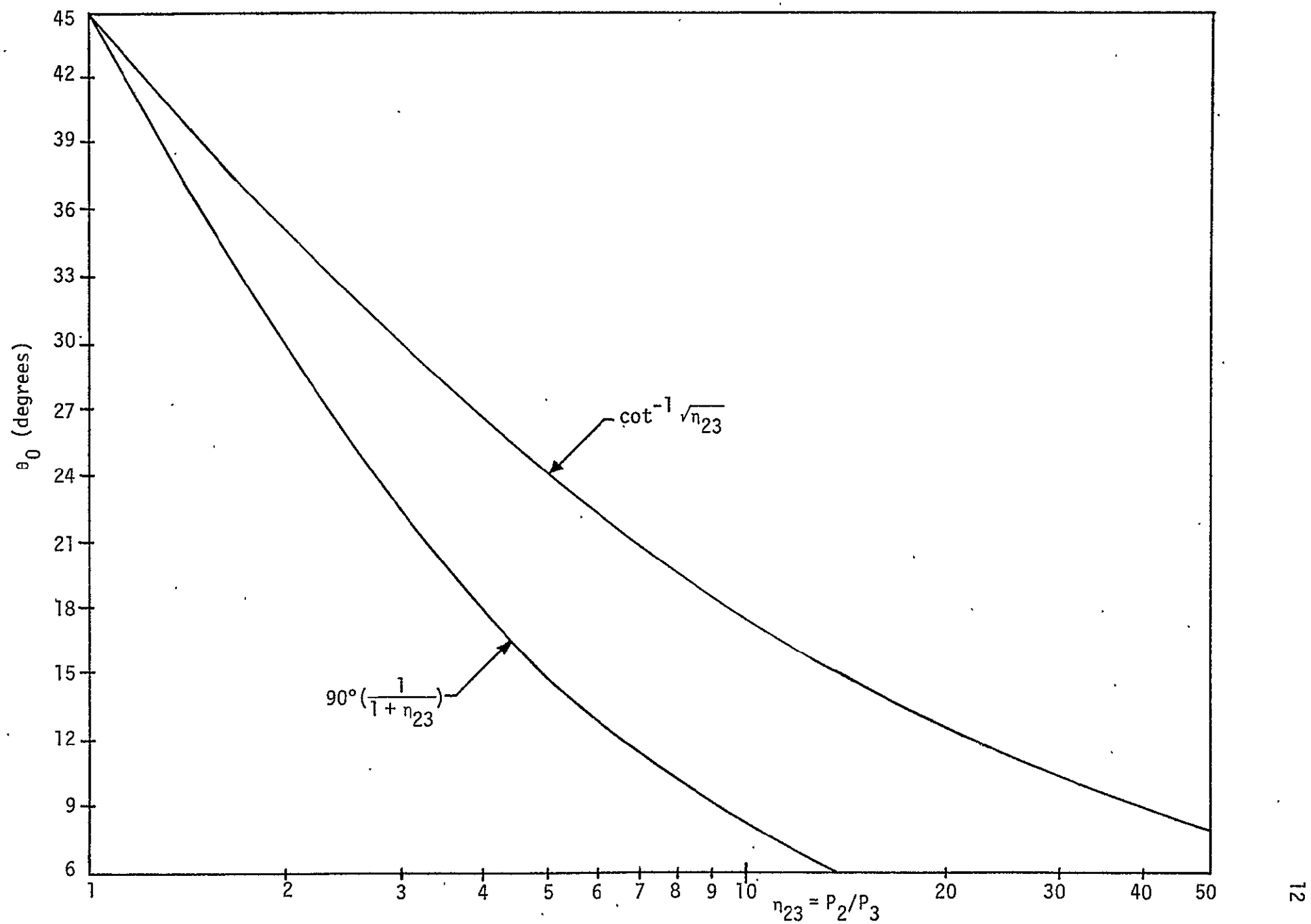


Figure 5. Phase Modulation Angle vs. Ratio of Transmitted Powers in Two Lower Rate Data Channels

HAC version with bandpass filter. Alternately, if the digital phase modulator implementation of Figure 2 were designed for Mode 2, wherein a bandpass filter is available preceding the subcarrier demodulator, then $\theta_0 = 26.57^\circ$ would be the proper choice. If this value of modulation angle were than also used in Mode 1 where the bandpass filter is absent, then from (15), we find that the ratio of the transmitted powers would be $\eta_{23} = 2.387$, rather than the desired value—4.

Before going on to a discussion of subcarrier demodulation and tracking performance for the various implementations, we review the results given in [1] for the effect of passing the HAC version modulator output through a bandpass hard-limiter which typically precedes the TWT power amplifier in the transmitter.

EFFECT OF PASSING THREE-CHANNEL SIGNAL THROUGH A BANDPASS HARD-LIMITER

We now consider the limiter suppression effect (if any) of passing $s(t)$ with $C(t)$ as defined in (1) through a bandpass hard-limiter. Expressing (3) in polar coordinates (amplitude and phase) gives

$$s(t) = \sqrt{2} V(t) \sin (\omega_0 t + \phi(t)) , \quad (25)$$

where

$$\begin{aligned} V(t) &= \sqrt{C^2(t) + S^2(t)} \\ \phi(t) &= \tan^{-1} \frac{C(t)}{S(t)} . \end{aligned} \quad (26)$$

Since passing $s(t)$ of (25) through a bandpass hard-limiter preserves the phase $\phi(t)$, then the resultant first zone output is given by

$$z_1(t) = \sqrt{2P} \sin (\omega_0 t + \phi(t)) , \quad (27)$$

where P is the total power in the first zone after amplification. In terms of in-phase and quadrature components, (27) can be rewritten as

$$z_1(t) = \sqrt{2P} \left[\frac{S(t)}{V(t)} \sin \omega_0 t + \frac{C(t)}{V(t)} \cos \omega_0 t \right] . \quad (28)$$

From (1), (4), and (26), we have that

$$\begin{aligned}
 V(t) &= \sqrt{P_1 m_1^2(t) + P_s \sin^2(\omega_{sc} t + \theta(t))} \\
 &= \sqrt{P_1 + P_2 + P_3} \triangleq \sqrt{P_T},
 \end{aligned} \tag{29}$$

where $P_T = P_1 + P_2 + P_3$ is the total input power. If we arbitrarily set the level of the power amplifier equal to the total input power level, i.e., $P = P_T$, then from (28) and (29), we have that

$$\begin{aligned}
 z_1(t) &= \sqrt{2} [C(t) \cos \omega_0 t + S(t) \sin \omega_0 t] \\
 &= s(t);
 \end{aligned} \tag{30}$$

i.e., the limiter (insofar as its first zone output is concerned) has no effect on the signal present at its input. Comparing this with the results for the quadrature multiplex case [4, Appendix C] wherein $C(t)$ is given by (21), we see that the power allocations among the three data channels are changed by the presence of the limiter in addition to the introduction of a triple cross-modulation product signal.

DEMULATION OF THE THREE-CHANNEL SIGNAL PRODUCED BY THE DIGITAL PHASE MODULATOR IMPLEMENTATION

Demodulation of the three-channel Ku-band return link signal on the ground is accomplished by first demodulating the carrier, thereby separating the 50 Mbps high rate digital data from that corresponding to the two lower rate channels. A three-channel carrier tracking loop for achieving the above carrier demodulation was described in Appendix C of [4], wherein the quadrature-multiplex type of transmitter was assumed. Since the carrier demodulation process is virtually transparent to the subcarrier demodulation which follows it, we can assume that the above carrier tracking loop is also appropriate to the digital phase modulator implementation of the transmitter in Mode 1 (see Figure 2). The real question then as to whether or not the digital phase modulator implementation is practical depends on the ability to demodulate the 8.5 MHz subcarrier and the ultimate performance of this demodulator.

Since the ground station ultimately desires an 8.5 MHz sinusoidal signal as their subcarrier reference, and we have available a digitally phase modulated squarewave subcarrier at nominally 8.5 MHz, several alternatives must be examined for accomplishing the necessary subcarrier demodulation.

A. Subcarrier Demodulation of the HAC Version Using a Costas Loop With Switching Type In-Phase and Quadrature Phase Detectors and Analog Type Error Signal Multiplier

Consider first the Mode 1 case wherein a bandpass filter is not necessarily available preceding the subcarrier demodulator. Thus, the total (all harmonics included) modulator output as given by (1) or, equivalently, (11) is available for demodulation. The simplest form of demodulator one might consider would be the in-phase-quadrature type which also forms the front end of a conventional Costas loop (see Figure 6). In this regard, several options are available for the design of this loop, namely, choice of in-phase and quadrature phase detector type, choice of error signal multiplier type, selection of VCO waveform (typically sinusoidal or squarewave), and choice of low-pass arm filter type. Clearly, if the VCO reference is a squarewave, then the choice of in-phase and quadrature phase detector type (i.e., analog or switching) is theoretically immaterial. Alternately, if these same multipliers are chosen to be of the switching type, then the selection of either a sinusoidal or squarewave VCO reference produces the same results. In what follows, we shall assume that the input in-phase and quadrature multipliers are of the switching type and the error signal multiplier is of the analog type, the latter choice leading to a somewhat simpler analysis. Finally, at this point, the arm filters need only be specified in terms of their transfer function $G(s)$.

Consider the Costas loop illustrated in Figure 6 when the input $x(t)$ is the unbalanced QPSK signal of (11) plus noise, i.e.,

$$x(t) = \sqrt{P_s} m_2(t) S^+(\omega_{sc} t; \theta_0) + \sqrt{P_s} m_3(t) S^-(\omega_{sc} t; \theta_0) + n_i(t), \quad (31)$$

where the additive channel noise $n_i(t)$ can be expressed in the form of a narrowband process about the subcarrier frequency, i.e.,

$$n_i(t) = \sqrt{2} \{N_c(t) \cos \omega_{sc} t - N_s(t) \sin \omega_{sc} t\}. \quad (32)$$

In (32), $N_c(t)$ and $N_s(t)$ are approximately statistically independent, stationary, white Gaussian noise processes with single-sided noise spectral density N_0 w/Hz, and single-sided bandwidth $B_H < \omega_{sc}/2\pi$.

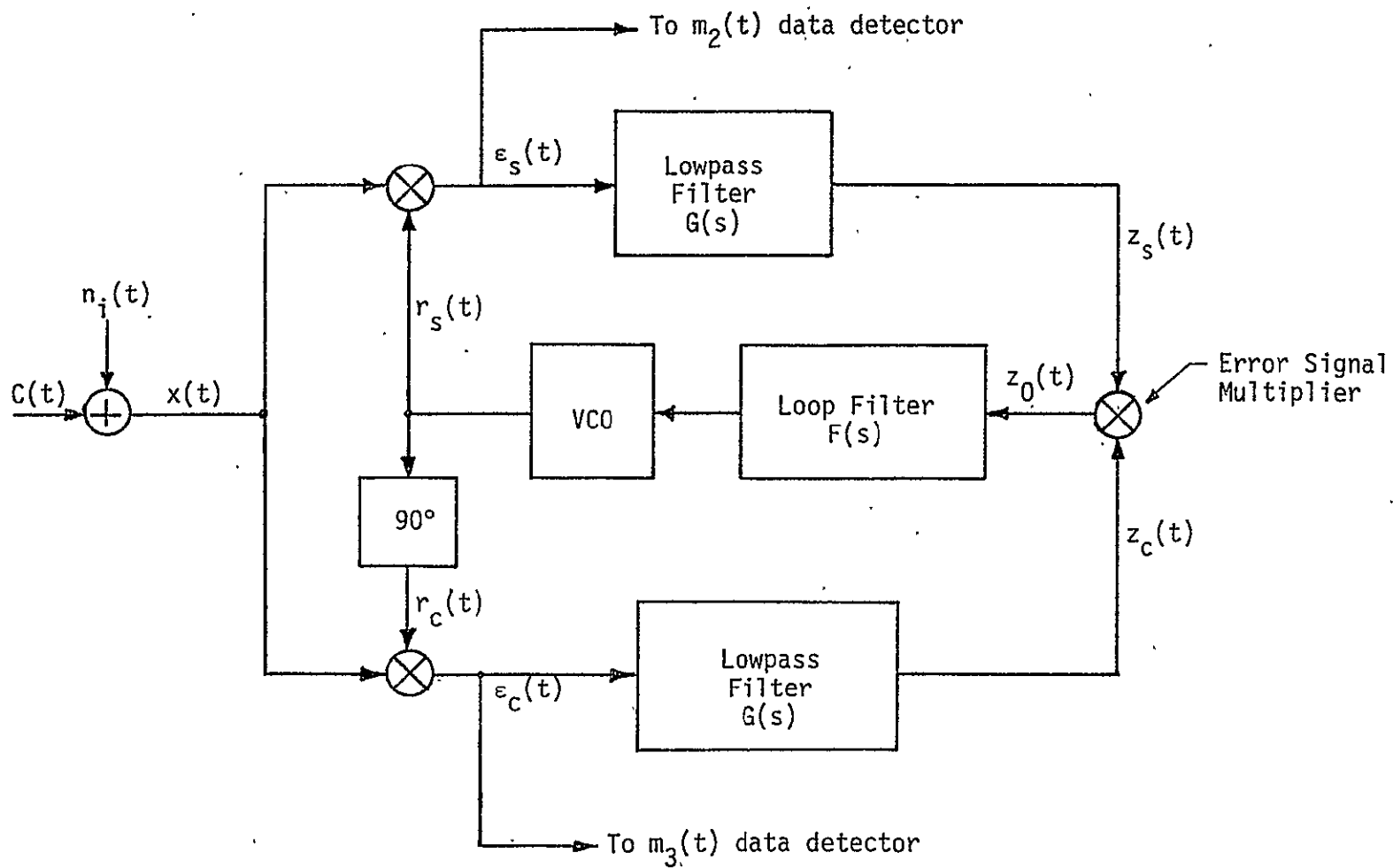


Figure 6. Costas Loop for Subcarrier Tracking

With switching-type phase detectors employed, the input signal $x(t)$ is equivalently demodulated by the reference signals

$$\begin{aligned} r'_s(t) &= \sin [\omega_{sc} t - \varphi(t)] = \sum_{n=1,3,5,\dots}^{\infty} \frac{4}{n\pi} \sin [n\omega_{sc} t - n\varphi(t)] \\ r'_c(t) &= \cos [\omega_{sc} t - \varphi(t)] = \sum_{n=1,3,5,\dots}^{\infty} \frac{4}{n\pi} (-1)^{\frac{n-1}{2}} \cos [n\omega_{sc} t - n\varphi(t)] \end{aligned} \quad (33)$$

to produce the corresponding phase detector outputs (ignoring second and higher order harmonic terms),

$$\begin{aligned} \epsilon_s(t) &\triangleq x(t) r'_s(t) \\ &= \sqrt{P_s} m_2(t) \sum_{n=1,3,5,\dots}^{\infty} \frac{4}{n^2 \pi^2} \{ \cos n[\varphi(t) - \theta_0] + \cos n[\varphi(t) + \theta_0] \} \\ &\quad - \sqrt{P_s} m_3(t) \sum_{n=1,3,5,\dots}^{\infty} \frac{4}{n^2 \pi^2} \{ \cos n[\varphi(t) - \theta_0] - \cos n[\varphi(t) + \theta_0] \} \\ &\quad - \frac{2\sqrt{2}}{\pi} N_s(t) \cos \varphi(t) - \frac{2\sqrt{2}}{\pi} N_c(t) \sin \varphi(t) \end{aligned} \quad (34a)$$

$$\begin{aligned} \epsilon_c(t) &\triangleq x(t) r'_c(t) \\ &= \sqrt{P_s} m_2(t) \sum_{n=1,3,5,\dots}^{\infty} \frac{4}{n^2 \pi^2} (-1)^{\frac{n-1}{2}} \{ \sin n[\varphi(t) + \theta_0] + \sin n[\varphi(t) - \theta_0] \} \\ &\quad + \sqrt{P_s} m_3(t) \sum_{n=1,3,5,\dots}^{\infty} \frac{4}{n^2 \pi^2} (-1)^{\frac{n-1}{2}} \{ \sin n[\varphi(t) + \theta_0] - \sin n[\varphi(t) - \theta_0] \} \\ &\quad - \frac{2\sqrt{2}}{\pi} N_s(t) \sin \varphi(t) + \frac{2\sqrt{2}}{\pi} N_c(t) \cos \varphi(t), \end{aligned} \quad (34b)$$

where $\varphi(t)$ is the loop phase error. Before continuing with the Costas loop analysis, we digress a moment to examine the power relationships at the phase detector outputs.

Since $\epsilon_s(t)$ and $\epsilon_c(t)$ represent the points of extraction for the data in channels 2 and 3, respectively, it is of interest to examine the power available in these channels and their ratio. Ignoring crosstalk,

i.e., assuming $\varphi(t) = 0$, we get

$$\begin{aligned}
 p'_2 &\triangleq \text{Signal power in } \varepsilon_s(t) \Big|_{\varphi=0} = p_s \left[\sum_{n=1,3,5,\dots}^{\infty} \frac{8}{n^2 \pi^2} \cos n\theta_0 \right]^2 \\
 p'_3 &\triangleq \text{Signal power in } \varepsilon_c(t) \Big|_{\varphi=0} = p_s \left[\sum_{n=1,3,5,\dots}^{\infty} \frac{8}{n^2 \pi^2} (-1)^{\frac{n-1}{2}} \sin n\theta_0 \right]^2.
 \end{aligned} \tag{35}$$

Using the trigonometric identities

$$\begin{aligned}
 \frac{4}{\pi} \sum_{n=1,3,5,\dots}^{\infty} (-1)^{\frac{n-1}{2}} \frac{\sin nx}{n^2} &= T(x) \\
 \frac{4}{\pi} \sum_{n=1,3,5,\dots}^{\infty} \frac{\cos nx}{n^2} &= T(x + \frac{\pi}{2}),
 \end{aligned} \tag{36}$$

where $T(x)$ is the triangular correlation function (see Figure 7) defined by

$$T(x) = \begin{cases} x; & |x| \leq \pi/2 \\ -x[1 - \frac{\pi}{|x|}]; & \pi/2 \leq |x| \leq \pi \end{cases}$$

$$T(x) = T(x + 2\pi), \tag{37}$$

then, letting $x = \theta_0$, we find that, for $\theta_0 \leq \pi/2$,

$$\begin{aligned}
 p'_2 &= p_s \left[\frac{2}{\pi} T(\theta_0 + \frac{\pi}{2}) \right]^2 = p_s (1 - \frac{2}{\pi} \theta_0)^2 \\
 p'_3 &= p_s \left[\frac{2}{\pi} T(\theta_0) \right]^2 = p_s (\frac{2}{\pi} \theta_0)^2
 \end{aligned} \tag{38}$$

and

$$\eta'_{23} \triangleq \frac{p'_2}{p'_3} = \frac{(1 - \frac{2}{\pi} \theta_0)^2}{(\frac{2}{\pi} \theta_0)^2} = \eta_{23}^2$$

$$p'_s \triangleq p'_2 + p'_3 = p_s \left[(1 - \frac{2}{\pi} \theta_0)^2 + (\frac{2}{\pi} \theta_0)^2 \right]. \tag{39}$$

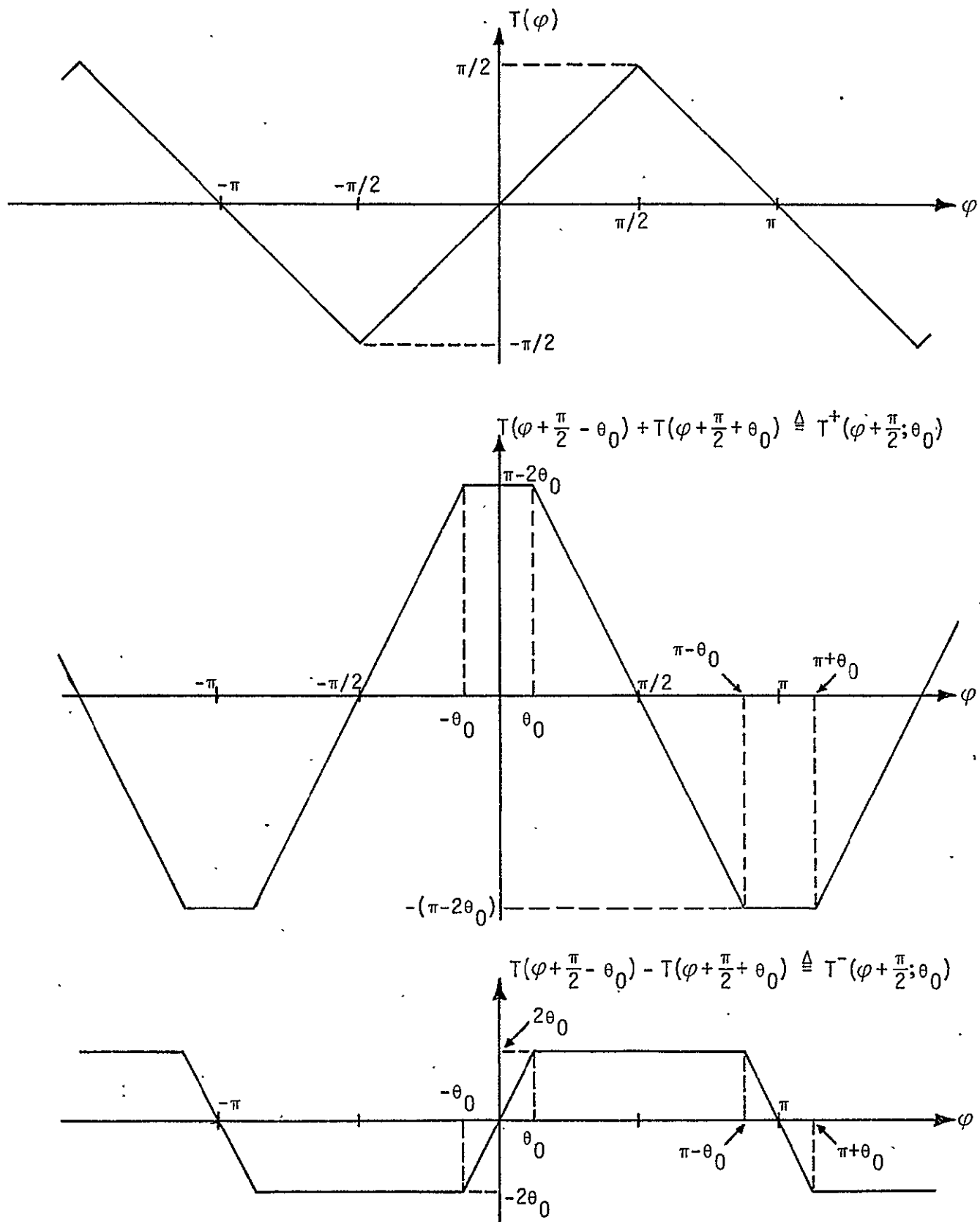


Figure 7. Phase Detector Output Correlation Functions for Channels 2 and 3

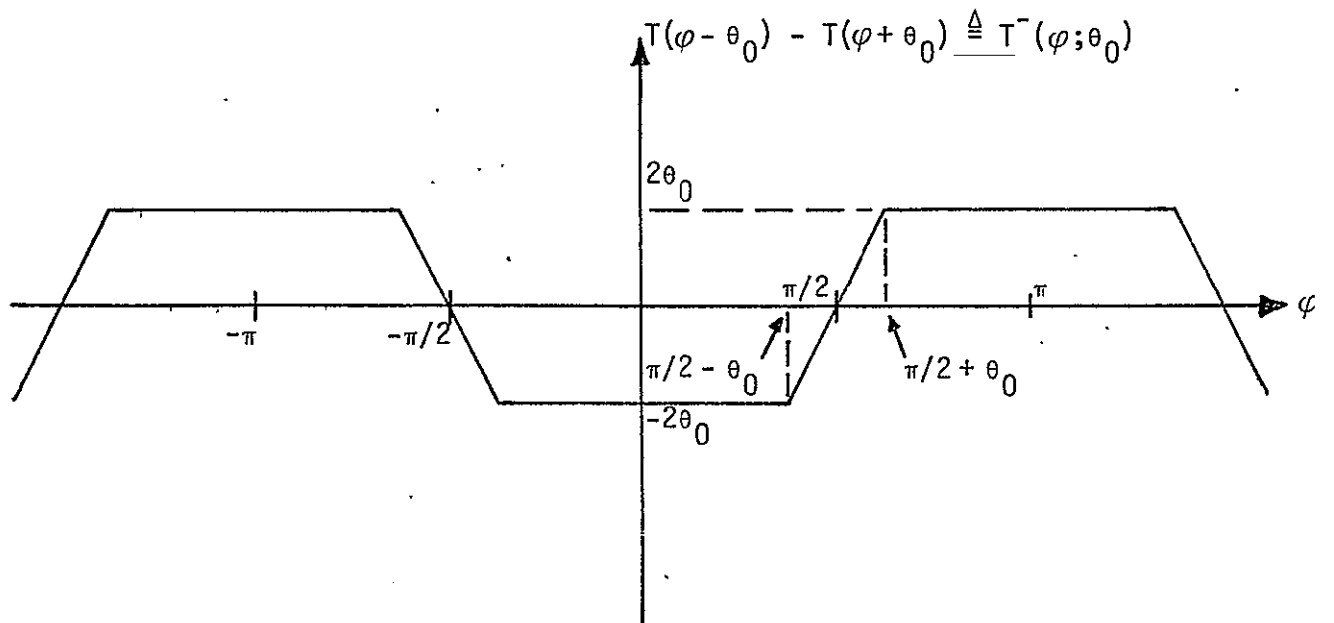
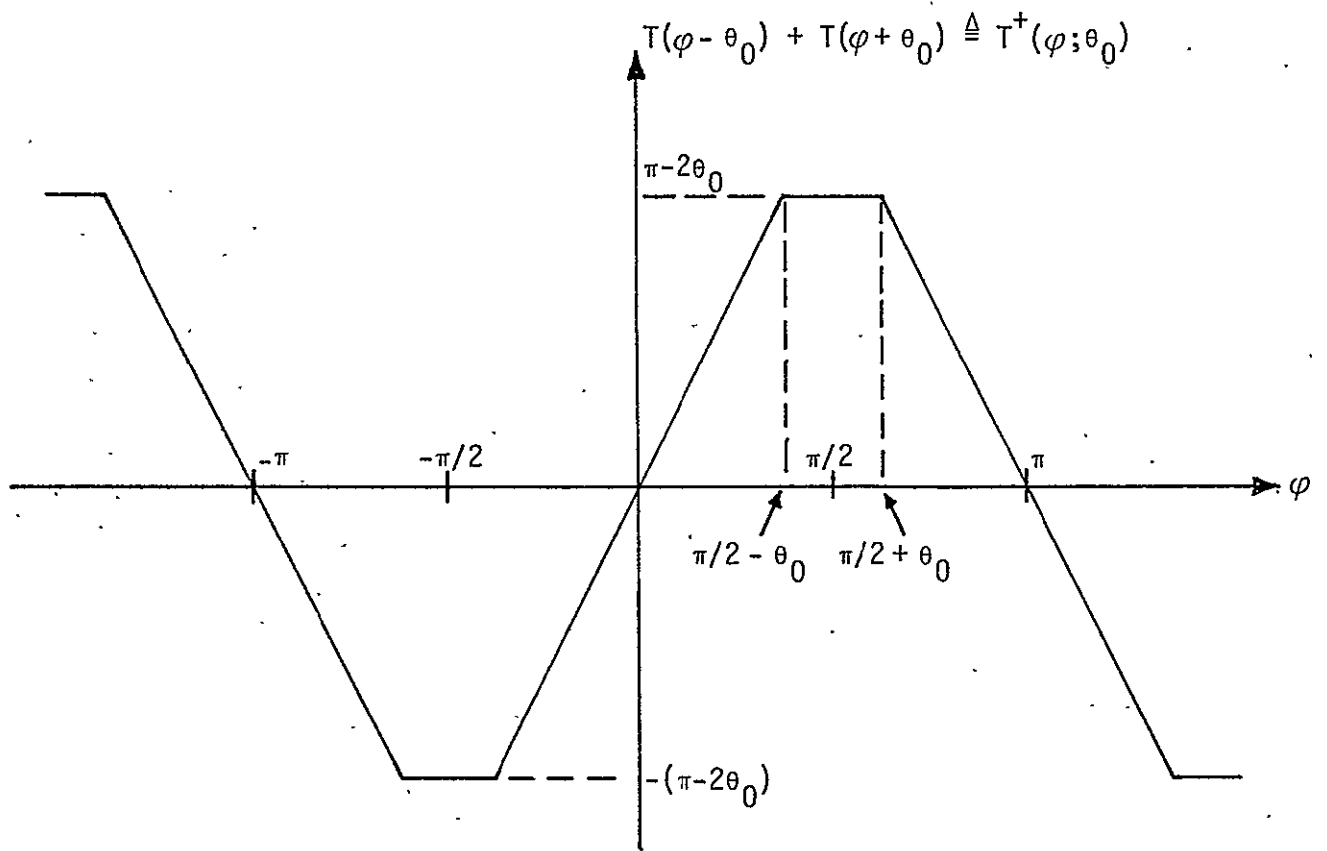


Figure 7 (continued)

Note that P'_S represents the total power available for data detection and n'_{23} is the corresponding ratio of powers in the two data detection channels (assuming zero crosstalk). Thus, if we desire $n'_{23} = 4$, then $n_{23} = 2$ and $\theta_0 = 30^\circ$. Also, $P'_S = 5P_S/9$, i.e., only 55.6% of the total power available at the transmitter is available for data detection.

The power allocation relationships of (38) can also be derived in a simpler and perhaps more illuminating way. First, note from Figure 4 that $S^+(\omega_{sc}t; \theta_0)$ is a gated version of $\sin \omega_{sc}t$ and $S^-(\omega_{sc}t; \theta_0)$ is similarly a gated version of $\cos \omega_{sc}t$ in the sense that

$$\begin{aligned} S^+(\omega_{sc}t; \theta_0) \sin(\omega_{sc}t) &= [S^+(\omega_{sc}t; \theta_0)]^2 \\ S^-(\omega_{sc}t; \theta_0) \cos(\omega_{sc}t) &= [S^-(\omega_{sc}t; \theta_0)]^2. \end{aligned} \quad (40)$$

Also,

$$\begin{aligned} S^+(\omega_{sc}t; \theta_0) \cos(\omega_{sc}t) &= 0 \\ S^-(\omega_{sc}t; \theta_0) \sin(\omega_{sc}t) &= 0. \end{aligned} \quad (41)$$

Thus, we immediately have that

$$\begin{aligned} \epsilon_s(t) \Big|_{\substack{\varphi=0 \\ n_i(t)=0}} &= \sqrt{P_S} m_2(t) \langle S^+(\omega_{sc}t; \theta_0) \sin(\omega_{sc}t) \rangle \\ &\quad + \sqrt{P_S} m_3(t) \langle S^-(\omega_{sc}t; \theta_0) \sin(\omega_{sc}t) \rangle \\ &= \sqrt{P_S} m_2(t) \langle [S^+(\omega_{sc}t; \theta_0)]^2 \rangle = \sqrt{P_S} m_2(t) \left[1 - \frac{2\theta_0}{\pi} \right] \\ \epsilon_c(t) \Big|_{\substack{\varphi=0 \\ n_i(t)=0}} &= \sqrt{P_S} m_2(t) \langle S^+(\omega_{sc}t; \theta_0) \cos(\omega_{sc}t) \rangle \\ &\quad + \sqrt{P_S} m_3(t) \langle S^-(\omega_{sc}t; \theta_0) \cos(\omega_{sc}t) \rangle \\ &= \sqrt{P_S} m_3(t) \langle [S^-(\omega_{sc}t; \theta_0)]^2 \rangle = \sqrt{P_S} m_3(t) \left(\frac{2\theta_0}{\pi} \right). \end{aligned} \quad (42)$$

Applying the definitions of P'_2 and P'_3 given in (35) to (42), we immediately get the results of (38).

The identities of (40) raise an interesting question regarding the necessity of using squarewave VCO quadrature reference signals.

which are clearly not matched to the effective in-phase and quadrature subcarriers $S^+(\omega_{sc}t; \theta_0)$ and $S^-(\omega_{sc}t; \theta_0)$. In fact, if one were to generate as in-phase and quadrature references the signals

$$\begin{aligned} r_s(t) &= S^+[\omega_{sc}t - \varphi(t); \theta_0] \\ r_c(t) &= S^-[\omega_{sc}t - \varphi(t); \theta_0], \end{aligned} \quad (43)$$

then in the absence of noise and for zero phase error, the demodulator output would be identical to (42). Thus, we conclude that, from a demodulated signal power standpoint, it is sufficient to generate the gated in-phase and quadrature reference signals of (43) rather than full duty cycle squarewaves, i.e., one should match the demodulation signals to the effective in-phase and quadrature subcarriers. The advantage of using (43) as reference signals lies, of course, in their effect on the demodulated noise since, clearly, the first harmonic of $r_s(t)$ and $r_c(t)$ of (43) has less power than the first harmonic of $r_s(t)$ and $r_c(t)$ of (33). At the conclusion of this report, we shall return to a consideration of this alternate approach and present the analysis for the tracking performance of a Costas-type loop which employs the demodulation references of (43).

Continuing now with the development leading to the determination of the Costas loop performance for the HAC version, we find that, from the trigonometric identities of (36), the phase detector outputs of (34) can be written in the simpler form

$$\begin{aligned} \epsilon_s(t) &= \sqrt{P_s} m_2(t) \frac{1}{\pi} [T(\varphi + \frac{\pi}{2} - \theta_0) + T(\varphi + \frac{\pi}{2} + \theta_0)] \\ &\quad - \sqrt{P_s} m_3(t) \frac{1}{\pi} [T(\varphi + \frac{\pi}{2} - \theta_0) - T(\varphi + \frac{\pi}{2} + \theta_0)] \\ &\quad - \frac{2\sqrt{2}}{\pi} N_s(t) \cos \varphi(t) - \frac{2\sqrt{2}}{\pi} N_c(t) \sin \varphi(t) \end{aligned} \quad (44a)$$

$$\begin{aligned}
& \text{--- } T^+(\varphi; \theta_0) \text{ ---} \\
\varepsilon_c(t) &= \sqrt{P_s} m_2(t) \frac{1}{\pi} [T(\varphi - \theta_0) + T(\varphi + \theta_0)] \\
& - \sqrt{P_s} m_3(t) \frac{1}{\pi} [T(\varphi - \theta_0) - T(\varphi + \theta_0)] \\
& \text{--- } T^-(\varphi; \theta_0) \text{ ---} \\
& - \frac{2\sqrt{2}}{\pi} N_s(t) \sin \varphi(t) + \frac{2\sqrt{2}}{\pi} N_c(t) \cos \varphi(t). \quad (44b)
\end{aligned}$$

After lowpass filtering $\varepsilon_s(t)$ and $\varepsilon_c(t)$ with arm filters $G(s)$, these signals become, respectively,

$$\begin{aligned}
z_s(t) &\triangleq G(p) \varepsilon_s(t) \\
&= \sqrt{P_s} \hat{m}_2(t) \frac{1}{\pi} T^+(\varphi + \frac{\pi}{2}; \theta_0) - \sqrt{P_s} \hat{m}_3(t) \frac{1}{\pi} T^-(\varphi + \frac{\pi}{2}; \theta_0) \\
& - \frac{2\sqrt{2}}{\pi} \hat{N}_s(t) \cos \varphi(t) - \frac{2\sqrt{2}}{\pi} \hat{N}_c(t) \sin \varphi(t) \\
z_c(t) &\triangleq G(p) \varepsilon_c(t) \\
&= \sqrt{P_s} \hat{m}_2(t) \frac{1}{\pi} T^+(\varphi; \theta_0) - \sqrt{P_s} \hat{m}_3(t) \frac{1}{\pi} T^-(\varphi; \theta_0) \\
& - \frac{2\sqrt{2}}{\pi} \hat{N}_s(t) \sin \varphi(t) + \frac{2\sqrt{2}}{\pi} \hat{N}_c(t) \cos \varphi(t), \quad (45)
\end{aligned}$$

where the "hats" denote filtering of the corresponding signals, e.g., $\hat{m}_2(t) \triangleq G(p) m_2(t)$. Thus, the output of the third (error signal) multiplier is the dynamic error signal

$$\begin{aligned}
z_0(t) &\triangleq z_s(t) z_c(t) \\
&= \frac{P_s}{2} \left\{ \hat{m}_2^2(t) T^+(\varphi + \frac{\pi}{2}; \theta_0) T^+(\varphi; \theta_0) - \hat{m}_3^2(t) [-T^-(\varphi + \frac{\pi}{2}; \theta_0) T^-(\varphi; \theta_0)] \right. \\
& + \hat{m}_2(t) \hat{m}_3(t) [-T^+(\varphi + \frac{\pi}{2}; \theta_0) T^-(\varphi; \theta_0) - T^-(\varphi + \frac{\pi}{2}; \theta_0) T^+(\varphi; \theta_0)] \left. \right\} \\
& + \frac{1}{2} v_2[t, 2\varphi(t)], \quad (46)
\end{aligned}$$

where

$$\begin{aligned}
v_2[t, 2\varphi(t)] = & \frac{8}{\pi^2} \left\{ [\hat{N}_s^2(t) - \hat{N}_c^2(t)] \sin 2\varphi(t) + 2\hat{N}_c(t) \hat{N}_s(t) \cos 2\varphi(t) \right\} \\
& + \frac{4\sqrt{2}}{\pi^2} \sqrt{P_s} [\hat{m}_2(t) T^+(\varphi + \frac{\pi}{2}; \theta_0) - \hat{m}_3(t) T^-(\varphi + \frac{\pi}{2}; \theta_0)] \\
& \times [\hat{N}_c(t) \cos \varphi(t) - \hat{N}_s(t) \sin \varphi(t)] \\
& - \frac{4\sqrt{2}}{\pi^2} \sqrt{P_s} [\hat{m}_2(t) T^+(\varphi; \theta_0) - \hat{m}_3(t) T^-(\varphi; \theta_0)] \\
& \times [\hat{N}_c(t) \sin \varphi(t) + \hat{N}_s(t) \cos \varphi(t)] . \quad (47)
\end{aligned}$$

The instantaneous frequency relative to ω_{sc} of the VCO output is related to $z_0(t)$ by

$$\frac{d\varphi(t)}{dt} = -K[F(p) z_0(t)] \quad (48)$$

and hence the stochastic equation of loop operation becomes

$$\begin{aligned}
\frac{2d\varphi(t)}{dt} = & -KF(p) \left\{ \frac{2P_s}{\pi^2} \hat{m}_2^2(t) S_2(2\varphi; \theta_0) - \frac{2P_s}{\pi^2} \hat{m}_3^2(t) S_3(2\varphi; \theta_0) \right. \\
& \left. + \frac{2P_s}{\pi^2} \hat{m}_2(t) \hat{m}_3(t) S_{23}(2\varphi; \theta_0) + v_2[t, 2\varphi(t)] \right\} , \quad (49)
\end{aligned}$$

where the S-curve components $S_2(2\varphi; \theta_0)$, $S_3(2\varphi; \theta_0)$ and $S_{23}(2\varphi; \theta_0)$ are defined by

$$\begin{aligned}
S_2(2\varphi; \theta_0) & \triangleq T^+(\varphi + \frac{\pi}{2}; \theta_0) T^+(\varphi; \theta_0) \\
S_3(2\varphi; \theta_0) & \triangleq -T^-(\varphi + \frac{\pi}{2}; \theta_0) T^-(\varphi; \theta_0) \\
S_{23}(2\varphi; \theta_0) & = -T^+(\varphi + \frac{\pi}{2}; \theta_0) T^-(\varphi; \theta_0) - T^-(\varphi + \frac{\pi}{2}; \theta_0) T^+(\varphi; \theta_0) \quad (50)
\end{aligned}$$

and illustrated in Figure 8. As has been previously done [12-13] in problems of this type, we shall now decompose each of the signal terms in (49) into its mean value plus the variation about this mean, e.g.,

$$\hat{m}_2^2(t) S_2(2\varphi; \theta_0) = \overline{\hat{m}_2^2(t)} S_2(2\varphi; \theta_0) + [\hat{m}_2^2(t) - \overline{\hat{m}_2^2(t)}] S_2(2\varphi; \theta_0) , \quad (51)$$

where the overbar denotes statistical expectation. It is easily shown that

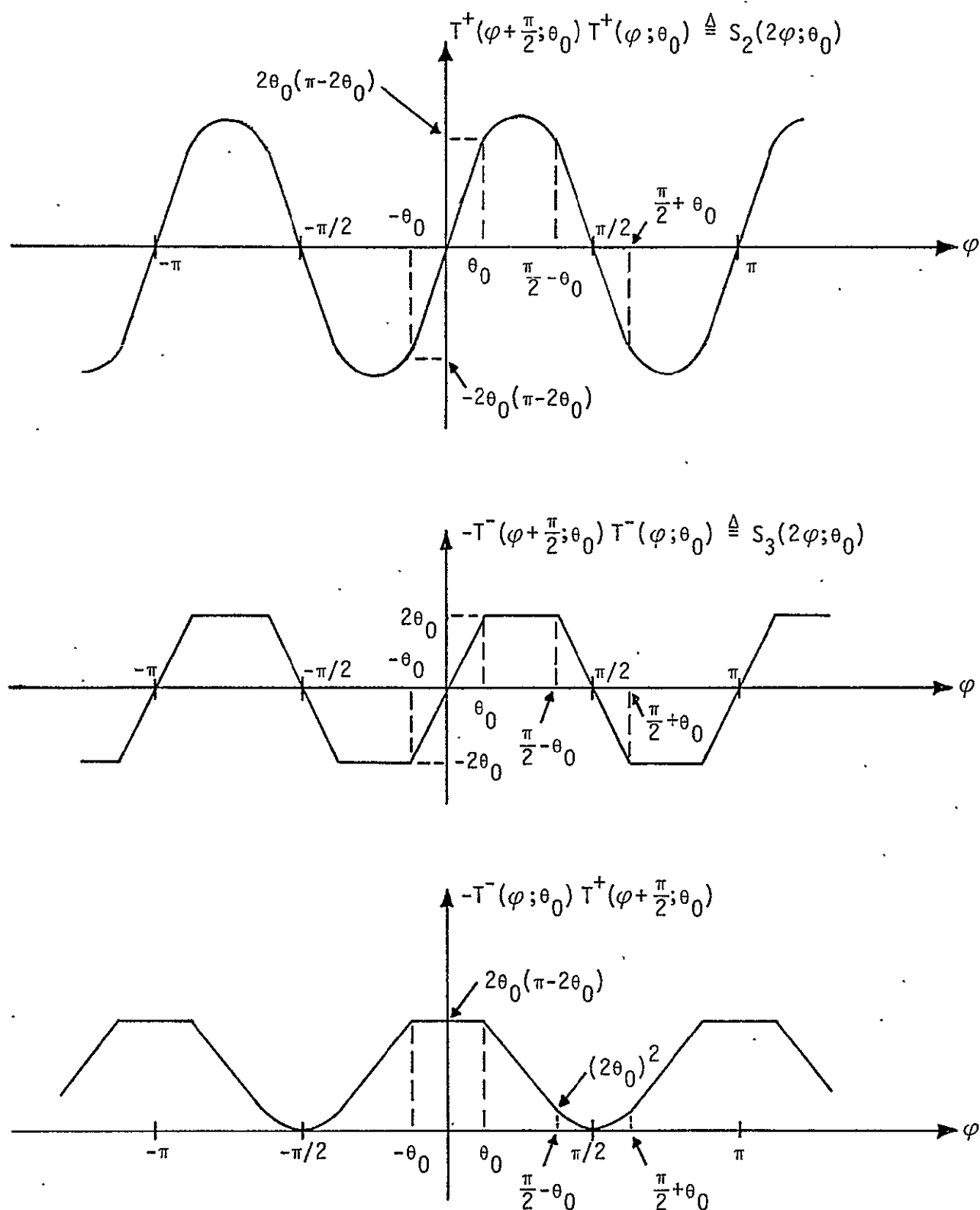


Figure 8. S-Curve Components

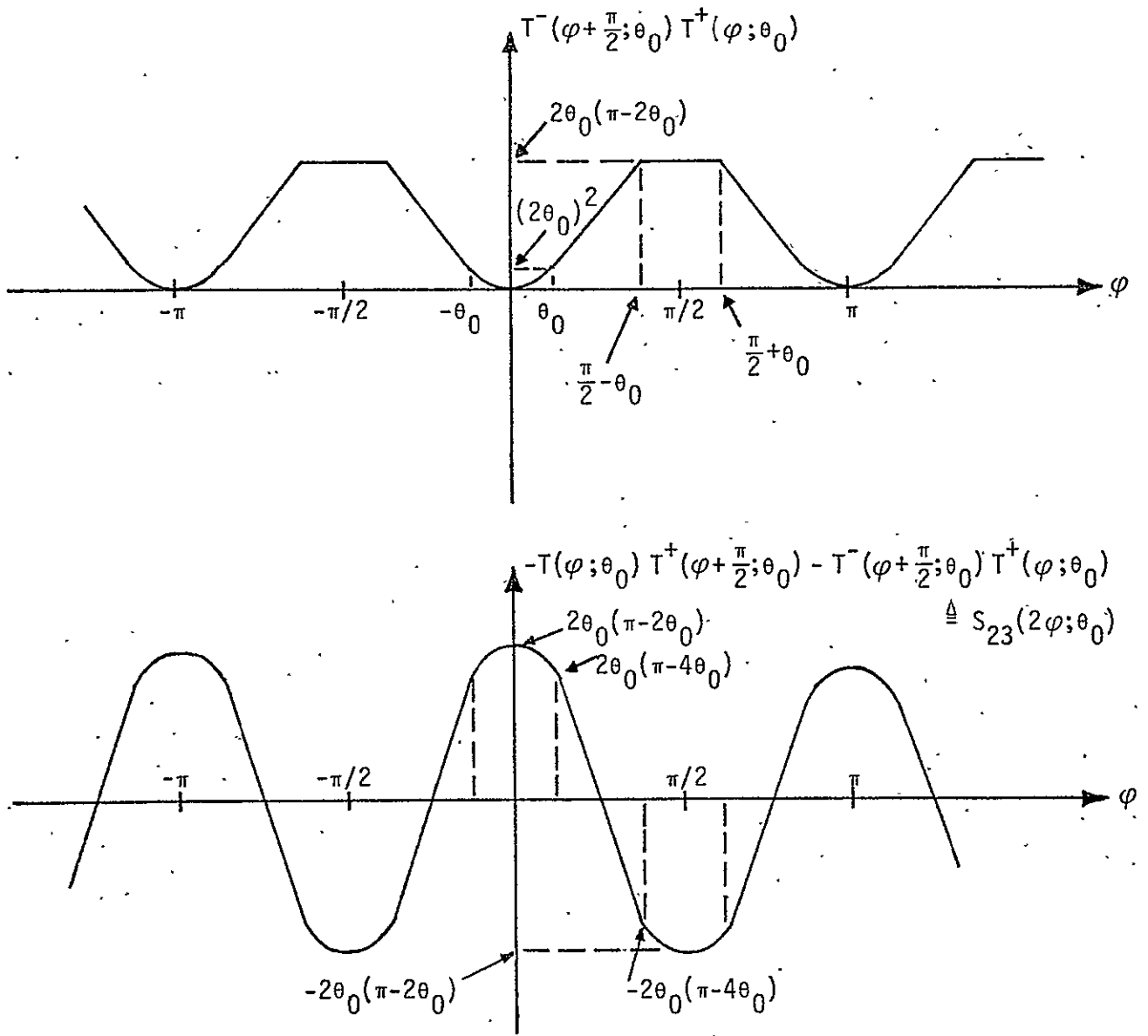


Figure 8. (continued)

$$\overline{\hat{m}_k^2(t)} \triangleq D_k = \int_{-\infty}^{\infty} S_{m_k}(f) |G(j2\pi f)|^2 df; \quad k=2,3 \quad (52)$$

and since $m_2(t)$ and $m_3(t)$ are independent,

$$\overline{\hat{m}_2(t) \hat{m}_3(t)} = 0. \quad (53)$$

In (52), $S_{m_k}(f)$ denotes the power spectral density of $m_k(t)$; $k=2,3$; and $|G(j2\pi f)|^2$ is the magnitude squared of the arm filter transfer function. Rewriting (49) using the above decompositions gives*

$$\frac{2d\varphi}{dt} = -KF(p) \left\{ \frac{2P_s}{\pi} [D_2 S_2(2\varphi; \theta_0) - D_3 S_3(2\varphi; \theta_0)] + n_e(t, 2\varphi) \right\}, \quad (54)$$

where the total equivalent noise $n_e(t, 2\varphi)$ is given by

$$\begin{aligned} n_e(t, 2\varphi) \triangleq & v_2(t, 2\varphi) - \frac{2P_s}{\pi} n_3(t) S_3(2\varphi; \theta_0) + \frac{2P_s}{\pi} n_2(t) S_2(2\varphi; \theta_0) \\ & + \frac{2P_s}{\pi} n_{23}(t) S_{23}(2\varphi; \theta_0) \end{aligned} \quad (55)$$

with the self-noise $n_k(t)$; $k=2,3$; and the cross-modulation noise $n_{23}(t)$ defined by.

$$\begin{aligned} n_k(t) &\triangleq \hat{m}_k^2(t) - \overline{\hat{m}_k^2(t)}; \quad k=2,3 \\ n_{23}(t) &\triangleq \hat{m}_2(t) \hat{m}_3(t). \end{aligned} \quad (56)$$

Equivalent Loop S-Curve

The equivalent loop S-curve in (54) is

$$S(2\varphi; \theta_0) \triangleq \frac{2P_s}{\pi} [D_2 S_2(2\varphi; \theta_0) - D_3 S_3(2\varphi; \theta_0)]. \quad (57)$$

The slope $K_{2\varphi}$ of the S-curve at the origin, i.e., $\varphi = 0$, is then

$$K_{2\varphi} \triangleq \left. \frac{dS(2\varphi; \theta_0)}{d2\varphi} \right|_{\varphi=0} = \frac{P_s}{\pi} D_2 \left. \frac{dS_2(2\varphi; \theta_0)}{d\varphi} \right|_{\varphi=0} - \frac{P_s}{\pi} D_3 \left. \frac{dS_3(2\varphi; \theta_0)}{d\varphi} \right|_{\varphi=0}, \quad (58)$$

* For simplicity of notation herein, we drop the dependence of the phase error φ on time t .

which, from (50) and Figure 7, becomes

$$\begin{aligned} K_{2\varphi} &= \frac{P_s}{\pi^2} \left\{ D_2 [2(\pi - 2\theta_0)] - D_3(4\theta_0) \right\} \\ &= \frac{2P_s}{\pi} \left[D_2 \left(1 - \frac{2\theta_0}{\pi} \right) - D_3 \frac{2\theta_0}{\pi} \right]. \end{aligned} \quad (59)$$

Statistical Characterization of the Equivalent Additive Noise

The self-noise and cross-modulation noise processes all have zero mean and a continuous power spectral density component. Since the bandwidth of these processes is very wide with respect to the loop bandwidth, it is sufficient to find for each one only the power spectral density at the origin which, when multiplied by the loop bandwidth, gives the contribution to the total noise power of that modulation component. From (55), the autocorrelation of $n_e(t, 2\varphi)$ is easily shown to be

$$\begin{aligned} R_e(\tau, 2\varphi) &\triangleq \overline{\langle n_e(t, 2\varphi) n_e(t+\tau, 2\varphi) \rangle} \\ &= \frac{4P_s^2}{\pi^4} S_3^2(2\varphi; \theta_0) R_{n_3}(\tau) + \frac{4P_s^2}{\pi^4} S_2^2(2\varphi; \theta_0) R_{n_2}(\tau) \\ &\quad + \frac{4P_s^2}{\pi^4} S_{23}^2(2\varphi; \theta_0) R_{n_{23}}(\tau) + R_{v_2}(\tau, 2\varphi), \end{aligned} \quad (60)$$

where

$$\begin{aligned} R_{n_k}(\tau) &\triangleq \overline{\langle n_k(t) n_k(t+\tau) \rangle} ; \quad k=2,3 \\ R_{n_{23}}(\tau) &\triangleq \overline{\langle n_{23}(t) n_{23}(t+\tau) \rangle} = R_{\hat{m}_2}(\tau) R_{\hat{m}_3}(\tau) \\ R_{\hat{m}_k}(\tau) &\triangleq \overline{\langle \hat{m}_k(t) \hat{m}_k(t+\tau) \rangle} = \int_{-\infty}^{\infty} S_{m_k}(f) |G(j 2\pi f)|^2 df ; \quad k=2,3 \\ R_{v_2}(\tau, 2\varphi) &\triangleq \overline{\langle v_2(t, 2\varphi) v_2(t+\tau, 2\varphi) \rangle}. \end{aligned} \quad (61)$$

The equivalent noise power spectral density at the origin is then

$$N_e(2\varphi) = 2 \int_{-\infty}^{\infty} R_e(\tau, 2\varphi) d\tau. \quad (62)$$

In [12], it was shown that, for cases of practical interest, the effect of the self-noise power on loop tracking performance was negligible. Thus, for all practical purposes, we may concern ourselves only with $N_e(2\varphi)$ evaluated at $\varphi = 0$, i.e.,

$$N_e \triangleq N_e(2\varphi) \Big|_{\varphi=0} = \frac{8P_s^2}{\pi^4} [2\theta_0(\pi - 2\theta_0)]^2 \int_{-\infty}^{\infty} R_{\hat{m}_2}(\tau) R_{\hat{m}_3}(\tau) d\tau + 2 \int_{-\infty}^{\infty} R_{v_2}(\tau, 0) d\tau. \quad (63)$$

From (47) and Figure 7,

$$\begin{aligned} v_2(t, 0) = & -\frac{16}{\pi} \hat{N}_c(t) \hat{N}_s(t) + \frac{4\sqrt{2}}{\pi} \sqrt{P_s} \hat{m}_2(t) [\pi - 2\theta_0] \hat{N}_c(t) \\ & - \frac{4\sqrt{2}}{\pi} \sqrt{P_s} \hat{m}_3(t) (2\theta_0) \hat{N}_s(t), \end{aligned} \quad (64)$$

and thus

$$\begin{aligned} R_{v_2}(\tau, 0) = & \left(\frac{16}{\pi}\right)^2 R_{\hat{N}}^2(\tau) + \left(\frac{4\sqrt{2}}{\pi}\right)^2 P_s \left[1 - \frac{2\theta_0}{\pi}\right]^2 R_{\hat{m}_2}(\tau) R_{\hat{N}}(\tau) \\ & + \left(\frac{4\sqrt{2}}{\pi}\right)^2 P_s \left(\frac{2\theta_0}{\pi}\right)^2 R_{\hat{m}_3}(\tau) R_{\hat{N}}(\tau), \end{aligned} \quad (65)$$

where

$$\begin{aligned} R_{\hat{N}}(\tau) \triangleq \overline{\hat{N}_c(t) \hat{N}_c(t+\tau)} &= \overline{\hat{N}_s(t) \hat{N}_s(t+\tau)} \\ &= \frac{N_0}{2} \int_{-\infty}^{\infty} |G(j 2\pi f)|^2 e^{j 2\pi f \tau} df. \end{aligned} \quad (66)$$

Substituting (59) together with (65) and (66) into (63) and using Parseval's Theorem yields

$$\begin{aligned} N_e = & \left(\frac{16}{\pi}\right)^2 \frac{N_0^2}{2} \int_{-\infty}^{\infty} |G(j 2\pi f)|^4 df + \frac{32}{\pi^2} P_s N_0 \left(1 - \frac{2\theta_0}{\pi}\right)^2 \int_{-\infty}^{\infty} S_{m_2}(f) |G(j 2\pi f)|^4 df \\ & + \frac{32}{\pi^2} P_s N_0 \left(\frac{2\theta_0}{\pi}\right)^2 \int_{-\infty}^{\infty} S_{m_3}(f) |G(j 2\pi f)|^4 df \\ & + 8 P_s^2 \left[\left(\frac{2\theta_0}{\pi}\right) \left(1 - \frac{2\theta_0}{\pi}\right)\right]^2 \int_{-\infty}^{\infty} S_{m_2}(f) S_{m_3}(f) |G(j 2\pi f)|^4 df. \end{aligned} \quad (67)$$

Recalling the relationship in (38) for the demodulator output channel powers, then (67) can be written in a somewhat more compact form, namely,

$$N_e = 8 P_2' P_3' D_{23} + 4 \left(\frac{8}{\pi} \right) \left\{ P_2' N_0 D_2 K_{D_2} + P_3' N_0 D_3 K_{D_3} + \left(\frac{8}{\pi} \right) \frac{N_0^2}{2} B_i K_L \right\}, \quad (68)$$

where D_k ; $k=2,3$; is defined in (52),

$$\begin{aligned} D_{23} &\triangleq \int_{-\infty}^{\infty} S_{m_2}(f) S_{m_3}(f) |G(j 2\pi f)|^4 df \\ K_{D_k} &\triangleq \frac{\int_{-\infty}^{\infty} S_{m_k}(f) |G(j 2\pi f)|^4 df}{\int_{-\infty}^{\infty} S_{m_k}(f) |G(j 2\pi f)|^2 df}; \quad k=2,3 \\ K_L &\triangleq \frac{\int_{-\infty}^{\infty} |G(j 2\pi f)|^4 df}{\int_{-\infty}^{\infty} |G(j 2\pi f)|^2 df} \end{aligned} \quad (69)$$

and

$$B_i \triangleq \int_{-\infty}^{\infty} |G(j 2\pi f)|^2 df \quad (70)$$

is the two-sided arm filter lowpass bandwidth.

Effective Loop Signal-to-Noise Ratio and Phase Jitter

From the loop equation of operation given in (54) and the equivalent S-curve of (57), we can see that the effective loop signal-to-noise ratio is given by

$$\rho_e = \frac{K_{2\phi}^2}{N_e B_L}, \quad (71)$$

where B_L is the single-sided loop bandwidth. Substituting (59) and (68) into (71) and simplifying results in

$$\rho_e = \frac{\rho}{4} S_L, \quad (72)$$

where $\rho \triangleq P_S / N_0 B_L$ with the total transmitted subcarrier power $P_S = P_2 + P_3$, and S_L is the loop "squaring loss" which is given by

$$S_L = \frac{[\sqrt{P_2'} D_2 - \sqrt{P_3'} D_3]^2}{2 \left\{ P_2' D_2 K_{D_2} + P_3' D_3 K_{D_3} + \frac{8}{\pi^2} \left(\frac{N_0 B_i}{2} \right) K_L \right\} + \frac{\pi^2}{2} \left(\frac{P_2' P_3' D_{23}}{N_0} \right)} \quad (73)$$

Defining the modulation indices,

$$\begin{aligned} \eta_2' &\triangleq \frac{P_2'}{P_s} = \left(1 - \frac{2}{\pi} \theta_0 \right)^2 \\ \eta_3' &\triangleq \frac{P_3'}{P_s} = \left(\frac{2}{\pi} \theta_0 \right)^2, \end{aligned} \quad (74)$$

then (73) simplifies to

$$S_L = \frac{[\sqrt{\eta_2'} D_2 - \sqrt{\eta_3'} D_3]^2}{2 \left\{ \eta_2' D_2 K_{D_2} + \eta_3' D_3 K_{D_3} + \frac{8}{\pi^2} \left(\frac{N_0 B_i}{2 P_s} \right) K_L + \left(\frac{\pi^2}{8} \right) 2 \eta_2' \eta_3' \frac{P_s}{N_0} D_{23} \right\}} \quad (75)$$

Ordinarily, to optimize tracking performance, i.e., maximize ρ_e , the arm filter bandwidth is selected relative to the higher of the two data rates. Thus, arbitrarily assuming that $R_2 > R_3$, we rewrite (75) in the final form

$$S_L = \frac{[\sqrt{\eta_2'} D_2 - \sqrt{\eta_3'} D_3]^2}{2 \left\{ \eta_2' D_2 K_{D_2} + \eta_3' D_3 K_{D_3} + \left(\frac{8}{\pi^2} \right) \frac{B_i / R_2}{2 R_{s2}} K_L + \left(\frac{\pi^2}{8} \right) 2 \eta_2' \eta_3' R_{s2} \left(\frac{D_{23}}{T_2} \right) \right\}}, \quad (76)$$

where $R_{s2} \triangleq P_s T_2 / N_0$.

What remains is to characterize the tracking phase jitter performance. In the linear region of operation, the variance of the loop phase error 2ϕ is given by

$$\sigma_{2\phi}^2 = \frac{1}{\rho_e} = \frac{4}{\rho S_L} \quad (77)$$

We conclude then that characterization of the loop squaring loss in terms of the system parameters is sufficient for predicting the loop's tracking performance. Before offering a numerical evaluation of this performance for system parameters of interest, we shall first present the theoretical

analysis for Costas loop tracking of the signal produced by the modified HAC modulator wherein a bandpass filter follows the subcarrier modulator output. Following this, a comparison of the tracking performance corresponding to the two HAC modulator versions will be given.

B. Subcarrier Demodulation of the Filtered HAC Version Using a Costas Loop With Switching Type In-Phase and Quadrature Phase Detectors and Analog Type Error Signal Multiplier

In this part of the report, we shall draw heavily on the results given in [13], which apply to Costas loop tracking of UQPSK. If a bandpass filter follows the subcarrier modulator of Figure 2, then assuming that this filter passes only the fundamental harmonic of the modulated squarewave subcarrier, its output would be given by (18).

Letting

$$\begin{aligned} P_2 &= \left[\frac{1}{2} \left(\frac{4}{\pi} \right)^2 \cos^2 \theta_0 \right] P_s \\ P_3 &= \left[\frac{1}{2} \left(\frac{4}{\pi} \right)^2 \sin^2 \theta_0 \right] P_s \\ P_2 + P_3 &= \frac{8}{\pi^2} P_s ; \end{aligned} \quad (78)$$

then (18) can be written as

$$C_1(t) = \sqrt{2P_2} m_2(t) \sin \omega_{sc} t + \sqrt{2P_3} m_3(t) \cos \omega_{sc} t, \quad (79)$$

which is in the identical form of (1) of [13]. Although analog type in-phase and quadrature phase detectors were implicitly assumed in this reference, the results given there equally apply when switching type phase detectors are used, the reason being that only the first harmonic of the equivalent VCO squarewave reference signals correlates with the input modulated sinusoids. Thus, we can immediately adapt the result given in (4) of [13] for the in-phase and quadrature phase detector outputs, namely,

$$\begin{aligned} \epsilon_s(t) &\triangleq [C_1(t) + n_i(t)] r'_s(t) \\ &= \frac{2\sqrt{2}}{\pi} [\sqrt{P_2} m_2(t) - N_s(t)] \cos \varphi(t) - \frac{2\sqrt{2}}{\pi} [\sqrt{P_3} m_3(t) + N_c(t)] \sin \varphi(t) \end{aligned} \quad (80a)$$

$$\begin{aligned}
\epsilon_c(t) &\triangleq [c_1(t) + n_i(t)] r'_c(t) \\
&= \frac{2\sqrt{2}}{\pi} [\sqrt{p_2} m_2(t) - N_s(t)] \sin \varphi(t) + \frac{2\sqrt{2}}{\pi} [\sqrt{p_3} m_3(t) + N_c(t)] \cos \varphi(t) .
\end{aligned} \tag{80b}$$

Once again examining the signal power available in channels 2 and 3 in the absence of crosstalk, i.e., $\varphi = 0$, we now find that

$$\begin{aligned}
P'_2 &= \text{Signal power in } \epsilon_s(t) \big|_{\varphi=0} = \frac{8}{\pi^2} P_2 = \left(\frac{8}{\pi^2}\right)^2 \cos^2 \theta_0 P_s \\
P'_3 &= \text{Signal power in } \epsilon_c(t) \big|_{\varphi=0} = \frac{8}{\pi^2} P_3 = \left(\frac{8}{\pi^2}\right)^2 \sin^2 \theta_0 P_s
\end{aligned} \tag{81}$$

and

$$\begin{aligned}
n'_{23} &= \frac{P'_2}{P'_3} = \cot^2 \theta_0 = n_{23} \\
P'_s &= P'_2 + P'_3 = \left(\frac{8}{\pi^2}\right)^2 P_s .
\end{aligned} \tag{82}$$

Note that, as previously mentioned, the power ratio at the demodulator output is identical to the transmitted power ratio and, furthermore, the total signal power available for data detection is now $(8/\pi^2)^2 = 0.657$ of the total transmitted power P_s . Comparing (80) and (34), we observe that the noise power at the demodulator output is identical for the two cases. Thus, from (82) and the statements following (39), we conclude that, for equal demodulated noise powers and a desired channel power ratio of 4 to 1 at the demodulator outputs, the filtered HAC version of the three-channel modulator offers $65.7 - 55.6 = 10.1\%$ more total signal power available for data detection on channels 2 and 3 than the unfiltered version.

In terms of the squaring loss performance of the subcarrier Costas loop when tracking the filtered HAC modulator output, we can use (28) of [13] directly which, in the notation used here, becomes

$$S_L = \frac{(n_2 D_2 - n_3 D_3)^2}{n_2 D_2 K_{D_2} + n_3 D_3 K_{D_3} + \frac{B_i/R_2}{2 R_{s2}} K_L + 2 n_2 n_3 R_{s2} \left(\frac{D_{23}}{T_2}\right)} \tag{83}$$

where, from (78), the modulation indices η_2 and η_3 are now given by

$$\begin{aligned}\eta_2 &\triangleq \frac{P_2}{P_s} = \frac{8}{\pi} \cos^2 \theta_0 \\ \eta_3 &\triangleq \frac{P_3}{P_s} = \frac{8}{\pi} \sin^2 \theta_0.\end{aligned}\quad (84)$$

C. Numerical Evaluation and Comparisons of System Tracking Performance

To graphically illustrate the theory previously developed, it would be convenient to obtain closed-form expressions for the parameters defined in (52), (69), and (70) for practical filters and data modulation formats. Indeed, such is possible for certain special cases of interest, in particular, the Ku-band return link. Let us consider a simple RC filter with 3 dB cutoff frequency f_c for the Costas loop arm filters. Then,

$$|G(j 2\pi f)|^2 = \frac{1}{1 + (f/f_c)^2}.\quad (85)$$

Substituting (85) into (70) and carrying out the integration gives the relationship between two-sided noise bandwidth and cutoff frequency, namely,

$$B_i = \pi f_c.\quad (86)$$

Also, from (69), substituting the square of (85) into the numerator of the expression for K_L and recognizing that the denominator is merely equivalent to B_i of (70) gives, upon integration,

$$K_L = \frac{1}{2}.\quad (87)$$

Evaluation of D_k , K_{Dk} ; $k=2,3$; and D_{23} requires that we further specify the forms of the two data modulations. For NRZ data on channel 2 with power spectral density

$$S_{m_2}(f) = T_2 \frac{\sin^2 \pi f T_2}{(\pi f T_2)^2},\quad (88)$$

it has been previously shown [13] that

$$\begin{aligned}
D_2 &= 1 - \frac{1}{2B_i/R_2} [1 - \exp(-2B_i/R_2)] \\
K_{D_2} &= \frac{1 - \frac{3 - (3 + 2B_i/R_2) \exp(-2B_i/R_2)}{4B_i/R_2}}{1 - \frac{1}{2B_i/R_2} [1 - \exp(-2B_i/R_2)]} .
\end{aligned} \quad (89)$$

For Manchester code on channel 3, where the power spectral density is

$$S_{m_3}(f) = T_3 \frac{\sin^4(\pi f T_3/2)}{(\pi f T_3/2)^2} , \quad (90)$$

it has also been shown [13] that

$$\begin{aligned}
D_3 &= 1 - \frac{1}{2B_i/R_3} [3 - 4 \exp(-B_i/R_3) + \exp(-2B_i/R_3)] \\
K_{D_3} &= \frac{1 - \frac{9 - 4(3 + B_i/R_3) \exp(-B_i/R_3) + (3 + 2B_i/R_3) \exp(-2B_i/R_3)}{4B_i/R_3}}{1 - \frac{3 - 4 \exp(-B_i/R_3) + \exp(-2B_i/R_3)}{2B_i/R_3}} .
\end{aligned} \quad (91)$$

Furthermore, when $m_2(t)$ is NRZ and $m_3(t)$ is Manchester, and $R_2 \geq 2R_3$, the cross-modulation coefficient D_{23} is given by [13]:

$$\begin{aligned}
D_{23} &= T_2 (1 - T_2/T_3) - 3T_2 (T_2/T_3) \frac{1}{(B_i/R_2)^2} + \frac{1}{8} T_2 (T_2/T_3) \frac{1}{(B_i/R_2)^3} \\
&\times \left\{ 15 - 3(5 + 2B_i/R_2) \exp(-2B_i/R_2) - 4(5 + B_i/R_3) \exp(-B_i/R_3) \right. \\
&\quad + (5 + 2B_i/R_3) \exp(-2B_i/R_3) + 2 \left[5 + 2 \left(\frac{T_3}{2T_2} - 1 \right) B_i/R_2 \right] \exp \left[-2 \left(\frac{T_3}{2T_2} - 1 \right) B_i/R_2 \right] \\
&\quad - \frac{1}{2} \left[5 + 2 \left(\frac{T_3}{T_2} - 1 \right) B_i/R_2 \right] \exp \left[-2 \left(\frac{T_3}{T_2} - 1 \right) B_i/R_2 \right] \\
&\quad + 2 \left[5 + 2 \left(\frac{T_3}{2T_2} + 1 \right) B_i/R_2 \right] \exp \left[-2 \left(\frac{T_3}{2T_2} + 1 \right) B_i/R_2 \right] \\
&\quad \left. - \frac{1}{2} \left[5 + 2 \left(\frac{T_3}{T_2} + 1 \right) B_i/R_2 \right] \exp \left[-2 \left(\frac{T_3}{T_2} + 1 \right) B_i/R_2 \right] \right\} .
\end{aligned} \quad (92)$$

Assuming $P_s T_2/N_0$ fixed, Figure 9 illustrates the Costas loop squaring loss as computed from (76) and (83) versus the ratio of two-sided arm filter bandwidth B_i to high data rate R_2 . The values of R_2 and R_3 selected are the maximum data rates to be supported by channels 2 and 3, respectively, namely, $R_2 = 2$ Mbps and $R_3 = 192$ kbps. Clearly, we see that the filtered HAC version is superior to the unfiltered version. Specifically, for a bandwidth-to-data-rate ratio of about 15, the unfiltered HAC version suffers about a 4 to 4.5 dB squaring loss penalty (depending on the value of $P_s T_2/N_0$) relative to the filtered version. At this large bandwidth-to-data-rate ratio, one can essentially ignore the arm filter distortion effects on the two modulations, in which case, $D_2 = D_3 = K_{D2} = K_{D3} \cong 1$ and $D_{23} \cong T_2(1 - T_2/T_3)$. Using either (76) or (83) in (77), Figure 10 illustrates $\sigma_{2\varphi}$ (in % radians) versus B_i/R_s for $P_s T_2/N_0$ again fixed, where the equivalent linear loop signal-to-noise ratio ρ can be related to the system parameters by

$$\rho \triangleq \frac{P_s}{N_0 B_L} = \frac{P_s T_2}{N_0} \left(\frac{B_i}{B_L} \right) \frac{1}{B_i/R_2} = R_{s2} \left(\frac{B_i}{B_L} \right) \frac{1}{B_i/R_2} \quad (93)$$

In Figure 10, we have assumed an arm filter bandwidth to loop bandwidth ratio of 10^4 . Again, as in Figure 9, we note the far superior performance of the filtered HAC version.

DEMODULATION OF THE THREE-CHANNEL SIGNAL PRODUCED BY THE QUADRATURE-MULTIPLEX TRANSMITTER IMPLEMENTATION

In the quadrature-multiplex (NASA version) implementation of the three-channel modulator (Figure 1), the subcarrier output signal $C(t)$ is given by (21). Demodulating this signal with the equivalent square-wave VCO reference signals of (33) produces the phase detector outputs (ignoring second and higher order harmonic terms)

$$\begin{aligned} \epsilon_s(t) &= [C(t) + n_i(t)] r'_s(t) \\ &= -\frac{2}{\pi} \sqrt{P_3} m_3(t) T(\varphi) + \frac{2}{\pi} \sqrt{P_2} m_2(t) T(\varphi + \frac{\pi}{2}) \\ &\quad - \frac{2\sqrt{2}}{\pi} N_s(t) \cos \varphi(t) - \frac{2\sqrt{2}}{\pi} N_c(t) \sin \varphi(t) \end{aligned} \quad (94a)$$

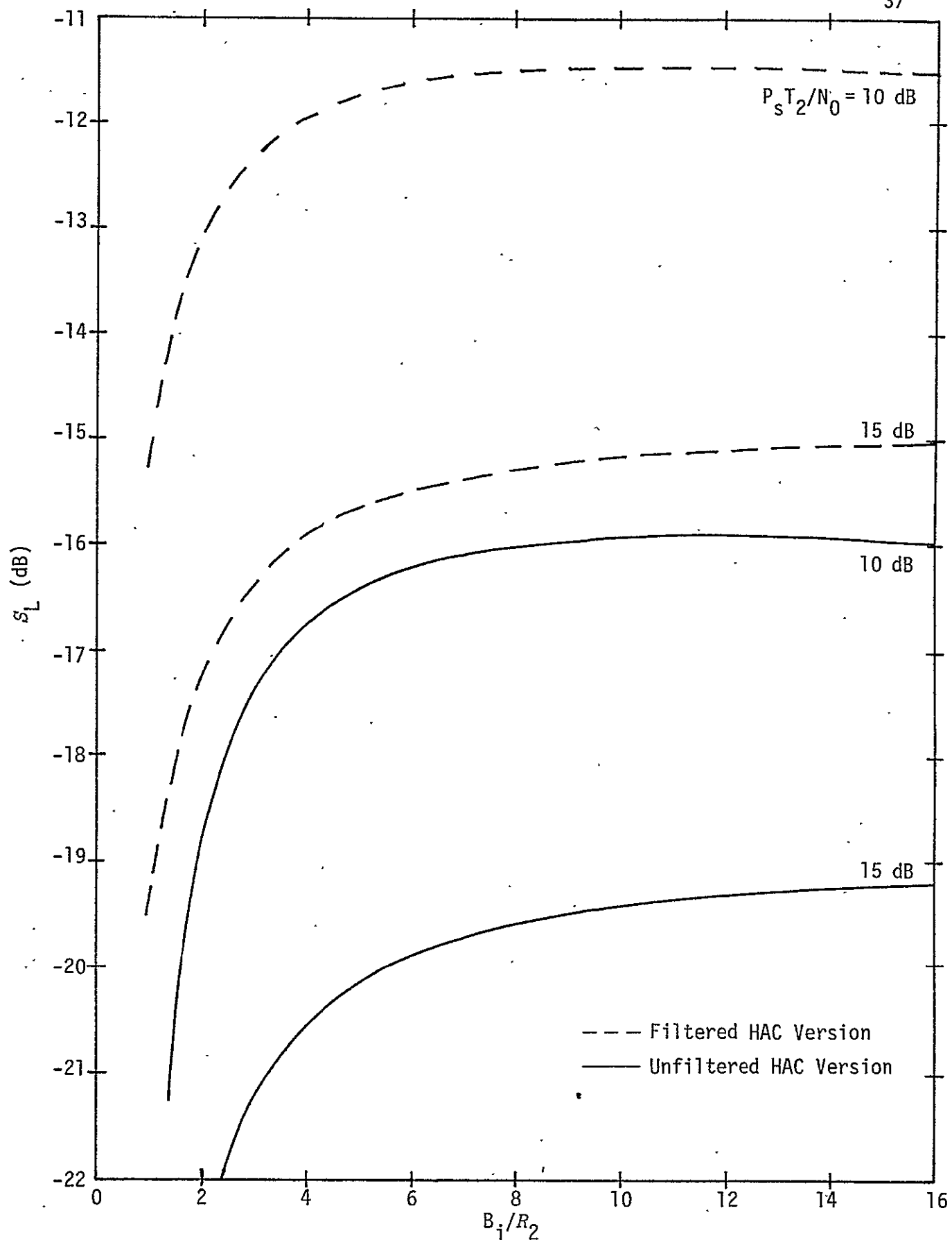


Figure 9. Squaring Loss Vs. Ratio of Two-Sided Arm Filter Bandwidth to High Data Rate; $m_2(t)$ is NRZ Data at $R_2 = 2$ Mbps, $m_3(t)$ is Manchester Coded Data at $R_3 = 192$ kbps

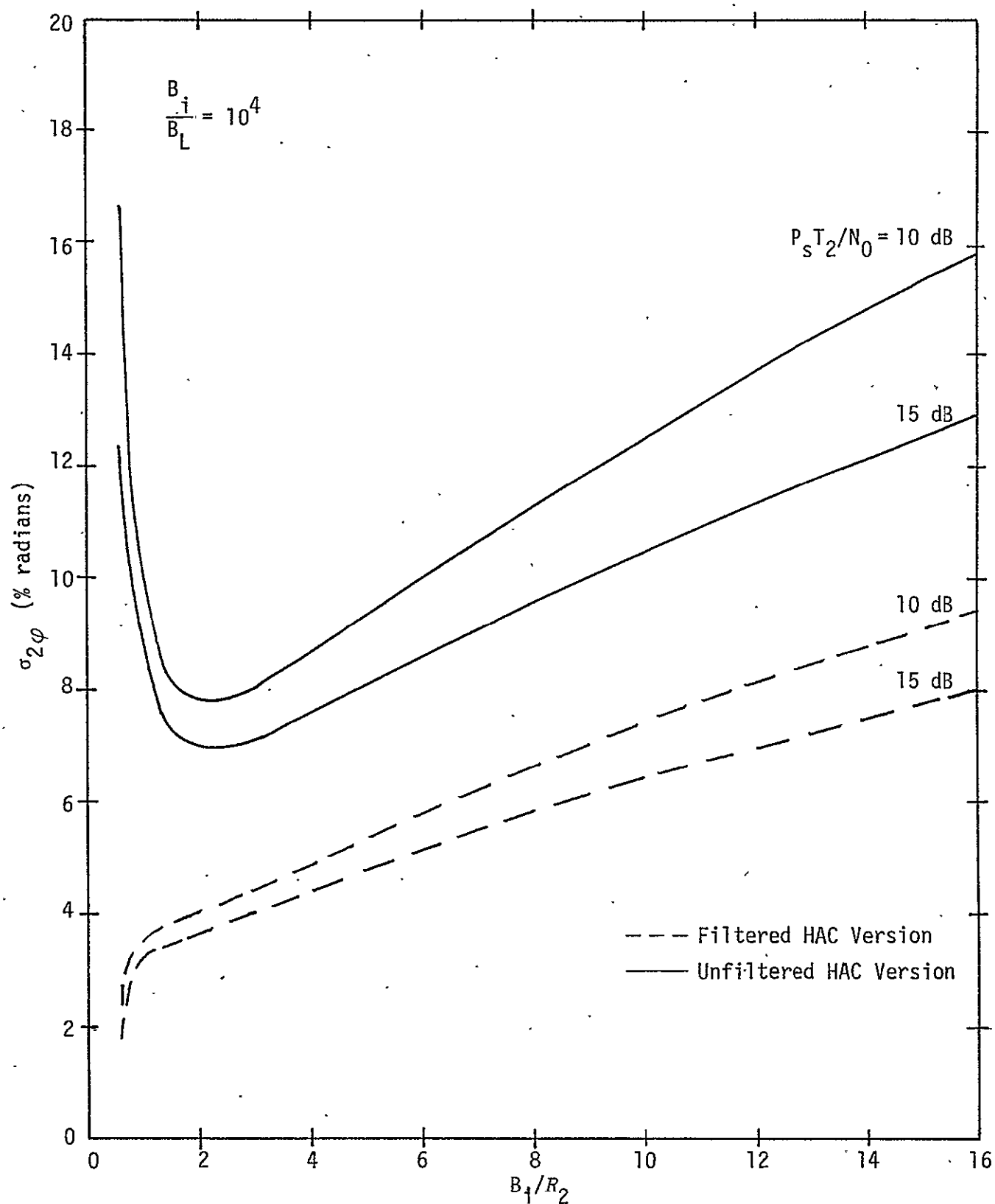


Figure 10. Tracking Jitter Standard Deviation vs. Ratio of Arm Filter Bandwidth to Data Rate; $m_2(t)$ is NRZ Data at $R_2 = 2$ Mbps, $m_3(t)$ is Manchester Coded Data at $R_3 = 192$ kbps.

$$\begin{aligned}
\varepsilon_c(t) &= [C(t) + n_i(t)] r'_c(t) \\
&= \frac{2}{\pi} \sqrt{P_3} m_3(t) T(\varphi + \frac{\pi}{2}) + \frac{2}{\pi} \sqrt{P_2} m_2(t) T(\varphi) \\
&\quad - \frac{2\sqrt{2}}{\pi} N_s(t) \sin \varphi(t) + \frac{2\sqrt{2}}{\pi} N_c(t) \cos \varphi(t), \quad (94b)
\end{aligned}$$

where the triangular correlation function $T(x)$ is defined in (37). Once again, we examine the channel power distribution at the phase detector outputs. From (94), we immediately find that

$$\begin{aligned}
P'_2 &= \text{Signal power in } \varepsilon_s(t) \big|_{\varphi=0} = \left(\frac{2}{\pi} \sqrt{P_2} \frac{\pi}{2} \right)^2 = P_2 \\
P'_3 &= \text{Signal power in } \varepsilon_c(t) \big|_{\varphi=0} = \left(\frac{2}{\pi} \sqrt{P_3} \frac{\pi}{2} \right)^2 = P_3. \quad (95)
\end{aligned}$$

Thus, the demodulated powers (in the absence of crosstalk) in channels 2 and 3 are identical to the transmitted powers in these same channels as is the ratio of these powers. After lowpass filtering by the Costas loop arm filters and multiplication in the analog error signal multiplier, the dynamic error signal becomes

$$\begin{aligned}
z_0(t) &\triangleq z_s(t) z_c(t) \\
&= \frac{4}{\pi^2} [P_2 \hat{m}_2^2(t) - P_3 \hat{m}_3^2(t)] T(\varphi) T(\varphi + \frac{\pi}{2}) \\
&\quad + \frac{4}{\pi^2} \sqrt{P_2 P_3} \hat{m}_2(t) \hat{m}_3(t) [T^2(\varphi + \frac{\pi}{2}) - T^2(\varphi)] + \frac{1}{2} v_2[t, 2\varphi(t)], \quad (96)
\end{aligned}$$

where

$$\begin{aligned}
v_2[t, 2\varphi(t)] &= \frac{8}{\pi^2} \{ [\hat{N}_s^2(t) - \hat{N}_c^2(t)] \sin 2\varphi(t) - 2\hat{N}_c(t) \hat{N}_s(t) \cos 2\varphi(t) \} \\
&\quad + \frac{8\sqrt{2}}{\pi^2} [\sqrt{P_2} \hat{m}_2(t) T(\varphi + \frac{\pi}{2}) - \sqrt{P_3} \hat{m}_3(t) T(\varphi)] \\
&\quad \times [\hat{N}_c(t) \cos \varphi(t) - \hat{N}_s(t) \sin \varphi(t)] \\
&\quad - \frac{8\sqrt{2}}{\pi^2} [\sqrt{P_2} \hat{m}_2(t) T(\varphi) + \sqrt{P_3} \hat{m}_3(t) T(\varphi + \frac{\pi}{2})] \\
&\quad \times [\hat{N}_c(t) \sin \varphi(t) + \hat{N}_s(t) \cos \varphi(t)]. \quad (97)
\end{aligned}$$

Letting (see Figure 11)

$$S_0(2\varphi) \triangleq T(\varphi) T(\varphi + \frac{\pi}{2})$$

$$S_{23}(2\varphi) \triangleq T^2(\varphi + \frac{\pi}{2}) - T^2(\varphi), \quad (98)$$

and making similar assumptions as before leading to the derivation of (54), we get the stochastic differential equation of operation

$$\frac{2d\varphi}{dt} = -KF(p) \left\{ \frac{8}{\pi} (P_2 D_2 - P_3 D_3) S_0(2\varphi) + n_e(t, 2\varphi) \right\}, \quad (99)$$

where

$$n_e(t, 2\varphi) = v_2(t, 2\varphi) - \frac{8}{\pi} P_3 n_3(t) S_0(2\varphi) + \frac{8}{\pi} P_2 n_2(t) S_0(2\varphi) + \frac{8}{\pi} \sqrt{P_2 P_3} n_{23}(t) S_{23}(2\varphi) \quad (100)$$

with $v_2(t, 2\varphi)$ now given by (97) and $n_2(t)$, $n_3(t)$, and $n_{23}(t)$ still defined by (56).

From (99), we observe that the equivalent S-curve is given by

$$S(2\varphi) \triangleq \frac{8}{\pi} (P_2 D_2 - P_3 D_3) S_0(2\varphi) \quad (101)$$

with slope at the origin (see Figure 11),

$$K_{2\varphi} \triangleq \left. \frac{dS(2\varphi)}{d2\varphi} \right|_{\varphi=0} = \frac{2}{\pi} (P_2 D_2 - P_3 D_3). \quad (102)$$

Furthermore, by analogy with the reasoning used to arrive at the equivalent noise spectral density given in (68), we now get

$$N_e \triangleq 2 \int_{-\infty}^{\infty} \langle n_e(t, 0) n_e(t + \tau, 0) \rangle d\tau$$

$$= 8 P_2 P_3 D_{23} + 4 \left(\frac{8}{\pi} \right) \left\{ P_2 N_0 D_2 K_{D_2} + P_3 N_0 D_3 K_{D_3} + \left(\frac{8}{\pi} \right) \frac{N_0^2}{2} B_i K_L \right\}. \quad (103)$$

Thus, substituting (102) and (103) in (71) and relating the result to the equivalent expression for effective loop signal-to-noise ratio given in (72), we get the loop squaring loss, namely,

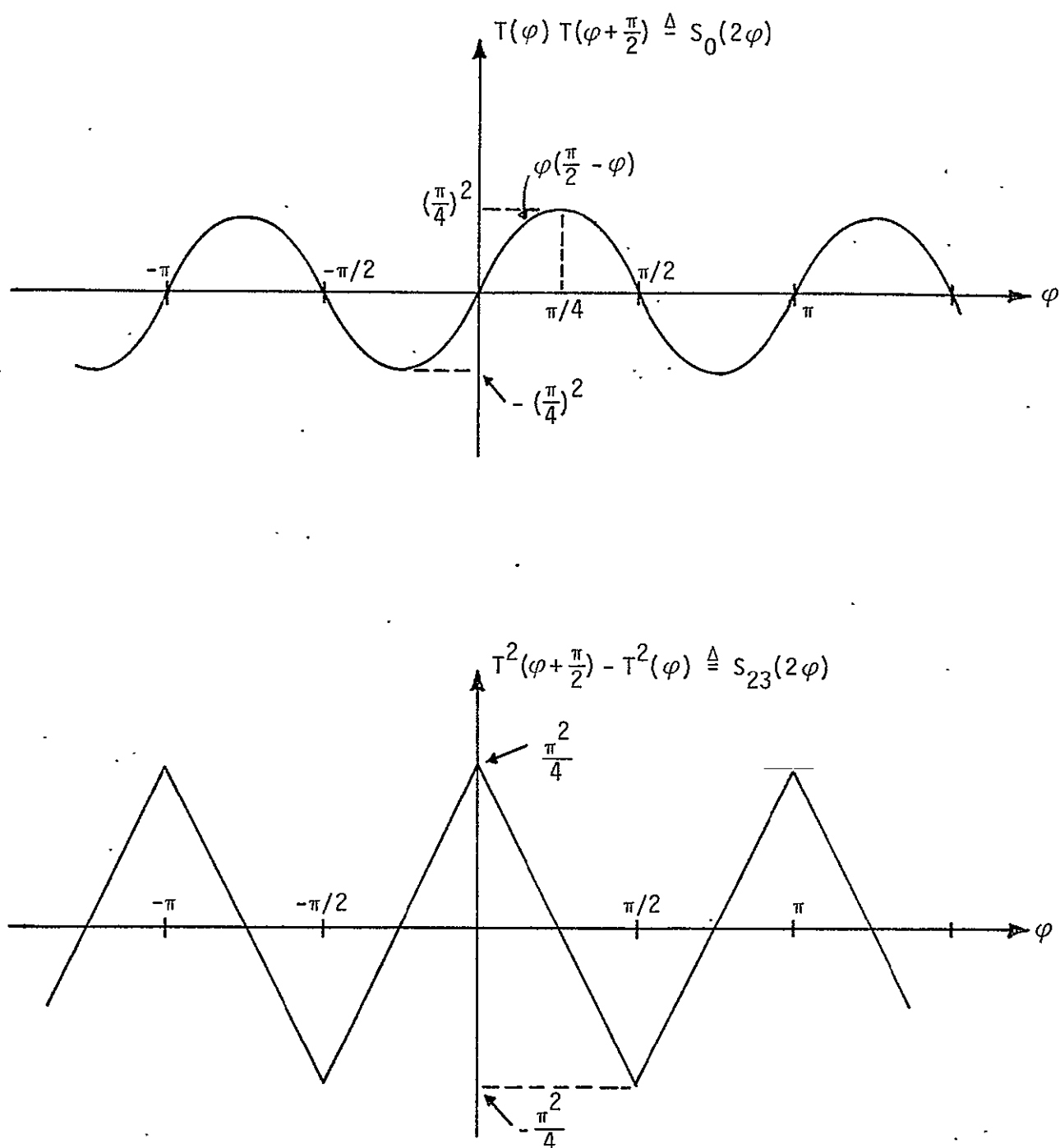


Figure 11. S-Curve and Cross-Modulation Noise Correlation Function for Quadrature-Multiplex Implementation

$$S_L = \frac{(P_2 D_2 - P_3 D_3)^2 / P_s}{2 \left\{ P_2 D_2 K_{D_2} + P_3 D_3 K_{D_3} + \frac{8}{\pi^2} \left(\frac{N_0 B_i}{2} \right) K_L \right\} + \frac{\pi^2}{2} \left(\frac{P_2 P_3 D_{23}}{N_0} \right)} \quad (104)$$

Alternately, in terms of the modulation indices

$$n_i = \frac{P_i}{P_s}; \quad i = 2, 3$$

and the total signal-to-noise ratio $R_{s2} = P_s T_2 / N_0$ in the high data rate bandwidth, (104) simplifies to

$$S_L = \frac{(n_2 D_2 - n_3 D_3)^2}{2 \left\{ n_2 D_2 K_{D_2} + n_3 D_3 K_{D_3} + \left(\frac{8}{\pi^2} \right) \frac{B_i / R_2}{2 R_{s2}} K_L + \left(\frac{\pi^2}{8} \right) 2 n_2 n_3 R_{s2} \left(\frac{D_{23}}{T_2} \right) \right\}} \quad (105)$$

Figure 12 illustrates S_L as computed from (105) versus B_i / R_2 for the same parameters as in Figure 9. Figure 13 is the corresponding plot of rms tracking jitter performance as computed from (77) together with (105) and (93).

SUBCARRIER DEMODULATION OF THE HAC VERSION USING A COSTAS-TYPE LOOP WITH REFERENCES MATCHED TO THE EQUIVALENT IN-PHASE AND QUADRATURE SUBCARRIERS

In our discussion of Costas loop tracking of the HAC version of the three-channel modulator, we alluded to the fact that, in the absence of crosstalk, an improvement in performance could be obtained by using a pair of demodulation reference signals which were matched to the equivalent in-phase and quadrature subcarriers. A Costas-type loop which incorporates such a pair of demodulation references [see (43)] is illustrated in Figure 14. As before, we shall assume that the in-phase and quadrature phase detectors are of the switching type and the error signal multiplier is analog. With (31) as an input signal and (43) as demodulation references, the in-phase and quadrature phase detector outputs are (ignoring second and higher order harmonic terms)

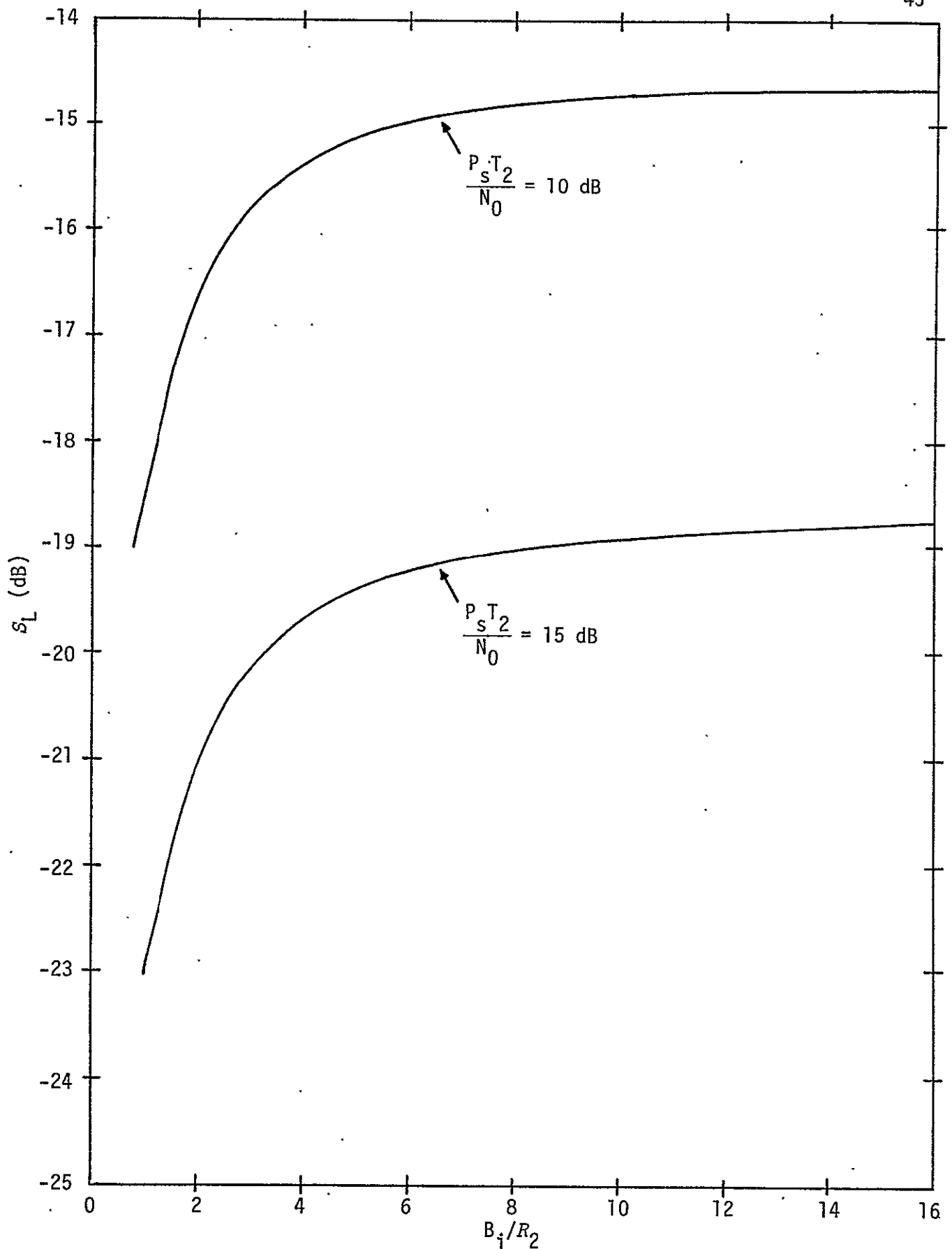


Figure 12. Squaring Loss vs. Ratio of Two-Sided Arm Filter Bandwidth to High Data Rate for Quadrature Multiplex Implementation (NASA Version) With Squarewave Subcarriers; $m_2(t)$ is NRZ Data at $R_2 = 2$ Mbps, $m_3(t)$ is Manchester Coded Data at $R_3 = 192$ kbps

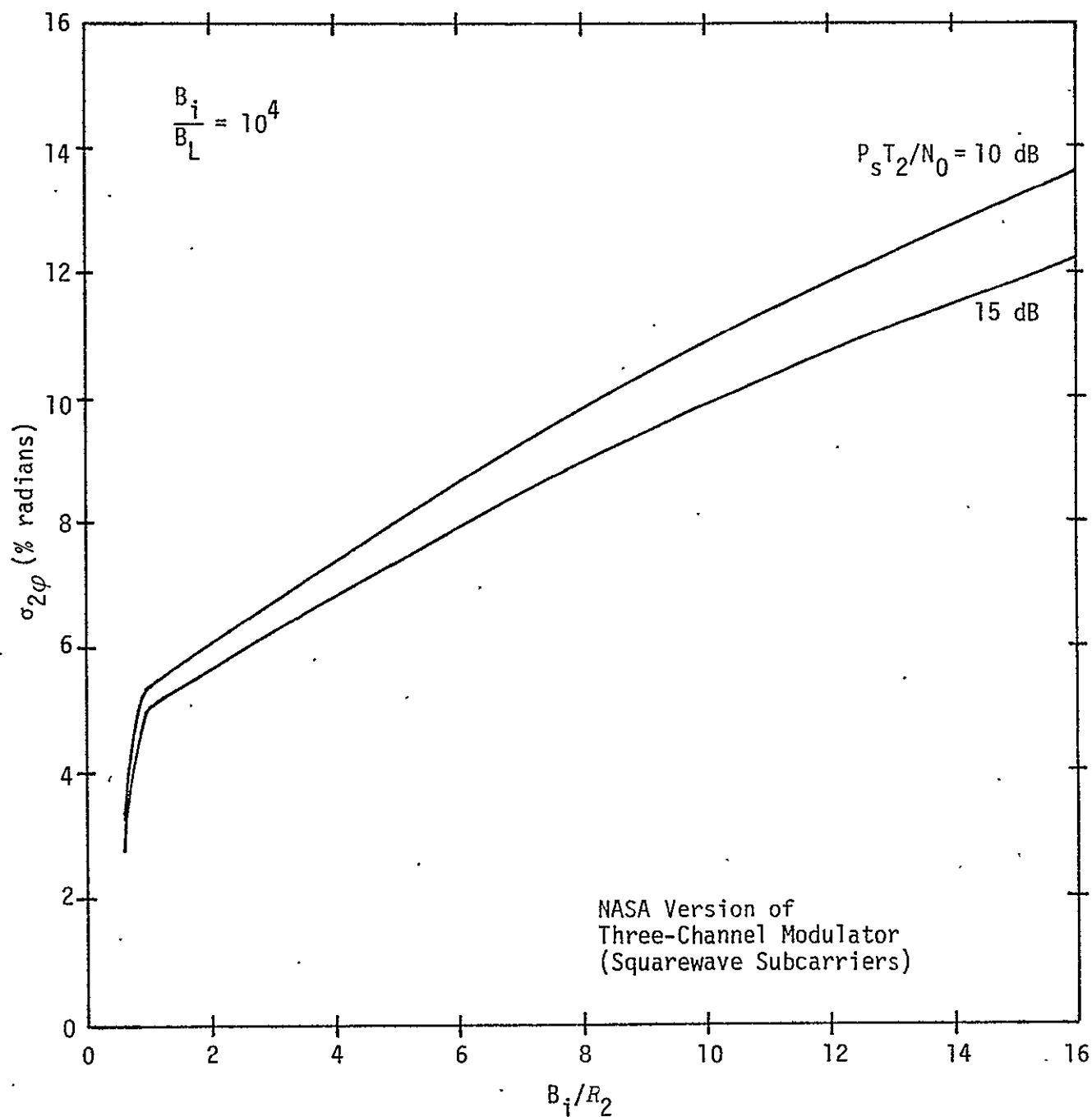


Figure 13. Tracking Jitter Standard Deviation vs. Ratio of Arm Filter Bandwidth to Data Rate; $m_2(t)$ is NRZ Data at $R_2 = 2 \text{ Mbps}$; $m_3(t)$ is Manchester Coded Data at $R_3 = 192 \text{ kbps}$

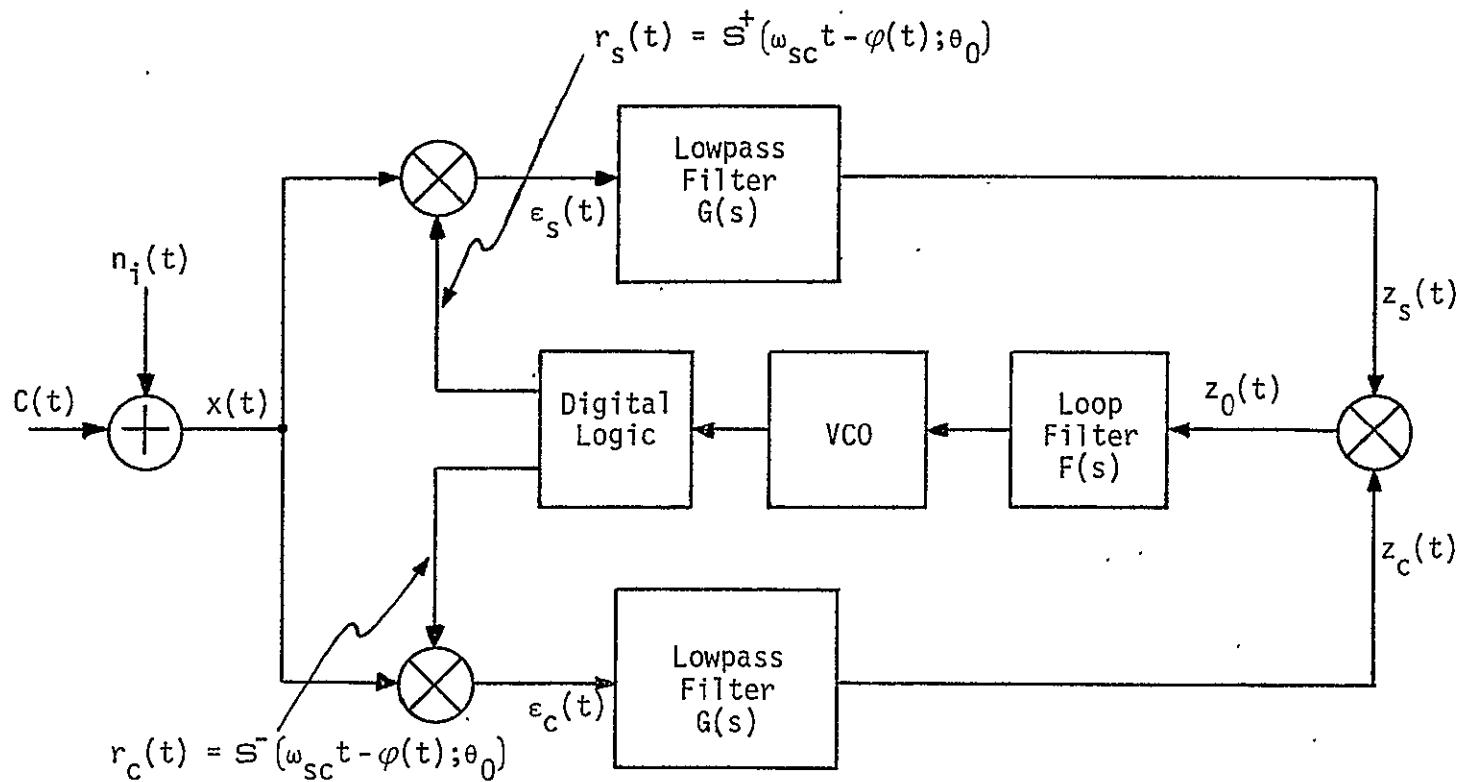


Figure 14. Costas-Type Subcarrier Tracking Loop With References Matched to Equivalent In-Phase and Quadrature Subcarriers

$$\begin{aligned}
\varepsilon_s(t) &= \sqrt{P_s} m_2(t) \langle S^+(\omega_{sc} t; \theta_0) S^+(\omega_{sc} t - \varphi; \theta_0) \rangle \\
&\quad + \sqrt{P_s} m_3(t) \langle S^-(\omega_{sc} t; \theta_0) S^+(\omega_{sc} t - \varphi; \theta_0) \rangle \\
&\quad + \sqrt{2} N_c(t) \langle \cos \omega_{sc} t S^+(\omega_{sc} t - \varphi; \theta_0) \rangle \\
&\quad - \sqrt{2} N_s(t) \langle \sin \omega_{sc} t S^+(\omega_{sc} t - \varphi; \theta_0) \rangle \\
\varepsilon_c(t) &= \sqrt{P_s} m_2(t) \langle S^+(\omega_{sc} t; \theta_0) S^-(\omega_{sc} t - \varphi; \theta_0) \rangle \\
&\quad + \sqrt{P_s} m_3(t) \langle S^-(\omega_{sc} t; \theta_0) S^-(\omega_{sc} t - \varphi; \theta_0) \rangle \\
&\quad + \sqrt{2} N_c(t) \langle \cos \omega_{sc} t S^-(\omega_{sc} t - \varphi; \theta_0) \rangle \\
&\quad - \sqrt{2} N_s(t) \langle \sin \omega_{sc} t S^-(\omega_{sc} t - \varphi; \theta_0) \rangle .
\end{aligned} \tag{106}$$

From the definitions of $S^+(\omega_{sc} t; \theta_0)$ and $S^-(\omega_{sc} t; \theta_0)$ given in (12), one can simplify (106) to

$$\begin{aligned}
\varepsilon_s(t) &= \frac{\sqrt{P_s}}{\pi} m_2(t) T_{22}(\varphi + \frac{\pi}{2}; \theta_0) - \frac{\sqrt{P_s}}{\pi} m_3(t) T_{23}(\varphi + \frac{\pi}{2}; \theta_0) \\
&\quad - \frac{2\sqrt{2}}{\pi} \cos \theta_0 [N_s(t) \cos \varphi(t) + N_c(t) \sin \varphi(t)] \\
\varepsilon_c(t) &= \frac{\sqrt{P_s}}{\pi} m_2(t) T_{23}(\varphi + \frac{\pi}{2}; \theta_0) + \frac{\sqrt{P_s}}{\pi} m_3(t) T_{33}(\varphi + \frac{\pi}{2}; \theta_0) \\
&\quad - \frac{2\sqrt{2}}{\pi} \sin \theta_0 [N_s(t) \sin \varphi(t) - N_c(t) \cos \varphi(t)] ,
\end{aligned} \tag{107}$$

where (see Figure 15)

$$\begin{aligned}
T_{22}(\varphi + \frac{\pi}{2}; \theta_0) &= T(\varphi + \frac{\pi}{2}) + \frac{1}{2} T(\varphi + \frac{\pi}{2} + 2\theta_0) + \frac{1}{2} T(\varphi + \frac{\pi}{2} - 2\theta_0) \\
T_{33}(\varphi + \frac{\pi}{2}; \theta_0) &= T(\varphi + \frac{\pi}{2}) - \frac{1}{2} T(\varphi + \frac{\pi}{2} + 2\theta_0) - \frac{1}{2} T(\varphi + \frac{\pi}{2} - 2\theta_0) \\
T_{23}(\varphi + \frac{\pi}{2}; \theta_0) &= \frac{1}{2} T(\varphi + \frac{\pi}{2} - 2\theta_0) - \frac{1}{2} T(\varphi + \frac{\pi}{2} + 2\theta_0) .
\end{aligned} \tag{108}$$

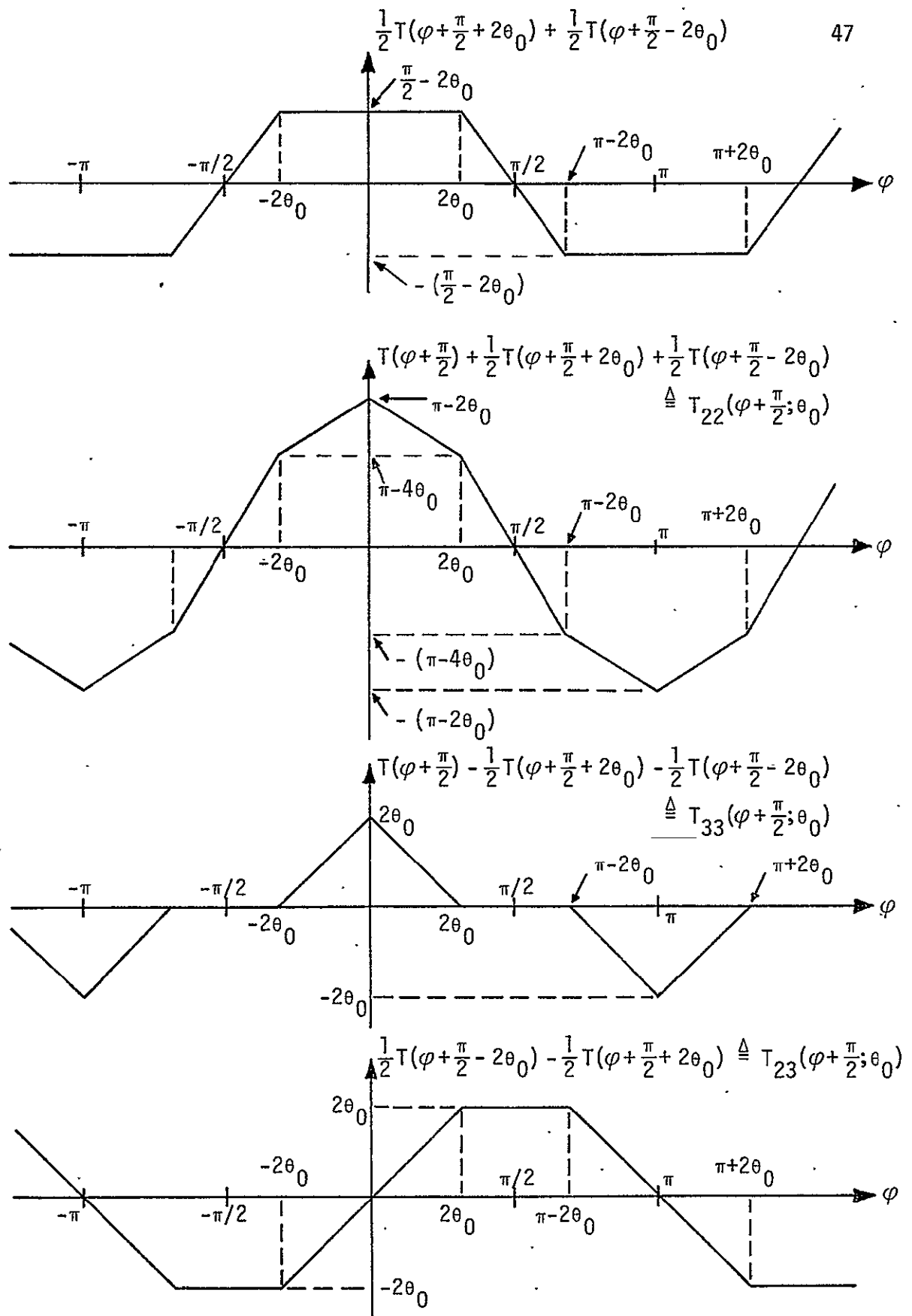


Figure 15. Phase Detector Output Correlation Functions for Channels 2 and 3

After lowpass filtering in the Costas loop arm filters and multiplication in the analog error signal multiplier, the dynamic error signal becomes

$$\begin{aligned}
 z_0(t) &\triangleq z_s(t) z_c(t) \\
 &= \frac{P_s}{\pi} \left\{ \hat{m}_2^2(t) S_2(2\varphi; \theta_0) - \hat{m}_3^2(t) S_3(2\varphi; \theta_0) + \hat{m}_2(t) \hat{m}_3(t) S_{23}(2\varphi; \theta_0) \right\} \\
 &\quad + \frac{1}{2} v_2[t, 2\varphi(t)], \tag{109}
 \end{aligned}$$

where (see Figure 16)

$$\begin{aligned}
 S_2(2\varphi; \theta_0) &\triangleq T_{22}(\varphi + \frac{\pi}{2}; \theta_0) T_{23}(\varphi + \frac{\pi}{2}; \theta_0) \\
 S_3(2\varphi; \theta_0) &\triangleq T_{33}(\varphi + \frac{\pi}{2}; \theta_0) T_{23}(\varphi + \frac{\pi}{2}; \theta_0) \\
 S_{23}(2\varphi; \theta_0) &\triangleq T_{22}(\varphi + \frac{\pi}{2}; \theta_0) T_{33}(\varphi + \frac{\pi}{2}; \theta_0) - T_{23}^2(\varphi + \frac{\pi}{2}; \theta_0) \tag{110}
 \end{aligned}$$

and

$$\begin{aligned}
 v_2[t, 2\varphi(t)] &= \frac{8}{\pi} \sin \theta_0 \cos \theta_0 \left\{ [\hat{N}_s^2(t) - \hat{N}_c^2(t)] \sin 2\varphi(t) \right. \\
 &\quad \left. - 2 \hat{N}_c(t) \hat{N}_s(t) \cos 2\varphi(t) \right\} \\
 &\quad + \frac{4\sqrt{2}}{\pi} (\sin \theta_0) \sqrt{P_s} [\hat{m}_2(t) T_{22}(\varphi + \frac{\pi}{2}; \theta_0) - \hat{m}_3(t) T_{23}(\varphi + \frac{\pi}{2}; \theta_0)] \\
 &\quad \times [\hat{N}_c(t) \cos \varphi(t) - \hat{N}_s(t) \sin \varphi(t)] \\
 &\quad - \frac{4\sqrt{2}}{\pi} (\cos \theta_0) \sqrt{P_s} [\hat{m}_2(t) T_{23}(\varphi + \frac{\pi}{2}; \theta_0) + \hat{m}_3(t) T_{33}(\varphi + \frac{\pi}{2}; \theta_0)] \\
 &\quad \times [\hat{N}_c(t) \sin \varphi(t) + \hat{N}_s(t) \cos \varphi(t)] . \tag{111}
 \end{aligned}$$

Comparing (109) and (111) with (46) and (47), we can immediately observe that the stochastic differential equation of loop operation and equivalent additive noise are given once again by (54) and (55), respectively, with, however, $S_2(2\varphi; \theta_0)$, $S_3(2\varphi; \theta_0)$, $S_{23}(2\varphi; \theta_0)$ defined by (110) and $v_2[t, 2\varphi(t)]$ defined by (111).

The equivalent loop S-curve is still given by (57) but its slope is now (see Figure 16)

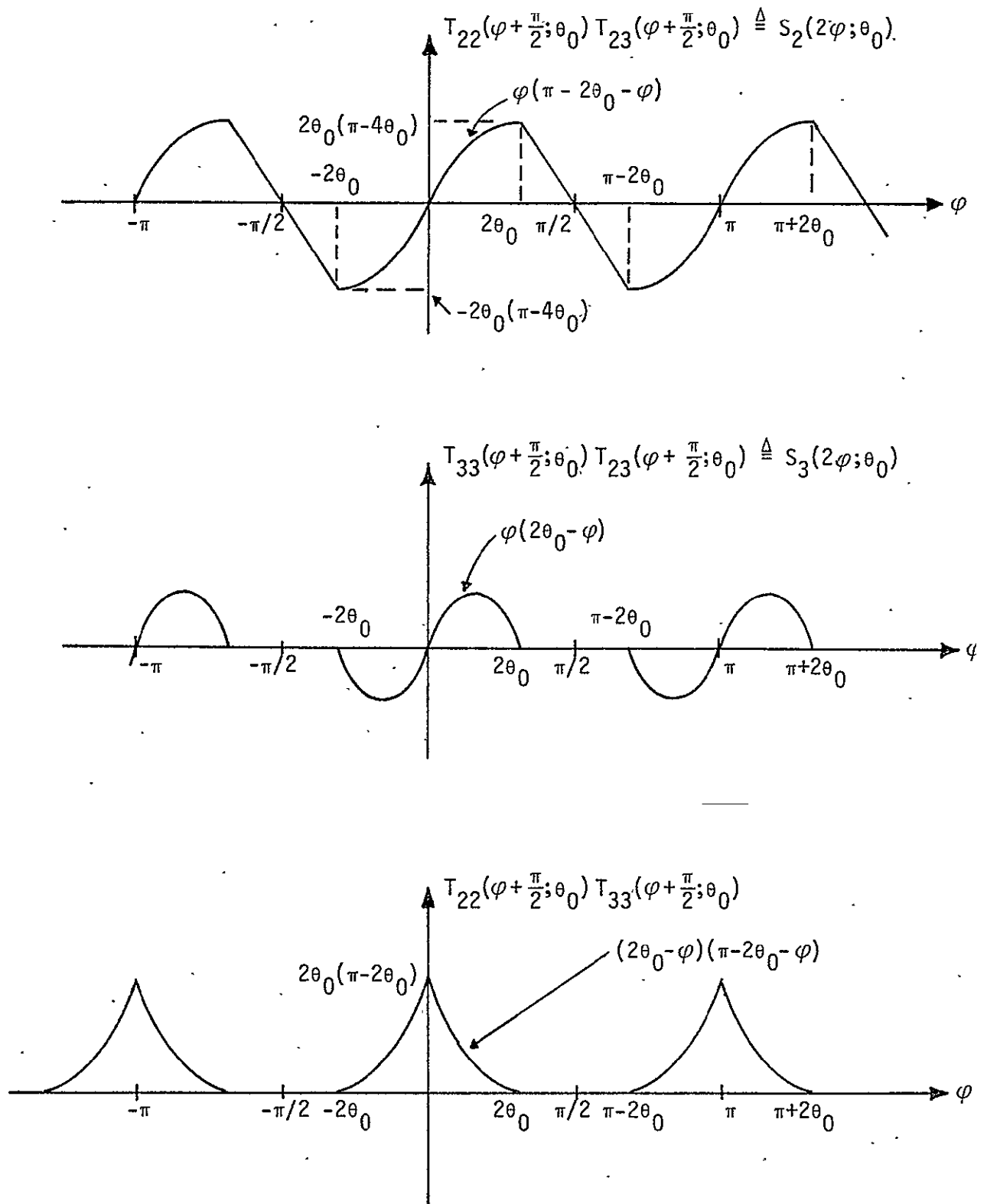


Figure 16. S-Curve Components

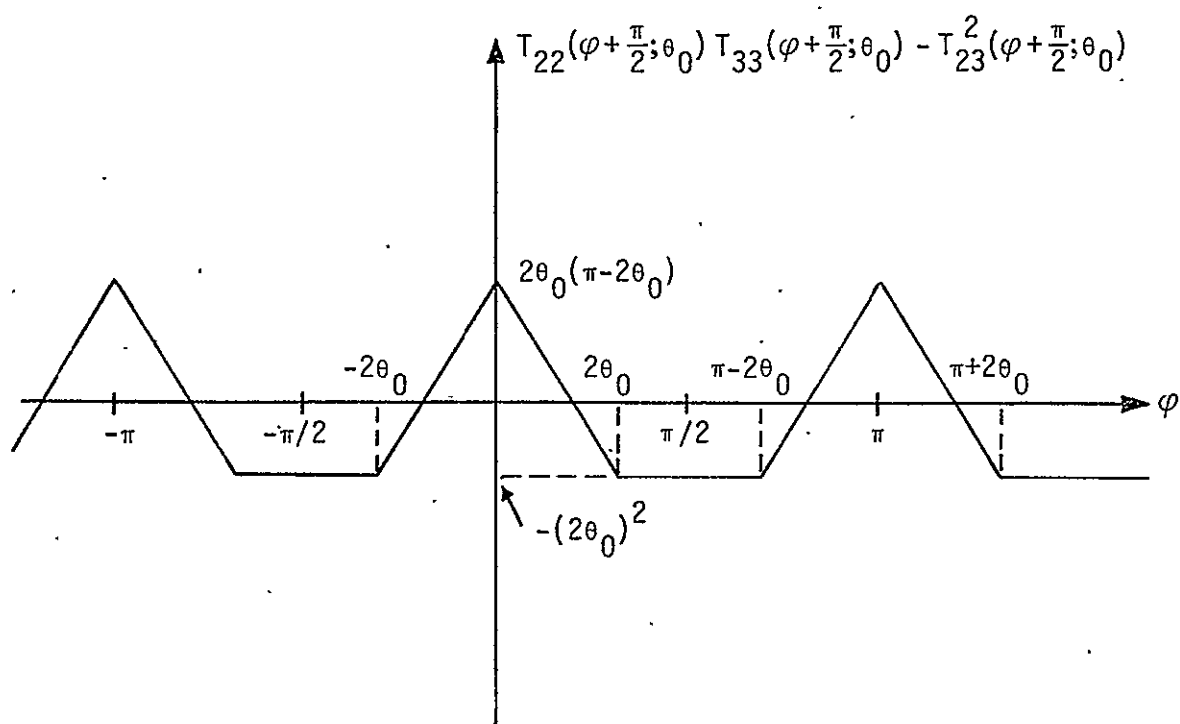
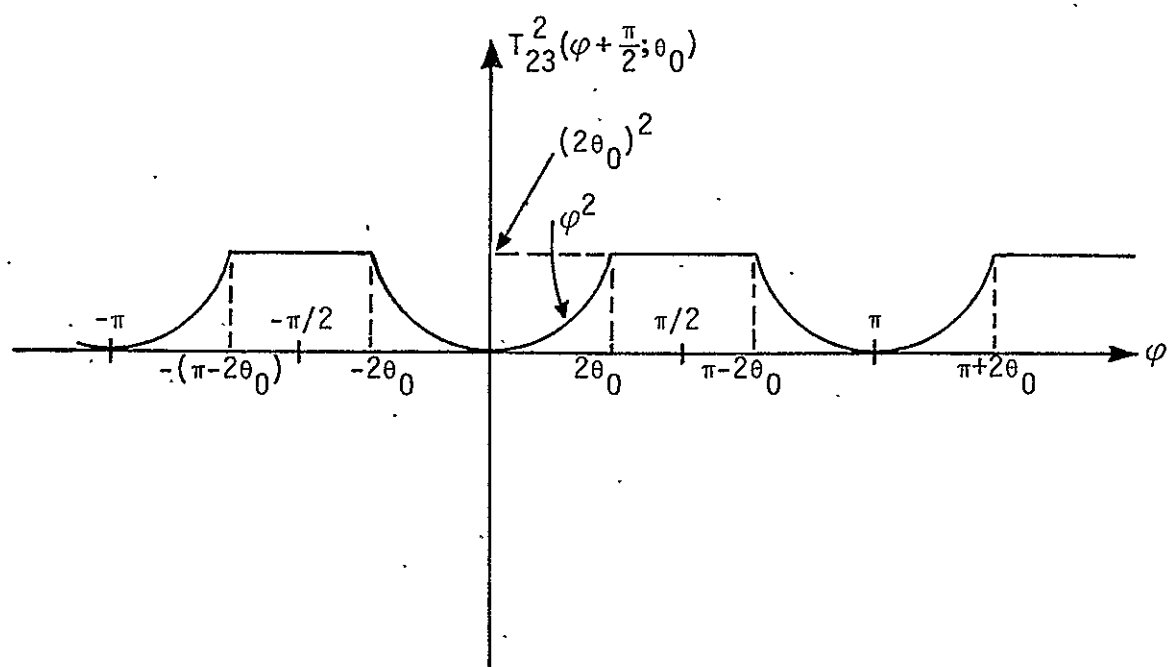


Figure 16 (continued)

$$\begin{aligned}
K_2 &\triangleq \left. \frac{dS(2\varphi; \theta_0)}{d2\varphi} \right|_{\varphi=0} = \frac{P_S}{\pi^2} D_2(\pi - 2\theta_0) - \frac{P_S}{\pi^2} D_3(2\theta_0) \\
&= \frac{P_S}{\pi^2} \left[D_2\left(1 - \frac{2\theta_0}{\pi}\right) - D_3\left(\frac{2\theta_0}{\pi}\right) \right] \quad (112)
\end{aligned}$$

which is one-half the value given in (59) for Costas tracking using squarewave demodulation references. Furthermore, comparing (111) with (47), and recognizing that

$$\begin{aligned}
T_{22}\left(\frac{\pi}{2}; \theta_0\right) &= T^+\left(\frac{\pi}{2}; \theta_0\right) = \pi - 2\theta_0 \\
T_{23}\left(\frac{\pi}{2}; \theta_0\right) &= T^-\left(\frac{\pi}{2}; \theta_0\right) = T^+(0; \theta_0) = 0 \\
T_{33}\left(\frac{\pi}{2}; \theta_0\right) &= -T^-(0; \theta_0) = 2\theta_0, \quad (113)
\end{aligned}$$

we immediately arrive at the equivalent noise spectral density N_e , namely,

$$\begin{aligned}
N_e &= 8P_2'P_3'D_{23} + 4\left(\frac{8}{\pi^2}\right) \left\{ P_2'N_0D_2K_{D_2} \sin^2 \theta_0 + P_3'N_0D_3K_{D_3} \cos^2 \theta_0 \right. \\
&\quad \left. + \left(\frac{8}{\pi^2}\right) \frac{N_0^2}{2} B_i K_L \sin^2 \theta_0 \cos^2 \theta_0 \right\}. \quad (114)
\end{aligned}$$

Thus, substituting (112) and (114) in (71), we obtain the squaring loss of the Costas loop of Figure 14, namely,

$$\begin{aligned}
S_L &= \frac{[\sqrt{\eta_2'} D_2 - \sqrt{\eta_3'} D_3]^2}{8 \left\{ \eta_2' D_2 K_{D_2} \sin^2 \theta_0 + \eta_3' D_3 K_{D_3} \cos^2 \theta_0 + \frac{8}{\pi^2} \frac{B_i/R_s}{2R_{s2}} K_L \sin^2 \theta_0 \cos^2 \theta_0 + \left(\frac{2}{8}\right) 2\eta_2'\eta_3'R_{s2} \left(\frac{D_{23}}{T_2}\right) \right\}} \quad (115)
\end{aligned}$$

where, in addition, we have used the definitions of the modulation indices η_2', η_3' given in (74). Also from (74), we have that

$$\begin{aligned}
\sin \theta_0 &= \sin \left(\frac{\pi}{2} \sqrt{\eta_3'} \right) \\
\cos \theta_0 &= \cos \left(\frac{\pi}{2} \sqrt{\eta_3'} \right) \quad (116)
\end{aligned}$$

which, when substituted in (115) gives the final expression for squaring loss. Figure 17 illustrates S_L of (115) versus B_1/R_2 with R_{s2} fixed and the same data rates and formats used to plot Figure 9. Comparing Figure 17 with Figure 9, we observe that the Costas-type loop with matched subcarrier waveforms has considerably poorer tracking performance than the Costas loop with quadrature subcarriers. The principal reason for this stems from the reduction by a factor of two of the equivalent S-curve slope or in terms of squaring loss, which is directly proportional to the square of this slope, a loss of 6 dB. Some of this 6 dB is recovered by the fact that, with the matched equivalent subcarrier references, the signal \times noise and noise \times noise terms are reduced relative to their values when quadrature squarewaves are used. Nevertheless, the overall effect is dominated by the reduction in S-curve slope.

CONCLUSIONS

In this report, we have examined and compared the performance of several implementations of the three-channel Ku-band modulator on-board the SS0. In particular, we have studied the power allocation properties both at the transmitter and the receiver (after demodulation) of these configurations and their ability, in terms of squaring loss and subcarrier phase jitter, to be tracked by an in-phase-quadrature type subcarrier reconstruction loop, e.g., a Costas loop.

We have found from the power allocation study that much care must be exercised in choosing a modulation angle for the unbalanced QPSK subcarrier since, depending on the modulator implementation, the transmitted and demodulated power ratio can be considerably different. For example, for the NASA version and the HAC version with bandpass filter following the subcarrier modulator, the transmitted and demodulated power ratios are identical, whereas for the unfiltered HAC version, the demodulated power ratio is the square of the transmitted ratio.

In all cases, we have assumed a Costas-type tracking loop with switching type in-phase and quadrature phase detectors, single pole (RC) Butterworth arm filters, and an analog type error signal multiplier. This is not to say that the analyses cannot be carried out for the case where the error signal multiplier is of the switching type. However, due to the increased complexity of calculating the equivalent noise spectral density, it was decided to first present the tradeoff study

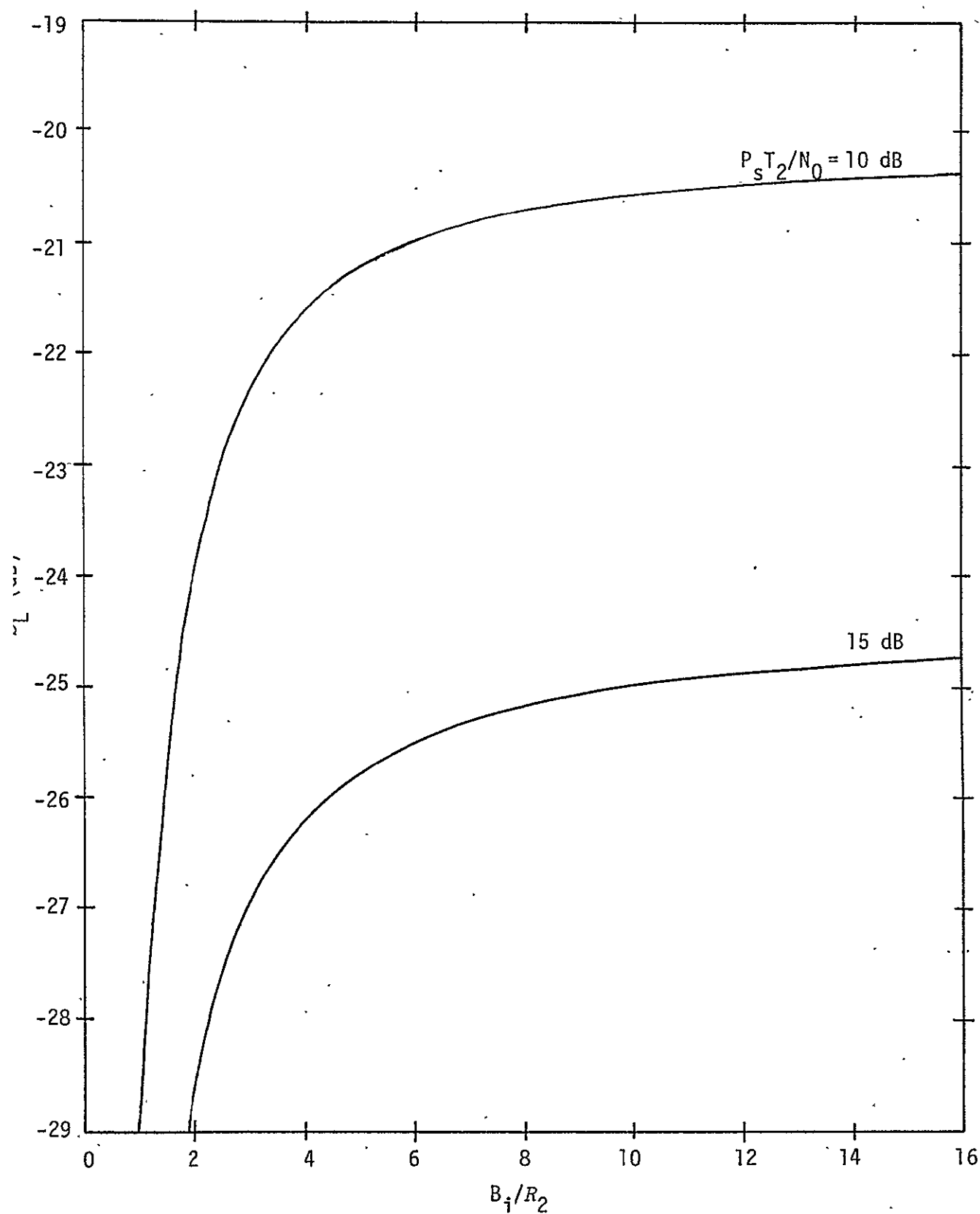


Figure 17. Squaring Loss vs. Ratio of Two-Sided Arm Filter Bandwidth to High Data Rate for Costas Loop Tracking with References Matched to Equivalent In-Phase and Quadrature Subcarriers of HAC Version

for the simpler-to-analyze case of the analog error signal multiplier. We also point out that one should not attempt to draw conclusions either quantitative or qualitative about the performance of the loop with a switching error signal multiplier from the results given in this report for the analog error signal multiplier case. Indeed, the S-curves are quite different for the two cases and, moreover, the tracking performance as measured by mean-squared jitter would be similarly different.

To conclude this report, we shall summarize in the tables below the principal results obtained. Table 1 gives the signal and noise powers available in each channel for data detection, and the detection signal-to-noise ratio obtained by taking the ratio of these two powers. The assumption made is that the outputs of the input in-phase and quadrature phase detectors in the Costas loop demodulator are filtered with integrate-and-dump circuits respectively matched to the data rates R_2 and R_3 . The outputs of these filters in the absence of crosstalk, namely,

$$\begin{aligned} z_s^* &= \frac{1}{T_2} \int_0^{T_2} \epsilon_s(t) \Big|_{\varphi=0} dt \\ z_c^* &= \frac{1}{T_3} \int_0^{T_3} \epsilon_c(t) \Big|_{\varphi=0} dt, \end{aligned} \quad (117)$$

have signal and noise components whose powers are, respectively, the channel 2 and channel 3 entries in Table 1. In all cases, the ratio of detected signal power in channel 2 to detected signal power in channel 3 is chosen equal to 4.

In Table 2, we give the squaring loss and rms tracking jitter for several values of arm filter bandwidth (two-sided) to high data rate.

Table 1

	Modulation Angle θ_0	Detected Signal Power Channel 2	Detected Signal Power Channel 3	Detected Noise Power Channel 2	Detected Noise Power Channel 3	$(\text{SNR})_2$ $\frac{P_s T_2}{N_0}$	$(\text{SNR})_3$ $\frac{P_s T_3}{N_0}$
HAC Version	30°	$(1 - \frac{2}{\pi} \theta_0)^2 P_s$ $= 4/9 P_s$	$(\frac{2}{\pi} \theta_0)^2 P_s$ $= 1/9 P_s$	$(\frac{8}{\pi})^2 \frac{N_0}{T_2}$	$(\frac{8}{\pi})^2 \frac{N_0}{T_3}$	0.548	0.137
Filter HAC Version	26.57°	$(\frac{8}{\pi})^2 \cos^2 \theta_0 P_s$ $= 0.8 (\frac{8}{\pi})^2 P_s$	$(\frac{8}{\pi})^2 \sin^2 \theta_0 P_s$ $= 0.2 (\frac{8}{\pi})^2 P_s$	$(\frac{8}{\pi})^2 \frac{N_0}{T_2}$	$(\frac{8}{\pi})^2 \frac{N_0}{T_3}$	0.648	0.162
NASA Version with Squarewave Subcarriers	26.57°	$\cos^2 \theta_0 P_s$ $= 0.8 P_s$	$\sin^2 \theta_0 P_s$ $= 0.2 P_s$	$(\frac{8}{\pi})^2 \frac{N_0}{T_2}$	$(\frac{8}{\pi})^2 \frac{N_0}{T_3}$	0.987	0.247
HAC Version with Demodulation by Equivalent In- Phase and Quadra- ture Subcarriers	30°	$(1 - \frac{2}{\pi} \theta_0)^2 P_s$ $= 4/9 P_s$	$(\frac{2}{\pi} \theta_0)^2 P_s$ $= 1/9 P_s$	$(\frac{8}{\pi})^2 \cos^2 \theta_0 \frac{N_0}{T_2}$	$(\frac{8}{\pi})^2 \sin^2 \theta_0 \frac{N_0}{T_3}$	0.731	0.548

Table 2

$m_2(t)$ is NRZ data at $R_2 = 2$ Mbps;

$m_3(t)$ is Manchester coded data at $R_3 = 192$ kbps

$\frac{P_s T_2}{N_0} = 10 \text{ dB}$	$B_i/R_2 = 5$		$B_i/R_2 = 10$		$B_i/R_2 = 20$	
	$S_L, \text{ dB}$	$\sigma_{2\phi} (\% \text{ radians})$	$S_L, \text{ dB}$	$\sigma_{2\phi} (\% \text{ radians})$	$S_L, \text{ dB}$	$\sigma_{2\phi} (\% \text{ radians})$
HAC Version	-16.42	9.36	-15.93	12.5	-16.04	17.92
Filtered HAC Version	-11.73	5.46	-11.44	7.47	-11.56	10.71
NASA Version with Squarewave Subcarriers	-15.12	8.07	-14.72	10.89	-14.66	15.29
HAC Version with Demodulation by Equivalent In-Phase and Quadrature Subcarriers	-21.28	16.38	-20.56	21.33	-20.31	29.3

$\frac{P_s T_2}{N_0} = 15 \text{ dB}$	$B_i/R_2 = 5$		$B_i/R_2 = 10$		$B_i/R_2 = 20$	
	$S_L, \text{ dB}$	$\sigma_{2\phi} (\% \text{ radians})$	$S_L, \text{ dB}$	$\sigma_{2\phi} (\% \text{ radians})$	$S_L, \text{ dB}$	$\sigma_{2\phi} (\% \text{ radians})$
HAC Version	-20.16	8.1	-19.41	10.51	-19.1	14.36
Filtered HAC Version	-15.66	4.82	-15.16	6.44	-14.95	8.9
NASA Version with Squarewave Subcarriers	-19.4	7.42	-18.9	9.89	-18.64	13.61
HAC Version with Demodulation by Equivalent In-Phase and Quadrature Subcarriers	-25.8	15.49	-25.0	20.0	-24.63	27.1

REFERENCES

1. M. K. Simon. "Design Considerations Associated with a Digital Phase Shift Implementation of the Three-Channel Orbiter Ku-Band Modulator," Axiomatix Report No. R7708-1 (under Contract NAS 9-14614), August 1, 1977.
2. G. K. Huth and S. Udalov. Unpublished notes.
3. R. Cager. "Phase-State/Power Division Relationships in the Return Link Baseband Modulator," Hughes Aircraft Company Interdepartmental Correspondence HS237-782, June 14, 1977, and unpublished notes.
4. G. K. Huth et al. "Integrated Source and Channel Encoded Digital Communication System Design Study - Final Report," Axiomatix Report No. R7607-3 (under Contract NAS 9-13467), July 31, 1976.
5. S. Udalov. "Feasibility Study of an Interplex Modulation System for the Orbiter's Ku-Band Link," Axiomatix Report No. R7410-5 (under Contract NAS 9-13467), October 7, 1974.
6. S. Udalov. "Multiplexing Modulation Format for the Orbiter's Ku-Band Return Link," Axiomatix Report No. R7502-1 (under Contract NAS 9-13467), February 13, 1975.
7. D. Cartier et al. "Shuttle Communications Design Study - Final Report," Magnavox Report DRL No. T-975, March 31, 1975.
8. K. Tu. "Performance Analysis of the Proposed Three Channel Quadrature Modulation System," Lockheed Electronics Co., Inc., February 1976.
9. W. C. Lindsey. "Power Division Analysis of a Three Channel Unbalanced QPSK Signal Out of a Bandpass Limiter," LinCom Corporation Report TR No. 04-7604-8, April 1976.
10. M. K. Simon. "An Analysis of the Power Division Structure of a Bandpass Hardlimited Three-Channel Signal with Sinusoidal Subcarriers," Appendix G to "Study to Investigate and Evaluate Means of Optimizing the Ku-Band Communications Function for the Space Shuttle - Final Report," Axiomatix Report No. R7703-2 (under Contract NAS 9-13467), March 31, 1977.
11. M. K. Simon. "Subcarrier Tracking Analysis for Three-Channel Orbiter Ku-Band Return Link," Axiomatix Report No. R7707-4 (under Contract NAS 9-15240), July 28, 1977.
12. M. K. Simon and W. C. Lindsey. "Optimum Performance of Suppressed Carrier Receivers with Costas Loop Tracking," IEEE Transactions on Communications, Vol. COM-25, February 1977, pp. 215-226.
13. M. K. Simon and W. K. Alem. "Tracking Performance of Unbalanced QPSK Demodulators: Part I - Biphase Costas Loop With Passive Arm Filters," submitted for publication in the IEEE Transactions on Communications. Also see Axiomatix Report No. R7707-5, July 29, 1977.